



FIBER-OPTIC FABRY-PÉROT INTERFEROMETERS FOR FORCE SENSING ON THE TIP OF A NEEDLE

T.P.A. LEMBRECHTS
APRIL 2015



FIBER-OPTIC FABRY-PÉROT INTERFEROMETERS FOR FORCE SENSING ON THE TIP OF A NEEDLE

MASTER OF SCIENCE THESIS

For the degree of Master of Science in Mechanical Engineering
at Delft University of Technology

T.P.A. Lembrechts

April 2015

Faculty of Mechanical, Maritime and Materials Engineering (3mE)
Department of BioMechanical Engineering

Abstract

Physicians use small variations in the needle insertion force to identify tissue properties and detect membrane punctures during needle insertion. Navigation of a needle towards the target tissue, for example to take a biopsy, is often based on detecting these variations in force. Literature shows that presenting physicians force feedback based on forces on the needle tip instead of forces sensed by the physician at the hub of the needle, results in improved detection of membrane puncture events. Measurement of forces on the needle tip is also of interest for other applications like research on needle-tissue interaction forces. The currently studied FBG-based (optical) sensors for the measurement of forces on the needle tip suffer from a cross-sensitivity to temperature, which causes large measurement errors when the needle is inserted into the body of a patient [1, 2].

This thesis investigated several concepts for the design a force sensor based on a fiber-optic Fabry-Pérot interferometer to measure forces on the tip of a needle (18 G). Special attention was given to concepts for a force sensor with an intrinsic low cross-sensitivity to temperature. Three concepts, using either a quartz glass capillary, an Invar capillary or a thin polyimide film to convert force on the needle tip to a quantity measurable by the Fabry-Pérot interferometer, were investigated in more detail by means of (FE-)modeling and testing of prototypes.

Usage of a quartz capillary resulted in a sensor with a very low cross-sensitivity to temperature of 12 mN/°C and a good accuracy for the measurement of static forces (maximum observed measurement error of 65 mN for a range of 10 N). Limited strength of the sensor is however expected to prevent usage of the concept for small diameter needles. Prototypes of concepts using an Invar capillary or polyimide thin film did not perform equally good, although they are better suited for real applications due to better strength, while the latter concept could be suited for the design of a flexible, entirely MRI-compatible polymer needle.

Suggestions for methods to improve the measurement accuracy of the latter two prototypes were presented. It was concluded that a triaxial instead of uniaxial force sensor will be required to pursue a very high accuracy by compensating for measurement errors due to transverse forces on the needle tip. Usage of low coherence interferometry was furthermore identified to be better suited than homodyne interferometry to interrogate the FPI-based sensors in most occasions and enable the design of a sensor with an intrinsic low cross-sensitivity to temperature without using highly dimensionally stable but fragile materials like quartz glass.

Contents

1	Introduction	11
1.1	Background	11
1.2	Goal of this thesis	12
1.3	Motivation	13
1.3.1	Applications	13
1.3.2	Measurement of needle insertion forces and needle tip forces	15
1.3.3	Fiber-optic sensing	17
1.4	Structure of this thesis	23
2	Design problem	25
2.1	Problem statement	25
2.2	Requirements	26
3	Morphological scheme and Concepts	31
3.1	Elements of the design	31
3.2	Morphological scheme	32
3.2.1	Cannula	32
3.2.2	Stylet tube	32
3.2.3	Stylet tip	36
3.2.4	Optical fiber	37
3.2.5	FPI sensor interrogator	37
3.2.6	Temperature cross-sensitivity reducing method	38
3.2.7	Fabry-Pérot Interferometer	46
3.2.8	Force sensitive element	48
3.2.9	Temperature sensitive element	52
3.2.10	Reference FPI mirror	53
3.2.11	Second FPI mirror	53

3.2.12	FPI cavity medium	54
3.2.13	Light adsorbing/double cavity preventing element	54
3.2.14	Seal	56
3.2.15	Fiber-force/temperature sensitive element connection	57
3.2.16	Force sensitive element-needle tip connection	61
3.2.17	Stylet tube-force/temperature sensitive element connection	62
3.3	Concepts	62
3.3.1	Description of the concepts	62
3.4	Review of the concepts	70
4	Quartz-column concepts	73
4.1	Evaluation of the machined-quartz-columns concept	73
4.2	Design of prototypes of the unmachined-quartz-column concept	78
4.2.1	Manufacturing method	78
4.2.2	Strength of the design	79
4.2.3	Sensitivity of the FPI to force	81
4.2.4	Causes of measurement errors	82
4.3	Calibration method	85
4.3.1	Calibration setup and method	85
4.3.2	Analysis of the results	88
4.4	Calibration results of the unmachined-quartz-column concept	89
4.5	Discussion	95
5	Stylet tube concept	101
5.1	Design and manufacturing of the prototype	101
5.1.1	Manufacturing method	101
5.1.2	Sensitivity of the FPI to force and temperature and other causes of measurement errors	103
5.2	Calibration method	104
5.3	Calibration results	104
5.4	Discussion	112
6	Thin film concept	119
6.1	Design and manufacturing of a proof-of-concept	119
6.2	Calibration method	122
6.3	Calibration results	122
6.4	Discussion	127
7	Discussion	131
7.1	General insights	131
7.2	Achievements	133
7.3	Conclusions	135

7.4	Recommendations for further research	136
	Acknowledgements	139
	Appendices	141
A	The Fabry-Pérot interferometer	143
A.1	Operating principle	143
A.2	Fabrication methods	148
A.2.1	Air-filled cavities	148
A.2.2	Non-air filled cavities	151
B	Calibration of the ATI Nano 17	153
B.1	Objective of the calibration procedure	153
B.2	Definition of the true value	154
B.3	Experimental setup	155
B.4	Results	158
B.4.1	Noise and resolution	158
B.4.2	Measurement uncertainty	159
B.5	Discussion	162
C	Requirements in detail	167
C.1	Needle/stylet design	167
C.2	Measurement system/sensor design	170
C.3	Guidelines FPI design	175
C.4	Other guidelines	176
D	Details	177
D.1	The refractive index of air	177
D.2	Material selection for the spring of a force sensitive element	178
D.2.1	Constraints	178
D.2.2	Optimality criterion	179
D.2.3	Results	180
D.2.4	Discussion	181
D.3	Determination of temperature and force by using two FPIs	184
D.4	Selection of the optimal beam	185
D.5	Strength of quartz glass	188
D.6	'Low coherence interferometry' with the second generation OP1550	190
D.7	Details calibration results	197
D.8	Tables and graphs	218

List of symbols 243

1 Introduction

1.1 Background

Needle-like instruments were already in use by the Babylonians and Egyptians to clear natural orifices [3]. Sir Christopher Wren had the revolutionary idea to start performing intravenous injections with a needle-like instrument in the year 1657 [4]. Sir Wren was inspired by the detailed description of the blood circulation by William Harvey and proposed that the blood circulation could be used to carry liquid medicine throughout the entire body [4]. Wren experimented with intravenous injections of wine, ales and opium in dogs using a quill as needle and a bladder a syringe [3, 5]. His experiments inspired many investigators and physicians, despite initial dreadful outcomes of attempts at blood transfusion in that era (which, as we now know, were the result of immunologic reactions and the lack of the notion of sterility) [3, 6]. The first hollow drip type needle with syringe, which used gravity as driving force to inject a drug, was invented by Francis Rynd in 1844 [7, 8, 9, 3, 10, 11]. The invention, in 1853, of the first sharp needle tip that could cut tissue and the realization that a needle could be used to inject fluids very deep into the human body, is accredited to instrument maker Daniel Ferguson and physician Alexander Wood. Physician Charles Pravaz developed a needle with detachable syringe in the same year and is regarded together with Alexander Wood as the inventor of the needle and the syringe. Since then many inventors and physicians have proposed variations on the design of needles to reduce the amount of trauma due to the insertion of the needle and optimize the needle for certain procedures [11].

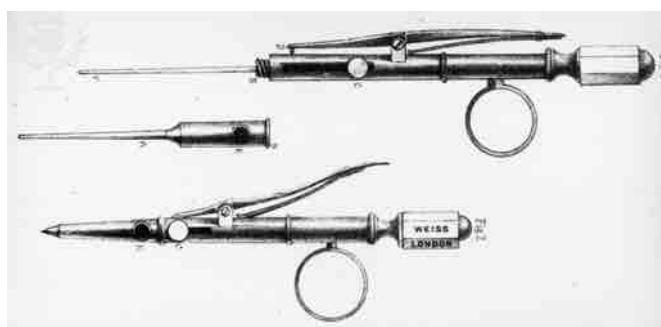


Figure 1.1: Needle and syringe designed by Francis Rynd in 1844 [12]

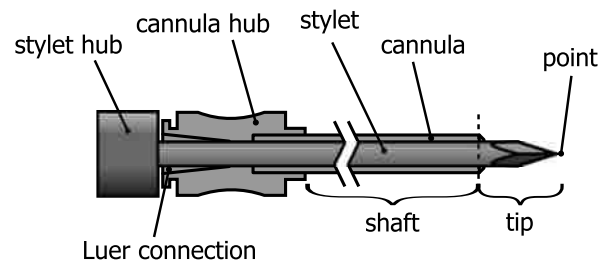


Figure 1.2: Overview of needle terminology [13]

The general design of a medical needle has remained more or less the same since its invention. A schematic representation of a needle is given in figure 1.2. A needle consists of a cannula, a hub and optionally an obturator. The cannula is a hollow tube, of which the inside is called the lumen [14, 13]. A cannula has often a ground bevel at its distal end. Conventional cannula diameters range from 10 G (3.4 mm) to 30 G (0.31 mm) [13]. A rod, called an obturator when the tip of the rod is blunt or a stylet when the tip is sharp, can be inserted in the lumen to prevent tissue from entering the lumen of the cannula during insertion of the needle into tissue. The fitting attached to the proximal end of the cannula, called the hub, can be used to connect the cannula to a syringe or other system or can be used by the surgeon to hold the needle. The needle tip is defined as the distal part of the cannula, which contains the bevel and, if present, the beveled part of the stylet [14]. The shaft of the needle is the part of the cannula that does not belong to the tip.

Needles are nowadays used for a wide variety of therapeutic as well as diagnostic medical procedures, as percutaneous (through the skin) needle insertion has proven to be an ideal method to gain invasive access to regions deep into the human body with minimal tissue damage [13, 15]. Percutaneous needle insertion has become one of the most common procedures in medicine [15, 16]. Regional anesthesia, biopsy, neurosurgery, deep brain stimulation, catheterization, ablation and brachytherapy are examples of complex procedures that rely heavily on the use of medical needles and accurate needle insertion [13, 17, 18]. New developments to improve needle insertion are of great interest due to the frequent occurrence of percutaneous needle insertions in healthcare [15]. One of the main developments of the last decennia in the field of needle insertion is image-guided needle insertion [19]. Many recent academic studies related to needle insertion focus on tissue and tissue-tool-interaction models to model needle insertion, force feedback, robot assisted needle insertion devices, steerable needles and instrumented needles [20, 21, 15, 22, 23, 24, 2].

1.2 Goal of this thesis

Accurate measurement of forces acting on a needle tip can be useful for multiple applications related to needle insertion, including research on tissue-tool interaction and (enhancing) force feedback. However, all force sensors integrated in a needle for the measurement of forces on the tip of a needle shown in literature are unsuited for in vivo applications [1, 2]. The current sensors are unsuited for in vivo applications due to their large cross-sensitivity to temperature. The goal of this thesis is to design a fiber-optic force sensor, incorporated in a needle tip, for the measurement of forces acting on the needle tip in axial direction of the needle. The sensor should have a very low cross-sensitivity to temperature of the needle or the design should incorporate a method to compensate for cross-sensitivity of the force sensor to temperature of the needle. It was therefore chosen, based on literature research, to design a fiber-optic sensor based on Fabry-Pérot interferometry [25]. A needle with an FBG-based fiber-optic force sensor for the

measurement of needle tip forces, designed a few years ago at Delft University of Technology, was difficult to assemble [1]. The secondary goal of this thesis is therefore to develop a sensor and needle that are relatively easy to manufacture and assemble.

1.3 Motivation

There are quite a few applications for a good, small fiber-optic force sensor that can be integrated into a needle shaft to measure forces on the tip of a needle during in vivo procedures. The following sections will motivate, based on literature research, applications of such a small force sensor to measure forces on a needle tip, why an optical force sensor might be advantageous for those applications and why a Fabry-Pérot interferometer seems the most attractive sensing principle for such an optical force sensor [25].

1.3.1 Applications

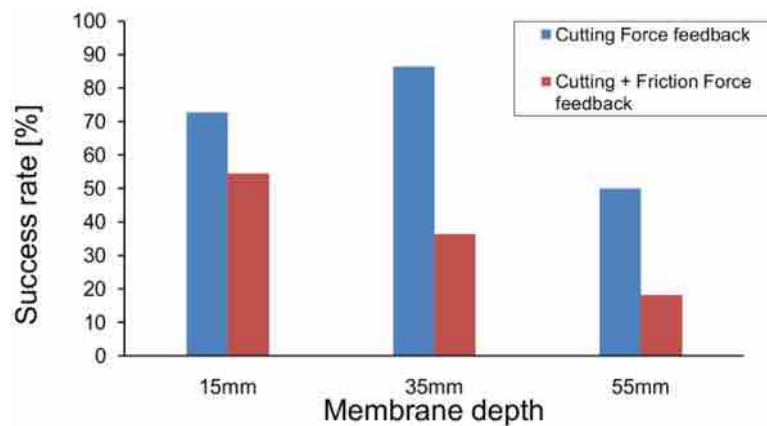
Force feedback

Physicians have only very limited visual feedback during blind needle insertion and rely mainly on kinesthetic feedback of the needle, palpation of the patient (to determine anatomical structures inside the patient) and their own mental visualization of the anatomical structures inside the patient to navigate a needle to its target, while tissue inhomogeneity, tissue anisotropy, tissue deformation and physiological processes like respiration cause the needle to deviate from its intended trajectory [18, 26, 27]. Kinesthetic feedback of the needle is used by physicians to detect transitions between organs and cavities and identify the nature of tissue during (manual) needle insertion [22, 28]. Physicians state that they "learn to trust their feel as much as their eyes" after doing years of biopsies [29]. The amount of force feedback during manual percutaneous procedures is however quite limited compared to open procedures [30]. It becomes for example nearly impossible to feel anything (interesting) when the needle is inserted 5 to 7 cm into tissue during percutaneous biopsies of the liver, because relevant forces on the needle tip become obscured by frictional forces between the needle shaft and tissue that increase with insertion depth [29, 31]. This effect is not unsurprising and can be explained with Weber's law, which states that the minimum perceivable difference between stimuli and the magnitude of the stimulus is constant. Small changes in force on the needle tip become thus undetectable for humans when the total experienced force is large due to friction between the needle shaft and tissue [31, 32].

Force feedback of the needle can be enhanced by measuring the forces acting on (the tip of) a needle very accurately with a force sensor, optionally processing and amplifying the measured forces and presenting the forces to the physician with a haptic interface [31, 27]. It has been demonstrated that the usage of force feedback purely based on forces acting on the needle tip results in a significant increase in the detection rate of membranes in tissue during needle insertion compared to the usage of force feedback based on both friction and cutting forces acting on the needle tip as well as the needle shaft (figure 1.3) [31, 29]. A similar need for force feedback solely based on instrument tip forces, instead of force feedback based on tip forces and friction forces between the instrument and tissue, was stated for applications of force feedback during minimal invasive surgery [33].

Analysis and processing of data acquired by measuring 'natural' force feedback of the needle can furthermore be used to assist physicians with identification of the nature of tissue in which a needle is inserted in a more quantitative way compared to the qualitative and subjective way tissue is identified by a physician during normal manual needle insertion. Attempts have been made to identify tissue types based on tissue stiffness, determined by inserting the needle with a cyclic motion into tissue and analyzing the corresponding force feedback [34]. The value of information about tissue stiffness is known for a while and has been assessed by

Figure 1.3: Results of a study by Lorenzo et al. comparing the success rate in detecting the presence of membranes before puncture of the membrane with a needle, using force feedback based on cutting forces on the needle tip and force feedback based on cutting and friction forces [31].



physicians for ages using palpation during physical examination to detect and identify anatomical structures and diseased tissue by feeling the differences in stiffness related to different tissue types and the pathological state of tissues [35]. Patho-physiological processes, for example inflammation, certain forms of cancer, cardiovascular disease, hepatitis, multiple sclerosis and Alzheimer's, are often accompanied by changes in mechanical properties of tissues and living cells [36, 37, 38, 39, 40]. The ability to solely measure forces acting on the tip of the needle was also noted as beneficial for this type of usage of 'force feedback' to eliminate the effects of friction between tissue and the needle shaft on the tissue stiffness measurement.

Image guidance during needle insertion is being used since a few decades to overcome some of the difficulties of blind needle insertion and can be used to steer a needle towards a target or ensure a safe trajectory to the target. Image guided needle insertion has been shown to significantly improve the accuracy of needle insertion [41, 42, 43]. Imaging modalities like ultrasound, fluoroscopy and CT are frequently used to guide physicians during needle insertion, while MRI is used only occasionally despite its technical advantages [17, 44, 41, 45, 24]. MRI guidance has a good spatial resolution, three dimensional imaging capabilities and provides, contrary to CT imaging, intrinsically good soft tissue contrast and does not use ionizing radiation, which is harmful to both patient and physician [46, 47, 48, 49, 24]. The narrow gantry of the MRI scanner does however prevent easy access to a patient to perform manual needle insertion, which makes procedures cumbersome as the patient has to be moved in-and-out of the scanner to follow the trajectory of the needle [50, 49, 2, 51]. Manual needle insertion during realtime fluoroscopy or CT is possible, but not preferred, as the physician is exposed to damaging ionizing radiation [52]. Robotized needle insertion systems have therefore begun to appear quite recently to assist physicians with needle insertion inside CT or MRI scanners under 'real-time' guidance by means of facilitating teleoperation and can also be used to improve insertion accuracy by means of facilitating shared control [15, 22, 24, 31, 53, 24, 52]. Shared control can for example be used to reduce tremor, which is useful when needle insertion is performed near critical tissues [31, 52, 17]. Furthermore, developments are being made to actuate steerable needles with robotic needle insertion devices, which is beneficial as deviations from the intended insertion trajectory do not necessarily require reinsertion of the needle, but can be corrected with a steering action [24].

Measurement of insertion forces during needle insertion with a robotic needle insertion can be valuable for multiple purposes, for example for the control systems of the robot to enable accurate motion control, but also for presenting force feedback to the physician [54, 22]. Some state that force feedback adds little value during needle insertion when good visual feedback is present [55]. Many others do however disagree, for example by stating that purely relying on visual cues will saturate cognitive load or noting (in 2004) that force feedback is still lacking in

many robot assisted needle insertion systems, while it is acknowledged as an important factor in accurate needle navigation and therefore particularly valuable for robotic needle insertion devices for teleoperation that lack any form of 'natural' force feedback [22, 2]. Since then, some effort has been paid to the development of robotic needle insertion devices with some form of force feedback [29, 31, 52, 23, 24, 51, 56, 57, 54]. No robotic needle insertion devices (practically suited for in vivo needle insertion) capable of presenting force feedback solely based on needle tip forces could however be found in literature, very likely due to the lack of 'good', small force sensors that can be integrated into the needle shaft to measure forces on the needle tip.

Development of models for various applications

Tissue and tissue-tool/needle-interaction models can be used to design better and more advanced needles and improve the design of needle insertion simulators and surgical simulators used for the training of physicians [20, 58, 13]. Tissue and tissue-tool-interaction models can furthermore serve for preoperative planning and can be used by control systems of robot assisted needle insertion devices [20]. Development of these models and simulators requires measurement of tissue-tool interaction forces and other relevant parameters during real procedures to identify the relevant mechanics and tissue parameters describing the tissue-tool interaction and to validate the developed models and verify the physical fidelity of simulators [58, 59]. These measurements require needles equipped with force sensors. Separation of the cutting forces on the needle tip from the friction forces between the shaft of the needle and tissue is valuable for these kind of experiments.

Researchers have to resort to inaccurate and cumbersome work-arounds to perform separation of cutting and friction forces due to the lack of 'good' force sensors that can be integrated in the needle tip to measure cutting forces on the needle tip separately from frictional forces on the needle shaft [60, 61]. One of the proposed work-arounds for separating friction forces from cutting forces is subtracting the friction forces measured during needle retraction from the friction and cutting forces measured during needle insertion [61]. This method relies on the assumption that friction forces remain identical during insertion and retraction. Others have attempted to separately measure friction forces by inserting a needle twice at the same location, under the assumption that the needle will follow the same trajectory during reinsertion and will therefore not experience any cutting forces on the needle tip [62]. It is however far from certain that the needle will follow the same trajectory and that the pathway created during the first insertion will not collapse before reinsertion due to pressure inside the tissue [60]. A third work-around, only capable of quantifying the frictional forces, is inserting the needle tip throughout the entire tissue sample, such that the tip is again outside the tissue, so tip-tissue interaction cannot influence the friction measurement anymore [63]. It is clear that a force sensor capable of measuring solely forces on the needle tip would be much more convenient for research on needle-tissue interaction.

1.3.2 Measurement of needle insertion forces and needle tip forces

Research on needle-tissue interaction and enhanced force feedback during needle insertion (for example with robotic needle insertion devices) rely on accurate measurement of forces acting on a needle. There is a distinct advantage for many applications to be able to separately measure cutting forces on the needle tip and friction forces between the needle shaft and the tissue in which the needle is inserted. Three approaches of measuring forces acting on a needle can be distinguished in literature.

The most popular (and easy) approach is to measure the total axial force on the needle at the hub of the needle, which lumps the cutting and friction forces inseparably together and requires dubious work-arounds to separate the two components. The ATI Nano 17 sensor from ATI Industrial Automation appears to be the most popular sensor to measure both the cutting

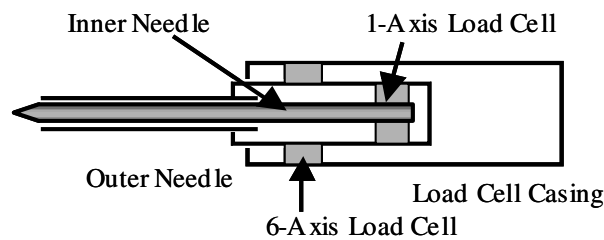


Figure 1.4: System to measure forces on a needle tip at the hub of the needle without the influence of friction between the needle and tissue, by inserting a stylet, with a force sensor at its base, through a cannula into tissue [28].

forces and friction forces at the hub of a needle, probably due to its measurement resolution (up to 1/320 N for a range of 17 N according to the manufacturer) and in some cases also due to its relatively small size and capability to measure both forces and torques in 3 directions simultaneously [64, 13, 29, 65, 66, 67, 34, 1, 26, 22, 16, 68, 15, 69, 70, 71, 72, 73, 74, 75, 54]. The ATI Nano 17 sensor is also used in devices for the measurement of tissue stiffness by means of indentation in a minimal invasive way [76, 77, 78] and calibration of force sensing minimal invasive instruments [79, 54].

Some investigators attempted to measure solely forces on a needle tip by measuring the forces at the base of a stylet or obturator, inserted through a cannula into tissue, to avoid the influence of friction between the stylet or obturator shaft and tissue on the measurement of axial force on the stylet or obturator tip (figure 1.4) [28, 31, 34]. It was however concluded by investigators using this method that significant measurement errors were introduced by friction between the stylet and the cannula (quite ironic, as the cannula was introduced to prevent friction between the stylet and the tissue in which the needle is inserted). These errors due to friction occurred in particular when insertion forces became large, which was for example detrimental for the force feedback based on needle tip forces measured with this method [31, 34]. No exact magnitude of the errors is mentioned in literature, though one can imagine that the measurement error can become intolerable large when the needle undergoes significant bending during needle insertion. This could lock the stylet and the outer needle together and almost completely prevent transfer of needle tip forces to the force sensor at the base of the stylet.

The third approach to measure forces acting on a needle is locating a force sensor shaft of a needle, near the needle tip. This method omits by design the influence of friction between the needle shaft and tissue in which the needle is inserted on the measurement of tip forces entirely [2]. Only a few studies presented force sensors integrated in a needle shaft near the needle tip to solely measure forces on the needle tip [1, 29]. The requirement that the force sensor should have a very low cross-sensitivity to temperature, because the sensor will experience a quite large temperature difference when it is introduced from an environment at room temperature into the warm body of a patient, is one of the challenging obstacles of including a force sensor in a needle tip [2, 29, 1]. Solely examples of optical force sensors based on FBGs could be found in literature for force sensors located in the tip of a needle to measure axial forces on a needle tip [2, 29, 1]. Optical force sensors based on FBGs and FPIs were shown for very small diameter, needle-like instruments for vitreoretinal surgery to measure axial and transverse forces on the tip of the instrument [80, 81]. The demonstrated optical force sensors based on FBGs have however an extremely large cross-sensitivity to temperature (in the order of 1 N/°C), which severely limits practical use of the sensors for in vivo applications [2, 29, 1]. An uniaxial FBG-based needle tip force sensor, with a bandwidth of less than 10 Hz (a 5th order butterworth lowpass filter with a cutoff frequency at 10 Hz in combination with a moving average filter was used), designed by Gähler et al. had a claimed an average 'linearity error' of 0.1 N at constant temperature for a

measurement range of 10 N [1]. Only the presence but not the magnitude of measurement errors due to temperature fluctuations was mentioned explicitly [1]. Elayaperumal et al. claim to have designed a triaxial FBG-based needle tip force sensor (suited for measuring force in axial as well as transverse direction on the needle tip) capable of discerning forces above 5 mN, with an average interpolation error for axial forces of -1.2 mN (std 4.4 mN) for a measurement range up to approximately 0.25 N and usage of the sensor at constant temperature [2, 29]. A change of 1°C did however cause the same change in measurement signal as application of a force of 1 N [2]. Measurement errors due to cross-sensitivity to temperature can be very effectively eliminated from the measurements of transverse forces on the tip of a needle (with multiple FBG sensors), but this is not possible for measurement of axial forces, as thermal strain is indistinguishable from strain due to a pure axial force on a needle tip to a strain gauge [29, 80]. Iordachita et al. also concluded that the cross-sensitivity to temperature of FBG-based sensors for the measurement of axial forces on their vitreoretinal surgery tool could not easily be removed [80]. This is likely the reason that a later paper from the same group proposed an FPI-based sensor specifically for the measurement of axial forces on the instrument, though it was briefly mentioned that this sensor is also cross-sensitive to temperature, but no quantification was given [81]. The resolution of their FBG-based sensor was 0.25 mN, while the resolution of their FPI-based sensor was somewhere between 0.05 and 0.25 mN [81, 80]. No quantification of the measurement accuracy was however given for the presented sensors.

1.3.3 Fiber-optic sensing

The advantages and disadvantages of fiber-optic sensing

There seems, based on the few examples presented in literature, to be a preference for optical sensors for the measurement of forces on the tip of a needle. This preference is presumably caused by some distinct advantages of fiber-optic force sensors over electronic force sensors, despite the quite vast array of principles that can be used by electronic force sensors to measure force (e.g. resistive, inductive, capacitive, piezoelectric, electromagnetic, magnetoelastic, galvanomagnetic and vibrating wire force sensors [82]).

One of the main advantages of fiber-optic sensors in general, according to literature, is the potentially small size of the sensors as well as the required cabling [83]. The size of the sensor and cabling can be as small as a single optical fiber with a 125 μm diameter (or even smaller when non-standard fibers are used). Force sensors based on (electronic) strain gauges can however also be extremely small, as was shown very recently in a study which demonstrated strain gauges 'printed' onto a 18 G needle to measure needle deflection [84].

Fiber-optic sensors (to be precise, their optical sensing part) are inherently immune to electromagnetic interference, while electronic sensors are inherently susceptible to electromagnetic interference to at least some degree. This is an important advantage of fiber-optic force sensors used in medical applications, as it allows usage of the sensor in combination with RF-ablation and MRI scanners, environments that are not optimal for electronic sensing systems though where a need exists for force sensors to measure forces on the tip of a needle for haptic feedback (in robotic needle insertion devices) [85, 51]. There are nonetheless examples of (attempts at) the usage of electronic force sensors, like shielded strain gauges, in combination with MRI [86, 87, 51, 88]. A study by Yamamoto et al. concluded however that a significant increase of noise in the measured force as well as the acquired MR images was observed due to electromagnetic interference when the shielded strain gauges entered the MR coils, which limited usage of the strain gauges to applications inside the MRI room but outside the MR coils [86]. Another group noted after experimenting with strain gauges in combination with MRI that an optical strain gauge technique might be more appropriate, while a third group concluded that the 'MRI compatible' electronic force sensor used in their 'MRI compatible' robotic needle

insertion system suffered from electromagnetic interference in such an amount that further studies should look into possibilities for (additional) compensation of these interference effects or usage of optical sensors [88, 51]. A paper by Monfaredi et al. states however that shielding of strain gauges (to a RF-magnetic field) will in never resolve issues with image degradation due to electromagnetic interference, which seems plausible as shielding relies on the induction of eddy currents in the shielding material that will induce magnetic fields that disturb the magnetic field of the MRI scanner locally [54]. Usage of an electrical force sensor in a needle tip seems therefore no option when the needle has to be MRI compatible, as the electronics will have to enter the MR coils and the strongest distortions due to the presence of the (shielded) electronic components will occur precisely at the location of interest, the needle tip. Optical fibers are thus MR compatible, as they will not disturb MR images by their presence in the field of view nor will the presence of the RF-field disturb operation of the sensor, but optical fibers also MR safe, as they are not attracted or repelled by the magnetic field nor susceptible to RF heating due to eddy currents [87]. Optical fibers that connect a sensor to the electronic processing equipment of the measurement system can be very long without significant loss of quality of the transported signals due to the low attenuation coefficient of modern optical fibers [89]. Electronic processing equipment can therefore be placed easily at sufficient distance of devices causing electromagnetic interference like MRI scanners.

Fiber-optic sensors have a few other small advantages and properties that make usage of fiber-optic sensors interesting for medical applications. Fiber-optic sensors are for example fully dielectric, hence there is no chance of electrocution of patients with an optical fiber. This is the reason why Peirs et al. specifically chose for a fiber-optic force sensor for their robotic surgery system [33, 83, 89]. Optical fiber are biocompatible and can thus be used without problems for invasive measurements [89]. Finally, quite a few types of fiber-optic sensors are suited to be multiplexed on the same fiber [83]. The multiplexing ability of fiber-optic sensors is advantageous for usage in slender medical minimal invasive instruments, as all sensors in the instrument can potentially be integrated in- and powered and interrogated with a single optical fiber, which is not (as easily) possible with electronic sensing systems [83, 89]. One of the disadvantages of fiber-optic sensors are the costs of components of optical measurement systems compared to conventional electronic measurement systems. Component costs are lowering quickly though, because fiber-optic technology is still rather young [83, 89].

Types of fiber-optic sensors

Fiber-optic sensors have been developed to measure a wide array of quantities including strain, temperature, acceleration, acoustics, magnetic and electric fields, humidity, chemical composition, pressure and refractive indices [83, 89]. Fiber-optic sensors can be used to measure quantities that influence either the amplitude/intensity (intensity modulating sensors), phase (interferometric sensors), polarization (polarimetric sensors) or spectral content (wavelength modulating sensors) of light [89, 90]. Modulation of one of these properties of light by a measur- and will always in some way be converted to modulation of the light intensity so that the signal can be measured with a photodetector. Optical sensors based on interferometry and wavelength modulation using Fiber Bragg Gratings (FBGs) are the most sensitive and most studied types of fiber-optic sensors for high performance optical sensing systems [83, 91].

Fiber-optic sensors based on intensity modulation are simple and potentially very low cost sensors because they can be used with low cost light sources like LEDs, simple photodetectors and cheap multimode fibers [89]. The sensitivity of intensity based fiber-optic sensors is generally lower than the sensitivity of interferometry based sensors [89]. Usage of micro- or macro-bending, manipulation of the evanescent field by means of frustrated total internal reflection and extrinsic coupling of light between fibers are the most popular techniques to achieve intensity modulation in fiber-optic strain and force sensors [89]. Sensors based on extrinsic coupling are potentially

the most suited type of intensity modulating sensors for a needle tip force sensor, as they are sensitive in axial direction of the fiber and therefore do not require a mechanism to translate axial forces on a needle to transverse forces on an optical fiber. Examples of intensity modulating force sensors based on extrinsic coupling, used in (minimal invasive) medical devices, are a triaxial sensor for robotic surgery devices with a resolution of 40 mN and a range of 2.5 N designed by Peirs et al., a triaxial sensor with a 20 N range and sub-Newton resolution by Su et al. for a MRI compatible robotic needle insertion device, an uniaxial sensor for a MRI compatible catheter with a 0.85 N range and 0.01 N resolution by Polygerinos et al. and a triaxial sensor for the same application by the same group with a 500 mN range and a 10 mN resolution [79, 33, 92, 93].

Polarization modulating force sensors are based on stress induced birefringence due to the photo-elastic effect (the change in refractive index in a certain direction of a material due to stress in the material). Polarimetric sensors have been demonstrated for hydrophones and pressure sensors, but interest in polarization modulating sensors based on the photo-elastic effect has faded [83]. Polarimetric sensors based on the photo-elastic effect are however still regarded as low cost sensors for applications that do not require a very high accuracy [83, 94]. Polarimetric sensors have to be quite long compared to wavelength and interferometry based sensors to achieve reasonable sensitivity, which is not particularly attractive for a sensor that should be sensitive solely near the needle tip [94, 90]. Polarimetric sensors will therefore not be considered for the fiber-optic needle tip force sensor.

Modulation of the wavelength of light by a measurand like strain, force or pressure can be achieved with grating based sensors of which Fiber Bragg Gratings (FBGs) are the most popular [89]. The ability to encode a measurand as a wavelength is the most important advantage of wavelength modulating sensors over interferometric, polarimetric and intensity modulating sensors, as the measurand encoded as wavelength is insensitive to disturbances like irradiance fluctuations of the optical source, losses inside the fiber-optic system or birefringence effects inside used fibers [94, 95, 96]. An FBG consists of a short section of fiber, normally between 1 and 20 mm long, with a periodic modulation of the refractive index [97, 94]. The FBG-based force sensors for the measurement of forces on the tip of a needle or instrument for vitreoretinal surgery, mentioned on page 16, used 5 and 10 mm long FBGs [80, 2]. Only light with a wavelength that 'fits' into the grating period, called the Bragg wavelength, is reflected by an FBG. The grating period can therefore be determined by measuring the wavelength of the light reflected by an FBG [94]. Several schemes have been shown for interrogation of FBGs, but the interrogation equipment is in general quite expensive [89, 98, 99, 95]. The costs of an interrogation system were reported to range between \$10000 to \$40000 in 2007, while the costs of fibers with FBGs (purchased in small quantities) were reported vary from \$80 to over \$500 in 2007, which makes FBG-based sensing systems particularly expensive [100]. FBG based sensors can be multiplexed very easily [94]. This was for example used to sense the shape of a needle by measuring deformation at several positions along the needle with three optical fibers, each with multiple FBGs, in integrated in the needle [24, 101].

An FBG is very sensitive to strain as well as temperature [95]. The wavelength shift of the Bragg wavelength as function of a change in strain of the FBG or a change in temperature (in degrees Celsius) can be approximated with equation 1.1 [97].

$$\frac{\Delta\lambda_B}{\lambda_B} \approx 0.78 \cdot 10^{-12} \Delta\varepsilon + 6.67 \cdot 10^{-6} \Delta T \quad (1.1)$$

The sensitivity of an FBG interrogated at a wavelength of 1550 nm is thus 1.2 pm/ $\mu\varepsilon$ and 10.3 pm/ $^\circ\text{C}$. The change in the Bragg wavelength of FBGs due to changing temperature is determined for about 95% by the thermo-optic coefficient of silica optical fibers (the dependence of the refractive index on the temperature) and the remainder by the thermal expansion coefficient of the fiber [95]. Compensation of the cross-sensitivity to temperature of an FBG intended for

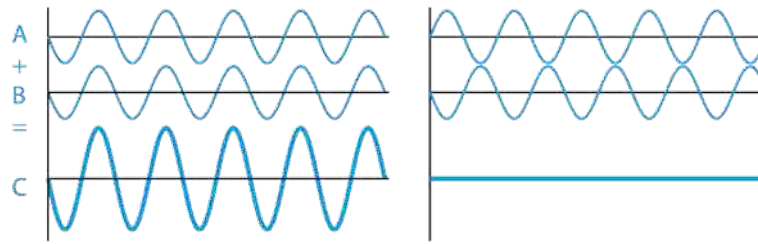


Figure 1.5: On the left, constructive interference of wave A and B, resulting in wave C. On the right, destructive interference of wave A and B, resulting in 'wave' C.

force measurements is required in many practical applications. This is for example possible by introducing a second, stress free, reference fiber with an FBG to solely measure temperature [102]. This method seems relatively complicated for compensation of the cross-sensitivity to temperature of an FBG used to sense forces on the tip of a needle, because the exact location of the relatively long FBG is often unclear and hard to determine. Quite a significant length of the stress free optical fiber will thus have to be suspended inside the needle in such a way that it does not contact deforming parts of the needle, which seems difficult to assemble in a miniature device like a needle. One of the first alternative solutions presented in literature to separate temperature and strain measurements obtained with (approximately) collocated FBG sensors is superimposing two FBG gratings with very different periods at the same location of the fiber and interrogating the FBGs with light with two very different wavelength bands [103]. The wavelength shift induced by thermal and by mechanical effects can then be discriminated due to the wavelength dependence of the photo-elastic and thermo-optic coefficients of silica, both factors influencing the change in Bragg wavelength due to a change in temperature or strain of the FBG [104]. The performance of this method is not very high because the inversion matrix used to separate the strain and temperature measurement is poorly conditioned, even when light sources are used with widely separated wavelengths [100]. Superimposing two gratings furthermore complicates the measurement setup and adds significant costs [100]. Quite a few other techniques, combining various types of optical sensors, including Fabry-Pérot interferometers, with FBGs have been presented since then to correct for cross-sensitivity of FBGs to temperature [104, 105]. All presented solutions seem however quite significantly more complex than a standard fiber with an FBG and will therefore likely be quite expensive and complex to manufacture.

Phase modulation based sensors, often called interferometric sensors, are potentially the most sensitive fiber-optic sensors and can achieve a very high dynamic range compared to other types of fiber-optic sensors [89, 106, 107]. The measurand modulates the phase difference between interfering light waves in interferometric sensors. The intensity of a bundle of light with a certain wavelength increases due to constructive interference when the waves are in phase or decreases due to destructive interference when the beams are out of phase (see figure 1.5) [83]. The intensity after interference of two beams of monochromatic light with the same wavelength and the intensity I_1 and I_2 and a phase difference ϕ can be described with equation 1.2 [108].

$$I = I_1 + I_2 + 2\sqrt{I_1 I_2} \cos \phi \quad (1.2)$$

The modulation of the phase difference between light waves is achieved by modulation of the difference in the optical distance (geometrical length times the refractive index) traveled by two (or more) 'light bundles' that are combined such that the waves of the light of the bundles will 'interfere' with each other [89]. The difference in optical path length of the bundles is called the OPD, the Optical Path Difference [89]. The phase difference between waves of interfering light waves is a function of the OPD and the wavelength of the interfering light waves. It is

The intensity of the light after interference as function of the phase difference is a periodic function and describes a so called 'fringe pattern' (figure 1.6).

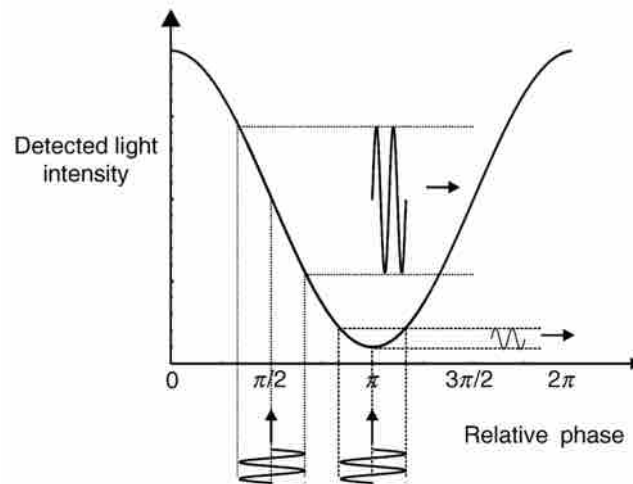


Figure 1.6: Part of the fringe pattern of a two-beam interferometer showing the intensity after interference as function of the phase difference between the beams. A two beam interferometric sensor is most sensitive and linear to changes of the 'OPD' around its quadrature point. A two beam interferometer is at quadrature when the phase difference between both interfering beams is equal to $\pi/2 \pm k\pi$ [97]

possible to perform interferometry with light a large spectral width (light containing 'many different wavelengths'), which is called low coherence interferometry, instead of performing interferometry with monochromatic light (light with a 'single wavelength'), which is called homodyne interferometry [109]. The 'distribution' of the intensity of the light bundle over the different wavelengths contained in the light bundle will be a periodic fringe pattern after interference of two beams with a large spectral width and a certain optical path difference. After all, the phase difference between waves with a certain wavelength depends on the wavelength. The change in OPD and thus the change in measurand can therefore be measured as a change in light intensity of the entire light bundle after interference when homodyne interferometry is performed or be derived from the light intensity of the bundle as function of wavelength when low coherence interferometry is performed.

Four major fiber-optic interferometer classes, Fabry-Pérot, Sagnac, Michelson and Mach-Zehnder interferometers, can be distinguished based on the method to create two (or more) separate light bundles of a single source, how they are made to interfere with each other and which (part) of the optical fibers will be used to sense the measurand [110, 89, 83, 90]. Sagnac and Mach-Zehnder interferometers cannot have a sensitive optical fiber-end where the change in OPD is induced by the measurand, as the Sagnac and the Mach-Zehnder interferometer require access to both ends of the sensing fiber to couple light in and out of the fiber. Both are therefore not suited for measuring forces on the tip of a needle [89]. The Michelson interferometer can be used inside a needle tip, though the entire 'sensing' fiber in the needle is sensitive to strain and temperature fluctuations, which is not convenient when the sensor should be solely sensitive near the tip of the needle [89]. An interferometric sensor based on the Michelson interferometer can only be made sensitive at the tip of the needle by placing a fiber-optic coupler inside the needle near the needle tip to ensure a very short sensing fiber, which seems an unnecessary challenge. The Fabry-Pérot interferometer (FPI) consists of a single fiber with a (optionally very short to extremely short) sensitive part at the end of the fiber and is thus suited to measure forces on a needle tip. Two (or more) 'light bundles' are created and made to interfere with each other by

placing two partially reflective mirrors at the end of the fiber with a distance in between to create an optical path difference (figure A.1). A more detailed description of the operating principle of an FPI and examples of manufacturing methods of fiber-optic FPIs are given in chapter A of the appendix. This is recommended reading for readers without some background in the principles of interferometry, as the remainder of this thesis will assume that the readers is acquainted with these principles and related terminology.

A comparison of an FBG-based strain gage and an FPI-based strain gage for the measurement of cutting forces of a surgical scissor was shown in literature (but seems to be tested without either the FPI or FBG attached to the scissor) [111]. The used FPI-based strain gage outperformed the FBG-based strain gage with a nearly twice as high sensitivity to strain, a nearly ten times lower sensitivity to temperature, lower manufacturing costs and lower costs of the interrogation equipment (particularly in case homodyne interferometry is used, but according to this study also when a low coherence interferometry is used for interrogation of the FPI) [111]. FPI-based strain gages with even lower cross-sensitivities to temperature have been presented (a sensitivity to strain of $10.3 \text{ pm}/\mu\epsilon$ and a sensitivity to temperature of $0.95 \text{ pm}/^\circ\text{C}$, which corresponds to about a factor 90 lower cross-sensitivity to temperature compared to an FBG [112]). The larger costs of equipment required for the interrogation of FBGs compared to the costs of interrogation equipment for FPI sensors (based on homodyne interferometry) is confirmed by a study on the design of a force transducer located in needle driver of an MRI compatible needle insertion robot and several other studies [23, 113]. The lower cross-sensitivity to temperature of many FPIs is the result of the usage of an FPI cavity filled with air, which has a very low thermo-optic coefficient compared to the thermo-optic coefficient of fused silica used in FBGs that makes a FBG very sensitive to temperature [95]. Very small, though very sensitive force sensors can be made with FPI sensors, as was shown with an entirely fiber-optic Atomic Force Microscope [114]. Fiber-optic AFMs, based on a Fabry-Pérot interferometer, with resolutions up to 3 nN have been shown in literature [115].

Choice of the most appropriate sensing technique

The to-be-designed force sensor for the measurement of forces on a needle tip should ideally be suited for as many applications as possible, including applications inside an MRI scanner or applications using RF-ablation needles. MRI compatibility is particularly of interest, because availability of a needle insertion robot with good force feedback might enable more frequent usage of MRI guided needle insertion. A force sensor from the class of fiber-optic sensors is therefore more suited compared to electronic sensors for the measurement of forces on the tip of a needle.

Within the class of fiber-optic force sensors a choice should be made between the extremely cheap, though not particularly high performance intensity modulating sensors, high performance, very expensive FBG-based sensors with an extremely low sensitivity to irradiance disturbances, excellent multiplexing capabilities but a quite a large cross-sensitivity to temperature (for which certainly compensation will be required) or very small, short, reasonably affordable FPI-based sensors in case homodyne interferometry is used for interrogation or an extremely low sensitivity to irradiance disturbances when low coherence interferometry is performed and with a potentially low cross-sensitivity to temperature (for which no compensation might be required). Intensity modulating sensors were discarded because of the significantly larger chance that the required performance might not be achieved due to the relatively low dynamic range of intensity modulating sensors compared to the dynamic range of FPI-based sensors shown in literature [106, 107]. The higher sensitivity of FPI sensors compared to the sensitivity of intensity modulating sensors for measuring displacements will furthermore allow the elastic element of FPI-based force sensors, which converts force to a displacement measurable by the optical sensor, to be smaller than the elastic element of intensity modulating sensors. This

will ensure that an FPI-based sensor will fit more easily in a very thin needle. It was chosen to pursue an FPI-based sensor instead of an FBG-based sensor because there is a possibility that an FPI-based sensor will not require any form of temperature compensation to achieve the requirements on the measurement uncertainty. The relatively short length and well defined location of the sensitive part of FPI sensors will furthermore increase possibilities for simple integration of a stress free reference sensor based on Fabry-Pérot interferometry to compensate for temperature cross-sensitivity, in case this is required to achieve a certain required accuracy. The relatively low cost of an FPI based measurement system is finally also quite attractive.

1.4 Structure of this thesis

This chapter, the introduction, described the goal of the design project of this master thesis; the design of a fiber-optic force sensor to measure forces on the tip of needle. Furthermore, the choice for the sensing principle that will be used in the design was motivated, based on a literature review of potential applications of the design and available technologies. The second chapter will state the precise design problem and briefly specify all requirements on the design. Requirements were partially based on the performance of the ATI Nano 17 sensor, the currently most commonly used force sensor for the type of applications of the needle tip fiber-optic force sensor is intended. An analysis of the performance of the ATI Nano 17 and the requirements in more detail can be found in the second and third appendix. The third chapter analyzes the components of which the design should consist and evaluates possible concepts for each of the components. Eight different concepts for the needle tip containing the fiber-optic force sensor are proposed based on the solutions found for the different components. The fourth to the sixth chapter describe the exploratory investigation of three of the eight concepts, the first focussing on achieving an intrinsic low cross-sensitivity to temperature, the second on a strong sensor and needle tip and the last on an easily manufacturable and completely MRI-compatible force sensor. Each chapter presents the details of the manufacturing process of a prototype or proof-of-concept of the concept, analyzes the performance of the concept more in depth by means of a finite element analysis and presents and discusses results of calibration of the prototypes of the concepts. The last chapter of the thesis briefly evaluates the results of the exploratory investigation into the three different concepts and makes recommendations for improvements and further research. The first appendix describes the operating principle of the Fabry-Pérot interferometer and some of the manufacturing methods of fiber-optic FPIs proposed in literature in more detail. The last appendix presents some parts of the thesis in more detail and shows calibration results of variants of prototypes made for this thesis that were regarded valuable for comparative purposes.

2 Design problem

2.1 Problem statement

The objective of this thesis is to investigate options to design and manufacture a fiber-optic force sensor based on Fabry-Pérot interferometry, integrated in the shaft of a needle as close as reasonably possible to the tip of the needle, for the measurement of needle insertion forces acting axially on the tip of a stylet of a core biopsy needle. The sensor is preferred to be fiber-optic force sensor, to facilitate potential MRI-compatibility of the needle. The problem of current fiber-optic force sensors used for the measurement of axial forces on a needle tip is their cross-sensitivity to temperature (1 N/°C [2]). *The primary goal of this thesis is to design a force sensor with either a significantly lower cross-sensitivity to temperature, such that requirements on the accuracy of the sensor are met in the entire range of temperatures that the sensor can reasonably be expected to be used during medical procedures, or with a mechanism or method to compensate for cross-sensitivity of the sensor to temperature in such a way that the requirements on the accuracy of the sensor are met.* The usage of an FPI-based sensor to measure forces exerted on a needle tip, nor a fiber-optic force sensor designed to have a specifically low cross-sensitivity to temperature for the measurement of forces on the tip of a very small needle-like medical instrument has been shown before to the writer's knowledge. Secondary goals of the thesis are to design an easily manufacturable needle and sensor and design a sensor with a significantly shorter sensitive part of the sensor compared to the sensitive part or region expected to contain the sensitive part of FBG-based sensors such that the sensor should be more easily placeable near the very tip of the needle.

Applications for which the force sensor will be designed are applications involving haptic feedback of the needle, for which the detection of transitions between tissue layers during needle insertion is in particular relevant, research on needle insertion forces, for which a high accuracy is important, and (possibly with slight modifications to the design) measurement of tissue stiffness during needle insertion with methods similar to the method described by Hogervorst [34], for which a high resolution and accuracy are beneficial. Haptic feedback will be regarded as the application of main importance, as a low cross-sensitivity to temperature is in particular important for this application because feedback is mainly required for in vivo needle insertions. This project originated as part of the 'ADAPT' project. The ADAPT project focusses on the development of a compliant steerable needle that can adapt its stiffness to prevent buckling of the needle when the needle penetrates very stiff tissues. The sensor should therefore also be suited to measure the

load on the tip that contributes to the buckling load.

The accuracy of the the ATI Nano 17, the currently most used force sensor for the kind of applications for which the fiber-optic needle tip sensor is intended, will serve as the ultimate goal for the accuracy of the fiber-optic sensor. The measurement uncertainty of the ATI Nano 17 is evaluated in depth in appendix B. The ATI Nano 17 is an expensive force sensor, developed by a company with years of experience in the design of force sensors. Designing a fiber-optic force sensor with a similar accuracy that is maintained during quite large temperature disturbances might therefore be a very hard to reach goal. Requirements on the performance of the fiber-optic sensor are therefore based on the performance of an FBG-based fiber-optic force sensor for the measurement of forces on the tip of a needle designed, during a master thesis, by Gähler [1]. The performance of the new fiber-optic sensor should be such that the performance of the force sensor designed by Gähler at constant temperature can be achieved while the new sensor is exposed to the entire range of expected temperature disturbances. Gähler reports an average interpolation error of 110 mN of the FBG-based force sensor. This should be the average error of all readings obtained during 5 calibration series, with calibration forces up to 10 N, per tested temperature with respect to the optimal interpolation function determined for each of the 8 tested temperatures (figure D.26). However, measurement errors of the FBG-based sensor up to at least 250 mN occur within the measurement range at constant temperature (disregarding outliers). Hence, the reported average error is not a particularly fair representation of the performance of the FBG-based force sensor. Analyzing other figures in the report in more detail, in particular figure 7 of the paper (figure D.27 in the appendix) [1], shows that errors up to at least 0.75 N with respect to the interpolation function occur when the calibration load is gradually decreased, which is significantly above the reported outliers of 0.5 N elsewhere in the report. It appears like the interpolation errors reported by Gähler are solely based on calibration series with increasing loads and reversibility errors are neglected. The accuracy of the FBG-based sensor for approximately static loading was for comparative purposes therefore assessed as 0.5 N (the mean of the maximum observed measurement error in the report of 0.75 N and the maximum reported error in the chapter about the calibration of the sensor, disregarding outliers, of 0.25 N).

The required measurement range of the fiber-optic sensor can be estimated based on literature. Several different maxima of axial loads on needles measured during needle insertions with 17 and 18 G needles are reported in literature (table 2.1). There is quite some variation in data, which can be expected due to differences in, for example, needle insertion velocity, insertion location, penetrated tissue types and needle tip shape [60]. Some of the reported axial loads are measured at the needle tip, most of the reported forces were measured at the needle hub and therefore also incorporate frictional forces between the needle shaft and tissue. Tip forces are expected to be significantly lower than the total axial force on the needle measured at the hub. Transverse loads at hub of the needle are small in general. Maurin et al. report transverse loads in the order of 2 mN and Podder et al. report transverse forces up to 0.71 N during manual insertion of 18 G needles in respectively in vivo pig tissue and human tissue [22, 67].

2.2 Requirements

There are quite a few requirements which the final design of a force sensor for the measurement of axial forces on the tip of a needle should fulfill. Achieving all requirements and verifying whether all requirements are met, will be too time consuming for a thesis project. Requirements were therefore designated a certain priority. Requirements designated with a high priority should (preferably) be validated and preferably met during this thesis project. A distinction is made for most requirements between goals and what actually is required or seems reasonably achievable during this thesis project. Goals are the ultimate target, but might be extremely hard or even

Table 2.1: Reported maxima of needle insertion forces in axial direction of the needle, for needles with a gauge of approximately 18 G, measured at the hub of the needle or at the tip of the needle, as reported in literature.

Needle gauge (G)	Maximum tip force (N)	Maximum hub force (N)	Tissue type	Source
17	-	15.6	In vivo insertion into human prostate tissue (through the skin)	[67]
17.5	1	2	Insertion into the exposed prostate of a beagle cadaver	[28]
18	-	8.9	In vivo insertion into human prostate tissue (through the skin)	[67]
18	-	4	In vivo pig tissue, maximum of (manual) insertions into various organs	[22]
18	1.75	3	Phantom tissue	[2]
18	5.4 (estimate)	-	Insertion into kidney of human cadaver	[13]

impossible to achieve. A detailed description of the requirements and possible methods to validate whether the requirement is achieved is given in appendix C. A brief overview of the requirements is given in the next sections.

Needle/stylet design

Needle gauge: Diameter of the needle in which the force sensor should fit.

Priority: High

Goal: Fits inside the stylet of a 18 G trocar needle ($\varnothing 1$ mm).

Required: Fits inside the stylet of a 14G or smaller diameter needle.

Rationale: The range of 14 G to 18 G represents commonly used core needle biopsy needles.

Needle length: Length of the needle for which the force sensor will be designed.

Priority: Low

Goal: About 200 mm.

Rationale: The trocars readily available at the university (Cook DTN-18-20.0-U) are 200 mm long.

Stylet tip shape: Shape of the tip that will be used for the stylet.

Priority: Medium

Goal: A reflectional symmetric tip shape of a commercially available stylet of a trocar needle.

Required: A reflectional symmetric conventional needle tip shape.

Rationale: Reflectional symmetry of the tip will ensure minimal transverse forces on the needle tip.

Strength: Loads that the needle and sensor should be able to support without permanent damage (for a 200 mm long 18 G needle).

Priority: High

Goal: 18 N in axial direction towards the needle hub (compressive loading of the sensor) and 2 N transverse load on the needle tip for 1 cycle. 9 N in axial direction towards the hub and 1 N transverse load on the tip for a preferably infinite number of cycles or at least 10^4 loading-unloading cycles.

Required: 9 N in axial direction towards the needle hub (compressive loading of the sensor) and 1 N transverse force on the needle tip for a large number of cycles (100+) and should survive handling during calibration procedures.

Rationale: It is highly undesirable that the needle breaks down during needle insertion.

Material Material used for the tubing of the stylet/needle and the needle tip.

Priority: Low

Goal: Biocompatible and MRI compatible materials.

Rationale: A hypodermic needle is a medical device for invasive usage. Applications of the needle in combination with MRI guidance are preferably possible (with some minor modifications to the design).

Measurement system/sensor design

Quantity to measure: Quantity that has to be measured with the sensor integrated in the tip of the needle.

Priority: High

Required: Force exerted axially on the tip of the needle.

Rationale: The quantity of interest for enhancing haptic feedback of a needle, research on needle insertion forces and prediction of buckling of the needle is the force in axial direction on the needle tip.

Range: Range of forces that the sensor should be able to measure with the required accuracy (for a 18 G needle).

Priority: High

Goal: 10 N.

Required: 6 N.

Rationale: Ideally the entire range of forces exerted on the needle tip should be measurable with the required accuracy during normal usage of the needle.

Measurement uncertainty: Maximum dispersion of the obtained sensor readings around the true value of the measured quantity due to random and non-compensated systematic errors [109].

Priority: High

Goal: A maximum half-error-interval of ± 16 mN or smaller at zero load and a half-error-interval of ± 45 mN or smaller for a load of 10 N under disturbances induced by temperature fluctuations between 17°C and 41°C , transverse loads on the sensor, bending of optical cables among others, as specified in box C.2.1 in appendix C.

Required: A half-error-interval of 500 mN or better throughout the entire measurement range while the sensor is exposed to temperature variations of the environment between 17°C and 41°C , as specified in box C.2.1 in appendix C.

Rationale: A low measurement uncertainty is beneficial when the sensor is used for research on needle insertion forces or measurement of tissue stiffness and ensures that temperature differences are not mistaken as tissue properties during applications of the sensor involving haptic feedback. The 'half-error-interval' is defined as the maximum observed difference in readings of the force sensor and the true value. The error-interval is thus at most twice the half-error-interval, which is the case when errors are distributed symmetric round the true value. The 'half-error-interval' should be comparable in magnitude to the expanded measurement uncertainty.

Bandwidth: Cut-off frequency (-3 dB) of the measurement system, which determines the

frequency up to which the system has a good sensitivity to the measured quantity.

Priority: Medium

Goal: 500 Hz or more.

Required: 100 Hz or more.

Rationale: Frequencies up to 500 Hz are required for convincing kinesthetic feedback, though most interesting frequencies for needle insertion into soft tissue are in the tens of Hertz [18, 2].

Resolution: (Half the) range of fluctuations of acquired readings of the sensor under constant load after signal processing like lowpass filtering.

Priority: Medium

Goal: 3 mN or better.

Rationale: A good resolution is beneficial during haptic feedback to discern very small changes in force related to puncture of soft membranes and detect small variations in tissue stiffness.

Measurement principle: Principle of operation of the force sensor inside the needle tip.

Required: The sensor should make use of a fiber-optic Fabry-Pérot interferometer.

Rationale: Fiber-optic sensors were shown to be preferable over electronic sensors when the sensor is used in combination with MRI in chapter 1. Sensors based on Fabry-Pérot interferometry were furthermore argued to be suited for the construction of small, sensitive sensors with a relatively low cross sensitivity to temperature.

Sensor location: Distance between beginning of the bevel of the needle tip and the sensitive part of the force sensor.

Priority: High

Goal: 5 mm or less.

Rationale: The sensor should be located as close as possible to the needle tip to reduce influence from frictional forces between the stylet and tissue or the outer cannula of the needle by design to a minimum.

Readout device: Device/equipment containing an optical source and photodetector to 'interrogate' the FPI in the needle tip.

Goal: The OP1550 of Optics11 .

Rationale: An OP1550 is made available for this thesis project.

Number of FPIs: Number of Fabry-Pérot interferometers used in the needle tip.

Goal: 1 FPI.

Rationale: The needle tip should preferably contain a uniaxial force sensor based on a single FPI, as it will be impossible or difficult during this thesis project to obtain interrogation equipment to interrogate more FPIs, for example for a triaxial force sensor. A design with 1 FPI will furthermore be cheaper to manufacture.

Guidelines FPI design

FPI cavity length Geometrical length of the cavity between the two mirrors of the FPI.

Goal: 10-100 μm (for an air filled cavity).

Rationale: The longer the cavity length, the worse the visibility of the fringe pattern becomes for extrinsic FPI sensors, while very short cavity lengths can cause issues with using the FPI at quadrature (maximum sensitivity).

Wedge angle mirrors Angle of deviation of parallelism of the mirrors of the FPI sensor.

Goal: A wedge angle below 2° .

Rationale: Non-parallelism of the mirrors should be minimized to ensure fringe visibility and a good signal to noise ratio [116].

Other guidelines

Manufacturability: Ease of manufacturing parts of the system and assembling the system.

Priority: High

Goal: Designs using fewer and more simple manufacturing steps are preferred. Designs that are more robust to slight errors in manufacturing are also preferred. Designs that can be produced easily with high repeatability and controllability are strongly preferred.

3 Morphological scheme and Concepts

3.1 Elements of the design

Several requirements on the design for a system to measure forces acting on the tip of the stylet of a needle with a sensor integrated in the needle tip were presented in the previous chapter. The most important goal of the project was that the measurement system should have a low cross-sensitivity to temperature of the needle tip, which was expressed as a requirement on the measurement uncertainty of the sensor, while the system should use a force sensor based on a Fabry-Pérot interferometer. The design of the system can be divided in several 'elements', based on the the functions that have to be performed, for which separate concepts can be generated. Figure 3.1 shows the 'elements' of which the system should consist to illustrate the relation between different elements. A single physical part of final design could perform the functions of multiple 'elements'. It should furthermore be noted that the structure in which elements are connected in figure 3.1 is merely intended to visualize the relation between elements, while the final concept or design could 'look' quite differently. The design of specifically the sensor in the needle tip is the main focus of the project.

The system requires a needle, consisting of an outer cannula, a hollow stylet tube and a stylet tip. These elements are not critical to demonstrate the performance of the measurement system and in particular the sensor used to measure forces on the needle tip, hence not much attention will be given to their specific design. The hollow stylet tube, inserted in the outer cannula, will house a force sensor (and optionally a temperature sensor) based on a Fabry-Pérot interferometer and an optical fiber connecting the force/temperature sensor to the FPI interrogation device (containing a light source, photodetector, some electronics and an AD-converter). The measurement system, consisting of all electronics and optical sensors, should have a low cross-sensitivity to temperature of the needle tip or be able to compensate for cross-sensitivity induced errors that exceed the required measurement uncertainty of the measurement system. Hence, methods to achieve this characteristic should be evaluated.

The force/temperature sensor should contain at least one or more Fabry-Pérot interferometers to convert force on the needle tip/temperature of the needle tip to an optical signal. Interferometry is a technique to measure changes in optical path difference (OPD), which consist of the product of the geometrical length of an optical path and the refractive index of the medium of the optical path. The force/temperature sensor should therefore contain an element, which will be called the force/temperature sensitive element, for the conversion of force/temperature to a change

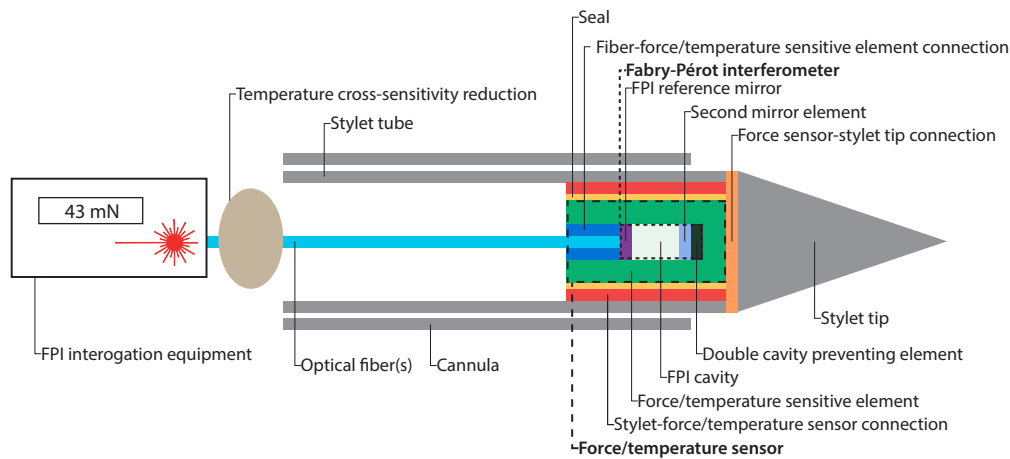


Figure 3.1: Illustration of the elements of which a system for the measurement of needle tip forces using a FPI-based sensor should consist.

in OPD of the Fabry-Pérot interferometer. The Fabry-Pérot interferometer itself consists of a reference mirror, a 'second' mirror of which the displacement with respect to the reference mirror is determined and a medium between both mirrors called the Fabry-Pérot cavity. A 'double cavity preventing element' will almost certainly be required in most concepts to prevent light that left the Fabry-Pérot cavity from re-entering the Fabry-Pérot cavity due to reflections on surfaces inside the needle tip (figure 3.14). These undesirable reflections would result in an apparent second FPI cavity that will cause measurement noise and potentially a large cross-sensitivity to temperature. A sealing element could be necessary to prevent substances from entering the Fabry-Pérot cavity depending on the medium used for the Fabry-Pérot cavity. Finally, some attention should be given to methods to connect different elements of the design or possibilities for integration of several functions of elements into one physical part. An overview of the elements of which the design should consist and the functions they should fulfill is given in table 3.1.

3.2 Morphological scheme

A morphological scheme, showing the various conceptual options to fulfill the required functions of each element of the system, is presented in figure 3.2 and 3.3.

3.2.1 Cannula

The outer cannula does not significantly contribute to the performance of the measurement system, except to the mechanical strength and MRI compatibility of the needle. The only relevant design parameter of the outer cannula is the material used for the capillary. Compliant PEEK capillaries could be used to ensure excellent MRI compatibility of the needle, but (stainless) steel and titanium needles with a high strength are currently also regarded as MRI compatible [24, 117].

3.2.2 Stylet tube

Attention could be given to different options of materials for the stylet tube, but the most fundamental choice that should be made with respect to the design of the stylet tube is the way the force sensor will be housed inside the tube. The stylet tube can merely support the base of the sensor in axial and radial direction (figure 3.4 A), also support the circumference of the sensor in radial direction (B & C) or support the base and circumference of the sensor in radial

Table 3.1: Overview of the elements of a system for the measurement of axial forces on the tip of a needle using a FPI and the functions each element should fulfill.

Element	Functions
Cannula	Contain stylet, provide channel for extraction of biopsy samples.
Stylet tube	Contain a fiber-optic force (and optionally temperature) sensor and the optical fiber connecting the sensor to the interrogation equipment.
Stylet tip	Cut tissue in front of stylet during needle insertion and prevent accumulation of tissue inside the lumen of the cannula during needle insertion.
Optical fiber	Transport light from the source of the FPI interrogation equipment to the force sensor and light modulated by the measurand back to the detector of the FPI interrogation equipment.
Fabry-Pérot interrogation equipment	Send a light bundle towards the sensor(s) located in the needle tip, convert returning light with to an electrical signal, process and filter the electrical signal, convert the analog signal to a digital measurement and convert the digital measurement to a digital measurement of force/temperature.
Temperature cross-sensitivity reducing method	Reduce the influence of temperature on the acquired force measurements (possibly by using a temperature sensor).
Force/temperature sensor	Encode forces exerted axially on the needle tip and/or temperature of the needle tip as an optical signal. Contains one ore more Fabry-Pérot interferometers
Force/temperature sensitive element	Convert forces exerted on the force sensor or temperature of the sensor to a change in OPD of an FPI.
Fabry-Pérot interferometer	Encode displacements of the second FPI mirror, attached to the force/temperature sensitive element, with respect to the reference mirror and/or encode changes in refractive index of the medium inside the Fabry-Pérot cavity into an optical signal.
Reference mirror	Provide a reference to the displacements of the other mirror(s) of the Fabry-Pérot interferometer, partially reflect light back to the detector of the FPI interrogation equipment and transmit light into the FPI cavity, be connected to the fiber-end and be connected, as rigidly as possible, to the force/temperature sensitive element.
FPI cavity	Provide waveguide for light resonating between the reference mirror and other mirrors of the Fabry-Pérot Interferometer.
Second FPI mirror	Move with displacement of force/temperature sensitive element and reflect (some) light back to the reference mirror, be connected as rigidly as possible to the force/temperature sensitive element.
Double cavity preventing element	Prevent light from returning into the FPI cavity after it left the cavity due to reflections on surfaces inside the needle tip.
Fiber-force/temperature sensitive element connection	Connect the force/temperature sensitive element to the optical fiber and ensure alignment between the fiber, the force/temperature sensitive element and the mirror elements of the Fabry-Pérot interferometer.
Seal	Keep fluids out of FPI cavities.
Stylet-force/temperature sensor connection	Connect the force sensor (and optionnaly the temperature sensor) to the stylet tube.
Force sensor-needle tip connection	Connect the needle tip to the force sensor and transmit forces of the needle tip to the force sensor.

Concepts	
Element	
Canula	Commercial 18 G needle canula
Stylet tube	Supports base of force sensor in radial and axial direction
Stylet tip	Standard stylet tip of a trocar needle
Optical fiber	Single-mode fiber Silica Plastic
FPI interrogation equipment	Homodyne interferometry system (e.g. OPI550)
Temperature cross-sensitivity reducing method	Acclimatize sensor in 37°C water-bath before insertion Remove disturbance
Fabry-Pérot Interferometer	Low finesse, equal reflectances of mirrors Axial load Column Beam (1-support) Elastic element Beam (2-supports) Transversal load Membrane Torsional load Stacked beams (1 or 2 supports) Torsion rod with moment arm
Temperature sensitive element	Thermo-optic properties FPI cavity medium Displacement Expansion column (CTE) Bending beam (difference CTE)
	Capillary tube
	Support base and circumference of force sensor: in radial and axial direction.
	Reflectional symmetric 'standard' needle tip
	Multimode fiber Silica Plastic
	Low coherence interferometry system (e.g. OCT system)
	Bandpass filter signals Filter signals based on a priori knowledge of the disturbance Use a time dependent model to filter signal/use sensor calibrated at 37°C
	Low cross-sensitivity due to material choice (CTE + thermo-optic coefficient) and dimensions One FPI force sensor inherently almost insensitive to temperature disturbance Low cross-sensitivity due to minimizing FPI cavity length
	High finesse, approximately equal reflectances
	Elasto-optic properties FPI cavity medium Mechanism to change FPI cavity medium
	Dependency of the refractive index of the FPI cavity medium on force/stress
	Thermo-optic properties FPI cavity medium Mechanism to change FPI cavity medium
	Dependency of the refractive index of the FPI cavity medium on temperature
	Leaf springs Lubrication
	Support base of sensor in axial and radial direction and circumference of sensor in radial direction
	Two in parallel one for force and temperature and one for temperature Two in series, one for force (and temperature) and one for temperature Two in series, both for force and temperature Two in parallel both for force and temperature
	Acquire knowledge about the disturbing force and temperature with more than 1 FPI sensor

Figure 3.2: Part 1 of the morphological scheme showing the overview of different concepts that can be used for each element of the design of the system

Element		Concepts				
Optical fiber-force/temperature sensitive element connection	Adhesion Glue (ferruled) fiber in borehole Elastic element Thin film adhesion	Friction Press fit Shrink fit	Semi-monolithic Fuse glass Glass-frit bonding	Shape based		
Reference mirror	Difference in refractive index between fiber and FPI cavity medium	Thin layer of material with different index of refraction than fiber or FPI cavity medium Fusion splice Dielectric film Metal film				
FPI cavity medium	Air	Combine with elastic/temperature sensitive element (thin film)	Optical fiber	Vacuum/other gas than air		
Second FPI mirror	Thin layer of material with different index of refraction than fiber or FPI cavity medium Fusion splice Dielectric film Metal film	Difference in refractive index between fiber and FPI cavity medium	Reflecting surface of other element	Force/temperature sensitive element Force sensor-needle tip connection		
Double cavity preventing element	Adsorb energy with second FPI mirror	Divert energy Long 'second' FPI cavity (divergence) Wedge shaped mirror elements Diffuse light with rough surface	Detect all cavities: low coherence interferometry			
Seal	No seal required by using solid medium inside FPI cavity	Sealed by stylet tube-needle tip connection	Plastic foil	Viscous paste		
Stylet-force/temperature sensor connection & Force sensitive element-needle tip connection	No connection, monolithic	Fixed connection Glue joint Welding joint Cotter joint Lock in Snap connection	Semi detachable connection	Detachable connection		

Figure 3.3: Part 2 of the morphological scheme showing the overview of different concepts that can be used for each element of the design of the system

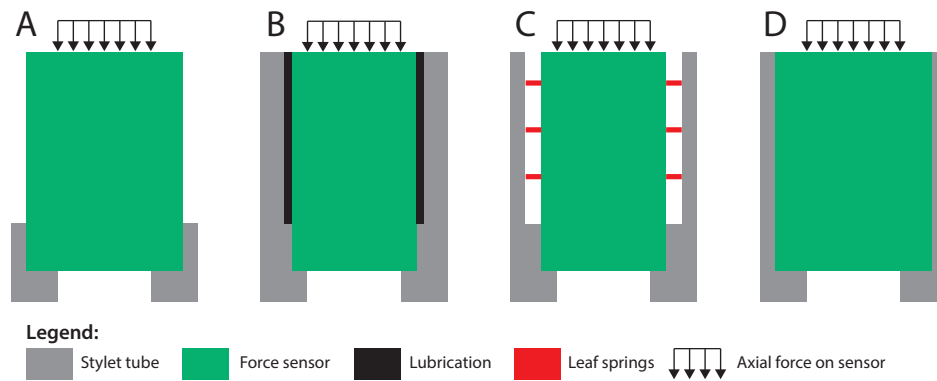


Figure 3.4: Four concepts to house and support the force sensor inside the stylet tube

and axial direction (D).

Supporting the entire force sensor in radial and axial direction by the stylet tube (D) results in the most robust needle, as part of the load exerted on the needle tip in transverse (as well as axial direction) is carried by the stylet tube, relieving a (potentially fragile) sensor of the entire load applied on the needle tip. However, the force sensitive element of the force sensor will in this case behave like it is composed of the actual force sensitive element and the stylet tube due to the 'rigid' connection between the stylet tube and the force sensor. This could reduce the sensitivity of the force-sensitive element, but also increase the cross-sensitivity of the force sensitive element to temperature when the CTE of the force sensitive element and the stylet tube are not matched. The latter would not be a (large) issue when a temperature sensor besides the force sensor is used in the design.

Concepts where the stylet tube is not rigidly connected to the circumference of the force sensitive element of the force sensor greatly reduce the influence of the stylet tube on sensitivity to force and the cross-sensitivity to temperature of the force sensitive element of the force sensor. Supporting and constraining the base of the force sensor in axial and radial direction (A) requires the sensor to carry the entire load exerted on the stylet tip by itself, including transverse forces on the needle tip. The transverse forces could be partially supported by the stylet tube by allowing a sliding contact between the circumference of the force sensor and the stylet tube (B). Such a sliding contact will in practice introduce undesirable hysteresis in the behavior of the force sensor due to stick-slip behavior between the stylet tube and the force-sensitive element of the force sensor. Stick-slip behavior could be reduced by using a lubricant, but cannot be prevented entirely. Hysteresis could theoretically be avoided by using leaf springs or wire flexures to connect the stylet tube to the force sensor (C). However, machining and attaching these leaf springs to a 1 mm diameter stylet and a miniature force sensor seems practically infeasible.

3.2.3 Stylet tip

The stylet tip shape does not significantly influence the performance of the force sensor but affects the amount of transverse forces on the needle tip during needle insertion that might cause failure of the needle and result in effectively larger measurement errors due to sensitivity of the sensor to transversal forces. The tip should preferably be reflectional symmetric to prevent large transverse forces on the needle, which is the case for a standard trocar needle tip and a conical tip.

Table 3.2: Advantages and disadvantages of different concepts for housing the force sensor inside the stylet tube (see figure 3.4)

	Concept A	Concept B	Concept C	Concept D
Robustness of needle/sensor	-	0	0	+
Manufacturability	++	-+	--	++
Decoupling thermal/mechanical behavior of stylet tube	++	+	+	-
Absence of hysteresis	++	-	+	0
Discarded		X	X	

3.2.4 Optical fiber

The most common optical fibers are made of a thin filament of glass, generally fused silica [83, 108]. Plastic optical fibers are an alternative to silica fibers and have the advantage of a higher toughness. Plastics have however a high coefficient of thermal expansion compared to silica fibers, which could be a disadvantage when a dimensionally stable Fabry-Pérot interferometer has to be manufactured. A silica instead of plastic optical fiber seems therefore preferable (at least for most concepts of the measurement system).

A multimode or a single-mode optical fiber can be used to transport optical signals from the optical interrogation equipment to the Fabry-Pérot interferometer and vice-versa. Light is coupled more easily into a multimode fiber as the acceptance angle of multimode fibers is larger, which makes some cheaper light sources like LEDs solely usable with multimode fibers [118]. Multimode fibers are furthermore cheaper and more easily machinable than single-mode fibers [119]. FPI-based sensors based on multimode fibers suffer however from mode averaging, phase dependence, modal noise effects and other effects that reduce the performance of the sensor or complicate usage of the sensor [119]. Single-mode fibers are preferred for most types of fiber-optic sensors for the reduced amount of noise due to the absence of competing modes, alas at the cost of the difficulty of coupling light into the fiber [83, 118]. A single mode fiber is preferred for at least the prototype of this project, as this will result in superior performance and less difficulties with complex responses of the sensor due to multimode related effects.

3.2.5 FPI sensor interrogator

The OPD of a Fabry-Pérot interferometer can be determined with homodyne interferometry or low coherence interferometry (sometimes called white light interferometry). The advantages of homodyne interferometry compared to low coherence interferometry are the significantly low(er) cost of the light source and (photo)detector of the system. Moreover, the VU Amsterdam has made a device designed for interrogation of FPI-based sensors using homodyne interferometry available for this thesis project (the OP1550). Hence, no particular attention to the design of the FPI 'interrogation' system should be required in case homodyne interferometry is used. A choice for the ideal wavelength of the light source can be made when homodyne interferometry is performed. Most silica based fiber-optics use wavelengths around 1300 nm and 1550 nm (near infrared), as the attenuation coefficient of a fused silica optical fiber is the lowest for these wavelengths [118]. Attenuation inside the optical fiber connecting the FPI to the FPI interrogation equipment will however not be an issue for this application, as the fiber will be quite short. Usage of a shorter wavelength results in an increased sensitivity to changes in OPD of the FPI, as the sensitivity to changes in OPD of an FPI sensor doubles when the wavelength of the source is halved. The range of change in OPD that can be measured is however halved at the same time. A stiffer and stronger force sensitive element could be used when a source with a

shorter wavelength is used. The sensor should then however also be manufactured with a higher precision to ensure that the required measurement range will remain measurable.

Homodyne interferometry is not suited to 'interrogate' multiple FPIs multiplexed on a single fiber. Multiple FPIs on different fibers can be 'interrogated' with some inconveniences with a single light source and multiple photodetectors (tuning the wavelength of the monochromatic source such that the FPIs all operate at quadrature becomes for example impossible). Homodyne interferometry is therefore only suited for designs with FPIs on different optical fibers to sense force and temperature (figure 3.7). Low coherence interferometry can be used to interrogate a single FPI or multiple FPIs, either multiplexed on a single optical fiber or on different optical fibers, as long as the OPDs of each FPI differ significantly. No special 'double cavity preventing element' will be required when low coherence interferometry is used, because changes in OPD of multiple FPI cavities created by several (partially) reflective mirrors placed in series can be measured with low coherence interferometry (like in an OCT system [120]).

A second disadvantage of homodyne interferometry is that the method suffers from noise due to optical losses in the fibers connecting the FPI sensor to the interrogation device due to bending of the optical fiber or power fluctuations of the optical source. Compensation for noise introduced by the latter is possible by using an additional detector to assess the optical power of the source. Low coherence interferometry has the advantage over homodyne interferometry that the quantity measured by the FPI sensor is not transmitted as a light intensity to the detector of the interrogation system but as a periodic pattern in the frequency spectrum of the light and is therefore not (very) sensitive to optical losses in the fibers, nor sensitive to power fluctuations of the optical source.

The third disadvantage of homodyne interferometry is the limited range of change of the OPD of an FPI that can be measured, while the sensitivity to changes in OPD of the FPI differs significantly within the measurement range. The force and temperature sensitive elements of the force/temperature sensor have to be manufactured precisely to ensure that changes in OPD of the FPI will not exceed the maximum measurable change in OPD but still remain in a range where a good signal to noise ratio can be maintained. The range of change in OPD of an FPI that can be measured with low coherence interferometry with approximately constant sensitivity is significantly larger than the range of change in OPD of the FPI that can be measured with homodyne interferometry (although it can be necessary to use phase unwrapping which could potentially limit the bandwidth of the sensor), which simplifies manufacturing of the force/temperature sensitive element(s). Furthermore, it becomes possible to design a sensor with an extremely high sensitivity to force and a moderate sensitivity to temperature instead of a sensor with a moderate sensitivity to force and an extremely low sensitivity to temperature due to the larger measurement range. Hence, designing a sensor with a low cross-sensitivity to temperature (in °C/N) becomes easier.

It was chosen to use homodyne interferometry using the OP1550 light source for this project given the difficulty to obtain an alternative light source, in particular a source suited for low coherence interferometry. Low coherence interferometry was kept in mind during the concept phase because it might be particularly attractive for some concepts. Low coherence interferometry seems to have many technical advantages, which is probably the reason why most academic studies on fiber-optic Fabry-Pérot interferometers make use of low coherence interferometry. Designing a system using homodyne interrogation will be a more complex challenge, though valuable if it proves to be successful, as it will significantly reduce costs of the system.

3.2.6 Temperature cross-sensitivity reducing method

The measurement system will use at least one force sensor integrated in the needle tip to measure forces exerted on the needle tip. The aim is to design the entire measurement system in such

Table 3.3: Advantages and disadvantages of two methods for interrogation of FPI-based force/temperature sensor(s)

	Homodyne interferometry	Low coherence interferometry
Measurement range ('constant' sensitivity)	-	+
Insensitivity to power disturbances of the source	+ -	+
Insensitivity to optical losses in fibers	-	+
Ability to filter unintentional double cavities	-	+
Ability to multiplex sensors on a single fiber	-	+
Costs	+	- -
Availability for this project	+	-

a way that changes in temperature of the environment in which the needle is inserted do not result in measurement errors that prevent the system of achieving the required measurement accuracy. This is preferably achieved by designing the force sensor such that it has an intrinsic low cross-sensitivity to temperature, which will be investigated in the next section. Alternative methods to reduce the influence of temperature disturbances on the error of the measurement system will be evaluated thereafter.

How to design an FPI-based force sensor with an intrinsic low cross-sensitivity to temperature

It was chosen to use a sensor based on an FPI to measure force, as it was reported in literature that it should be possible to achieve a relatively low cross-sensitivity to temperature with FPIs compared to high performance optical sensors based on FBGs [111, 112, 121]. FPIs have a particularly low cross-sensitivity to temperature when an air filled Fabry-Pérot cavity is used [122, 123]. The change in OPD of the FPI will be measured by means of interferometry to determine the force exerted on the sensor. Determining how the OPD of an FPI depends on force exerted on the sensor and the temperature of the sensor can be used to analyze the options of designing a force sensor with an intrinsic low cross-sensitivity to temperature.

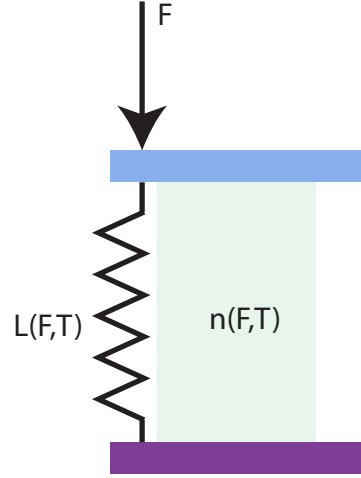
An FPI that can be used as force (or temperature) sensor was modeled as shown in figure 3.5. The two mirrors of the FPI are connected with a spring with a compliance 'c', which is assumed to depend linearly on the temperature of the sensor and to be independent of the force exerted on the sensor (equation 3.1).

$$c = \frac{\partial L}{\partial F} = c_0 + \frac{\partial c}{\partial T} T \quad (3.1)$$

The spring carries the entire load exerted on the force sensor. The change in length of the spring is assumed to depend on the force exerted on the spring according to Hook's law. The change in length of the FPI cavity is assumed to be equal to the change in length of the spring plus the change in geometrical length of the cavity due to expansion of material connecting both mirrors. The change in geometrical length of the cavity due to expansion of the material connecting the mirrors is assumed to depend linearly on the temperature of the sensor and to be proportional to the CTE of the spring's material and the length of the FPI cavity (this definition means that the length of the spring should not necessarily be equal to the length of the Fabry-Pérot cavity). The length of the cavity is L_0 when no force is exerted on the sensor and the temperature is 'zero'. The length of the FPI cavity is thus:

$$L = \left(L_0 + \frac{\partial L}{\partial T} T + \left(c_0 + \frac{\partial c}{\partial T} T \right) F \right) \quad (3.2)$$

Figure 3.5: Simplified model of the Fabry-Pérot interferometer inside the force sensor, showing the mirrors of the FPI in purple and light blue with an FPI cavity medium in between with a refractive index 'n' that depends both on temperature and stress inside the medium resulting from the force applied on the sensor. The mirrors are separated by an elastic element with distance L that depends on the temperature of the sensor and the force exerted on the elastic element.



The refractive index of the medium between the FPI mirrors is assumed to depend linearly on the force exerted on the sensor (which will only be the case when the FPI cavity medium is a solid material) and on the temperature of the sensor. The refractive index is n_0 when no force is exerted on the sensor and the temperature of the sensor is 'zero'. The refractive index is thus:

$$n = \left(n_0 + \frac{\partial n}{\partial T} T + \frac{\partial n}{\partial F} F \right) \quad (3.3)$$

The equation of the OPD of an FPI, given in literature, is a function of the FPI cavity length L and the refractive index of the FPI cavity medium:

$$OPD = 2 \cdot n \cdot L \quad (3.4)$$

The OPD of the FPI of the force sensor as function of the force exerted on the force sensor and the temperature of the force sensor is thus:

$$OPD(T, F) = 2 \cdot \left(n_0 + \frac{\partial n}{\partial T} T + \frac{\partial n}{\partial F} F \right) \left(L_0 + \frac{\partial L}{\partial T} T + \left(c_0 + \frac{\partial c}{\partial T} T \right) F \right) \quad (3.5)$$

The change in OPD as function of a change in temperature or a change in force can be calculated by calculating the gradient of the OPD as function of force exerted on the force sensor and temperature of the force sensor:

$$\nabla OPD(T, F) = \left[\begin{array}{l} 2 \cdot \frac{\partial n}{\partial T} \cdot \left(L_0 + \frac{\partial L}{\partial T} T + \left(c_0 + \frac{\partial c}{\partial T} T \right) F \right) + 2 \cdot \left(n_0 + \frac{\partial n}{\partial T} T + \frac{\partial n}{\partial F} F \right) \cdot \left(\frac{\partial L}{\partial T} + \frac{\partial c}{\partial T} F \right) \\ 2 \cdot \frac{\partial n}{\partial F} \cdot \left(L_0 + \frac{\partial L}{\partial T} T + \left(c_0 + \frac{\partial c}{\partial T} T \right) F \right) + 2 \cdot \left(n_0 + \frac{\partial n}{\partial T} T + \frac{\partial n}{\partial F} F \right) \cdot \left(c_0 + \frac{\partial c}{\partial T} T \right) \end{array} \right] \quad (3.6)$$

Thus, the change in OPD for an infinitesimal change in temperature and force exerted on the sensor is:

$$\Delta OPD = \nabla OPD \cdot \left[\begin{array}{l} \Delta T \\ \Delta F \end{array} \right] \quad (3.7)$$

The partial derivatives of equation 3.5 are (proportional to) material properties, like the thermo-optic and elasto-optic coefficients of the cavity medium (resp. $\frac{\partial n}{\partial T}$ and $\frac{\partial n}{\partial F}$) and the CTE

of the spring ($\frac{\partial L}{\partial T} = CTE \cdot L_0$). These properties were assumed to be independent of temperature of the sensor or force exerted on the sensor in the range of temperatures and forces to which the sensor will be exposed. The compliance of the spring is proportional to the Young's modulus of the material of which the spring is made. The current model assumes that the compliance of the spring and thus the Young's modulus will depend significantly on the temperature of the force sensor. The dependency of the Young's modulus of ceramics and metals on temperature, for example the modulus of quartz glass, AISI 304 stainless steel or Invar alloy, is almost negligible in the temperature range that the force sensor will be used [124, 125, 126]. The Young's modulus of polymers can however change drastically due to 'small' variations in temperature [127, 128]. Cross-Sensitivity of the force sensor to temperature can occur in the form of a constant error and a modifying error. Change of the OPD as result of a change in temperature due to thermal expansion of the spring of the force sensor and a change in refractive index of the FPI cavity medium will result in a constant measurement error throughout the measurement range. The dependency of the Young's modulus of the material of the spring on the temperature will on the other hand cause a modifying error in the measurement of force exerted on the force sensor that will increase with increasing force exerted on the sensor. The measurement error due this effect on the measurement of a force of 10 N, assuming the measured force is proportional to the deflection of the spring, measured with a sensor calibrated at 17°C, will be about 0.11 N, 0.12 N and 0.04 N when the spring of the FPI is made respectively of AISI 304 stainless steel, Invar alloy, or clear fused quartz and the sensor is used at 41°C (based on the interpolation functions for the Young's modulus as function of temperature given in the COMSOL materials library [129]). The error on the measurement of a force of 10 N can be as large as 0.33 N, 3.73 N, 0.37 N, 3.17 N and 0.07 N when respectively polycarbonate, high-density polyethylene, PMMA, PTFE or PET would be used for the spring of the FPI [129]. The magnitude of the modifying error seems to correlate for polymers and glasses with the glass transition temperature of the material. Literature furthermore suggests that most polymers exhibit significant hysteresis, hence polymers should thus be avoided as spring element [130].

Equation 3.6 and 3.7 can be simplified when the compliance of the spring does not significantly depend on temperature and by linearizing the gradient around a certain reference state:

$$\Delta OPD_{linearized} = 2 \cdot \left(\frac{\partial n}{\partial T} \cdot L + 2 \cdot n \cdot CTE \cdot L \right) \Delta T + 2 \cdot \left(\frac{\partial n}{\partial F} \cdot L + n \cdot c \right) \Delta F \quad (3.8)$$

This linearization assumes that the temperature of the sensor does not have no significant influence on the sensitivity of the FPI to force and vice-versa. This is a reasonable assumption, as long as the compliance of the spring of the sensor is independent of the temperature and derivatives of the refractive index of the FPI cavity medium to force or temperature and derivative of the length of the FPI cavity to temperature remain approximately constant within the range of temperatures and forces that the linearization is used. The measurement error due to temperature disturbances of an FPI sensor used to measure force can thus be achieved by minimizing equation 3.9.

$$\min \left(\frac{\Delta OPD(\Delta T)}{\Delta OPD(\Delta F)} \right) = \min \left(\frac{2 \cdot L \cdot \left(\frac{\partial n}{\partial T} + n \cdot CTE \right) \Delta T}{2 \cdot \left(L \cdot \frac{\partial n}{\partial F} + n \cdot c \right) \Delta F} \right) \quad (3.9)$$

Equation 3.8 shows that the cross-sensitivity to temperature of an FPI used to measure force can be minimized by balancing the thermo-optic coefficient of the medium inside the FPI cavity, which seems to be a negative number for most materials, and the CTE of the spring of the FPI, which is nearly always positive. Both the thermo-optic coefficient and CTE should nonetheless be preferably as small as possible to minimize cross-sensitivity to temperature, as both material properties will likely never be sufficiently 'perfect' in balance. Minimizing the FPI

cavity length will also minimize the cross-sensitivity to temperature, as long as other parameters like the compliance of the spring remain constant (of which the machined-quartz-columns and quartz-beam concept shown in section 3.3 are examples). The latter method of reducing the cross-sensitivity to temperature is limited by the manufacturing methods and the minimum required length of the FPI cavity stated in the requirements. The cross-sensitivity to temperature can furthermore be minimized by maximizing the compliance of the elastic element of the FPI or maximizing the elasto-optic coefficient of the FPI cavity medium. This method of reducing the measurement error due to temperature disturbances is strongly limited by the range in which changes of OPD can be measured. The compliance of the elastic element can be increased by choosing an appropriate material with a low Young's modulus for the elastic element and optimizing the dimensions and geometry of the elastic element of the FPI.

FPIs using a spring as force sensitive element and an air filled FPI cavity were identified as the type of FPI sensors that will likely have the lowest possible cross-sensitivity to temperature, as air has a very small thermo-optic coefficient. The measurement error due to temperature disturbances of such an FPI depends thus strongly on the material used for the 'spring' of the FPI. The 'optimal' type of material for the spring for these kind of FPIs, used in the unmachined-quartz-column, stylet-tube and in-fiber-FPI-concept, which will be detailed in section 3.3, was determined using a simplified version of the design of these concepts, shown in figure 3.5, and some back-of-the-envelope calculations. The 'spring' was assumed to be made out of an elastic 'column' with a circular cross-section with diameter 'd', protruding out of the stylet tube (figure 3.6). The 'column' has a cylindrical FPI cavity with a 125 μm diameter. The 'column' was assumed to be made of a single material, although it will in practice also contain at least one optical fiber leading to the first mirror of the FPI. The change in length of the FPI cavity due to application of a force on the needle tip was assumed to depend solely on the Young's modulus of the material of the 'column', the cross-section of the 'column' at the location of the FPI cavity and the length of the FPI cavity. The strain of the 'column' at the location of the cavity is supposed to be transferred 1:1 to displacement of the mirrors of the FPI. This will not be the case in practice, as the mirrors are connected to an optical fiber which is attached by means of glue to the 'column'. The glue connection between the fiber and the 'column' will affect the sensitivity to force and temperature of the sensor significantly. The influence of the connection between the optical fiber and the column will be investigated more elaborately on page 57 and in the next chapters.

The material selection procedure considered the yield strength, the Young's modulus and the thermal expansion coefficient of materials that could be used for the 'column' and materials contained in the CES Edupack materials database [131]. Materials were selected using a criterion based on equation 3.9, a constraint on the yield strength of the material in combination with the diameter of the 'column' and a constraint on the Young's modulus of the material in combination with the diameter of the 'column'. A constraint on the yield strength was used, as plastic deformation or failure of the 'column' due to transverse loads on the tip should not occur. A constraint on the Young's modulus was used to ensure that the change in geometrical cavity length will not exceed 100 nm due to application of a 10 N force for the minimum FPI cavity length, as defined in the requirements. The desired maximum change in geometrical cavity length was chosen to ensure a good sensitivity and linearity of the sensor and is based on data presented in section 3.2.7. Details of equations used for the materials selection and more elaborate results are presented in appendix D.2.

Glasses were identified as ideal materials for the 'column', behaving as a spring, of an FPI with a low cross-sensitivity to temperature. Glasses were identified as ideal materials because of their low CTE, that in some cases even nearly cancels out the thermo-optic coefficient of air. Fused quartz glass was identified as the most practical material, as it is available in the form of

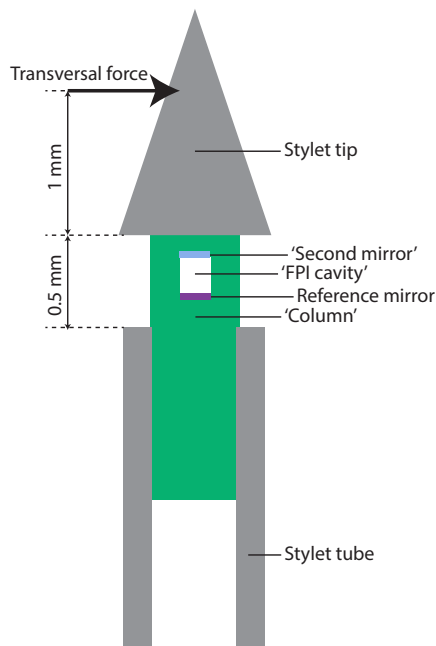


Figure 3.6: Simplified design of the un-machined-column-concept and the in-fiber-FPI-concept used for material selection for the spring of the FPI. The spring is made out of a 'column'. Only the part of the column not supported by the stylet tube is assumed to be required to carry transverse forces on the needle tip.

fiber-optic ferrules (figure 4.5). A ferrule is a cylindrical element with a borehole for an optical fiber and has thus already the shape of the 'column' and provides space for the optical fiber. This is a large advantage, as no equipment was available at the TU Delft to machine glass. A disadvantage of glasses is their brittleness, hence unexpectedly large transverse forces can cause fracture of the 'column' and loose parts in the body of the patient. An advantage of glasses is that they are completely MRI compatible. Metals are far less MRI compatible, but do suffer (in most cases) not from brittleness. Invar alloy was identified as the best non-glass alternative for the column, in particularly because of its very small CTE compared to other metals. Invar alloy is however ferromagnetic, which does make it, besides not very MRI compatible, also very likely MRI-unsafe. The measurement error due to a change of temperature of the needle from 17°C to 41°C, for a sensor calibrated at 17°C, is between 0.2 and 0.3 N when a quartz column with optimal diameter is used as spring and 0.1 to 0.4 N when an Invar column is used as spring, according to the simplified model of an FPI used for the material selection.

A criterion that was not taken into account in the simplified model used for the material selection of the 'column', is that the CTE of the material of the 'column' should preferably match the CTE of the optical fiber adhered to the column as close as possible to minimize cross-sensitivity of the FPI to temperature, as will be shown in section 3.2.15. Optical fibers are made of fused silica, practically identical to fused quartz that has an exactly matching CTE. Invar does have a low CTE, but the CTE of Invar is still a factor 2 to 4 larger than the CTE of fused silica. This makes fused quartz the most attractive material by far to construct the spring of an FPI for a force sensor with an intrinsic low cross-sensitivity to temperature.

Methods design a measurement system with a low cross-sensitivity to temperature

Designing or manufacturing a force sensor with an intrinsic sufficiently low cross-sensitivity to temperature to satisfy the requirements or goals on the accuracy while satisfying requirements on strength of the sensor using available materials and manufacturing methods might be impossible. Three different approaches, within the measurement system or measurement method, can be distinguished to correct for measurement errors due to temperature disturbances of the environment in which the needle is used when the force sensor in the needle tip has a significant cross-sensitivity to temperature.

The first option is to use a priori knowledge about the characteristics of the temperature disturbance, thus without actually measuring the disturbance, to remove the disturbance from the measurement by means of filtering. Filtering can be based on the frequency characteristics of the disturbance, which for temperature disturbances is assumed to be in the relative low frequency region. Filtering based on frequency content was investigated by Elayaperumal et al. for a needle containing an FBG-based force sensor. It was shown to be ineffective, as it did not sufficiently reduce cross-sensitivity to temperature of their measurement system and removed interesting information for haptic feedback purposes regarding forces on the needle tip [29]. Filtering can also be based on a time dependent model. A certain rise in temperature can be expected after starting the needle insertion into the patient, depending on the temperature difference between the room and the patient, the thermal conductivity of the needle and the contact area with the patient. The contact area with the patient and the exact temperature difference are however not accurately known in advance, as the insertion velocity, insertion depth and temperature gradients in the patient are unknown. There are quite significant temperature gradients in human tissue. Differences in skin temperature can be up to 15°C [132]. These large gradients are caused by the low temperatures of the extremities and will not be observed during most needle insertion procedures where measurement of force on the needle tip is relevant. Temperatures between internal organs vary in general with 0.2 to 1.2°C and variations within individual organs can be as large as 0.9°C, although temperature variations in the brain can be as large as 1.4°C. Filtering based on a time dependent model is thus only useful to reduce the measurement error due to large change in temperature between room and average body temperature. The method is therefore only effective when the cross-sensitivity to temperature of the used force sensor is not particularly large, such that temperature gradients inside human tissue do not significantly affect the measurement accuracy (which is for example not the case for the FBG-based needle tip force sensors presented in literature, as the unpredictable temperature variations of 1°C will result in measurement errors of 1 N [2]). Measurement errors during penetration of the skin are however often not very relevant, hence using a sensor calibrated at 37°C instead of filtering using a time dependent model might be equally effective.

The second option to compensate for cross-sensitivity to temperature disturbances is to remove the temperature disturbances during usage of the sensor. The temperature disturbance observed by the sensor can be removed by acclimatizing the sensor to patient temperature, for example in a hot water bath, before the needle is inserted into a patient. The sensor and needle will cool down very quickly due to their small size, unless heating takes place from within the needle itself or the sensor is very well insulated. Both options, and certainly the latter option, are not very realistic given the small dimensions of the needle. Using a sensor calibrated at 37°C is equivalent to using a sensor acclimatized at 37°C that cools down before needle insertion.

The third, most accurate, option to compensate for cross-sensitivity of the force sensor to temperature is measuring the 'disturbance' during needle insertion so that compensation can be based on the actual temperature disturbance and not the expected disturbance. This method is necessary when it proves impossible to design or manufacture a force sensor with a relatively low intrinsic cross-sensitivity to temperature and the previously mentioned work-arounds will thus not be sufficient to minimize measurement errors. The method is however not desired at all, as it will complicate the design of the needle tip and result in a more expensive design, as more (complex) interrogation equipment will be required to also interrogate a temperature sensor. Cross-sensitivity of a force sensing FPI to temperature can furthermore become a difficulty when homodyne interferometry is used to interrogate the FPI. Large changes in OPD of the FPI due to changes in temperature will limit the range of the change in OPD that can be used to measure force on the needle tip. Moreover, minimization of the cross-sensitivity of the force sensor to temperature is desirable in general when a temperature sensor is used to compensate for

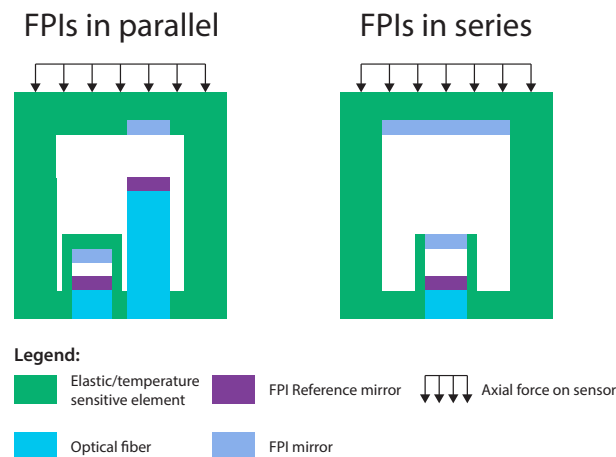


Figure 3.7: Example of a force and temperature sensor with one FPI sensitive to force and the other FPI sensitive to temperature integrated in parallel (on different fibers) and integrated in series (multiplexed on the same fiber) inside the force/temperature sensitive element of the force and temperature sensor in the needle tip.

cross-sensitivity. The absolute measurement error of the force on the needle tip will thereby be minimized given a certain relative accuracy with which the force sensor and temperature sensor used for compensation can measure temperature.

Four different concepts of needle tips incorporating a force and temperature sensor, both based on an FPI, could be identified. The first two concepts use two separate FPIs, one to measure force (and alas some temperature) and a second to measure temperature. The two FPIs can be either multiplexed on the same optical fiber (placed 'in series' in the needle tip) or placed on two separate optical fibers (placed 'in parallel' in the needle tip) (see figure 3.7 for an example). The two other concepts for the force/temperature sensor in the needle tip use two (or more) FPIs, all sensitive to both force and temperature, but each FPI with a different ratio of sensitivity to force and sensitivity to temperature. These FPIs can again be placed either in parallel (one FPI per optical fiber) or in series (all FPIs multiplexed on one fiber) inside the needle tip. The temperature of the needle tip and the force exerted on the needle tip have to be calculated based on the change in OPD of the FPIs. This is relatively simple by using equation 3.8, as shown in section D.3 of the appendix, which is possible when FPIs with springs with a compliance independent of the temperature are used and the ratio of sensitivity to temperature and force of each FPI is significantly different. Calculating the force exerted on the force sensor becomes significantly more complicated when the compliance of the springs of the FPIs (or the thermo-optic or elasto-optic coefficient of the FPI cavity medium or the CTE of the FPI) depends strongly on temperature. The temperature of the needle and force exerted on the needle tip can in such a case not be determined with a unique solution by using equation 3.6 and measuring the OPD of two FPIs by means of interferometry. An iterative method could in such a case be applied to determine the most likely temperature of the needle tip and force exerted on the sensor, based on a known previous state of the sensor, which would be quite complex (details of such a method will not be elaborated).

Bending of the needle will introduce errors when multiple FPIs, all sensitive to force and temperature, are used in a parallel configuration in the needle tip, as not all FPIs can be located on the neutral axis. Configuration of the FPIs in parallel is thus unfavorable, unless additional FPIs are integrated to also measure bending of the needle (which will be difficult due to space constraints in the tiny needle). Using FPIs in series configuration will require the use of a low-

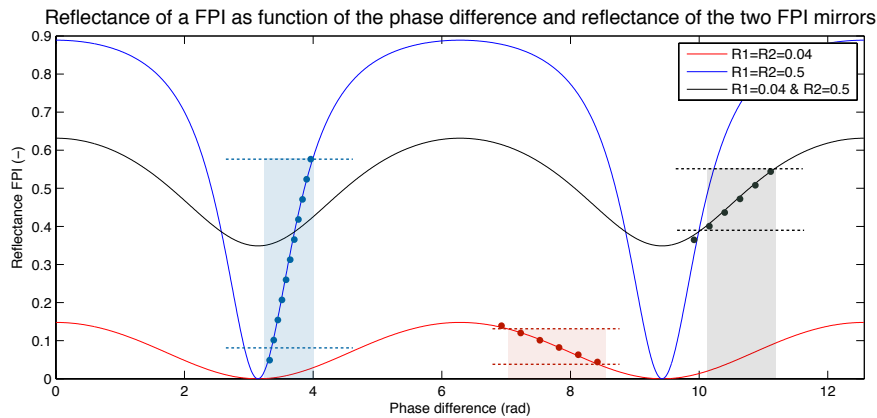


Figure 3.8: Reflectance of a Fabry-Pérot interferometer as function of the phase difference (which is proportional to the OPD as defined in equation A.2), and the reflectance of both FPI mirrors ($R1$ and $R2$). The dotted lines show the range of change in phase difference for which the sensitivity of the FPI to a change in OPD is almost constant. The colored boxes indicate the dynamic range of the photodetector of which the part between the dashed lines can be used to perform measurements with approximately constant sensitivity.

coherence interferometry based interrogation system, which is not preferable/possible for the prototype of the sensor that will be manufactured for this thesis project, as was already mentioned. Attaching a stress free FPI (approximately) in parallel configuration in the needle tip to measure temperature would computationally be the easiest solution to correct for cross-sensitivity of the force sensing FPI to temperature. Attaching this FPI could be a difficult, but part of the choice to use FPIs to sense force and temperature was based on the well defined short sensitive part of FPI based sensors. This should make it 'relatively' easy to attach a stress free FPI. The stress free FPI should be attached such that it has in worst case a low cross-sensitivity to force on the needle tip, such that the method of determining force on the needle tip and temperature of the needle tip can use equation 3.8 because the ratio of sensitivities of both FPIs to temperature and force will be very different.

Evaluation of methods to reduce cross-sensitivity to temperature

It can be concluded that, obviously, a force sensor with an intrinsic very low cross-sensitivity to temperature is preferable. This is even the case when a temperature sensor is used for compensation for the cross-sensitivity of the force sensor to temperature. The measurement errors of a force sensor with a moderate cross-sensitivity to temperature could be minimized, during relevant measurements inside the body of the patient, by using the sensor calibrated at 37°C and optionally applying some filtering based on a time dependent model. Integration of a method to measure the temperature disturbance will in all cases be significantly more complex and more expensive, though also potentially result in a far higher measurement accuracy under temperature disturbances.

3.2.7 Fabry-Pérot Interferometer

Two general properties an FPI, the finesse and the difference in reflectance of both FPI mirrors, can be optimized. These properties are of interest when the FPI will be interrogated with homodyne interferometry to modify sensitivity of the sensor and optimize the dynamic range of the photodetector that can be used to perform measurements (figure 3.8). Calculations to determine the influence of choices about the reflectance of the FPI mirrors were based on equation A.3.

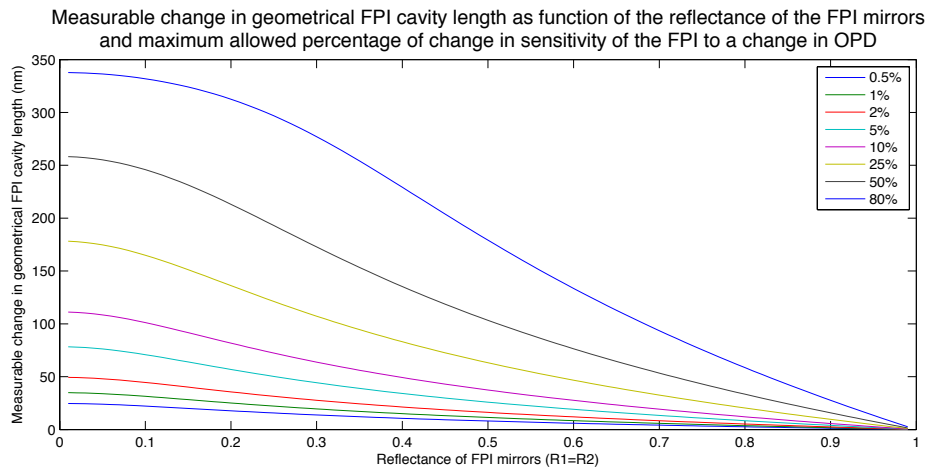


Figure 3.9: Measurable change in geometrical length of an air filled FPI cavity, interrogated with homodyne interferometry using a 1550 nm wavelength source, as function of the reflectance of the FPI mirrors ($R_1=R_2$) and, shown as separate lines, the percentage that the sensitivity of the FPI to a change in cavity length is allowed to deviate within the measurement range from the maximum sensitivity of the FPI.

Finesse

Increasing the finesse of an FPI, achieved by increasing the reflectance of both FPI mirrors, can be used to increase sensitivity of the FPI to changes in OPD at the cost of reducing the range of change in OPD that can be measured with approximately constant sensitivity (figure 3.8). Figure 3.9 shows the range of measurable change in geometrical length of an FPI with an air filled cavity, interrogated with homodyne interferometry at a wavelength of 1550 nm, as function of the reflectance of the FPI mirrors and the percentage of deviation of sensitivity within the measurement range from the maximum sensitivity. An FPI with a high finesse is beneficial in case the force sensitive element of the force sensor cannot create a large (enough) change in OPD of the FPI due to application of a force on the needle tip. Increasing the finesse of the FPI will however strongly decrease the ease with which the wavelength an FPI interrogation device like the OP1550 can be tuned to achieve quadrature and thus maximum sensitivity of the sensor.

An FPI with a higher finesse, interrogated with homodyne interferometry, enables usage of a slightly larger percentage of the dynamic range of the photodetector to perform measurements with approximately constant sensitivity. This should be beneficial to achieve a better signal-to-noise ratio. This is illustrated in figure 3.10, assuming that the photodetector saturates at the end of the required measurement range (part of the fringe pattern can thus not be measured because the photodetector is saturated). A marginal 5% increase in usage of the dynamic range of the photodetector can be achieved by increasing the finesse of an FPI using two glass-air transition mirrors ($R=0.04$) to the maximum finesse (which is practically unattainable manufacturing-wise). Pursuing a high-finesse FPI to maximize to obtain a better signal-to-noise ratio, by maximizing the dynamic range of the photodetector used for measurement of change of the OPD of the FPI, seems therefore a lot of effort for marginal gains. An FPI with a high finesse is furthermore inconvenient when low coherence interferometry is used.

Difference between reflectivity's

A difference in reflectivity of the FPI mirrors will cause an offset of the intensity of the fringe pattern of the FPI sensor (figure 3.8). The offset limits the percentage of the dynamic range of the photodetector that can be used for measurements of the change in OPD of the FPI and

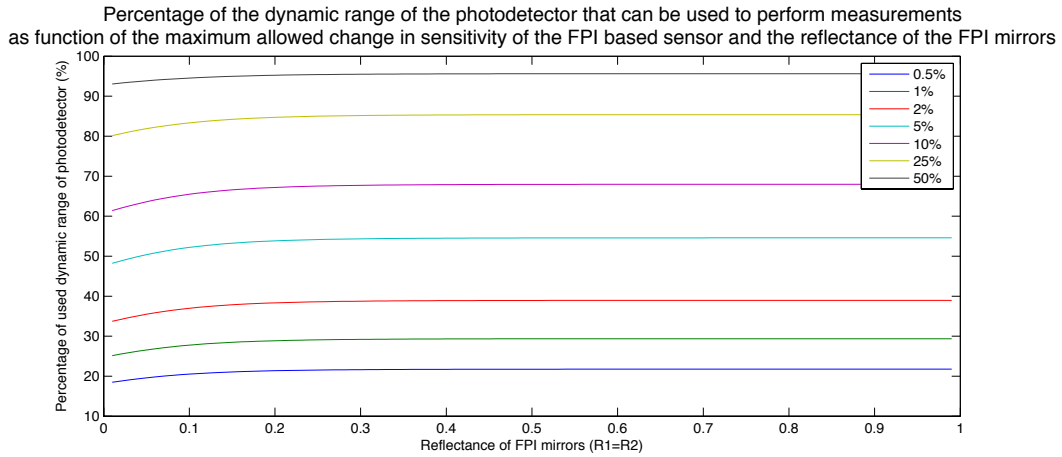


Figure 3.10: Percentage of the dynamic range of the photodetector that can be used to measure a change in OPD as function of the reflectance of the FPI mirrors ($R1=R2$) and, shown with separate lines, as function of the percentage that the sensitivity of the FPI to a change in OPD is allowed to deviate from its maximum sensitivity within the measurement range. The photodetector is assumed to saturate at the maximum of the measurement range.

thereby decreases the achievable signal-to-noise ratio of the measurement system. Figure 3.11 shows the percentage of the dynamic range of the photodetector that can be used to measure the change in OPD of an FPI in a measurement range where the sensitivity of the FPI to force or temperature deviates with at most 10% with respect to the maximum sensitivity that can be achieved, as function of the reflectivity of the FPI mirrors. It can be deduced from figure 3.11 that quite some difference between the reflectivity of the FPI mirrors can be tolerated. However, the combination of an glass-air transition mirror ($R=0.4$) and a gold mirror ($R=0.97$) with a very short FPI cavity is for example highly undesirable [133].

3.2.8 Force sensitive element

The force sensitive element of the FPI inside the needle tip should convert force applied onto the needle tip into a change of OPD of the FPI. This can be achieved by a change of the refractive index of the medium inside the FPI cavity or a change in geometrical length of the FPI cavity.

Dependency of the refractive index on applied force

The strain-optic coefficient (the dependency of the refractive index of a solid material on strain) of a solid FPI cavity medium, like a glass or polymer, can be used to change the refractive index of the FPI cavity medium as function of force applied onto the sensor. However, the strain of the FPI medium causes besides a change in refractive index also a change in geometrical length of the FPI cavity. The ratio of the change in OPD of an FPI due to the change in refractive index of the FPI cavity medium and the change in OPD due to the change in geometrical length of the FPI cavity, both due to strain of the cavity medium, can be calculated with equation 3.10 [134].

$$\frac{\Delta OPD(\Delta n)}{\Delta OPD(\Delta L)} = \frac{-\frac{n^2}{2}(p_{12}-\nu(p_{11}+p_{12}))}{1} \quad (3.10)$$

The strain-optic coefficient p_{11} and p_{12} and the poisson's ratio of quartz glass are 0.113, 0.252 and 0.2 respectively and 0.3, 0.297 and 0.34 for PMMA (a polymer) [135, 134]. The ratio of the change in OPD due to the change in refractive index and the change OPD due to the change in geometrical length of the FPI cavity, both due to strain of the FPI cavity medium, is thus -0.2 for quartz glass and -0.1 for PMMA. Hence, the change in geometrical length of the FPI cavity

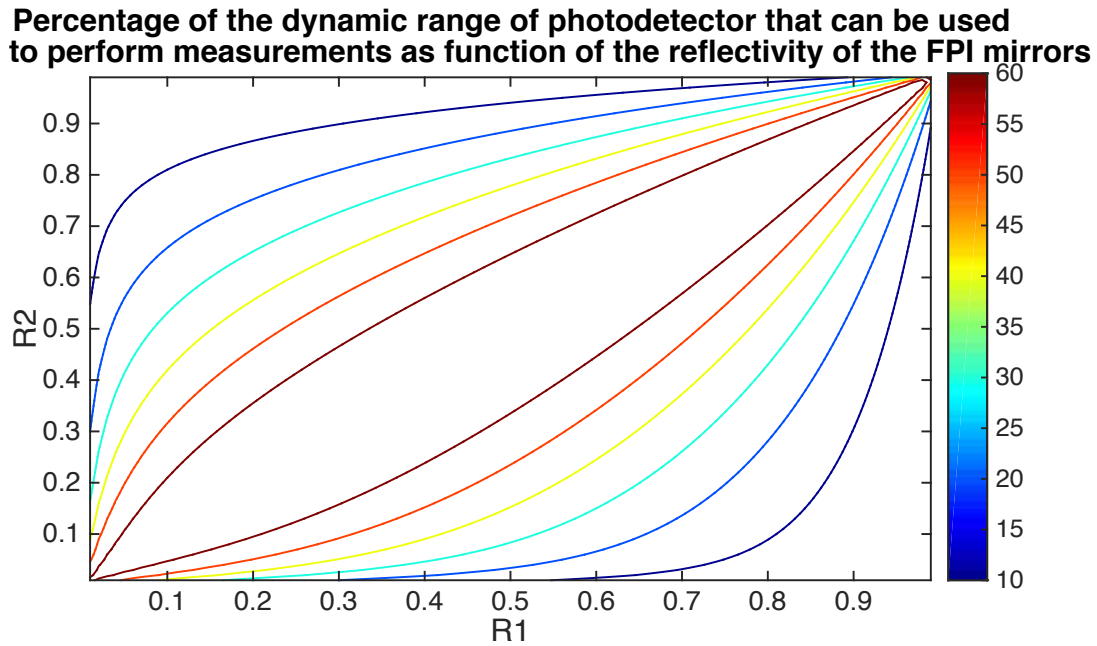


Figure 3.11: Percentage of the dynamic range of the photodetector that can be used to perform measurements with an FPI sensor in a range that the sensitivity of the sensor to force or temperature deviates with at most 10% of the maximum sensitivity that can be achieved, as function of the reflectance of both FPI mirrors ($R1$ and $R2$).

due to strain of the FPI cavity medium results in a far larger change in OPD than the change in OPD due to the change in refractive index, at least for the glass and polymer used as example. Furthermore, the changes in OPD due to both effects are in 'opposite' directions. The change in refractive index of the FPI cavity medium due to strain of the FPI cavity medium can thus be regarded as detrimental instead of beneficial for the functioning of the force sensitive element. The effect will thus reduce the sensitivity of an FPI-based sensor to force, using a solid FPI cavity medium, with about 10% to 20%.

Another option to change the refractive index of the FPI cavity medium is changing the type of medium by means of some mechanism as function force applied onto the needle tip (for example by pumping liquids with a different refractive indices in and out of the cavity). This seems however far too complex for a very small sensor that should fit into a needle. Force sensitive elements based on a change of the refractive index of the FPI cavity medium as function of force applied on the needle tip were therefore disregarded. It was chosen instead to focus solely on methods that primarily transform force onto the sensor into a change of geometrical length of the FPI cavity.

Dependency of the geometrical length on force

A change of geometrical length of the FPI cavity is achieved by displacing the second FPI mirror with respect to the reference mirror. A force can be translated into acceleration using a mass, velocity using a viscous material or a static displacement using a spring. A spring, made of some elastic element, connecting the two FPI mirrors with each other is strongly preferred, as the other two methods result in unconstrained change of the OPD for a constant force on the sensor.

Literature shows examples of classifying elastic elements that act as spring in force sensors [82]. However, it was chosen to use a simple classification based on the type of loading of the elastic elements with respect to their connection with the 'fixed world', as classifications in literature were rather specific on geometry and focussed on usage of strain gauges in Wheatstone

bridge configuration. Elastic elements subjected to axial loads, transverse and torsional loads could be distinguished. Any object of any shape can in principle be subjected to those types of loads. Hence, shapes of elastic elements were abstracted to their most fundamental shape, the shape of 'standard' textbook elements to illustrate deformation of an elastic body due to a certain type of load. The 'standard' textbook elastic elements are the column (for axial loads), the beam (for transverse loads) and the torsion rod (for torsional loads). Complete fixation of the the beam at either one or on both sides of the beam was considered, while more complex complex constraints were regarded as impossible and undesirable for a small force sensor. A membrane, supported along the entire circumference, was regarded as three dimensional variant of a beam fixated at both ends. The torsion rod requires an additional moment arm to convert force into a torsion moment (while the force still causes bending and shearing of the rod, which are the effects of a transverse load).

The compliance of the elastic element of the force sensitive element of the force sensor should be maximized, within certain boundaries, to minimize the measurement error of the FPI-based sensor due to temperature disturbances, as concluded in section 3.2.6). The compliance of all elastic elements can be optimized by choosing a material with a low elastic modulus, which was analyzed in the same section. The compliance of elastic elements can however also be optimized by optimizing the geometry of the element, within constraints regarding failure of the element due to forces in axial and transverse direction on the element and space inside the needle tip. A column is made more compliant by increasing the height or decreasing cross-section of the column. A beam is made more compliant by increasing the length of the beam, which is very limited due to the size of the needle tip. Beams can instead be stacked onto each other to create a more compliant structure. A beam can also be made more compliant by reducing its second moment of area, which goes at the cost of a significant increase of the maximum stress inside the beam (the optimal design of a beam with respect to compliance, stress and wedge angle of FPI mirrors connected to the beam was derived in section D.4 of the appendix). A torsion rod is also made more compliant by reducing its cross-sectional area and increasing its length, which is very limited due to the size of a needle tip. Force has to be exerted on a concentrated spot of the force sensitive element when a beam or torsion rod is used, which is manufacturing and strength-wise a large disadvantage. An overview of the geometries of elastic elements considered for the force sensitive element of the force sensor is given in figure 3.12.

The force sensitive element should be insensitive to transverse forces on the needle tip. A force sensitive element based on an elastic column should not be very sensitive to bending of the column due to transverse forces on the tip when the change in length of the column is measured along the neutral axis of a not particularly long column. Usage of a double side fixated beam will neither result in a large sensitivity to transverse forces, as long as deformation of the beam is measured perfectly at the center of the beam. A beam fixated at only one side (theoretically the most robust type of beam, as shown in the appendix), a stack of such beams and a torsion rod will however be very sensitive to transverse forces on the needle tip, particularly because the moment arm of transverse forces on the needle tip, causing bending of the elastic element identical to bending of the elastic element due to axial forces on the needle tip, will be quite large (figure 3.13).

Evaluation force sensitive elements

A force sensitive element based on changing the geometrical length of the FPI cavity due to application of a force on the needle tip seems most effective. An elastic element shaped like a column or a stack of beams fixated at two sides are the most promising option to be used as force sensitive element. A double side fixated beam and a membrane are options with a limited compliance and are manufacturing and strength-wise rather limited and complicated.

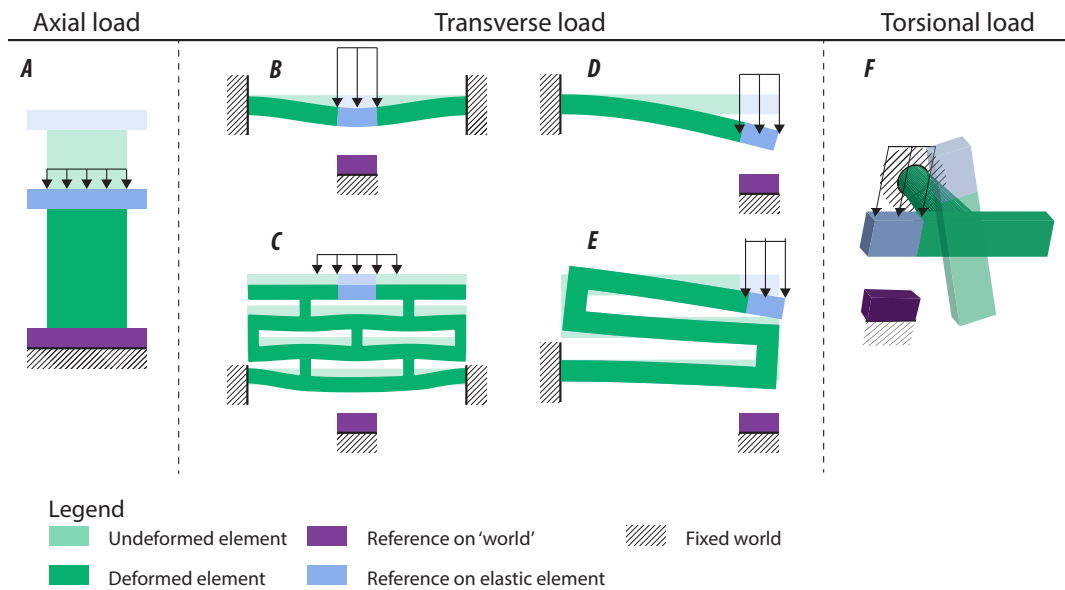


Figure 3.12: Overview of the fundamental elastic element types, classified on type of loading: the column A, the two side fixated beam/membrane B, a stack of two side fixated beams C, the one side supported beam D, a stack of one side supported beams E and the torsion rod F

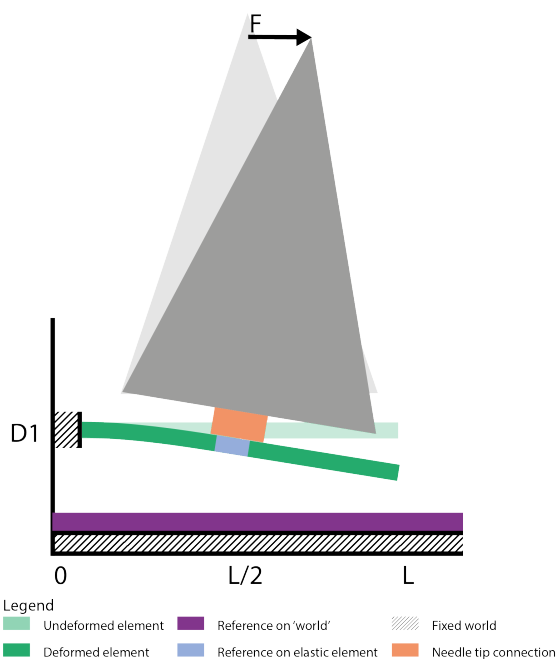


Figure 3.13: Transverse forces on the needle tip containing a one side supported elastic beam as force sensitive element (or stacked one-side supported beams or a torsion rod), will introduce large deflections of the beam, equal to deflections caused by an axial force to the needle tip, and thereby cause a large cross-sensitivity of the sensor to transverse forces on the needle tip.

Table 3.4: Comparison of strengths and weaknesses of different types of elastic elements

Element type	Compliance	Manufacturability	Strength	Insensitivity to transverse force
Column	++	++	++	+
1-side fixated beam	+-	+	+-	-
1-side fixated beams stack	++	+-	-	-
2-side fixated beam	-	-	-	+
2-side fixated beams stack	++	+	-	+
Membrane	-	-	-	+
Torsion rod	-	-	-	-

3.2.9 Temperature sensitive element

A temperature sensitive element is required in case a temperature sensor will be incorporated in the design to convert a change in temperature of the needle tip into a change in OPD of an FPI. Section 3.2.6 analyzed methods to create a force sensitive element and FPI for a FPI-based force sensor with a low (cross-)sensitivity to temperature. Hence, the temperature sensitive element of a FPI-based temperature sensor should have the 'opposite' properties of a 'good' force sensitive element. The change in OPD of the FPI-based temperature sensor can again be achieved by means of a change in geometrical length of the FPI cavity or a change in refractive index of the FPI cavity medium.

A change in geometrical length of the FPI cavity due to a change in temperature is almost unavoidable due to the coefficient of thermal expansion (CTE) of the material that connects the two FPI mirrors (one of the reasons why it is difficult to construct a good force sensitive element). Polymers have in general a quite large CTE compared to metals and ceramics. The sensitivity to temperature of the FPI can be further increased by increasing the length of the FPI cavity. Usage of the CTE of a 'column' connecting the two FPI mirrors is somewhat similar to the elastic 'column' concept for the force sensitive element. The equivalent of the elastic beam concepts for the force sensitive element is connecting the second FPI mirror to a beam made out of two materials with a different CTE, like a bimetal temperature sensor. The beam will then deflect due to a change in temperature due to the difference expansion of the materials. The latter concept is however unnecessarily complicated.

A change in refractive index of the medium inside the FPI cavity due to a change in temperature, due to the thermo-optic coefficient of the medium, is also almost unavoidable (another reason why it is difficult to construct a good force sensitive element). The decrease in density of a material is related to a decrease of refractive index of a material (hence the speed of light inside the material increases) [136]. Thermal expansion of the FPI cavity medium causes a decrease in density of the FPI cavity medium, hence the change in OPD due to the thermo-optic effect is in general in opposite direction of the change in OPD due to thermal expansion of the material connecting the FPI mirrors. The change in OPD of a FPI with a silica FPI cavity medium due to the thermo-optic coefficient of silica is significantly larger than the change in OPD due to the elongation of the cavity due to thermal expansion of the silica FPI cavity medium [95]. The thermo-optic coefficient of air is very small compared to the thermo-optic coefficient of polymers and glasses. Hence, the temperature sensitive element of an FPI with an air filled FPI cavity should rely mostly on the CTE of the connection of the FPI mirrors, while the temperature sensitive element should (likely) rely mostly on the thermo-optic coefficient of the FPI cavity medium when an FPI with a solid FPI cavity medium is used. Both methods should be quite effective and simple. An FPI with a solid FPI cavity medium does however require no seal to

prevent contamination of the FPI cavity, which is a slight advantage.

3.2.10 Reference FPI mirror

The reference FPI mirror should be connected as rigidly as possible to the force-sensitive or temperature sensitive element. A rigid connection is required to prevent that the connection will affect the performance of the force/temperature sensitive element by acting as a significant part of the force/temperature sensitive element itself. The reference mirror will be fabricated on the fiber-top of the optical fiber connecting the FPI to the FPI interrogator. The optical fiber should thus be connected as rigidly as possible to the force/temperature sensitive element, which will be investigated on page 57, while the mirror should be attached rigidly to the fiber-top.

A mirroring surface is made by an interface of two media with a different (complex) refractive index. The most simple way to create the FPI reference mirror is using the difference in refractive index of the optical fiber and the FPI cavity medium. A popular example is the transition from silica of the fiber ($n \approx 1.5$) to air ($n \approx 1$), which results in a mirror with a low reflectivity of about 4% suited for constructing a low-finesse FPI. Usage of a non-air filled FPI cavity could introduce issues, as many candidates for a solid FPI cavity medium have a refractive index close to the refractive index of glass. Mirrors just consisting of the interface between a silica fiber and a polymer film FPI cavity or a fusion splice in an optical fiber have been shown in literature, although the reflectance of such a mirrors will be very low due to the marginal difference in refractive index [137]. Layers of material can be added on top of the optical fiber to create a reference mirror with a more specific reflectance. A dielectric film, for example a TiO₂ film, could for example be used to increase the reflectance of the mirror to about 8% without introducing significant losses due to absorbance of light. Metal films can be used to create mirrors with a very high reflectivity. A metal film will however not transmit much light, as metals generally have a quite large extinction coefficient. Metal films are therefore not optimally suited for the construction of a reference mirror, except in extremely thin layers, as sufficient light should pass into the FPI cavity.

3.2.11 Second FPI mirror

The second mirror of the Fabry-Pérot interferometer should, for the same reasons as the FPI reference mirror, be connected as rigidly as possible to the force or temperature sensitive element. Fabrication options for the second FPI mirror are similar to options for the FPI reference mirror. The mirror can again be fabricated on top of a (non-functional) optical fiber attached to the force/temperature sensitive element. However, thick instead of thin metal films can be used for fabrication of the second FPI mirror, as light is not required to propagate past the second FPI mirror (unless it is chosen to use FPI sensors in series in the needle tip, multiplexed on the same fiber, to measure temperature and force simultaneously). The reflectance of the second mirror for a low finesse FPI can be quite high for long FPI cavity lengths without creating a large offset in the intensity of the fringe pattern, as argued in section 3.2.7, which would enable usage of gold coatings [138]. A metal film with a lower reflectance, created by using a metal with a moderate reflection and extinction coefficient like chromium (adheres very well to many substrates) or titanium, might be more appropriate when the FPI cavity length is short [133]. Finally, a surface of the force or temperature sensitive element or the surface of the needle tip could be used as second FPI mirror. Using the latter as mirroring surface requires a very rigid connection between the needle tip and the force sensitive element, as otherwise backlash, hysteresis or tilt of the force-sensitive element-needle tip connection might introduce large measurement errors. Furthermore, good access will be required to the surface during manufacturing to polish the surface to a mirror.

3.2.12 FPI cavity medium

The FPI cavity medium should primarily have a low extinction coefficient for radiation in the near infrared. The medium should preferably have a low thermo-optic coefficient in case it is used for a force sensing FPI to reduce cross-sensitivity to temperature. A medium with a high index of refraction might be advantageous to increase the sensitivity of the FPI to a change in geometrical length of the FPI cavity, although gains will be marginal given the range of refractive indices of common materials transparent to NIR.

A popular choice of FPI cavity medium for fiber-optic FPI-based strain sensors is air, which has very low thermo-optic coefficient. A thermo-optic coefficient of zero, achievable by using vacuum as medium, is however not beneficial. The thermo-optic coefficient of the medium can be used to compensate for the cross-sensitivity of the FPI to temperature induced by the CTE of the materials connecting the FPI mirrors (and achieving a CTE of zero is quite difficult, nor practical). Using other gases than air as FPI cavity medium does not seem easy manufacturing-wise, as it will be difficult to contain the gas inside the FPI cavity. Furthermore, it will be quite hard to find a gaseous medium that cancels out the effect of the CTE of the materials connecting the FPI mirrors more effectively than air.

A solid instead of gaseous (or liquid) material can also be used as cavity medium. The FPI cavity medium can then be combined with the force/temperature sensitive element of the 'column' type. Glasses and polymers are the most probable candidates for a solid FPI cavity medium to ensure a low extinction coefficient. One option is to manufacture the FPI cavity by means of a thin film deposited on the fiber top, another option is to use a piece of optical fiber as FPI cavity, attached by means of a fusion splice. An optical fiber is beneficial as solid FPI cavity medium to create a very long FPI cavity for a very sensitive FPI-based force sensor, as light cannot diverge out of the FPI cavity due to total internal reflection of the light inside the fiber. It is however expected that such a high sensitivity will not be necessary for this application. Usage of a thin film deposited on an optical fiber as FPI cavity medium and temperature sensitive element seems a very simple and elegant solution, as the properties of the force/temperature sensitive element will be well controllable by using thin film deposition techniques used in the semiconductor industry. A glass or polymer will have a significant thermo-optic coefficient compared to air, while a polymer will also have a large CTE compared to quartz glass. A glass, and probably also polymer, thin film are therefore likely unsuited as force sensitive element for an FPI-based force sensor with an intrinsic low cross-sensitivity to temperature. A compliant polymer film might still be suited, as long as the influence of the CTE and thermo-optic coefficient of the polymer on the change in OPD of the FPI due to a change in temperature cancel each other approximately out (which is not the case for a glass, as can be observed with FBG-based sensors). Prediction of the properties of a thin polymer film on a substrate is however difficult, as materials in thin film form often display anisotropic behavior and the apparent properties will depend significantly on the properties of the substrate [139].

3.2.13 Light adsorbing/double cavity preventing element

One of the problems of using an FPI interrogated with homodyne interferometry is re-entry of light into the FPI cavity that has propagated through the second FPI mirror and reflects back into the cavity via surfaces inside the needle (figure 3.14). Light re-entering the FPI cavity due to reflections on surfaces inside the needle tip will create the presence of a second FPI cavity behind the FPI cavity intended to sense force (or temperature) and cause (very large) measurement errors and likely a large cross-sensitivity to temperature. It is thus required that light is either not able to leave or not able re-enter the FPI cavity or that measurements of the change in OPD of the FPI cavity are performed such that the presence of a 'second' FPI cavity does not result in measurement errors. The latter can only be achieved by means of using low

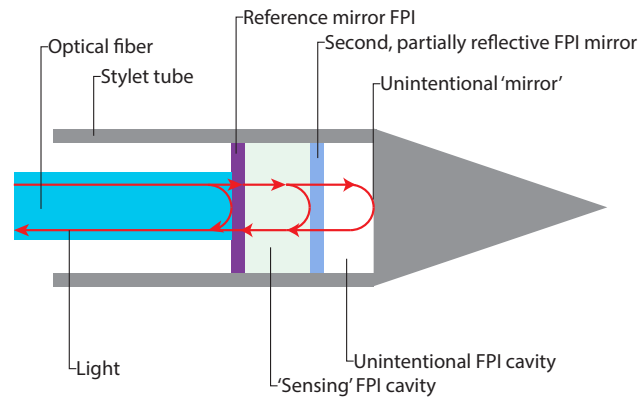


Figure 3.14: Light that leaves the Fabry-Pérot cavity intended for sensing force (or temperature) and re-enters the cavity due to reflections within the needle tip, will create presence of a second FPI cavity behind the cavity intended for sensing force. This second cavity will result in a more complicated response of the sensor and likely a high cross-sensitivity to temperature.

coherence interferometry, which was for availability reasons argued to be not possible for this project.

Preventing light from leaving the FPI-cavity through the second FPI mirror can be achieved by absorption of light that passes through the surface of the second FPI mirror by the material of which the mirror is made. Transmission of light through a medium decreases with increasing extinction coefficient of the medium. However, reflection on an interface with the medium increases with increasing extinction coefficient (equation A.9), which is not preferable in combination with a very short FPI cavity (page 47). A second FPI mirror made of a material with a moderate refractive index and extinction coefficient is therefore in most situations preferred. Transmission through the mirror can then be minimized by increasing the thickness of the mirror (Beer-Lambert law). An online materials database was used to find suited materials for a mirror with a relatively low reflectivity and a very low transmission for light at 1550 nm [133]. Amorphous carbon was in theory the most suited material ($R=0.24$), but was discarded based on advice from experts of the chemical engineering department because it is difficult to deposit in thin film form. Titanium and chromium have also quite appropriate properties for a light absorbing mirror, with reflectances of 0.59 and 0.65 respectively (for an air-metal transition). Both adhere, compared for example to gold, very well as thin film to glass [140]. Oxidation of titanium will form a TiO_2 layer of a few tens of nanometers thick, which has a very low extinction coefficient and does therefore not absorb light [141]. Hence, a titanium mirror should be sufficiently thick to prevent degradation of the light absorbing functionality of the mirror due to oxidation. An oxide layer of only a few atom layers thick will form due to oxidation of chromium [142]. Experiments with a rough prototype (page 101) showed furthermore that a stainless steel mirror, polished with grit P-2400, could serve as second FPI mirror with sufficiently low reflectivity, even for cavity lengths in the order of ten microns. Gold mirrors, with a theoretically extremely high reflectivity but also a very low transmission, were shown in literature for low-finesse FPIs with a relatively long FPI cavity [143].

Preventing light to re-enter the FPI cavity can be achieved by diverting light leaving the cavity to a 'safe' location. The first option to 'divert' light is to ensure a long 'second' FPI cavity behind the second FPI mirror, such that light passing through the second FPI mirror has time to diverge (to some unpredictable location). Light accidentally reflected back into the sensing FPI cavity should therefore have a low power and be incoherent (figure 3.15). An initial rough

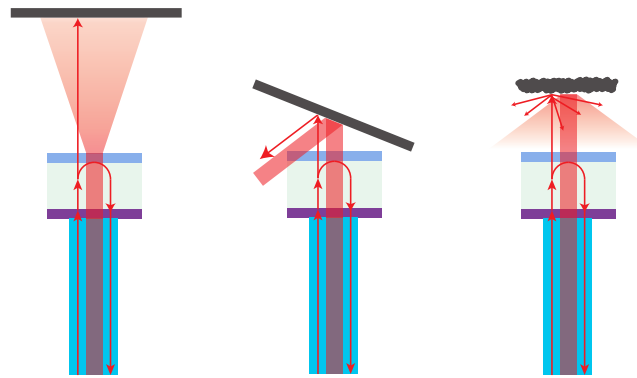


Figure 3.15: Different options to 'divert' light to a safe location after it passed through the second mirror of the FPI cavity to prevent light from re-entering the FPI cavity. The figures show an optical fiber in blue, with the FPI reference mirror in purple, the FPI cavity used for measurements in light green, the second FPI mirror in light blue and the light passing through the elements in red. A third reflecting surface, which could create a second FPI cavity when its parallel, smooth and close to the second FPI mirror, is shown in black.

prototype of such an FPI was constructed by using a 1 mm thick microscope slide as second FPI mirror. The top surface of the slide acted as the second FPI mirror while reflections on the back surface of the slide caused a second FPI cavity. A scan of the fringe pattern of this sensor, as function of the wavelength of the optical source, showed a very disturbing presence of the second FPI cavity, despite the 1 mm length of the second cavity in which divergence of light could take place. Usage of divergence of light to prevent visibility of a second FPI cavity in the response of the FPI-based sensor seems therefore unsuited for a very small and short sensor. A second option to divert light away from the FPI is reflecting light passing the second FPI mirror with a third mirror with a well-defined angle to a 'special' location where the light is absorbed or has space to diverge. A special variant is possible when the second FPI mirror is made on the fiber-top of an optical fiber, such that there is a piece of optical fiber behind the mirror that forms the 'second' FPI cavity. This piece of fiber can then be terminated with a 8°-angled cleave instead of a perpendicular cleave (easily made with a special fiber cleaver). The angled cleave will cause all light propagating past the second FPI mirror, through the 'second' FPI cavity, to be reflected into the cladding of the fiber such that no reflections occur [144, 145]. Finally, an intentionally rough surface can be placed directly behind the second FPI mirror to scatter light leaving the FPI cavity in all directions in the hope that most of the light will not end up back in the FPI cavity. Effectiveness of the latter method is however very unpredictable.

The advantage of diverting light instead of absorbing light by the second FPI mirror is that a second FPI mirror with a very low reflectivity can be used. Designing an FPI with mirrors with equal reflectance will therefore be easier. However, all options to divert light, except using a 8°-angled cleaved fiber, seem manufacturing-wise quite complicated compared to using a light adsorbing mirror, while their effectiveness remains questionable.

3.2.14 Seal

Particles and fluids should be prevented from entering the FPI cavity, as otherwise measurement errors will occur due to changes in refractive index of the FPI cavity medium or particles reflecting and absorbing light in the cavity (as was the case with an FPI-based sensor for a vitreoretinal surgery instrument [81]). The simplest solution to prevent contamination of the FPI cavity is using a solid medium as FPI cavity medium instead of an air filled FPI cavity. This was however argued to be very likely not ideal for the cross-sensitivity to temperature of an

FPI-based force sensor. Sealing the access to the cavity with some element is thus required when an air filled FPI cavity is used. One option is to make the design of the needle tip such that the FPI cavity is sealed by other functional elements of needle that surround the cavity. The entire sensor can for example be inserted in the stylet tube after which the needle tip is attached such to the stylet tube that no fluid can enter the stylet tube. This is in many cases not desired, as it was argued that this method of integration of the force sensor in the stylet tube will affect the performance of the sensor (page 32). The entry to the FPI cavity could also be closed by filling the entrance to the cavity with a highly viscous adhesive. There will be a risk that, despite the high viscosity of the glue, the FPI cavity will be filled with glue. Finally a seal, made of a polymer foil or thin plastic tube, could be used to package the entire sensor. A very thin foil should not significantly affect performance of the sensor. The sensor could be packaged in a foil or tube by shrinking the foil or tube around the sensor, like heat shrinking tube around electrical wires or the vacuum-sealing of food.

3.2.15 Fiber-force/temperature sensitive element connection

The connection between the FPI reference mirror and the force/temperature sensitive element will behave like it is part of the physical structure intended to behave as the force/temperature sensitive element of the force/temperature sensor. Non-rigid behavior of the connection, like elastic, viscous, hysteric or slip(-stick) behavior due to force exerted on the needle tip or changes in temperature of the needle will cause a changes in OPD of the FPI. These changes in OPD of the FPI will in most cases result in measurement errors and potentially cross-sensitivity to disturbances of the environment, like disturbances of the temperature. The connection should therefore be as rigid as possible, or show the same behavior as the force/temperature sensitive element, to minimize the possible deteriorating influence of the connection between both elements on the behavior of the force/temperature sensitive element. The FPI reference mirror will reside on the fiber-top of the optical fiber connecting the FPI interrogation device with the Fabry-Pérot interferometer. Hence, the optical fiber should be connected as rigidly as possible to the force/temperature sensitive element of the force/temperature sensor. The fiber should preferably be attached in a precise borehole in the force/temperature sensitive element to ensure that the optical fiber and thus the FPI mirror is well aligned.

Rigid connections

The most rigid connection imaginable, is manufacturing the force sensitive element and the optical fiber as one (semi-)monolithic part by fusing the optical fiber and a quartz/silica glass force/temperature sensitive element together. An intermediate solution is to use glass frit bonding, where glass with a low melting point is used as solder to join the two parts [146]. Glass frit bonding seems however a rather difficult method to join miniature parts like optical fibers. Furthermore, no glass processing equipment is available at the manufacturing facilities of the TU Delft (DEMO). These very rigid bonding methods were therefore discarded for at least the prototype phase. Many techniques based on fusion splicing are presented in literature to manufacture FPIs in an optical fiber (of which examples are shown in chapter A). This is however not a suited method to manufacture the optical fiber and force sensitive element as one semi-monolithic part, because a fiber cannot carry the entire load exerted on the needle tip by itself and should thus be bonded to a supporting structure that will be part of the force sensitive element. Glass can in some cases be bonded directly and thus very rigidly to a metal or the oxide layer of a metal, which is used in vacuum seals [146, 147]. Bonding of a metal force/temperature sensitive element and a silica fiber seems extremely complicated, amongst others because CTEs of both materials have to match very well. Rigidly bonding a force/temperature sensitive element, either a glass or polymer, to the optical fiber by means of thin film deposition is possible when the FPI cavity medium serves as force/temperature sensitive element and the deposited material adheres

to the FPI mirror on top of the optical fiber at the atom/molecule level (which can sometimes be improved by using an adhesion promotor).

Friction and shape based connections

Fixation of the fiber by means of friction in the borehole of the force/temperature sensitive element, could be possible with, for example, a shrink or press fit. Fixating the fiber by means of friction is for multiple reasons not preferable. Such a connection can in the first place suffer from slip, which will result in significant measurement errors [148]. A shrink or press fit makes it furthermore difficult to position the optical fiber and thus determine the length of the FPI cavity. Shape based connections are neither a good option, as machining the optical fiber for a snap connection, lock-in connection or something similar, is not possible without affecting the light-guiding properties of the fiber.

Glue

Glueing the fiber into the borehole of the force/sensitive element is manufacturing-wise the most simple connection method, particularly when UV-curable glue is used which allows precise positioning of the optical fiber before the glue is cured. The glue layer will however become a part of the force/temperature sensitive element of the FPI. The viscoelastic behavior of the glue can therefore significantly affect the performance of the force/temperature sensitive element. Furthermore, the dependency of the modulus of elasticity of the glue on temperature could be significant for many types of glue (as was shown to be an issue for some polymers in section 3.2.6) and thus affect the compliance of the force-sensitive element as function of temperature.

Strain of the force/temperature sensitive element, due to force applied on the element or a change in temperature, will not be transferred 1:1 to strain of the optical fiber by the glue. The fiber-top of the optical fiber, on which the reference FPI mirror is located, can therefore move with respect to the position where the fiber-top is supposed to be connected to the force/temperature sensitive element when the force/temperature sensitive element strains (figure 3.16). A change in temperature will cause unequal strain of the force sensitive element and the optical fiber due to thermal expansion when the CTE of both elements is not matched. The difference in strain is not significantly reduced by the elastic glue connection between both parts. Movement of the FPI reference mirror due to the bad strain transfer of the glue layer, resulting from a change in temperature, will cause a change in OPD of the FPI and thus a cross-sensitivity of the force sensor to temperature. This problem can only be avoided by matching the CTE of the force sensitive element with the CTE of the fiber, which is quite hard as the CTE of the silica fiber is extremely low. Quartz glass, already identified as a suited candidate for the force sensitive element for a FPI-based force sensor with an intrinsic low-cross sensitivity to temperature, matches the CTE of silica fibers. The closest matching metal is Invar, although the CTE of a silica fiber and Invar still differ with a factor 2 to 4.

A finite element analysis was performed to investigate the severity of the errors induced by a cross-sensitivity to temperature due to a mismatch of the CTE of the force sensitive element and the optical fiber. A 125 μm diameter silica optical fiber (CTE: 0.55 $\mu\text{strain/K}$) was modeled to be inserted 2 mm into the borehole of a cylindrical force-sensitive element with a diameter of 1 mm. A Young's modulus of 150 GPa and a Poisson's ratio of 0.3 were assumed for the material of the force sensitive element, which corresponds to a moderately compliant metal. The influence of the CTE of the material of the force sensitive element up to 20 $\mu\text{strain/K}$ was investigated. The Young's modulus of the glue was assumed as either 0.1 GPa, which is somewhat compliant for a glue, 1 GPa, which is quite stiff, or 10 GPa, which seems to be nearly impossibly stiff (based on product data for epoxies from MasterBond and UV-curable glues from Norland Products [149, 150]). The Poisson's ratio of the glue was assumed to be 0.3 (the value of the Poisson's ratio of most epoxy glues of MasterBond [149]), which is not valid for example for rubbery

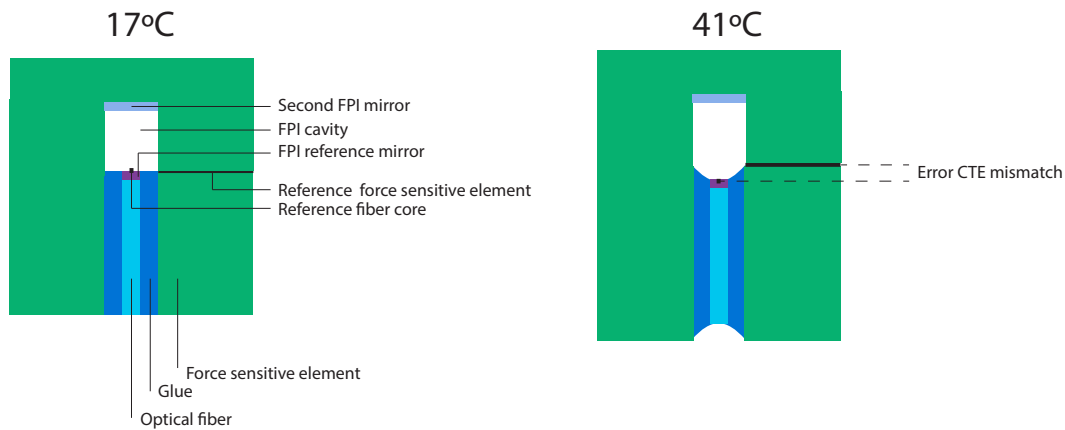


Figure 3.16: Illustration of the model used for the finite element analysis of the influence of the CTE mismatch between the force-sensitive element and the optical fiber on the cross-sensitivity to temperature of the force sensor. The mismatch between a high CTE of the force sensitive element and the low CTE of a silica fiber will cause the end of the fiber to move with respect to the force sensitive element during a change in temperature, of which the effect is depicted in the illustration on the right.

glues. The CTE of the glue was assumed to be equal to the CTE of the force-sensitive element, which is extremely low for most types of glue [151, 152]. The thickness of the glue layer was assumed to be either 10 μm or 25 μm , which is expected to be on the thin side in most cases. The 'error' in geometrical length of the FPI cavity due to a change in temperature was defined as the difference in displacement in vertical direction of the core of the fiber-top and the average of the displacement of the cross-section of the force sensitive element at the location where the optical fiber is supposed to be connected to the element (figure 3.16).

The 'error' in geometrical FPI cavity length as function of the Young's modulus of the glue, the thickness of the glue layer and the CTE of the force sensitive element due to a change in temperature of the assembly with 24°C, is given in figure 3.17. A change in geometrical length of the FPI up to approximately 100 nm due application of a 10 N load on the needle tip would be ideal when an FPI with an air filled cavity, interrogated with the OP1550, is used to measure force on the needle tip to ensure a good constant sensitivity throughout the measurement range. It is very clear, from the data presented in figure 3.17, that even a quite small mismatch in CTE of the force sensitive element and the optical fiber will result in very significant cross-sensitivity of the FPI-based force sensor to temperature. The displacement of the fiber-top with respect to the force sensitive element will quickly be in the order of 100 nm due to the mismatch in CTE. Moreover, a relatively small mismatch in CTE of the force sensitive element and the optical fiber can already make it difficult to use homodyne interferometry to interrogate the force sensing FPI of a needle containing a temperature sensor to compensate for cross-sensitivity to temperature, due to the limited measurement range of the change in OPD of the force sensing FPI (which will be largely or completely necessary to measure the change in OPD caused by the mismatch in CTEs). Expansion of the spring connecting both FPI mirrors and the mismatch in CTE of the force sensitive element and the optical fiber will both cause a cross-sensitivity of the force sensor to temperature and both cause a constant error as function of temperature. The constant error due to the mismatch in CTE will however be far larger than the constant error due to thermal expansion of the spring connecting both FPI mirrors, unless the CTE of the force sensitive element and the optical fiber are matched extremely well.

Reducing the glue layer thickness will reduce the effect of the CTE mismatch on the cross-sensitivity to temperature. However, the thickness of the glue layer cannot be reduced infinitely,

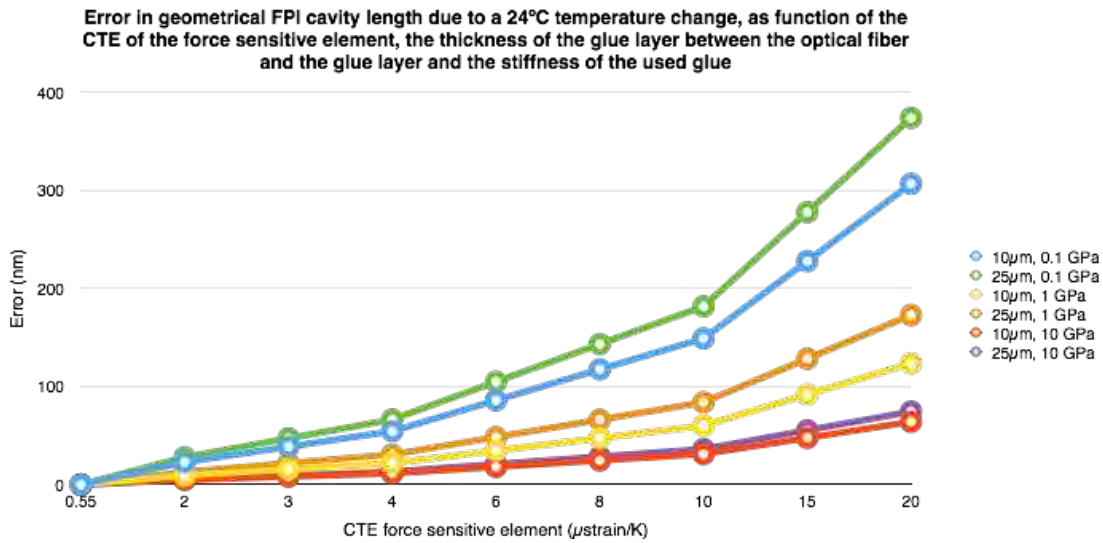


Figure 3.17: Displacement of the end of an optical fiber with respect to the cylindrical force sensitive element in which the fiber is glued due to a change in temperature of 24°C, as function of the Young's modulus of the glue, the thickness of the glue layer and the CTE of the force sensitive element.

as most glues require a bond thickness of a few tens of microns. The effect of the CTE mismatch can be reduced significantly by using a glue with a high stiffness, due to increased strain transfer of the glue layer. The error in geometrical cavity length due to the CTE mismatch will remain nonetheless quite large when there is a relatively small mismatch of 1.5 $\mu\text{strain/K}$ of the CTEs (mismatch between Invar and silica) and an adhesive with a very high Young's modulus of 10 GPa is used. An error in geometrical cavity length of 5 nm will occur according to the model, which contributes an error of 0.5 N to the total measurement error when a 100 nm change in geometrical length of the FPI cavity occurs due to a force of 10 N on the needle tip. Hence, the CTE of the force sensitive element of a force sensor with an intrinsically low cross-sensitivity to temperature should be matched perfectly with the CTE of the used optical fibers to stand a chance to achieve the goal on the required accuracy when the sensor is exposed to the entire range of expected temperature disturbances.

The model assumed the CTE of the glue to be equal to the CTE of the force-sensitive element. The CTE of the glue is in many cases significantly larger, generally in the order of a 50 to 400 $\mu\text{strain/K}$ [152, 153]. The large expansion of the glue will exert some additional stress on the optical fiber, fortunately in such a way that the strain of the fiber will be closer to the strain of the force sensitive element with a higher CTE than the CTE of the optical fiber. The effect is however only clearly present for very stiff glue and the resulting error due to the mismatches in CTE of the force sensitive element, glue and optical fiber will in practice become a lottery as the thickness of the glue layer, the properties of the glue and the force sensitive and the length of the fiber that is bonded to the force sensitive element are rather difficult to predict and control. The high CTE of 'real' glue is, according to the model, not a large issue when the CTE of the force sensitive element is matched to the CTE of the optical fiber as long as the glue remains relatively compliant (e.g. 0.1 GPa) and the glue layer as thin as possible.

The workshop of the TU Delft (DEMO) expects difficulties in machining a precise borehole for an optical fiber with a depth of a few millimeters. Glueing the fiber into a quartz glass fiber-optic ferrule (figure 4.5) and glueing the ferrule in a large borehole in the force/temperature sensitive element is therefore an alternative to glueing the fiber directly into the force/temperature sensitive element. A ferrule is a commercially available glass cylinder with a very precise pre-made borehole for an optical fiber. The precise borehole of the ferrule will ensure a very thin

(1-2 μm) glue layer between the ferrule and the optical fiber, which is advantageous. Moreover, the ferrule itself could potentially be used as force-sensitive element.

Evaluation of connection methods

There are two feasible options to attach the fiber to the force sensitive element. A thin-film force-sensitive element can be attached 'rigidly' by means of adhesion at the molecule/atom level to the fiber-top/reference mirror on the fiber top. The other option, suited for air filled FPI cavities, is glueing a (ferruled) optical fiber in a borehole of a force sensitive element, preferably a force sensitive element with a CTE perfectly matched to the CTE of the optical fiber.

3.2.16 Force sensitive element-needle tip connection

There are many different options to join parts that can be structured based on various characteristics. The relevant classes of joining methods presented in the handbook by Kals were used as main inspiration of available joining methods [154]. Advantages and disadvantages of joining methods will be briefly presented in this section, but the 'ideal' method will depend much on the other elements of the design of the needle.

Monolithic and semi-monolithic connections

Manufacturing the force sensitive element and needle tip as a single monolithic part will result in a strong connection but has several disadvantages. Quartz glass, identified as one of the most suited materials for the force sensitive element, is for example not suited for a strong needle tip nor easily machinable without specialized glass processing equipment. This is not an issue when Invar is used, but a monolithic Invar part will prevent easy access to the location where the second FPI mirror should be manufactured (by means of polishing) and is therefore neither a feasible solution.

Welding the needle tip to the force sensitive element is only possible when the force-sensitive element and needle tip are both made out of a metal or both made out of plastic. Welding will result in a strong and rigid connection. There is however a high risk that other parts of the design, for example the Fabry-Pérot cavity, will become damaged or deform due to the heat produced during welding. Joining a glass force-sensitive element with a metal needle tip as in a glass-metal-seal, is complicated and will likely not result in a strong bond [146, 147].

Friction and shape based connections

Machining of components in complex shapes at a very small size is not preferable, hence a cotter joint or a snap connection are discarded, although a snap connection would result in very easy assembly. A small screw joint is, with certain materials, possible (with a watch makers tap and die set). A cotter, snap and screw joint are susceptible to back-lash, which might make these types of connection unsuited when the back surface of the needle tip is used as second FPI mirror. The connection between the force sensitive element, needle tip and optionally the stylet tube can also be made by means of a lock-in connection. For example by moulding a polymer needle including needle tip around the force sensitive element. Small grooves or notches in the force sensitive element or stylet tube can be used to attach a moulded polymer needle tip to the needle.

A very clean connection could be made by joining both parts with an interference fit. Joining the parts could in theory be done by heating one of the parts and allowing it to shrink on the other part while it cools down. Such a shrink fit requires however extremely tight tolerances on the dimensions of both parts. Enormous temperature differences are required to correct for deviations from the nominal dimensions of parts when dimensions are small. Furthermore, assembling both parts in time will be difficult, because small parts cool down very rapidly. A more convenient approach to achieve an interference fit would therefore be a press fit (engineering handbooks also suggest to use press fits instead of shrink or expansion fits for small parts [148]). This is only

possible when the force sensitive element is not particularly fragile. Deviations of the nominal dimensions are in general not a large issue, as in the worst case some plastic deformation of parts will take place (this is not possible with glass). An interference fit can suffer from slip [148], which might result in measurement errors when the back surface of the needle tip is used as second FPI mirror.

Glue

Glueing the the needle tip and force sensitive element together seems a simple option. There is a risk that the FPI cavity will fill with glue in designs using an open air filled cavity. Furthermore, it remains the question whether glue will result in a sufficiently strong connection to support transverse loads on the needle tip, despite the availability of enormously strong glues, because the contact area will be limited. A combination of a partial lock-in connection to carry transverse loads, with a needle tip that fits partially around the top of the force sensitive element, and glue to prevent the partial lock-in connection from detaching in axial direction of the needle might therefore be required.

3.2.17 Stylet tube-force/temperature sensitive element connection

Options to connect the stylet tube with the force/temperature sensitive element are very similar to the options available to connect the needle tip to the force sensitive element. There is one particular option noteworthy, which is manufacturing the stylet tube and the force sensitive element as a monolithic part. The stylet tube will then act like a force sensitive element of the column variant.

3.3 Concepts

Several concepts for a system to measure forces on the tip of the stylet of a needle, with a low cross-sensitivity to temperature of the needle, could be generated based on the options for the different elements of the design presented in the morphological scheme. In particular many combinations of different types of force-sensitive elements and placements of FPI sensors for force and temperature measurement could be identified. The eight most promising concepts are presented in figure 3.18 (without presence of the 'standard' outer cannula of the needle) and will be briefly described in the next paragraphs. The concepts are shown in a form in which they are expected to be manufacturable as a prototype, but which is not necessarily ideal for the final design of the system. Methods to reduce the cross-sensitivity of the measurement system to temperature of the needle by means of filtering or calibrating the used sensors at body temperature are in principle compatible with all concepts. They are however not expected to be necessary to achieve the requirements on the measurement uncertainty for the concepts in their presented form and will therefore not be mentioned for each different concept. This chapter will conclude with a review of the strong and weak points of each concept based on the requirements on the design of the system.

3.3.1 Description of the concepts

Quartz-beam concept

The force sensitive element of the quartz-beam concept consists of a beam that will be machined by means of laser ablation in a quartz ferrule by making a very narrow cut in the ferrule. An optical fiber, terminated with a 8° cleave to prevent a second FPI cavity, is glued into the ferrule before the beam is machined (the fiber should ideally be fused into the ferrule). The FPI cavity will therefore be contained between two fiber-air transitions that act as FPI mirrors. The FPI cavity length will be minimal by minimizing the width of the cut made with laser ablation. The 8° cleaved fiber end is coated with a thick chromium film to ensure that the angled mirror keeps

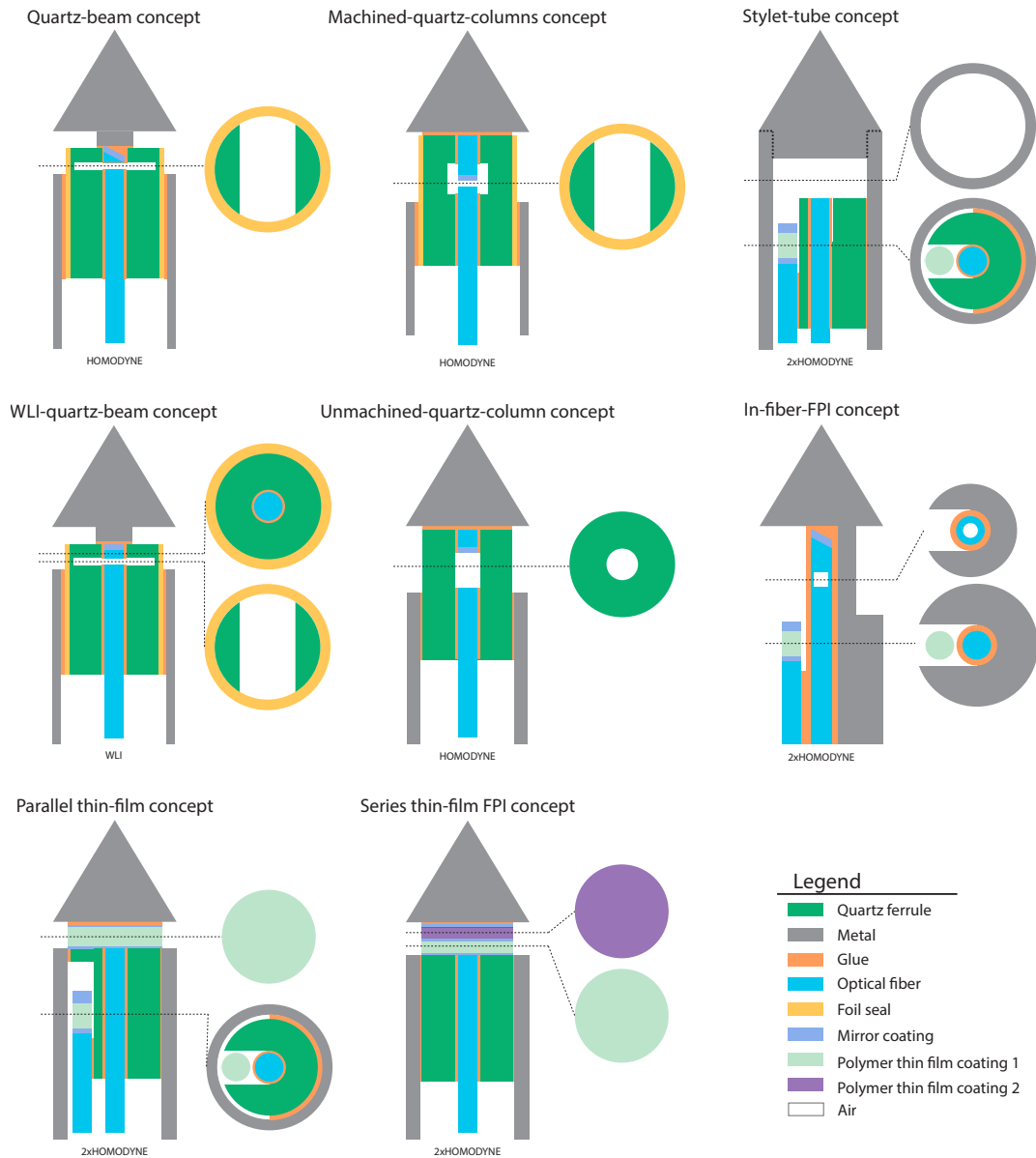


Figure 3.18: The eight most promising concepts for a fiber-optic force sensor, based on Fabry-Pérot interferometry, in the tip of the stylet of a trocar needle to measure forces in axial direction on the needle tip. The illustrations of each concept show an axial cross-section of the stylet tip and a transverse cross-section of the stylet tip at locations containing an FPI cavity. The terms homodyne or WLI indicate whether the concept is suited to be interrogated with a cheap homodyne based interrogation scheme or whether a much more expensive low coherence interferometry based method is required.

existing when glue with approximately the same index of refraction as glass is deposited on top of the cleaved fiber end. The needle tip, machined with a small diameter step to concentrate force on the center of the beam, is glued on top of the beam of the force sensitive element. The cavity is sealed by shrinking a thin foil around the ferrule, before the ferrule is glued inside the stylet tube. The sensor is inserted as far as possible into the stylet tube, such that the bending moment due to transverse forces on the needle tip is carried as soon as possible by the metal stylet tube instead of the quartz ferrule. The sensor can be interrogated with homodyne interferometry.

The cross-sensitivity to temperature of the force sensor should be very low due to the short FPI cavity, the usage of quartz with a very low CTE for the force sensitive element such that the thermo-optic coefficient of the air filled Fabry-Pérot cavity and the CTE of quartz cancel each other nearly out and by matching the CTE of the force sensitive element to the CTE of the silica fiber. Glueing the needle tip will be extremely difficult due to small contact area and the strength of the connection will depend strongly on the type of glue used (which will likely be not strong enough to carry transverse forces on the needle tip). Quartz is a brittle material, hence the maximum tensile stress in the beam is very limited. Tensile stresses up to at least 59 MPa will occur in the beam, based on equation D.32 (for a 18 G needle using a beam length of 0.7 mm, a beam width of 0.8 mm, which will cause an underestimation of the stress as the cross-section of the ferrule is circular and stresses will thus be much larger, a Young's modulus of fused quartz of 73 GPa [131] and a deflection of 100 nm due to a force of 10 N). The tensile strength of quartz is somewhere between 46 and 50 MPa, hence the beam will fail due to the applied axial load on the needle tip [131]. An increase of the finesse of the FPI would make it possible to use a thicker and stronger beam element. This is however not (easily) possible, as there is very limited access to apply a reflecting coating to the fiber-top surfaces. The concept is neither suited for larger than 18 G diameter needles that allow usage of a longer beam, as the axial force on such needle tips will become proportionally larger. It can thus be concluded that the quartz-beam concept can be discarded, despite its expected low-cross sensitivity to temperature, as the strength of the sensor will not fulfill the requirements at all and fail due to axial force on the needle tip and very likely also due to transverse force on the needle tip. A variant using stacked beams instead of a single beam will result in a stronger design, as the entire cross-section and circumference of the ferrule can be used to attach the needle tip to the ferrule and the stress within the separate beams can remain quite low. This variant will however lose the advantage of an extremely low cross-sensitivity to temperature as the FPI cavity length will have to become much larger. This variant is therefore regarded as unnecessarily complex compared to other concepts.

WLI-quartz-beam concept

The WLI-quartz-beam concept is very similar the quartz-beam concept, apart from the double-cavity preventing element that is not used in the WLI-quartz-beam concept because the two FPIs (due to absence of the double cavity preventing element) will be interrogated with low-coherence interferometry. The part of the optical fiber in the beam can be used as a second FPI cavity, besides the air cavity below the beam. This second FPI could be used to measure temperature. The already low-cross-sensitivity to temperature could be reduced even further this way and manufacturing of the sensor will be (somewhat) less complicated. This concept will however, just like the quartz-beam concept, not be strong enough to carry 10 N forces on the beam of its force sensitive element or transverse forces on the needle tip and can thus be discarded with certainty.

Machined-quartz-columns concept

The machined-quartz-columns concept should solve the issue of the lacking strength of the quartz-beam concept while maintaining a very low cross-sensitivity to temperature. Two 'columns', that will act as force sensitive element, will be manufactured by 'drilling' a hole in the center of

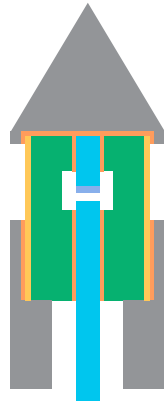


Figure 3.19: Illustration of the machined-quartz-columns concept where the ferrule is connected by a combination of a partial lock-in joint and glue to the stylet tube and the needle tip, which should result in a more robust design as the partial lock-in joint will relieve the used adhesives from the majority of the shear stress due to axial and transverse forces on the needle tip.

a quartz ferrule by means of laser ablation. The optical fiber connecting the FPI with the FPI interrogation device will be inserted in the borehole of the ferrule. A fiber with a thick metal coated fiber end to prevent double cavities, preferably using a chromium coating, is inserted in the borehole via the entry of the borehole on the opposite side of the ferrule. The air filled FPI cavity will thus be contained between a fiber-air transition and a chromium film deposited on a fiber end. The fibers are inserted such that their ends nearly touch each other in the manufactured hole in the ferrule. The fibers are fixated with UV curable glue, such that they can be positioned accurately before fixation (the fibers should ideally be fused into the ferrule). The FPI cavity is sealed from the environment by shrinking a thin polymer film around the ferrule. The ferrule is glued into the stylet tube such that the sensitive part of the sensor still protrudes from the metal stylet tube. The needle tip should be glued on top of the ferrule for prototypes of the design. A combination of partial lock-in joints and glue could be used to connect the ferrule to the stylet tube and needle tip in a more definitive and stronger version of the concept (figure 3.19). Using a partial lock-in joint could be useful to support the ferrule also from below by the stylet tube and relieve the glue from shear stress due to axial forces on the needle tip. A partial lock-in joint to connect the needle tip to the ferrule will be almost certainly be required to relieve the glue from stresses inside the glue due to transverse forces on the needle tip that will be quite large due to the limited contact area. Machining a stylet tube with a stepped borehole and in particular a very short needle tip with a borehole in which the ferrule can fit seems however too complicated for a first prototype of the design. The concept is suited to be interrogated with homodyne interferometry.

The CTE of the silica fibers and the quartz ferrule are matched, hence only the part of the columns with the length of the gap between the fiber ends will cause a change in geometrical length of the FPI cavity due to thermal expansion of the columns. The effect of the expansion of the remainder of the columns is balanced by expansion of the optical fibers protruding into the hole machined into the ferrule. The influence of the CTE of the columns is thus minimized by minimizing the gap between the fibers, while the columns can remain long and compliant such that application of a force on the needle tip can still result in a 'large' change in geometrical length of the FPI cavity. A minor disadvantage, compared to the quartz-beam concepts, is that

the fiber will expand somewhat later than the columns due to an increase in temperature of the environment. The heat should first be conducted through the ferrule and then through the very thin fiber to heat up the entire fiber. A (likely small) transient error due to a change in temperature will therefore occur.

Unmachined-quartz-column concept

The unmachined-quartz-column concept is much easier to fabricate than the machined-quartz-columns concept, as no laser ablation of a ferrule nor very precise positioning of optical fibers is required to manufacture the force sensor. These advantages come at the cost of a worse cross-sensitivity to temperature. The sensor is fabricated by glueing two fibers into a quartz ferrule with UV curable adhesive (the fiber should ideally be fused into the ferrule). One of the fibers is connected to the FPI interrogation device, which can be a homodyne interrogation device, while the other is coated with a thick chromium film to prevent a second FPI cavity. The FPI cavity between the two fiber ends is closed off from the environment by the ferrule and glue. The part of the ferrule around the FPI cavity full-fills the role of force sensitive element by acting as elastic 'column'. The ferrule can then be glued into the stylet tube such that the sensitive part of the sensor still protrudes from the stylet. The needle tip should be glued on top of the ferrule. Replacing the glue joints with a combination of a partial lock-in joint and a glue joint, like shown in figure 3.19 for the machined-quartz-columns concept, would again be preferable but too complicated for a first prototype.

The cross-sensitivity to temperature of unmachined-quartz-column concept will be significantly worse than the cross-sensitivity to temperature of the machined-quartz-columns concept. The expansion of the entire length of the 'column' of the force sensitive element will result in a change of geometrical length of the FPI cavity, as the FPI cavity will have to be longer to maintain sufficient sensitivity to force on the needle tip. The CTE of quartz nearly compensates the thermo-optic coefficient of air and matches the CTE of the silica fibers, hence the measurement error due to temperature disturbances, resulting from the thermal expansion of the quartz column and the thermo-optic coefficient of air, is expected to be lower than the measurement uncertainty of the sensor (as was derived on page 181). Sensors based on the unmachined-quartz-column concept are expected to be significantly stronger than the sensors based on the quartz-beam concept, as the brittle quartz of the ferrule will be mainly exposed to compressive stresses. The sensor is will also be stronger than a sensor according the machined-quartz-columns concept, as no stress concentration will be present due to a hole machined in the ferrule.

Stylet-tube concept

Fabrication of a sensor according to the stylet-tube concept is started by manufacturing a groove in a quartz ferrule with laser ablation or a diamond coated wire saw. A temperature sensing FPI is then made with thin films on top of an optical fiber. The fiber is first coated with (preferably) titanium-dioxide, which has a good adhesion to glass and a low extinction coefficient, to create a partially reflective mirror. A polymer film should be deposited on top of the titanium-dioxide film, after treatment of the surface with adhesion promoters. The polymer film will act as FPI cavity medium and temperature sensitive element. Parylene, deposited by means of CVD, or polyimide or UV-curable adhesive, deposited by means of a spin or dip coating are options for the polymer film. A thick chromium layer is afterwards deposited on top of the polymer film to form the second FPI mirror and double cavity preventing element. The chromium film can optionally be coated with a polymer for protection. The temperature sensitive FPI is glued into the groove of the quartz ferrule, by applying the glue droplet as far away as possible from the thin film layers. A second optical fiber is then glued into the borehole of the quartz ferrule (this fiber should ideally be fused into the ferrule). The quartz ferrule with two integrated fibers is carefully inserted into an Invar capillary stylet tube with slowly curing glue on one side of the

circumference of the ferrule in order to prevent accidentally glueing the the temperature sensitive FPI to the stylet tube or ferrule. The buffer coating of both fibers might have to be stripped to ensure that the fibers fit into the stylet tube. The ferrule is pushed to a certain depth into the stylet tube with a tool with a rod with a length equal to the required depth (figure 5.3). The insertion depth will determine the length of the FPI cavity. The end of a needle tip, made of Invar, is polished to create a mirroring surface. The needle tip is then attached to the stylet tube by means of a press fit. An air filled FPI cavity will thus be created between the fiber-air transition at the end of the second optical fiber and the polished surface of the Invar needle tip. The stylet tube will be used as elastic 'column' of the force sensitive element.

The big advantage of the stylet-tube concept compared to the quartz-beam and quartz-column concepts, is the strength of the sensor. The metal stylet tube will carry practically all the tensile stress due to transverse forces on the needle tip and the brittle quartz ferrule will practically not be exposed to large tensile stresses at all. The cross-sensitivity to temperature of the FPI intended to measure force is expected to be quite significant, due to the slight mismatch in CTE of the quartz ferrule and the Invar stylet tube that acts as force sensitive element. The glue layer between the ferrule and stylet tube will furthermore be rather thick. Hence, a temperature sensing FPI will very likely be required to be able to achieve the goal on the measurement uncertainty, although there might be a slim chance that the required accuracy can be achieved without the temperature sensing FPI (when other sources of measurement errors do not contribute much to the total measurement error). The relatively low cross-sensitivity to temperature of the force sensing FPI could still be interesting when other options to reduce cross-sensitivity to temperature, like filtering or usage of the sensor calibrated at body temperature, are used to diminish the measurement error due to cross-sensitivity to temperature. A second optical detector will be required when the two FPIs are interrogated with homodyne interferometry.

There is unfortunately quite some chance that slip of the press fit connection of the needle tip, which also acts as second mirror of the force sensing FPI, will introduce hysteresis errors of the force sensor. Using glue instead of a press fit to attach the needle tip to the stylet tube could be a solution for this problem. Usage of glue is however not preferred, as there is a great risk that glue will flow into the FPI cavity that cannot be removed before the glue is cured. Accidentally glueing the temperature sensitive FPI to the ferrule will not result in large issues. The transferred strain of the stylet tube or ferrule, due to forces on the needle tip, to the FPI made with the thin films should be minimal, as the FPI will be glued against stiff parts of the needle tip that will deform only slightly. The two FPIs in the needle could thus both become sensitive to force and temperature, but with very different ratio's of sensitivity to both quantities. Temperature of the needle and force on the needle tip can therefore still be calculated with the method presented in this chapter. The usage of Invar, a ferromagnetic material, is a slight disadvantage of the stylet-tube concept, as it makes the needle unsuited for MRI-related applications. It could be possible to replace Invar with a less MRI-unsafe metal. Ideal MRI-compatibility will however be impossible to achieve by using a metal force sensitive element, which is the reason why the stylet tube concept is stronger than earlier presented concepts.

In-fiber-FPI concept

The in-fiber-FPI concept uses a fiber with an air filled FPI cavity, made in the fiber itself with fusion splicing methods as proposed in literature (see the appendix on page 148). The cavity can for example be manufactured by splicing a fiber with an etched core to another fiber, such that a small air cavity remains at the splice location. The optical fiber should then be cut, as close as possible to the FPI cavity, with a 8° cleave to prevent a double cavity. It will be challenging to make this cleave close to the FPI cavity to ensure that the FPI can be located close to the needle tip. A metal coating should be deposited on top of the cut to ensure that the angled mirror will keep to exist when a layer of glue is deposited on top of the the fiber. The fiber containing the

FPI is then glued into a groove machined in an Invar stylet, that could for example be machined with EDM. The Invar stylet should preferably have a reduced diameter at the location of the FPI to increase the compliance of the column of the force sensitive element, that consists of the optical fiber, glue and the stylet. The needle tip and stylet are made as a monolithic part. The FPI can be interrogated with homodyne interferometry.

The cross-sensitivity of the FPI glued to the Invar stylet should be reasonable, but far from optimal due to the mismatch of the CTE of the Invar stylet and the silica fiber. The in-fiber-FPI concept is expected to have either a worse strength or worse cross-sensitivity to temperature compared to the stylet-tube concept, due its disadvantageous ratio of the cross-sectional area and the second moment of area at the location of the FPI. A low compliance of the force sensitive element will therefore always come at the cost of high stresses in the stylet tube due to transverse loads on the needle tip. Addition of a temperature sensing FPI, created with a method similar to the temperature sensing FPI of the stylet-tube concept, is very likely required to achieve the goal on the measurement uncertainty. The in-fiber-FPI concept does not suffer from measurement errors due to hysteresis of the needle tip-stylet tube connection or the chance that glue will flow into the FPI cavity, which are advantages of the design compared to the stylet-tube concept. Fabrication of a FPI with a controlled cavity length by means of fusion splicing will however be more complicated and more expensive. The usage of Invar is, for the same reasons as for the stylet-tube concept, a slight disadvantage of the in-fiber-FPI concept as it makes the needle unsafe for usage with MRI guidance.

Parallel thin-film concept

The up-to-now proposed concepts have FPI cavities that are somewhat to quite difficult to manufacture. It will in general be quite difficult to precisely determine the length of the cavity, reproduce this cavity length for multiple sensors, and prevent that the air filled cavities are accidentally filled with glue used to assemble the sensor and needle. The thin-film concept therefore uses polymer thin films as FPI cavity medium and force sensitive element. The length of such a cavity can be precisely controlled and reproduced with a thin film deposition method like CVD and to a reasonable extend with a spin or dip coating technique. A sensor based on the parallel thin-film concept is fabricated by first machining a groove into a quartz ferrule. The groove is preferably not made along the entire length of the ferrule, such that the top side of the ferrule remains intact and can be used entirely for the deposition of a thin polymer film. The groove should therefore be made with laser ablation instead of a diamond coated wire saw. A temperature sensitive FPI on an optical fiber, made with thin film deposition like the temperature sensitive FPI of the stylet-tube concept, is then glued into the groove. Next, a second optical fiber is inserted into the borehole of the ferrule. A titanium-dioxide film, which will act as reference mirror of the force sensing FPI, is afterwards deposited by means of sputtering or atomic layer deposition on top of the quartz ferrule. A polymer film is subsequently deposited on top of the titanium-dioxide layer after treatment of the surface with an adhesion promotor. A spin coated polyimide layer or a chemical vapour deposited parylene-C layer are some of the options the polymer layer. The elastic modulus of polyimide might be less dependent on temperature compared to parylene due to its much higher glass transition temperature [155, 156]. A thick chromium layer is finally deposited on top of the polymer layer by means of sputtering or thermal evaporation to serve as second mirror of the FPI and prevent a double FPI cavity. The needle tip can be glued on top of the ferrule and the ferrule can be glued into the stylet tube. A polymer needle tip (or a metal needle tip with a polymer transition piece) should ideally be attached by means of a partial lock-in connection and glue or moulded on top of the stylet tube containing the ferrule with the two FPIs to ensure a stronger connection of the needle tip, which is too complicated for the prototype phase. The sensor can be interrogated with a homodyne interferometry using at least two photodetectors because the two FPIs are placed in parallel in

the needle tip, located on two optical fibers.

A temperature sensitive FPI is expected to be required due to the large CTE and thermo-optic coefficient and the possible dependence of the Young's modulus on temperature of the polymer used for the combined FPI cavity medium and force sensitive element. These properties will likely cause a significant cross-sensitivity of the force sensitive element to temperature, causing a constant as well as modifying measurement error. The sensor is expected to be reasonably robust when a needle tip is moulded onto the stylet tube. Prototypes of the design where the needle tip is glued on top of the ferrule are however expected to be quite fragile, as adhesion of the thin film and glue layers to the ferrule should be able to withstand shear and tensile stresses due to transverse forces on the needle tip. The sensitive part of the temperature sensing FPI is preferably not glued to the stylet tube or ferrule to prevent the temperature sensing FPI from becoming sensitive to force exerted on the needle. However, failure to do so will not result in large issues, as the ratio of sensitivity to force and temperature of both FPIs will be significantly different. This will allow computation of the temperature of the needle tip and force exerted on the needle tip with a simple method presented in this chapter, as long as the Young's modulus of the used polymers does not significantly depend on temperature.

Series thin-film concept

Manufacturing of the parallel thin-film concept can even be further simplified at the cost that low coherence interferometry will be required to interrogate the FPIs of the force/temperature sensors in the needle tip. Fabrication of a prototype of the series thin-film concept starts by glueing an optical fiber in the borehole of a quartz ferrule. A titanium-dioxide layer will be deposited on top of the ferrule to act as reference mirror. A thin polymer layer, followed by another titanium-dioxide layer and second polymer layer of a different kind of polymer are deposited on top of the titanium-dioxide layer. A thick chromium film is deposited on top of the last polymer film. Hence, two FPIs multiplexed on the same fiber will exist in the needle tip, each using one of the polymer films as FPI cavity medium and force/temperature sensitive element. The FPI cavities should have a different ratio sensitivity to force and sensitivity to temperature, which could for example be achieved by using combinations of Parylene-C, Parylene-N, PMMA or polyimide [157, 156]. The needle tip can be glued on top of the chromium layer, after which the quartz ferrule can be glued into a metal stylet tube. However, a polymer needle tip (or a metal needle tip with a polymer transition piece) should ideally be attached by means of a partial lock-in connection and glue or moulded onto the stylet tube to ensure a stronger connection of the needle tip to the needle.

The production process of sensors according to the series thin-film concept seems very suited for batch processing and should have highly repeatable results. The strength of prototypes of the design with a glued needle tip is limited by the unknown adhesion strength of the thin films to the ferrule and each other and the strength of the glue connection of the needle tip. The strength of a more definitive version of the design, using a polymer needle tip, should be investigated with FE-analysis or by means of testing prototypes (for investigating the wear of the needle tip). Calculation of the temperature of the needle tip and force exerted on the needle tip might become cumbersome when one of the Young's moduli of the used polymers depends significantly on temperature but should otherwise be straightforward. A completely polymer needle could be made by depositing the FPIs on a plastic optical fiber and moulding the fiber in a polymer needle. This will ensure perfect MRI compatibility of the needle, though could result in quick wear of the needle tip.

3.4 Review of the concepts

The eight presented concepts were evaluated on based on the (relevant) requirements (mainly with a high priority). Important requirements are the expected strength of the needle, in particular the part containing the sensor, the expected measurement uncertainty, in particular the influence of the expected cross-sensitivity to temperature on the measurement uncertainty. The expected performance of the concepts with respect to the measurement uncertainty was subdivided in the expected accuracy of the force sensing FPI on itself and the expected accuracy of the combination of the force sensing FPI and the temperature sensitive FPI if present (which is somewhat more difficult to estimate). Moreover, the concepts were rated based on the number of FPIs contained in the needle tip, as usage of less FPIs is cheaper and can be tested in a prototype with the available equipment. The concepts are all expected to be suited to measure forces in the entire required measurement range when the sensor is carefully dimensioned and precisely manufactured. Hence, concepts were rated on the ease with which sensors are expected to be manufacturable with the required repeatability and controllability to achieve the required measurement range when homodyne interferometry is used to interrogate the FPIs. It was initially chosen to design a needle with an optical force sensor such that it could also be MRI compatible. The needle could very well also be used for non-MRI related interventions, hence the requirement on MRI-compatibility was rated with a low priority. Concepts were nonetheless also rated on potential MRI compatibility, although lacking potential for MRI compatibility is regarded as a slight disadvantage of a concept. The concepts were furthermore assessed based on their expected manufacturability and availability of the FPI interrogation equipment. Expected good performance was rated with one or more '+' symbols (more is better), while bad performance is rated with one or more '-' symbols. Concepts were rated with two minus symbols when the concept is expected to fail to meet a requirement in such a way that the total concept is unusable and the concept should be discarded. Performance was rated with a question mark when no sensible estimate could be made based on information found in literature, simple models presented so far or general knowledge. The assessment of the different concepts is presented in table 3.5.

Three of the eight concepts are discarded (at least for this thesis project) due to either failing the requirements on the strength of the sensor/stylet or requiring a low coherence interrogation method of the FPI. The series thin-film concept, with the manufacturing process that is expected to be the easiest and highly repeatable, is therefore unfortunately also discarded. The remaining concepts have all distinct advantages and disadvantages that are difficult to weigh against each other. A needle and sensor with a very low strength and a low measurement uncertainty and a needle with a large strength and a very high measurement uncertainty are both not preferable, though which is less preferable is hard to say without a more detailed quantification of the actual performance. A needle with a too low strength, which can be determined with a more detailed analysis of the concepts, will however always be a reason to discard the concept, even when the sensor has zero measurement uncertainty.

The machined-quartz-columns concept has the advantage over other concepts of an intrinsic low cross-sensitivity to temperature of the force sensing FPI and requires only one detector when homodyne interferometry is used to interrogate the FPI(s) in the needle tip. The parallel thin-film FPI concept should be relatively easily manufacturable with high repeatability compared to other concepts. The cross-sensitivity of the thin film based force sensing FPI to temperature could however be significant and compensation for this cross-sensitivity might be complex due to a possible dependence of the compliance of the force sensitive element on temperature. The stylet-tube and in-fiber-FPI concept should both result in strong designs compared to the other concepts. The stylet-tube concept is expected to result in the strongest design at the cost of an increased measurement uncertainty, because slip of the needle tip stylet tube connection could

Table 3.5: Assessment of the 8 proposed concepts for a system to measure forces on the tip of a needle. Concepts scoring a + are expected to perform good with respect to a particular requirement on the design, while scoring a minus indicates that a bad performance is expected with respect to the requirement.

Concept	Requirements							
	Strength	Accuracy I-FPI	Total accuracy	Manufac-turability	Reprodu-cibility	MRI safe	Interrogation equipment	Number FPIs
Quartz-beam concept	--	++	++	-	-	+	++	+
WLI-quartz-beam concept	--	++	+++	-	+	+	--	-
Machined-quartz-columns concept	-	++	++	+-	+-	+	++	+
Unmachined-quartz-column concept	+-	+	+	+	+-	+	++	+
Sty/et-tube concept	++	+-	++	+	-	-	+	-
In-fiber FPI concept	+	+-	++	+-	-	-	+	-
Parallel thin-film concept	+	-?	+	+	++	++	+	-
Series thin-film concept	+	-?	+	++	++	++	--	-

affect performance of the FPI significantly, as the needle tip also serves as second FPI mirror (which should be solvable by glueing the needle tip into the stylet tube). The force sensing FPIs of the latter two concepts are however expected to have a mediocre measurement uncertainty compared to quartz-column based concepts, due to cross-sensitivity to temperature caused by a mismatch of CTEs of used materials. They are furthermore very likely not MRI-safe/compatible due to usage of ferromagnetic Invar. They remain however of particular interest for non MRI-related applications due to their high strength. Invar could furthermore potentially be replaced by an MRI safe metal at the cost of a high cross-sensitivity of the force sensing FPI to temperature.

It was chosen to evaluate the machined-column-concept, parallel thin-film concept and the stylet-tube concept further, as all have a distinctly different advantage, to determine which of the concepts is able to achieve both the required measurement uncertainty and strength of the needle and remain preferably also easily manufacturable. The machined-column concept was regarded as the most interesting concept, because the aim of this thesis was to design a measurement system with a low-cross sensitivity to temperature which should be achievable with this concept and the available equipment. The next three chapters will analyze the performance of the concepts by means of finite element analyses and results of tests with prototypes of the needle tip containing only the force sensing FPI of each concept (as there was no time to also fabricate temperature sensing FPIs required for some of the concepts).

Evaluation of the machined-quartz-columns concept
Design of prototypes of the unmachined-quartz-column concept
Calibration method
Calibration results of the unmachined-quartz-column concept
Discussion

4 Quartz-column concepts

The machined-quartz-columns concept was selected as the most promising concept for a design of a needle with a force sensing FPI with an intrinsic low cross-sensitivity to temperature. Examination of the machined-quartz-columns concept by means of a finite element analysis and fabrication of a large scale prototype revealed however three reasons to discard the concept in favor of the unmachined-quartz-column concept, related to strength of the needle tip and force sensor, measurement uncertainty of the force sensor and manufacturability. The reasons to discard the machined-quartz-columns concept will be clarified in the first section of this chapter. The remainder of the chapter will focus on the evaluation of the unmachined-quartz-column concept, as this concept should have an approximately similar measurement uncertainty but a better strength and manufacturability compared to the machined-quartz-columns concept. The general design and manufacturing steps of prototypes of the unmachined-quartz-column concept will be presented first, with results of FE-analyses of the strength of the design and the sensitivity of the sensor to force. The influence of some disturbances on the measurement uncertainty will be investigated afterwards with a bit more detail than in the previous chapter. The method to test the performance of prototypes of the concept and results of the performed tests will be shown subsequently. The chapter will conclude with a discussion of the test results and recommendations for improvements of the design.

4.1 Evaluation of the machined-quartz-columns concept

An important criterion for the force sensitive element of the machined-quartz-column concept is that it should behave as a perfect elastic spring. The stiffness nor length of the spring should depend on temperature to transduce forces on the needle tip accurately to a change in geometrical length of the FPI cavity, irrespective of temperature disturbances. An important reason to choose for quartz glass as material for the force sensitive element of the machined-quartz-columns concept is the perfect match of the CTE of the material with the CTE of silica optical fibers. This should be beneficial for the dimensional stability of the FPI cavity, due to the absence of stresses due to large differences in thermal expansion of components in the force sensor. Quartz glass was furthermore expected to behave as a nearly perfect elastic material at room temperature, as the glass transition temperature of quartz glass, the temperature at which a material starts to behave rubbery and thus show viscoelastic instead of purely elastic behavior, is about 1600°C [131]. The low CTE of quartz glass should ensure that the length of the 'spring' does depend

minimally on temperature. The theoretical advantage of the machined-quartz-columns concept over the unmachined-quartz-column concept is that the same expansion of equally long quartz glass columns due to a change in temperature should result in a smaller change in geometrical length of the FPI cavity in the machined-quartz-columns concept. The CTE of the silica fibers and the quartz columns are matched, hence only the part of the columns with the length of the Fabry-Pérot cavity, which is very short for the machined-column-concept, will cause a change in geometrical length of the FPI cavity due to thermal expansion of the columns. The effect of the expansion of the remainder of the columns is balanced by expansion of the optical fiber.

The force sensitive element of the machined-quartz-columns concept will consist in practice of the quartz 'columns' machined in a quartz ferrule and an approximately 1 μm thick glue layer that fixates the used optical fibers, on which the FPI mirrors reside, in the borehole of the ferrule. The influence of such an extremely thin glue layer on the behavior of the force sensitive was expected to be negligible during the concept phase, as long as the CTE of the glued components is matched almost perfectly. This assumption was however proven to be untrue by finite element simulations performed for the unmachined-quartz-column concept. The FE-simulations showed that the presence of glue does not cause an extreme but certainly not negligible 'change in length' of the FPI cavity due to a change in temperature. The contribution of the expansion of the quartz glass column and the effect of the presence of the thin glue layer to the change in geometrical length of the FPI cavity due to a change in temperature is in the same order of magnitude for the unmachined-quartz-column concept (depending slightly on the used glue, see table 4.2). The force sensitive element of the machined-quartz-columns concept will suffer from the same presence of glue, which will in this case be the dominating factor determining the cross-sensitivity of the FPI to temperature. The machined-quartz-columns concept has therefore only a marginal advantage over the unmachined-quartz-column concept with respect to dimensional stability of the 'spring' used as force sensitive element.

The contribution of the compliance of the extremely thin glue layer used to bond optical fibers to the ferrule to the compliance of the entire force sensitive element that acts was assumed to be negligible during the concept phase. Finite element analyses performed for the design of the unmachined-quartz-column concept showed however that the compliant thin glue layer contributes very significantly to somewhat to the total compliance of the force sensitive element of the force sensor (depending on the used glue, see table 4.2). The sensitivity to force and modifying errors due to cross-sensitivity to temperature of the FPI of the machined-quartz-columns concept will thus be determined significantly to somewhat by the properties of the used glue. This might be problematic, as glue is expected to behave more like a viscoelastic material instead of an elastic material at room temperature, as the glass transition temperature of glue will be in the order of 100 to 200 $^{\circ}\text{C}$ at most [153, 152]. The viscous behavior will limit the bandwidth of the sensor and thus prevent accurate measurement of fast changing forces on the needle tip. The glue can also cause creep of a loaded force sensitive element, as creep increases when a material is used 'relatively' close to its melting point [158]. Furthermore, the compliance of the glue, a polymeric material, could depend strongly on temperature which would introduce a cross-sensitivity to temperature in the form of a modifying error.

It can be concluded that the measurement uncertainty of the machined- and unmachined-quartz column concepts will be very similar, because the properties of glue are expected to be a dominant factor determining the behavior of the force sensitive element. The preference for the machined-quartz-columns concept over other concepts presented in the previous chapter, based on the expected extremely low measurement uncertainty of the force sensor, is thus invalid. This means that the disadvantages of the unmachined-quartz-column concept, like the strength of the needle and manufacturing issues, would become reasons to discard the concept.

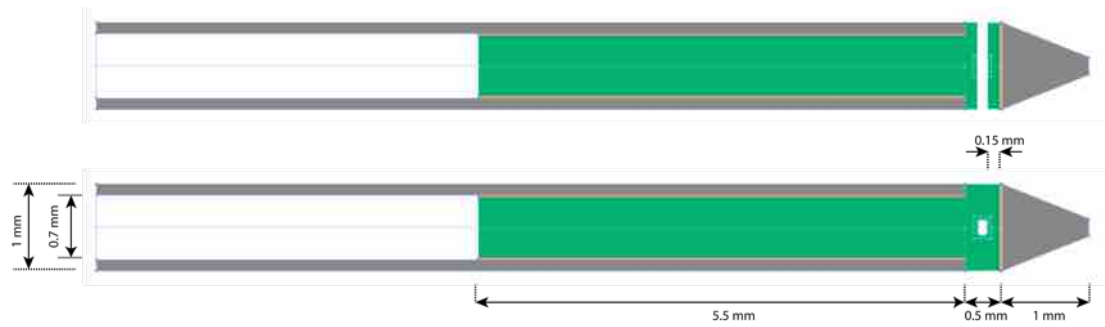


Figure 4.1: Cross-sections of the geometry of the machined-quartz-columns concept used for FE-simulations. The quartz ferrule is shown in green, the glue in orange and the RVS capillary and needle tip in grey. The hole machined in the ferrule, of which the dimensions were optimized, is through the entire ferrule.

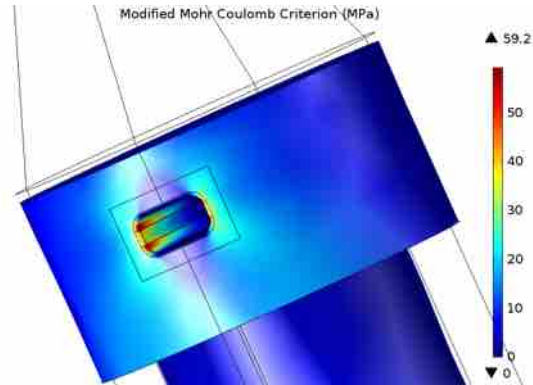
Strength of the machined-quartz-columns concept

The force sensitive element of the machined-quartz-columns concept, manufactured out of a quartz ferrule, protrudes from the stylet tube and should therefore be capable of carrying the entire transverse and axial load on the needle tip by itself. Stress concentrations will occur in the ferrule, as two compliant 'columns' will be machined in the ferrule by cutting a rectangular hole through the entire ferrule. The stress concentrations, occurring in the corners of the machined hole, can be partially reduced by using fillets with a large radius in the corners of the hole. A three dimensional FE-model of an RVS (AISI 304) stylet tube containing a machined quartz ferrule with an RVS needle tip on top was made with Solidworks and COMSOL Multiphysics to investigate the stresses inside the quartz ferrule due to axial and transverse loads on the needle tip [129]. Cross-sections of the geometry of the model are shown in figure 4.1. The optical fibers, glued in the borehole of the ferrule, were not modeled to reduce computational complexity. The change in distance between the FPI mirrors, located on the fiber-top of each fiber, was assumed to be equal to the change in dimension of the machined hole measured along the symmetry axis of the stylet tube.

The modified Mohr-Coulomb criterion was used to calculate the equivalent stress in the brittle quartz ferrule [159]. The maximum tensile strength of fused quartz glass, used to calculate the equivalent stress, was taken as 50 MPa (this value is evaluated in more detail in section D.5 of the appendix). The CES edupack database was used, where possible, to determine properties of other used materials [131]. The bond line thickness of the glue used to bond the ferrule to the needle tip and stylet tube, with an assumed Young's modulus of 0.5 GPa and a Poisson's ratio of 0.3 [160], was assumed to be 25 μm . The edge of the circumference of the rectangular hole machined into the ferrule was filleted with a radius of 10 microns. The vertices of the hole were filleted with the maximum possible radius, such that the fillet directly starts at the edge of the borehole in the ferrule for a 125 μm diameter optical fiber. The width of the hole between the columns and height of the columns was varied to search for an 'optimal' shape that resulted in the lowest maximum equivalent stress in the ferrule (usage of an optimization algorithm was not performed due to the required coupling between Solidworks, COMSOL and Matlab). The compliance of the columns acting as force sensitive element was required to be such that the change in geometrical length of the FPI cavity due to application of a 10 N force in axial direction on a needle tip would be in the order of 100 nm (neglecting the effect of the thin glue layer used to bond the optical fibers to the ferrule). This should ensure an approximately constant sensitivity of the sensor interrogated with homodyne interferometry throughout the measurement range (as determined section 3.2.7).

The maximum tensile stress in the ferrule occurs due to transverse forces on the needle

Figure 4.2: Stress distribution (equivalent stress according to the modified Mohr-Coulomb criterion) inside a machined quartz ferrule of a force sensor in the tip of a needle designed according to the machined-quartz-columns concept, due to a 1 N transverse force on the needle tip.



tip directed parallel with the axis of the hole machined in the ferrule. An illustration of the equivalent stress in the ferrule due to such a transverse force on the needle tip is shown in figure 4.2. The equivalent stress due to such a transverse force of 1 N, as function of the height of the

Table 4.1: Maximum equivalent stress in a machined quartz ferrule, serving as force sensitive element in the machined-quartz-columns concept, due to a 1 N transverse force on the needle tip, as function of the height of the used columns and the width of the hole between the two columns.

Equivalent stress (MPa)		Hole width (μm)			
		145	165	185	205
Column height (μm)	50	-	-	84.1	-
	100	75.1	64.2	61.7	63.3
	150	-	-	58.9	-

columns and the width of the hole between the columns is given in table 4.1. The maximum equivalent stress in the ferrule initially decreases with increasing width of the hole, as the radius of the fillet of the vertices of the hole can be larger. This reduces the stress concentrations in the corners of the hole. An increase of the space between the columns does however also reduce the second moment of area of the ferrule at the location of the hole, which increases the nominal stress caused by bending forces on the needle tip (the ferrule was already modeled to have a stepped diameter to maximize the second moment of area, although the diameter step cannot be machined with the available equipment at the TUD). The equivalent stress therefore starts to increase when the gap between 100 μm long columns becomes larger than approximately 185 μm . The stress in the ferrule can be slightly reduced, for the investigated configurations, by machining longer columns, which also increases the compliance of the columns. The change in geometrical length of the FPI cavity due to a 10 N force in axial direction on the needle tip, when the force sensitive element uses a 185 μm gap between 100 μm long columns, is 100 nm according to this FE-model. However, the glue used to attach the optical fibers in the borehole of the ferrule determines a significant part of the compliance of the force sensitive element of the FPI but was not taken into account in the FE-model. Increasing the column height to achieve a slight reduction of the maximum equivalent stress in the ferrule is thus not preferable as the change in geometrical cavity length of the FPI will become far larger than 100 nm due to application of a 10 N force on the needle tip, which will make homodyne interferometry potentially unsuited for interrogation of the FPI. It can thus be concluded that the maximum equivalent stress in a ferrule with a hole with approximately optimal dimensions (100 μm long columns / 185 μm gap) due to a transverse force of 1 N on the needle tip is with 61.7 MPa well above the used failure limit of quartz glass of 50 MPa.

There is a slight chance that a design according to the machined-quartz-column will be

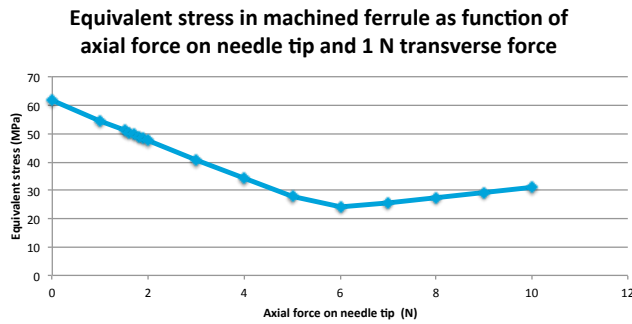


Figure 4.3: Maximum equivalent stress in a machined quartz ferrule, serving as force sensitive element in the machined-quartz-columns concept, due to a combination of a 1 N transverse force and an axial force on the needle tip, as function of the magnitude of the axial force.

strong enough in practice. The brittle glass of the quartz ferrule will fail due to tensile stresses induced by the transverse force on the needle tip. An axial force on the needle tip will induce compressive stresses in the ferrule that will cancel the dangerous tensile stresses. Figure 4.3 shows the maximum equivalent stress in the 'optimal' quartz ferrule due to a combination of a 1 N transverse force and an axial force on the needle tip as a function of the magnitude of the axial force on the needle tip. It can be observed that the maximum equivalent stress in the ferrule reduces to a critical maximum equivalent stress of 50 MPa when the axial force on the needle tip becomes larger than roughly 1.5 N. Moreover, a simple experiment presented in section D.5 of the appendix shows that the maximum tensile strength of the used quartz glass might even be quite a bit better than 50 MPa due to a good surface quality of the glass. Hence, some safety margin might even be present. It is however not sure that a transverse force will always be combined with sufficient axial force in practice. Furthermore, machining the hole in the ferrule will introduce small scratches in the glass and thereby increase the chance of fracture of the glass. It was therefore concluded that a needle with a force sensor according to the machined-quartz-columns concept is, based on simulations, very likely too fragile.

Manufacturing of the machined-quartz-columns concept

Machining a hole into a ferrule to create a prototype of the force sensitive element of the machined-quartz-columns concept proved to be impossible with available equipment. The laser ablation system of the TU Delft was too coarse and melted most of the ferrule, while the precise femto-second laser ablation system of the VU Amsterdam was reported to be incapable of drilling through the entire ferrule. Drilling the hole with a normal drill was neither an option, because the glass was too hard for a normal drill and no diamond coated drills were available. A large prototype was therefore manufactured out of borosilicate glass ferrules by means of sawing a large groove into the top of a ferrule with a diamond coated wire saw and glueing the machined and an unmachined ferrule together (figure 4.4). This production method is, besides extremely difficult, a disaster for the cross-sensitivity of the force sensing FPI to temperature. The glue layers used to join the two ferrules will practically determine the entire behavior of the force sensitive element of the FPI. Moreover, the CTE of glue will due to this manufacturing method strongly affect the cross-sensitivity of the FPI to temperature. A good assessment of the achievable measurement uncertainty of the machined-quartz-columns is thus not possible using the manufactured large scale prototype. Testing the strength of the prototype to transverse forces would neither give useful information, as the strength of the force sensitive element would be strongly determined by the glue used to bond both ferrules. The machined-quartz-columns concept was therefore abandoned, as the disadvantages of the concept and the difficulty to assess the magnitude of the disadvantages outweighed possible advantages compared to other concepts.

Figure 4.4: Large scale prototype of the force sensitive element of the machined-quartz-columns concept, manufactured by sawing a large groove in the bottom ferrule and glueing a second ferrule on top of the machined ferrule.

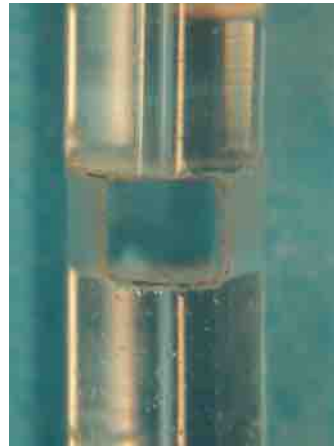


Figure 4.5: Example of a fiber-optic ferrule with a fiber glued into the ferrule.



4.2 Design of prototypes of the unmachined-quartz-column concept

4.2.1 Manufacturing method

Prototypes of the stylet tip of unmachined-quartz-column concept for an 18 G needle were made using 6 mm long and 0.7 mm outer diameter clear fused quartz ferrules. The ferrules had a $127 \pm 1 \mu\text{m}$ diameter borehole for an optical fiber with a 2 mm long tapered lead-in on one side of the ferrule to insert an optical fiber easily into the ferrule (figure 4.5). A cross-section of the geometry of the FE-model used to evaluate the performance of (prototypes of) the unmachined-quartz-column concept is shown in figure 4.6. Two optical fibers were inserted into the borehole of the ferrule such that a Fabry-Pérot cavity forms between the fiber ends. Three UV-curable adhesives (NOA68, NOA81 and Loctite 350), chosen because they allow precise positioning of the fibers before curing, were tested to bond the optical fibers in the ferrule. The UV-curable glues were however found to be too viscous in their cured state after testing of many prototype. The viscosity of the adhesives deteriorated the performance of the force sensitive element of the force sensor strongly. A heat curable epoxy (EPOTEK 353ND) with a relatively high glass transition temperature ($90 \text{ }^\circ\text{C}$) compared to the glass transition temperatures of the UV-curable glues (estimated to be around room temperature) was therefore chosen to glue the optical fibers in the borehole of the ferrule instead. The properties of the tested adhesives according to the manufacturers and suppliers are specified in table D.6 of the appendix. The heat curing epoxy is however quite difficult to handle, as the epoxy is very viscous in its uncured state but becomes a liquid for a short duration during curing. The epoxy flows in its liquid state easily in undesired locations like the FPI cavity (occurred for 2 out of 3 prototypes, although the large failure rate is likely caused by lack of experience with usage of the epoxy).

The second FPI mirror and double cavity preventing element were fabricated by sputtering a thick gold mirror of approximately 50 nm thick on the top of one of the optical fibers (in an argon atmosphere at a pressure of 0.1 mbar using a sputter coater for coating SEM samples). Gold was used instead of chromium due to availability reasons of the sputter coating device. The high reflectivity of the gold coating in combination with short FPI cavities required placement of a variable optical attenuator before the optical detector to prevent saturation of the detector

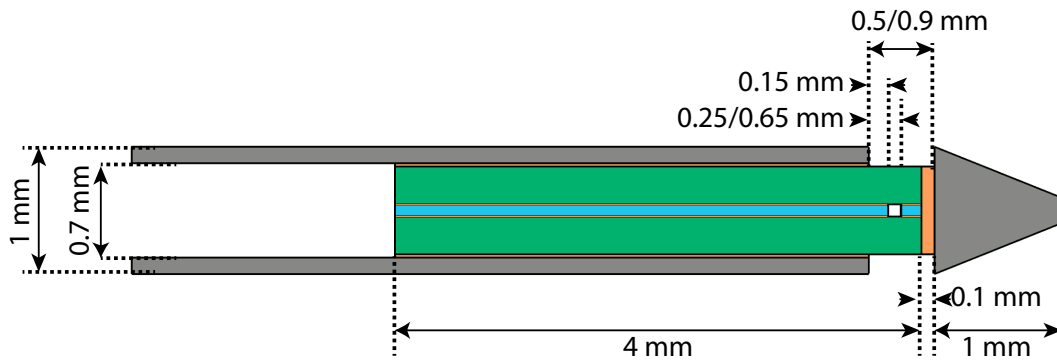


Figure 4.6: Cross-section of the geometry of the axisymmetric FE-model used to assess the performance of a needle with force sensor according to the unmachined-quartz-column concept. The metal stylet tube and needle tip are shown in grey, the quartz ferrule in green, the glue layers in orange and the silica optical fiber in blue. The thickness of the glue layer used to fixate the optical fibers in the borehole of the quartz ferrule is slightly enlarged for illustrative purposes. Two variants of the design were modeled, with a cavity length of respectively $100\ \mu\text{m}$ and $500\ \mu\text{m}$.

in some cases. The gold coated fiber had to be inserted through the tapered lead-in into the borehole of the ferrule to prevent damage of the gold coating. A diamond coated wire saw was used afterwards to remove the part of the ferrule containing the tapered lead-in.

The ferrule was glued into a short RVS (AISI 304) capillary with two component epoxy. UHU plus sofortfest epoxy was used for the fabrication of the first prototypes, but was replaced with UHU plus endfest (cured at 180°C) and 'Patex Power Epoxy Super Mix Universal' for the last prototypes. UHU plus sofortfest epoxy should in theory have been sufficiently strong given the contact area. Failure of the bond due to fatigue, caused by cycling axial forces on the needle tip up to about 10 N, occurred however in about 50% of the prototypes constructed with this epoxy. Prototypes made with either of the two other epoxies did not fail during testing, even for loads above 20 N on the needle tip (approximately 10 working prototypes of the unmachined-quartz-column concept were calibrated of which about half was constructed with the UHU Plus Sofortfest). The epoxies were for FE-modeling assumed to have a bond line thickness of $25\ \mu\text{m}$, an estimated Young's modulus of 0.5 GPa, a Poisson's ratio of 0.3 and a guessed CTE of $100\ \mu\text{strain/K}$ (none of those properties was specified by the manufacturer, the elastic modulus was later found to be likely a bit of an underestimation for most epoxies [153]). Needle tips were glued on the ferrule with UHU plus endfest epoxy and cured for half an hour at 180°C (figure 4.7). The 'heavy duty' epoxy (strength of $3000\ \text{N/cm}^2$) should in theory be strong enough to fixate the needle tips used for the prototype for transverse forces on the tip up to about 700 mN. The needle tips failed however to remain in place during testing of the prototypes. It was chosen not to machine a very short needle tip that is fixated by means of glue and a partial lock-in joint (figure 3.19), to relieve the glue from shear stress due to transverse force on the needle tip, as this would be too complicated to machine for a first prototype. It was chosen instead to let the quartz ferrules protrude 1.5 mm instead of 0.4 mm out of the RVS capillary. The additional length of the ferrule protruding out of the stylet acts as a fake needle tip and thus results in an equal moment arm of transverse forces on the the ferrule (the location of the FPI cavity remained as close as possible to the edge of the RVS capillary).

4.2.2 Strength of the design

Finite element simulations show that the maximum equivalent stress in a ferrule, protruding 0.4 mm out of the stylet tube, due to a pure 1 N transverse load on the needle tip will be



Figure 4.7: Prototype of the unmachined-quartz-column concept with needle tip.

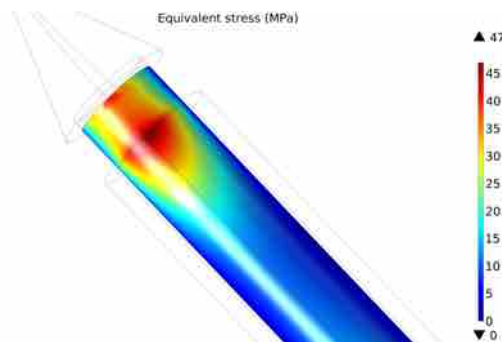


Figure 4.8: Equivalent stress, according to the modified Mohr-Coulomb criterion, in the quartz ferrule due to a 1 N transverse load on the needle tip.

approximately 47 MPa. This is marginally lower than the failure criterion of quartz glass defined at 50 MPa (figure 4.8). Bending stress in the ferrule scales with the inverse cube of the diameter of the ferrule. The maximum equivalent stress in a 0.8 mm diameter ferrule due to a 1 N transverse load is approximately 32 MPa. Ferrules with these dimensions were however not available for this project, as they would have to be custom made. Furthermore, a factor of safety of 1.5 is for a medical product and certainly in combination with a brittle material not sufficient. However, simple experiments indicated that the defined maximum tensile strength of quartz glass of 50 MPa might be a severe underestimation of the maximum tensile strength of the used quartz glass, due to the good surface quality of the quartz glass (section D.5 of the appendix). Very rough estimates of the maximum tensile strength indicate that a factor of safety of about 4.5 could be possible with a 0.8 mm diameter ferrule, as long as ferrules are not scratched during usage. More (reliable) tests of the strength of the used quartz ferrules are required though for confirmation. The maximum equivalent stress in the ferrule due to transverse forces on the tip will, also for the unmachined-quartz-column concept, be reduced greatly by compressive axial forces on the needle tip. It was therefore decided that limited strength of the unmachined-quartz-column concept is at this point not yet a reason to discard the concept, particularly because the concept can also be used for larger diameter needles that can house larger diameter ferrules more easily and thus sustain far larger transverse forces. The maximum equivalent stress in a 1.3 mm diameter ferrule, due to a pure transverse force of 1 N on the needle tip causing bending of the ferrule with a 1.5 mm long moment arm, is about 6.8 MPa (the maximum design stress for brittle quartz glass recommended by some manufacturers [161], which should result in a safety factor of more than 7 when the maximum tensile strength of quartz glass is assumed to be 50 MPa). This ferrule should just fit inside the stylet of a 16 G

and easily in the stylet of a 15 G core biopsy trocar needle (using a cannula with an identical wall thickness as the cannula of an 18 G core biopsy needle). It is however possible that the maximum transverse on such a needle tip and the moment arm of the transverse force will be slightly larger, as the needle tip could be slightly longer and a large diameter needle will bend less due to transverse force, making exertion of large transverse forces easier. It is however clear that the maximum equivalent stress in the ferrule can be reduced greatly by designing the sensor for a larger diameter needle.

4.2.3 Sensitivity of the FPI to force

The change in geometrical length of the FPI cavity according to FE-simulations due to application of a 10 N axial load on the needle tip of a prototype of the unmachined-quartz-column concept is shown in table 4.2. The change in cavity length is shown for sensors manufactured with NOA68 UV curable adhesive or EPOTEK 353ND epoxy to fixate optical fibers in the borehole of the ferrule such that the length of the FPI cavity is either 100 μm or 500 μm (all adhesives were assumed to have a Poisson's ratio of 0.3). Table 4.2 shows for comparison also the change in geometrical length of the FPI cavity due to a 10 N load on the needle tip when the optical fibers would be fused instead of glued into the ferrule. It can be observed, by comparing designs where the fibers are glued and fused into the ferrule, that glue quite significantly determines the compliance of the force sensitive element of the force sensor, particularly when compliant NOA68 adhesive is used. The change in FPI cavity length due to a 10 N axial load on the needle tip is preferably in the order of 100 nm to ensure that the sensor can be interrogated with homodyne interferometry with approximately constant sensitivity throughout the measurement range. The change in cavity length due to a 10 N load on the needle tip is far larger the desired 100 nm when the FPIs are constructed with UV curable glue and a 100 μm cavity length. A second issue, discovered during manufacturing of the first prototypes, is the difficulty to bond optical fibers over their entire insertion depth in the ferrule. The tested UV-curable adhesives had a too high viscosity to 'flow' together with the optical fiber deep into borehole of the ferrule. FE-simulations show that the change in geometrical length of the FPI cavity due to a 10 N load on the needle tip becomes unmeasurably large for homodyne interferometry performed with the OP1550 when the optical fibers are glued only over 2/3 of their insertion depth to the ferrule. Prototypes with FPIs with a cavity length significantly shorter than 100 μm were however not constructed. Primarily because accurately positioning and glueing the fibers to create a shorter FPI cavity proved to be difficult. A reduction of the cavity length would furthermore not be sufficient to reduce the compliance of the force sensitive element to a sufficient extend. The change in cavity length due to the presence of compliant UV-curable glue alone is already more than 100 nm (even when the fibers are not glued badly).

The viscoelastic behavior of the force sensitive element of the force sensor can be made to depend relatively more on the (expected) excellent elastic properties and good dimensional stability of quartz glass instead of the properties of adhesives used to bond optical fibers to the ferrule by increasing the length and thus compliance of the quartz glass column (which also increases the length of the FPI cavity). The change in FPI cavity length due to application of a 10 N force on the needle tip will thereby increase, because the total compliance of the force sensitive element increases. An opportunity was therefore taken in the final stages of the thesis project to use a second generation instead of first generation OP1550 to perform a variant of low-coherence interferometry instead of homodyne interferometry and thus measure changes in geometrical length of the FPI cavity over a practically infinite range (as described in section D.6 of the appendix). A few prototypes of the unmachined-quartz-column concept with a 500 μm cavity length were therefore also constructed. This cavity length was 'chosen' because the fringe pattern could still be observed clearly during placement of the optical fibers in the ferrule (the

ferrule was supposed to protrude an additional 400 μm from the stylet tube for FE-simulations presented in table 4.2). Furthermore, issues with the high reflectivity of the gold second FPI mirror will be reduced by using a longer FPI cavity length.

Table 4.2: Results of FE-analyses of the sensitivity of the FPI of the unmachined-quartz-column concept to force and temperature. The first column shows the type of glue used to bond optical fibers in the ferrule, the material of the stylet tube and needle tip and the length of the FPI cavity. The second column shows the change in geometrical cavity length due to application of a 10 N load on the needle tip. The third column shows the equivalent change in FPI cavity length that results in an identical change in OPD as the change in OPD of the FPI due to a change in temperature of 24°C, accounting for the CTE of materials used in the needle tip and the thermo-optic coefficient of air. The last column shows the expected measurement error in Newtons due to a 24 °C temperature change, based on the sensitivity of the FPI to force on the needle tip and temperature of the needle tip according to the FE-model.

Glue, metal, cavity length	Change in FPI cavity length due to 10 N axial force (nm)	Equivalent change in FPI cavity length due to 24°C temperature change (nm)	Measurement error due to cross-sensitivity to temperature (N)
NOA 68, RVS, 100 μm	-243.4	7.2	-0.30
EPO-TEK 353ND, RVS, 100 μm	-103.7	2.8	-0.27
Fused, RVS, 100 μm	-95.3	2.9	-0.30
NOA 68-badly glued (bondline is 2/3 of the insertion depth), RVS, 100 μm	-430.2	115.0	-2.67
NOA 68, RVS, 500 μm	-390.6	4.3	-0.11
EPO-TEK 353ND, RVS, 500 μm	-251.4	0.37	-0.01
NOA 68, Invar, 100 μm	-243.7	-1.7	0.07
EPO-TEK 353ND, Invar, 100 μm	-103.8	-1.1	0.11
Fused, Invar, 100 μm	-95.4	-0.7	0.07

4.2.4 Causes of measurement errors

An overview of possible sources of measurement errors in prototypes of the unmachined-quartz-column was made, without precisely quantifying the magnitude of the expected measurement errors (table D.7 of the appendix). Measurement errors of the force sensor in the needle tip could occur due to a plethora of reasons. A thorough analysis of all error sources was too complicated due to limited information and can thus be determined more easily by testing a prototype. A preciser estimate of the expected measurement error due to thermal expansion of materials used in the needle tip and the thermo-optic coefficient of air will however be presented by using the already available FE-model of the needle tip. The effect of transverse forces was not tested with high accuracy during calibration of prototypes, while the influence of bending of the optical fibers connecting the sensor to the FPI interrogation equipment was not tested at all during calibration of prototypes. Estimates of the errors due to these effects will therefore also be presented.

Handling and movement of the needle

Handling of the needle will result in macro bending of the optical fiber connecting the FPI to the FPI interrogation equipment. Macro bending results in loss of light from the optical fiber and thus in measurement errors when homodyne interferometry is performed. No extremely large bending related errors are expected, as long as bends in the fiber have a radius of more than 25 mm, based on the performance of Corning's SMF-28e+ fiber [162]. The intensity loss in such a fiber with 100 bends, each with a radius of 25 mm, is less than 0.03 dB. About 0.07% of the light intensity will be lost assuming that in practice only 10 of such bends occur at maximum in a fiber connecting the needle to the interrogation equipment. This intensity loss will introduce a maximum measurement error of 7 mN for a force of 10 N on the needle tip, when the light intensity is assumed to be a linear function of the force on the needle tip and the light intensity is zero for a force of 0 N. This assumption is in practice untrue, hence the error will be a bit larger depending on the non-linearity of the response of the sensor and the offset of the fringe pattern due to inequality of the reflectance of the FPI mirrors. Bending of the fiber will therefore cause a constant measurement error besides a modifying error. Errors due to bending are therefore certainly not negligible in case the force sensor should have a very high accuracy like the ATI Nano 17. Loss of light can be minimized by using special fibers with an extra low bend-loss, like Corning's SMF-28 Ultra fiber. The amount of bending can furthermore be minimized by using less flexible wires to connect the needle with the FPI interrogation equipment, such that only bends with a large radius can occur during usage of the needle. Temperature and humidity of the environment of the fiber do not seem to have a significant influence on the attenuation of optical fibers for variations in the expected range of environmental disturbances [162].

Temperature disturbances

The change in OPD of the FPI in the needle tip due to a change in temperature of 24°C of the needle tip, according to the FE-model of the unmachined-column concept accounting for the thermal expansion of materials used in the needle tip and the thermo-optic coefficient of air, is shown in table 4.2. The change in OPD is presented as the change in geometrical cavity length that causes the same change in OPD, by dividing the change in OPD by two times the refractive index of air. The equivalent change in geometrical cavity length was calculated for various fabrication methods of the needle tip to determine the influence of the fixation method of the fibers in the ferrule (type of glue/fusing), the cavity length and the material of the stylet tube. The measurement error due to a 24°C change in temperature of the needle tip was calculated based on the change in geometrical cavity length due to a 10 N force on the needle tip and the equivalent change in geometrical cavity length due to a change in temperature of 24°C.

A relatively strong influence of the material of the stylet tube, either RVS or Invar, on the change in OPD caused by a temperature change can be observed although the FPI itself is located outside the stylet tube. This was not anticipated to be a significant source of cross-sensitivity to temperature in the concept phase. Expansion of the stylet causes quite some deformation of the part of the ferrule inserted into the stylet tube. The forced strain of the ferrule is not transferred 1:1 by the glue to strain of the optical fiber glued into the ferrule and therefore causes a change in FPI cavity length. The advantage of an Invar stylet tube was however regarded as too minimal to use Invar capillaries for the prototypes, as the production of Invar capillaries (used for the stylet tube concept) was quite laborious.

The disadvantage of using a compliant glue with a very high CTE, like NOA68, compared to stiff glue with a comparatively low CTE, like EPO-TEK 353ND, or fusing the optical fiber to the ferrule seems marginal to non-existent according to the FE-model. The thin layers compliant glue with a large expansion coefficient are not stiff enough to deform the quartz ferrule and silica optical fiber with a far lower expansion coefficient extremely due to a temperature change, while the compliant glue increases the sensitivity of the FPI to force. The ratio of sensitivity of the

FPI to temperature and force is therefore approximately equal for sensors constructed with both adhesives. The FE-model does however not account for other properties of the glue that could result in measurement errors due to temperature changes, like creep or viscoelastic behavior of the glue or dependence of the compliance of the glue on temperature. These properties make usage of a compliant glue less attractive, as a compliant glue will dominate the behavior of the force sensitive element.

Transverse forces on the needle tip

Work by Gähler suggests that bending of the needle due to transverse force on the needle tip does not result in measurement errors when the force sensor is located on the neutral axis of the needle [1]. The force sensor will however never be located perfectly on the neutral axis due to manufacturing limitations. The cross-sensitivity to transverse forces was therefore estimated by calculating the stress in axial direction inside the quartz ferrule per Newton transverse force and the stress per Newton axial force on the needle tip (the ferrule was modeled as solid cylinder, without presence of optical fibers). The cross-sensitivity was approximated as the ratio of the stress in axial direction in the ferrule at the center of the FPI cavity per Newton transverse force and the stress per Newton axial force on the needle tip. The most important assumption of the approximation is that optical path of the light in the Fabry-Pérot cavity 'bends' with the bending of the ferrule, which is not the case in practice. The calculated measurement error is therefore an underestimation, as the change in geometric length of the optical path through the FPI cavity due to bending will be larger than approximated. Furthermore, bending of the ferrule causes a wedge angle of the FPI mirrors which reflects light out of the FPI cavity. The latter could contribute to significant measurement errors when homodyne interferometry is performed, particularly when the FPI cavity is long.

The ratio of the stress inside the ferrule per Newton transverse force and the stress per Newton axial force on the needle tip at the center of the FPI cavity was calculated with equation 4.1, where ' x ' is the eccentricity of the FPI from the neutral axis of the ferrule along the axis of the transverse force, ' r ' the radius of the ferrule and ' L_{tip} ' the moment arm of the transverse force with the respect to the location of the center of the FPI (based on the handbook equations for stress due to bending in a beam and stress due to axial force in a column).

$$\frac{\sigma_{trans}}{\sigma_{ax}} = \frac{4 \cdot L_{tip} \cdot x}{r^2} \quad (4.1)$$

The cross-sensitivity to transverse force on the needle tip is according to the simple model, using dimensions of the FE-model of the needle tip, approximately 42 mN per Newton transverse force per micron eccentricity of the FPI cavity.

Measurement errors due cross-sensitivity to transverse force become quickly quite significant in magnitude for increasing eccentricity of the borehole in the ferrule. The tolerance on the eccentricity of the boreholes in the ferrules was not requested from the supplier but should be quite good. Ferrules are normally used to align optical fibers in connectors, while the core of a single mode fiber is about 10 μm in diameter. However, light also propagates through the cladding of a single mode fiber (the evanescent field), hence the eccentricity is not with certainty limited to about 10 μm at most. The measurement error due to a 1 N transverse force on the needle tip, which is according to the requirements about the maximum force that will be encountered in practice, is estimated to be in the order of a few hundred milli-Newtons based on the simple model and the estimated tolerance on the eccentricity of the borehole in the ferrule. This measurement error has an order of magnitude that might prevent achieving the requirements on measurement uncertainty of the force sensor. Significantly reducing the sensitivity of an uniaxial force sensor in the needle tip to transverse force on the needle tip is difficult. Manufacturing precision prevents the FPI from being located perfectly centric in the ferrule. An increase in diameter of the ferrule can however in theory result in a lower sensitivity

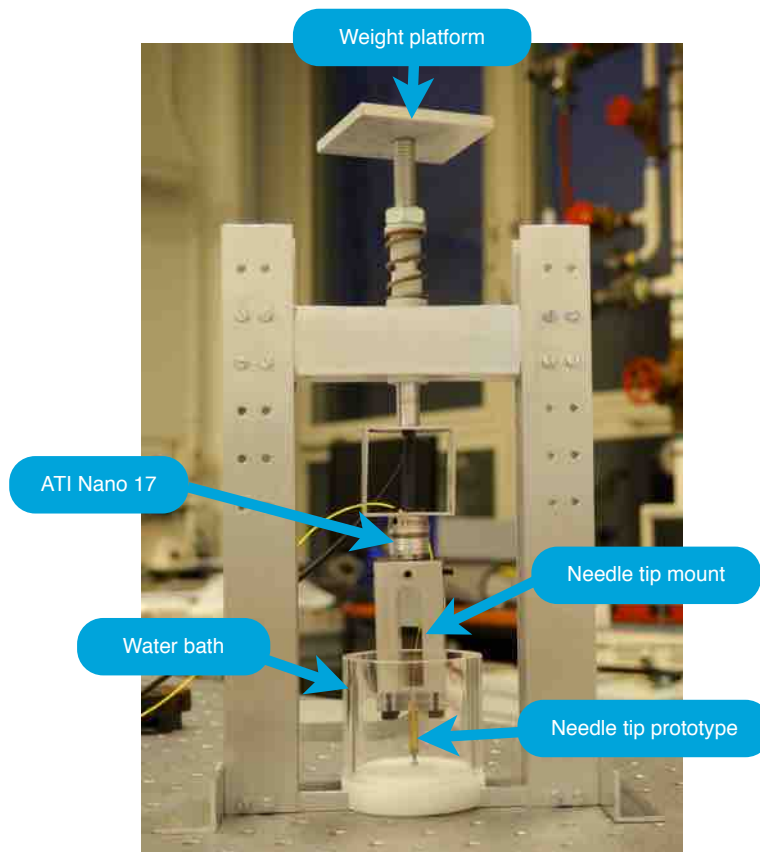


Figure 4.9: Calibration setup used to test prototypes of the needle tip containing an FPI-based force sensor.

to transverse forces, as the cross-sensitivity to transverse forces decreases with the inverse square of the diameter of the ferrule. Increasing the diameter of the ferrule is however severely constrained by the dimensions of the needle. Modifying the design of the uniaxial force sensor to a triaxial force sensor, with three force sensing FPIs to also measure bending of the needle, is the most effective option to reduce the effect of transverse forces on the measurement accuracy of axial forces. This was however not preferred for this project, as specified in the requirements.

4.3 Calibration method

4.3.1 Calibration setup and method

Prototypes of needle tips containing an FPI-based force sensor were tested using a custom made calibration setup shown in figure 4.9 (no standard calibration equipment was available at the VU Amsterdam where the prototypes were tested). The calibration setup was placed on a stabilized optical table to minimize the effect of vibrations of the environment on the assessment of the resolution of the force sensors. The calibration setup contained an ATI Nano 17 force sensor that served as the reference sensor to determine the calibration force on the needle tip. An assessment of the performance of the ATI Nano 17 sensor for the measurement of static axial forces is given in appendix B. Prototypes of the needle tips were mounted on the ATI Nano 17 sensor using a 'needle tip mount'. The ATI Nano 17 sensor was used to measure forces exerted in axial direction and transverse direction on the needle tip, as the calibration setup does not prevent accidental exertion of transverse forces on the needle tip. The coordinate system of the ATI Nano 17 reference sensor thereby 'defined' the axial and transverse loads on the needle tip. A difference in angle between the 'z-axis' of the reference sensor and prototype causes a small difference between the defined and real axial force on the needle tip and the defined and

real transverse forces on the needle tip. The prototypes were not remounted on the 'needle tip mount' during calibration procedures. Reproducibility errors due to this effect should therefore be marginal. A small part of the sensitivity of the FPI to transverse forces will however be mistaken as sensitivity to axial forces and vice-versa due to differences in orientation of the 'z-axis' of the reference sensor and the prototype.

Axial calibration forces were exerted on the needle tip by placing weights on the weight platform of the calibration setup for calibration of the prototype with static loads or by manually exerting force on the weight platform for calibration of the prototype with arbitrary dynamic forces. The force sensors were preloaded with the weight of the calibration setup, which was defined as a calibration force of 0 N. The needle tip was pressed onto the surface of a plastic water bath that could be filled with cold and hot water to test the cross-sensitivity of the prototype to temperature. A thermocouple was used to measure the water temperature. The accuracy of the thermocouple was in the order of 1°C, which was determined by comparing readings of the thermocouple with readings of the precise thermometer of the IKA C-MAG HS 7 heating plate used to heat water up to body temperature.

The force sensor of each prototype was first calibrated using homodyne interferometry with a second generation OP1550 [163]. Prototypes were calibrated with a 'variant' of homodyne interferometry, showing some of the properties of low coherence interferometry, during a second calibration procedure when the required measurement range of the force sensor could not be achieved (easily) by means of normal homodyne interferometry. The 'variant' of homodyne interferometry will be called 'low coherence interferometry' in this report in lack of a better name, although it is not really the same as low coherence interferometry. 'Low coherence interferometry' was performed with a second generation OP1550 as light source and detector and an SR830 DSP Lock-In Amplifier from Stanford Research systems, by means of the method described in detail in section D.6 of the appendix. The method basically consists of measuring the 'response' of a FPI with a certain OPD to light with a 'constant' wavelength by means of 'normal' homodyne interferometry while at the same the sensitivity of the FPI to a change in wavelength of the optical source is measured at the same time by means of probing the FPI with a very small oscillation of the wavelength of the light source (with a frequency in the order of 3 kHz). The two measurements are both a sinusoidal function of the OPD of the FPI, but 90° out of phase with each other (as can be described with respectively equation A.4 and the derivative of equation A.4 to the wavelength). This allows measurement of the OPD over a semi-infinite range. The change in OPD could be measured alternately with high sensitivity with one of both measurements. Both measurements are used at the same moment in practice, as the change in OPD is calculated from both (scaled) measurements using an arctangent function and phase unwrapping. The signal-to-noise ratio of the measurement of the change of in OPD of the FPI will depend on which of the two measurements is determining the sensitivity of the FPI to a change in OPD most dominantly for a certain OPD of the FPI. The response of the FPI measured using 'normal' homodyne interferometry is measured by lowpass filtering the oscillating light intensity measured at the photodetector. The measurement of the sensitivity of the FPI to a change in wavelength of the source is performed by measuring the amplitude of the oscillation of the light intensity at the photodetector at the frequency of the wavelength oscillation of the source using the lock-in amplifier. The light intensity measured with the photodetector of the OP1550 was passed, without additional filtering, to the lock-in amplifier, together with a TTL synchronization signal as reference of the frequency of the wavelength oscillation of the source. It was later deduced that a periodic nonlinearity is introduced in the response of prototypes by the absence of a lowpass filter between the photodetector and the lock-in amplifier. The nonlinearity cannot easily be described by a simple interpolation function describing the response of the FPI as function of the calibration force and therefore causes systematic measurement errors (as

described in section D.6 of the appendix). A third order polynomial interpolation function can describe the nonlinearity to some extent, as long as the nonlinearity is not very extreme and occurs only once in the response of the FPI as function of the calibration force.

Data acquisition during the calibration procedures was performed using a custom application written in MATLAB with a GUI to monitor the response of the reference force and temperature sensor and the response of prototypes in real-time. The signals of the OP1550 were lowpass filtered with an RC filter with a cutoff frequency of approximately 1 kHz before sampling with the A/D converter. Signals of the thermocouple were rather noisy and therefore lowpass filter with an RC filtered with a cutoff frequency of about 1 Hz before sampling. All signals were sampled at 5 kHz using a National Instruments USB5210 D/A converter. A digital lowpass filter (4th order Butterworth) with a cutoff frequency of 100 Hz was used to filter digitized signals of the FPI-based force sensors and the ATI Nano 17.

The intention of static calibration was assessment of the accuracy with which prototypes can measure static uniaxial forces in axial direction of the needle. Static calibration should thereby show how well the FPI can measure 'strain'. This would be useful information when a triaxial variant of the design would be made, capable for correcting for bending of the needle due to transverse forces on the needle tip. The prototype was first loaded 3 times for about a minute with the maximum calibration force before the static calibration procedure using homodyne interferometry to interrogate the FPI commenced. The wavelength of the optical source was subsequently tuned such that the required range of forces could be measured. The calibration procedure was then performed by loading-and-unloading the prototype at least three times in small steps up to the maximum measurable force with homodyne interferometry or to approximately 10 N at most while readings of the response of the reference force sensor and the prototype to each calibration force were obtained. A reading of the force sensors was obtained at least 5 seconds after changing the calibration force. The average of a one second long measurement was defined as a reading of the force sensors. Three times the standard deviation of the acquired 1 second long signal was defined as the resolution of the force sensor. Static calibration using 'low coherence interferometry' was performed by first loading the sensors a few times with such a large force that at least three-quarters of the fringe pattern due to the change in OPD of the FPI was observed (varied significantly from prototype to prototype), after which realtime measurement of the response of the FPI could commence. The remainder of the procedure was similar to the procedure of static calibration using homodyne interferometry. Static calibration of prototypes was always performed at room temperature without submerging the prototype in water, as the water temperature could not be kept approximately constant for a sufficiently long time. Static calibration took in practice at least 10 minutes per prototype. The sensor was loaded with half of the maximum calibration force on average during this period. Significant drift of readings of the sensor, for example due to creep of the force sensitive element, should therefore be visible in the static calibration results. The variation of transverse force on the needle tip was minimized as much as possible by using masses on the weight platform to create the calibration force. Small unintentional variations of the transverse force might however occur.

Dynamic calibration of the force sensors was in general performed with the needle tip submerged in water. Dynamic calibration using 'low coherence interferometry' commenced by loading the needle tip with such a large force that at least three-quarters of the fringe pattern due to the change in OPD of the FPI was observed, after which realtime acquisition of the response of the FPI could commence. Several 15 seconds long measurements were obtained during dynamic calibration. Arbitrary calibration forces were exerted on the prototype during these measurements. Water of the water bath was changed in between acquisitions of these measurements to change the temperature of the water bath. The temperature of the water bath

changes slightly during acquisition of the 15 second signals, hence dynamic calibration was never performed at a 'perfectly' constant temperature. The transverse force on the needle tip varied strongly during dynamic calibration. Dynamic calibration can therefore give an impression of the performance of the needle tip force sensors under practical circumstances, where they can also be exposed to transverse force, as long as there is no perfect correlation between the axial and transverse forces on the needle tip during calibration. Some prototypes could not be calibrated with the dynamic calibration procedure with changing temperatures because of extreme drifting of readings of the sensor as result of a temperature change. Dynamic calibration of those sensors was performed in air at room temperature. The sensors were afterwards submerged in cold and hot water baths to evaluate the drift due to the change in temperature. The IKA heating plate was used to keep the hot water bath at constant temperature during these drift experiments. Extreme interference between the readings of the thermocouple and activity of the heating plate was observed, which was corrected during data processing (as an approximately constant temperature of the water bath could be assumed).

4.3.2 Analysis of the results

Interpolation functions, describing the readings of the force sensor in the needle tip as function of the calibration force, were made by fitting an appropriate function to the data obtained during the static or dynamic calibration of the force sensor. Either a sinusoidal function, in case of usage of homodyne interferometry, or a polynomial function, in case of usage of low coherence interferometry, was used as interpolation function. The fit was optimized in a least squares sense. The measurement error was not subdivided in many components by following an elaborate method like the procedure described in ISO 376 [164]. The measurement error of prototypes was merely assessed as the difference between the calibration force according to the reference sensor and the force measured with the prototype, calculated from the reading of the FPI with the determined interpolation function. The measurement error of prototypes was evaluated using the same data used to determine a suited interpolation function for the response of the FPI of the prototype, as only a limited amount of data per prototype was obtained.

Errors will be made in the assessment of the measurement error of purely axial forces during static calibration when the transverse force on the needle tip varies during the calibration procedure. The axial force and the resultant transverse force on the needle tip are normally explanatory variables for the reading of the FPI. Corrections were made for variations of the latter, if necessary, to illustrate the possible influence of variation of transverse forces on the assessment of the measurement uncertainty of purely axial forces. The estimated response of the FPI to transverse forces on the needle tip was therefore subtracted from the measured response of the FPI. The resultant transverse force measured with the ATI Nano 17 reference sensor was for this reason used as additional explanatory variable in the interpolation function that is fitted to the obtained data, besides the reading of the FPI (e.g. as shown in equation 4.2, with the reading of the FPI 'X', the order of the polynomial used to describe the axial force on the needle tip based on the response of the FPI 'n' and the resultant transverse force 'Y').

$$F_{axial} = \sum_n a_n \cdot (X_{FPI} - b \cdot Y_{Transverse})^n \quad (4.2)$$

The implementation of the polynomial in the interpolation function is physically not entirely correct. The polynomial was nonetheless used in some cases to correct a bit for periodic nonlinearities in the response of the FPI caused by the implementation of 'low coherence interferometry'. Usage of an interpolation function using both the reading of the FPI as well as the resultant transverse force as explanatory variables can however result in an unfair assessment of the measurement error of purely axial forces on the needle tip. Transverse forces on the needle tip, measured with the ATI sensor, can correlate with the axial calibration forces. This would

enable the high accuracy of the ATI Nano 17 to influence the accuracy with which seemingly axial forces can be measured with the prototype of the needle tip force sensor.

The interpolation function determined based on data acquired during dynamic calibration will incorporate sensitivity of the FPI to transverse forces in the estimate of the sensitivity of the FPI to axial forces on the needle tip. This will occur when transverse forces on the needle tip correlated strongly with axial forces on the needle tip during dynamic calibration. The calibration method was not intended to quantify the sensitivity of the prototypes to transverse force, though an estimate of the contribution of those forces to the total measurement error is useful to determine where the most significant improvements of the design can be obtained. An estimate of the influence of transverse forces on the measurement error and the sensitivity of the FPI to transverse forces was therefore made by first calculating the part of the transverse forces on the needle tip uncorrelated with the axial calibration force, both measured with the reference sensor. The components of the transverse force uncorrelated with the axial calibration force are the residuals of multiple linear regression using both components of the transverse force as explanatory variables for the axial calibration force (e.g. function 4.3, fitted with a least-squares approach).

$$F_{axial} = a \cdot F_x + b \cdot F_y + c \quad (4.3)$$

Multiple linear regression using those residuals as explanatory variables for the measurement error was then performed to obtain an estimate of the influence of transverse forces on the measurement error and the sensitivity of the FPI to transverse forces on the needle tip (fitting the model of equation 4.4 in a least squares sense).

$$F_{Error-axial} = a \cdot F_{Y-uncorrelated} + b \cdot F_{X-uncorrelated} + c \quad (4.4)$$

Errors in this estimate will easily occur, for example be due to correlation between the variation of the transverse force on the needle tip and the derivative of the axial calibration force to time, which is also expected to be a source of measurement errors. The estimate of the cross-sensitivity of the FPI to transverse forces can furthermore not be made with high accuracy with the proposed method, as the estimate of the sensitivity of the FPI to axial forces on the needle tip will be influenced by the sensitivity of the FPI to transverse forces, due to correlation of the transverse forces on the needle tip with axial forces on the needle tip during the calibration procedure.

4.4 Calibration results of the unmachined-quartz-column concept

Calibration of prototypes showed that usage of UV-curable glue to bond optical fibers to the ferrule resulted in very poor performing force sensors, while usage of EPO-TEK 353ND epoxy resulted in far better performing sensors. Only calibration results of a prototype constructed with EPO-TEK 353ND epoxy are therefore presented in detail in this chapter. A few calibrations results of one of the prototypes constructed with UV-curable adhesive are presented in section D.7 of the appendix to illustrate the issues of prototypes constructed with UV-curable adhesive.

The tested prototype constructed with EPO-TEK 353ND epoxy had an FPI cavity length of roughly 500 μm according to a scan of the fringe pattern as function of the wavelength of the optical source. The prototype had a 'fake needle tip', as the ferrule protruded approximately 1.5 mm from the stylet tube (the FPI cavity was located as close as possible to the edge of the stylet tube). The change in FPI cavity length due to application of a load of 10 N force on the needle tip was about 310 nm, determined by analyzing the fringe pattern as function of force on the needle tip. Visibility of fringes was sufficient, the gold coating did not cause saturation issues and no presence of a second FPI cavity was observed during usage of the FPI.

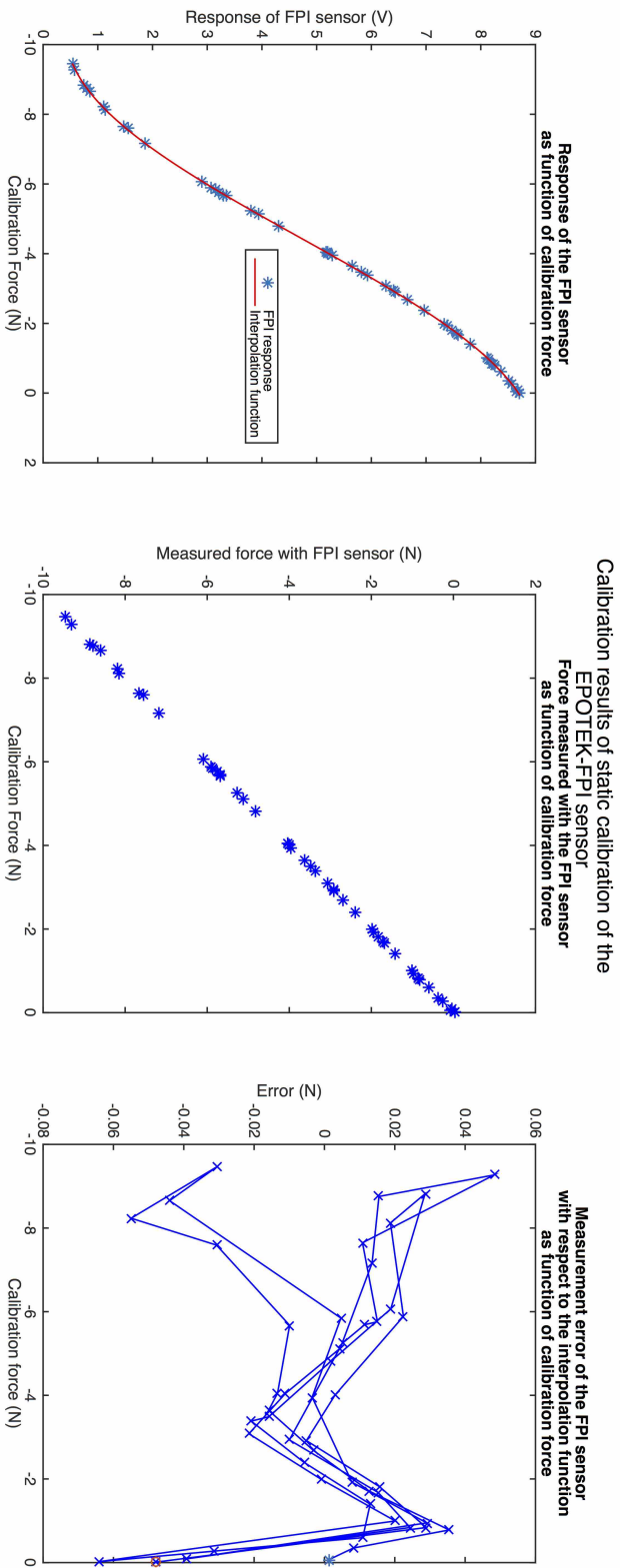


Figure 4.10: Results of static calibration of a prototype of the unmachined-quartz-column concept manufactured with EPOTEK epoxy using homodyne interferometry. The response of the FPI as function of the calibration force, together with a fitted sinusoidal interpolation function is shown on the left. The center figure shows the force measured with the FPI, calculated using the interpolation function, as function of the calibration force. The measurement error of the FPI sensor as function of the calibration force is shown on the right. The blue star and the red circle indicate respectively the first and last reading obtained during static calibration.

Results of static calibration of the prototype using homodyne interferometry are shown in figure 4.10. The maximum observed measurement error during static calibration remains below 65 mN (without accounting for the resolution of the sensor). The largest measurement errors are observed at the begin and end of the measurement range. The resolution of the force sensing FPI of the prototype and the resolution of the ATI Nano 17 reference sensor during the calibration procedure are shown in figure 4.11. The resolution of the FPI-based sensor deteriorates at the the begin and end of the measurement range, indicating that the resolution is limited by the performance of the photodetector of the OP1550 or other electronics and correct assessment of the resolution is not limited (in general) by vibrations of the environment. Some outliers of the measured resolution are likely the result of vibrations of the environment, as some disturbances of the optical table did occur during static calibration. The resolution of the FPI-based sensor and the ATI Nano 17 sensor is in general very similar. Furthermore, the distribution of noise of both sensors is, although not always particularly Gaussian, quite similar.

Results of dynamic calibration of the prototype at constant temperature using homodyne interferometry can be found in section D.7 of the appendix. Remaining within the measurement range suited for homodyne interferometry proved to be difficult during dynamic calibration. Extensive dynamic calibration of the prototype of the sensor was therefore performed using low coherence interferometry. A third order polynomial function was used as interpolation function. The temperature varied between room temperature (22°C) and the body temperature of a feverish patient (40°C) while the maximum resultant transverse force on the tip reached up to 1.1 N during dynamic calibration. Results of dynamic calibration of the prototype are shown in figure 4.12 and 4.13. The maximum observed measurement error was 534 mN for a measurement range up to 20 N. The sensor seems to suffer from a systematic error, periodic as function of the calibration force, caused by a non-linearity in the response of the FPI that cannot be described with the third order polynomial interpolation function. The systematic error is almost certainly caused by the way 'low coherence interferometry' was implemented (section D.6 of the appendix). There is a visible correlation between the derivate of the calibration force to time and the measurement error. Measurements of the prototype 'lag' measurably with respect to the reference sensor when the calibration force changes quickly (more easily observed in a small selection of the data obtained during dynamic calibration shown in figure D.11 of the appendix). A slight correlation between the measurement error and the two orthogonal components of the transverse force on the needle tip uncorrelated with the axial calibration force seems present in data shown in figure D.11 of the appendix. Multiple linear regression using the two 'uncorrelated' components of the transverse force as explanatory variables for the measurement error did indicate a correlation between the transverse force and the measurement error (the fitted model is shown in figure D.10 of the appendix). Transverse forces do however explain only a fraction of the variation in measurement error in the analyzed segment of the dynamic calibration results ($R^2 = 0.47$). The cross-sensitivity of the FPI to transverse forces was estimated to be about 0.3 to 0.5 N/N based on the regression model. Not much value is given to these estimates, as they varied for different selections of the data acquired during dynamic calibration (although the order of magnitude is not unexpected based on results from FE-analyses). Cross-sensitivity of the prototype to temperature was investigated by fitting separate linear interpolation functions to data obtained during dynamic calibration of the sensor at temperatures below 22.5°C and data obtained at temperatures above 40°C (shown in figure D.12). Usage of the interpolation function determined for the response of the prototype at a feverish body temperature (40°C) while the needle tip is at room temperature (22.5°C), would result in an error of varying between 190 mN and 240 mN within the measurement range (on average 215 mN) according to the fitted interpolation functions. The modifying and constant error due to cross-sensitivity to temperature cannot be separated, as the prototype was preload with the weight of the calibration setup for a defined calibration

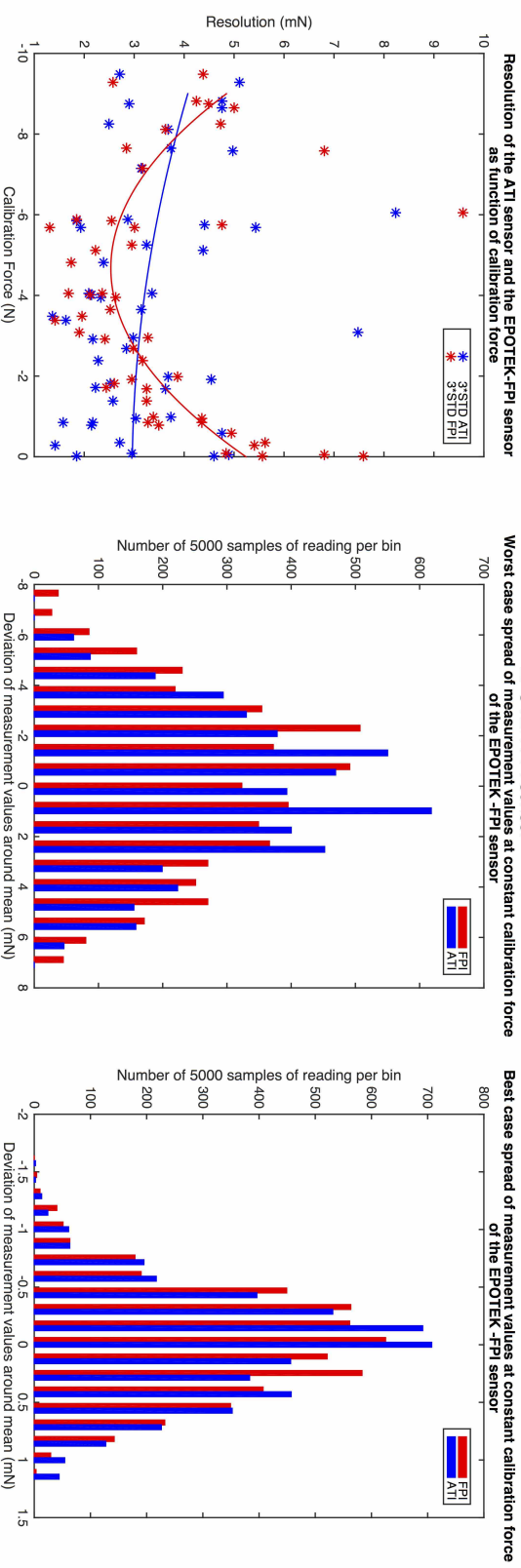


Figure 4.11: Analysis of the resolution of a prototype of the unmanufactured-quartz-column concept manufactured with EPOTEK epoxy during static calibration of the sensor using homodyne interferometry. The resolution of the FPI-based sensor of the prototype and the ATI Nano 17 sensor, used as reference sensor, are shown as function of calibration force on the left, together with a second order polynomial fit to the data to illustrate the relation between the resolution and calibration force. The histograms show the largest and smallest observed spread of measurement values around the mean of 1 second long readings of the prototype force sensor obtained during static calibration and the corresponding spread of measurement values of the reference sensor.

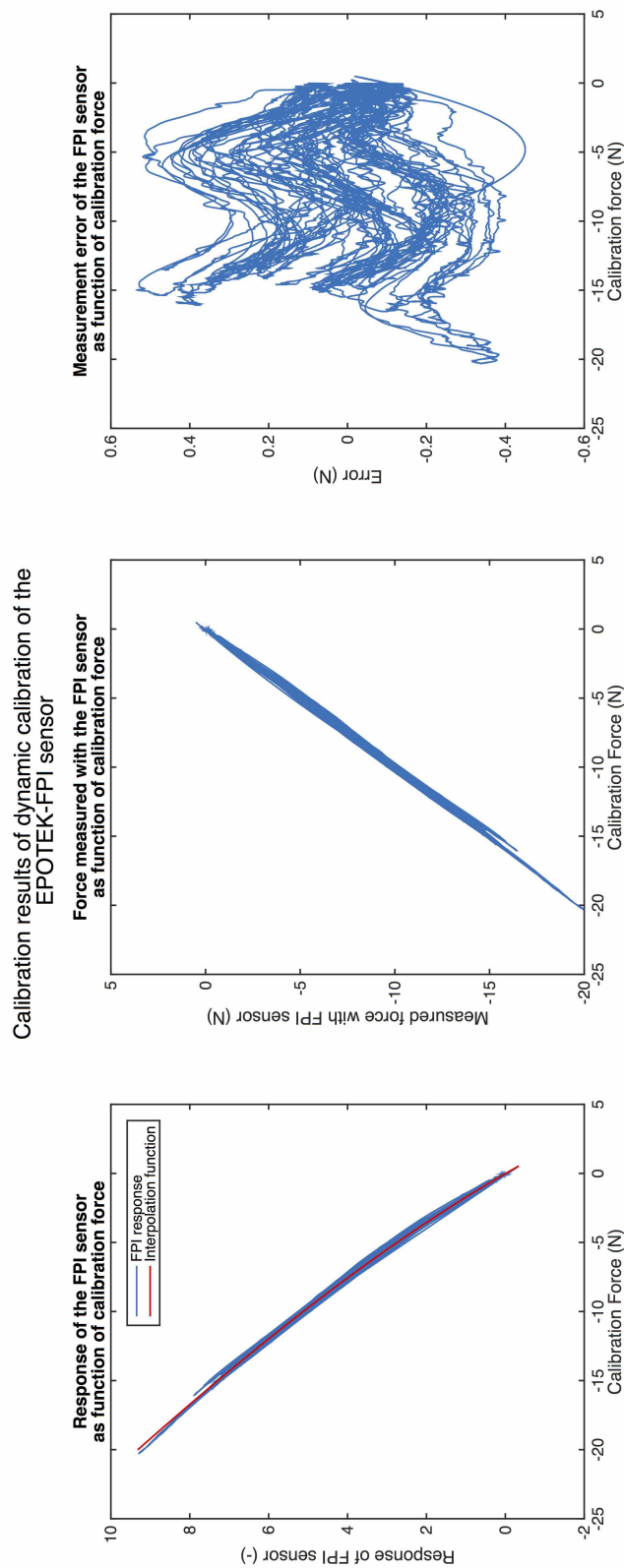


Figure 4.12: Calibration results of dynamic calibration with temperatures varying between 22°C and 40°C of a prototype of the unmachined-quartz-column concept manufactured with EPOTEK epoxy and interrogated with low coherence interferometry. The response of the FPI as function of the calibration force, together with a fitted third order polynomial interpolation function is shown on the left. The center figure shows the force measured with the FPI, calculated using the interpolation function, as function of the calibration force. The measurement error of the FPI sensor as function of the calibration force is shown on the right.

Force measured with the EPOTEK-FPI sensor subjected to dynamic calibration forces as function of time

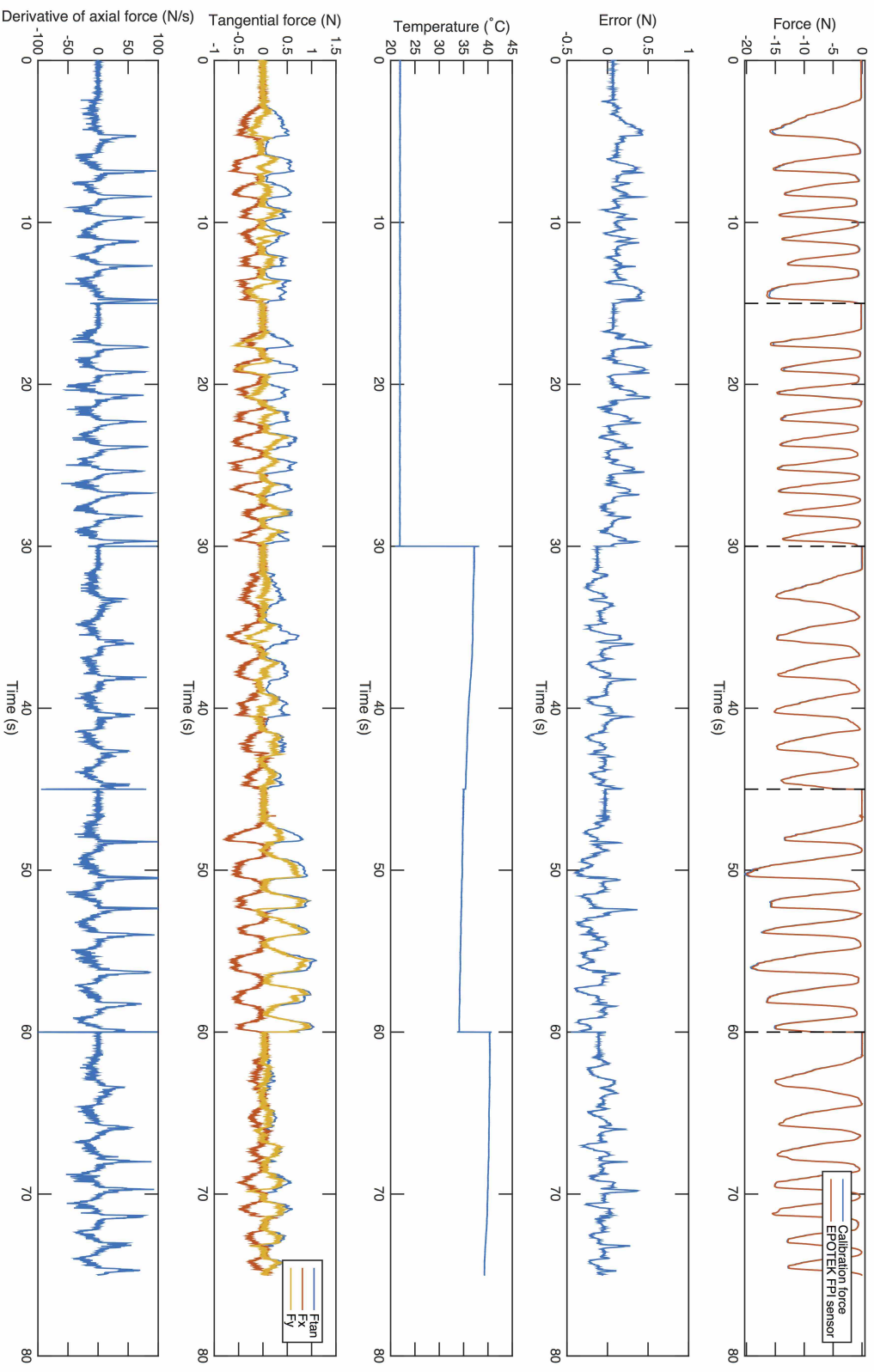


Figure 4.13: Results of dynamic calibration with temperatures varying between 22°C and 40°C of a prototype of the unmachined-quartz-column concept manufactured with EPOTEK epoxy and interrogated using low coherence interferometry, shown as function of time. The graphs show, from top to bottom: (1) the calibration force and the force measured with the prototype, calculated using the interpolation function shown in figure 4.12, (2) the measurement error of the prototype, (3) the temperature of the water bath in which the needle tip is submerged, (4) the transverse force on the needle tip, shown as the resultant transverse force 'Ftan' and its two orthogonal components 'Fx' and 'Fy', and (5) the derivative of the calibration force to time. The dotted lines in the top graph (1) indicate the 15 second long fragments of which the dynamic calibration dataset is composed.

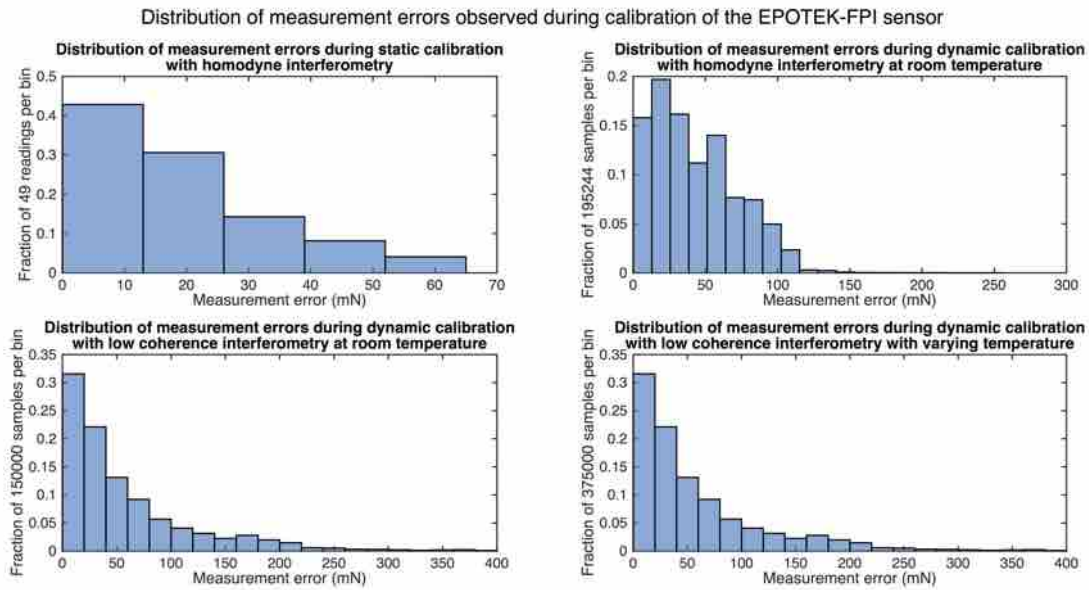


Figure 4.14: Histograms of the distribution of observed measurement errors during static and dynamic calibration at room temperature using either homodyne or 'low coherence interferometry' and dynamic calibration with varying temperatures using 'low coherence interferometry' of a prototype of the unmachined-quartz-column concept manufactured with EPOTEK 353ND epoxy.

force of 0 N. The resolution of the prototype interrogated with 'low coherence interferometry' was estimated to be 9.5 mN, by analyzing a 1 second long measurement of the response of the prototype for a calibration force of 0 N. This is worse than the resolution achievable with homodyne interferometry. The resolution of the reference force sensor, the ATI Nano 17, was at the same moment determined to be 2.7 mN. Electronics used for performing 'low coherence interferometry' introduce thus a significant additional source of measurement noise.

The dataset acquired during dynamic calibration with 'low coherence interferometry' was 'filtered' to analyze performance of the prototype subjected to dynamic forces at room temperature. The maximum observed measurement error at room temperature, using a third order interpolation function to describe the response of the FPI, was 388 mN. A comparison of the range and distribution of observed measurement errors during static calibration (not accounting for the resolution of the sensor), dynamic calibration at room temperature using either homodyne or 'low coherence interferometry' and dynamic calibration with varying temperature using 'low coherence interferometry' is given in figure 4.14.

4.5 Discussion

The histograms of the distribution of the observed measurement errors during calibration of the prototype of the unmachined-quartz-column concept shown in figure 4.14 are not an entirely fair representation of the actual performance of the prototype. The interpolation functions, used to calculate the measured force, were fitted to the response of the FPI sensor and the calibration force by minimizing the error between the data and the interpolation function in a least squares sense. The function is therefore better fitted to calibration forces of which relatively much data was sampled, like a calibration force of zero Newton. The average error of all obtained readings becomes therefore quite low, as the distribution of calibration forces in the datasets acquired with the various calibration procedures is in general not uniform at all. The graphs of the measurement error as function of the calibration force and the maximum observed measurement error give a

less biased representation of the performance of the prototype.

The prototype of the unmachined-quartz-column concept was very well suited to accurately measure static forces, provided that EPOTEK epoxy is used to glue the optical fibers into the ferrule and large variations of transverse forces on the needle tip remain absent. The goal on the half-error-interval was nearly achieved for the measurement of static forces without the presence of temperature disturbances and marginal variation of transverse forces on the needle tip (65 mN instead of 45 mN). This is a significant improvement in performance compared to the FBG-based needle tip force sensor designed by Gähler [1]. The goal was to achieve equal accuracy as the ATI Nano 17, which was used during calibration as reference sensor. It is therefore questionable whether the ATI Nano 17 could be used to assess the the maximum achievable accuracy of the prototype fairly and did not cause an underestimation of the potential measurement accuracy of the prototype. The largest measurement errors did occur at the outer ends of the measurement range during static calibration, where the sensitivity of the prototype interrogated with homodyne interferometry to calibration forces becomes very low due to the type of interferometry used to interrogate the sensor. These larger measurement errors at the outer ends of the measurement range are therefore not entirely unexpected, as small variations in light intensity due to disturbances, like bending of the optical fiber or an increase of the wedge angle of the FPI mirrors due to transverse force, can cause a relatively large measurement error. The used sinusoidal interpolation function is furthermore not perfectly suited to describe the response of the FPI near the minima and maxima of the fringe pattern, even for a low finesse FPI using mirrors with a reflectance of 0.04. The response of the FPI in combination with the used interpolation function does therefore also result in small systematic measurement errors at the outer ends of the measurement range that could be reduced by using a more complex interpolation function (for example equation A.3), usage of 'low coherence interferometry' or a less sensitive force sensitive element.

The measurement error due to temperature disturbances over the entire range of expected temperature disturbances was not tested (variations between 22°C and 40°C instead of 17°C and 41°C were tested). The cross-sensitivity to temperature is approximately 12 mN/°C, two orders of magnitude better than needle tip force sensors based on FBGs shown in literature [2]. This cross-sensitivity to temperature is in the range that could be expected based on FE-models, certainly given the fact that manufacturing imperfections like badly glueing optical fibers into the borehole of the ferrule, placing the FPI too close to the edge of the RVS capillary and the tolerance on the diameter of the borehole and thus the thickness of the glue layer, are factors that could strongly affect cross-sensitivity to temperature. The constant error due to a change in temperature from 17°C to 41°C, extrapolated based on acquired data, is approximately 290 mN. This results in a measurement error of about 145 mN when the sensor is calibrated at the average temperature of the expected range of temperature disturbances. Fluctuation of temperature does not seem to introduce a very significant modifying error. The prototype should be able to meet requirements on the measurement accuracy of static uniaxial forces on the needle tip easily with varying temperatures in the range of expected temperature disturbances.

Goals on the resolution can be achieved when the sensor is interrogated with homodyne interferometry within the required measurement range of the sensor (up to 6 N). The requirements on the resolution are however a bit exceeded within the measurement range set as the goal (up to 10 N). The resolution of the prototype slightly exceeds the resolution of the ATI Nano 17 at the begin and end of a 10 N measurement range, because the sinusoidal response of the sensor limits the sensitivity of the measurement system at the outer ends of the desired range. The sensitivity of the fabricated force sensitive element to force was approximately 25% larger than predicted with FE-models. This could be caused by not glueing the optical fibers over their entire insertion depth into the ferrule or a difference in thickness of the glue layer (the tolerance on the diameter

of the borehole of the optical fiber is such that a 1.5 times as thick glue layer as modeled could occur). A more constant but on average worse resolution could be achieved by reducing the cavity length of the FPI which will reduce the sensitivity of the force sensitive element to force, as was the intention for the FPIs used in combination with homodyne interferometry. The resolution could also be improved by improving the used electronics, to which no particular attention was given during this project. The resolution of the sensor interrogated with 'low coherence interferometry' is slightly lacking. This could likely be improved by optimizing the settings of the used lock-in amplifier, as not much time was available to optimize the configuration of the 'low coherence interferometry' setup. Further increasing the sensitivity of the force sensitive element to increase the resolution of the sensor interrogated with low coherence interferometry is difficult. Increasing the FPI cavity length further to increase the compliance of the force sensitive element will force the ferrule to protrude extremely far out of the stylet tube and increase chance of fracture of the ferrule.

The maximum observed measurement error of the prototype slightly exceeds the required measurement uncertainty (534 mN instead of 500 mN) under 'practical conditions' where the sensor is exposed to dynamic forces, temperatures varying between room temperature and body temperature and some transverse forces on the tip while the FPI is interrogated with low coherence interferometry. A significant part of the measurement error seems to be a systematic error caused by the method used to perform low coherence interferometry (by not performing any lowpass filtering of the signals measured at the photodetector passed to the lock-in amplifier, as described in section D.6 of the appendix). A simple 3rd order polynomial interpolation function seems not sufficient to describe the systematic nonlinearity in the response of the prototype. The problem should however be easily solvable by performing lowpass filtering. Another significant part of the measurement error is caused by cross-sensitivity of the sensor to transverse forces on the needle tip, which was already anticipated. The sudden changes in measurement error correlating with sudden changes in calibration force could be caused by a phase difference between the acquired signals of the reference sensor and the prototype, as measurements performed with the prototype lag visibly with respect to measurements performed with the reference sensor during sudden changes in calibration force. Correcting for a possible phase delay, by determining the delay with a cross-correlation of both signals and some manual tuning, could however not remove the correlation of sudden changes in calibration force with sudden changes in measurement error. It seems therefore that the prototype is not capable of achieving an apparent 'bandwidth' of 100 Hz, the cut-off frequency of the low-pass filter with which both signals of the reference sensor and prototype were filtered. The 'limitation in bandwidth' is likely due to viscoelastic behavior of the adhesive used to bond the optical fibers into the ferrule. Prototypes that used UV-curable glue instead of heat curing epoxy to bond the optical fiber into the borehole of the ferrule showed this effect more clearly, confirming that the issue is very likely glue related (see calibration results shown in figure D.16 of the appendix). The apparent 'limitation in bandwidth' is in that case merely caused by the fact that the sensor is more sensitive to very slowly varying forces due to creep/stress relaxation of the used adhesives. Forces with high frequencies can still be measured without much problems, though with a slightly lower sensitivity as there is no time for stress relaxation to occur. The frequency response of the sensor should therefore be 'flat' for relatively high frequencies, which should be tested by performing a measurement of the frequency response of the sensor. A frequency based filter, based on the inverse of a measurement of the frequency response of the sensor, could potentially be used to ensure that the response of the measurement system is entirely 'flat' within the required bandwidth to remove peaks in the measurement force correlating with sudden changes in force on the sensor. This does require that the response of the sensor is linear and time-invariant. The viscoelastic behavior of the adhesive and thus the frequency response of

the sensor could for example be quite temperature dependent. The viscoelastic behavior remains therefore quite inconvenient and possibly difficult to correct for. It is furthermore uncertain whether the reference sensor, the ATI Nano 17, meets and preferably exceeds the requirements on the accuracy and required bandwidth of the needle tip force sensor. Measurement errors could be contributed to the prototype of the needle tip force sensor while they are actually partially caused by measurement errors of the reference sensor.

The measurement accuracy of the prototype of the unmachined-quartz-column concept is likely sufficient for haptic feedback applications, except that an increase in mechanical bandwidth or at least a more constant frequency response could be beneficial for the precise detection of membrane punctures that cause a sharp peak in force on the needle tip. Some cross-sensitivity to transverse forces is not expected to be a particular problem from applications related to haptic feedback, as those forces also give information about the occurrence of 'events' during needle insertion. The measurement uncertainty should however preferably be improved or at least better quantified by measuring the frequency response of the sensor to be able to perform corrections for applications of the sensor like research on needle-tissue interaction forces, as the current maximum observed measurement error in dynamic conditions is quite large compared to the expected range of forces on the needle tip during needle insertion.

There is only marginal room for improvement of the measurement uncertainty of sensors designed according to the unmachined-quartz-column concept without completely altering the design. A reduction of the cross-sensitivity to temperature, an improved mechanical bandwidth, or constant frequency response for the measurement of high frequent forces and a reduced sensitivity to transverse forces are ways to improve the measurement uncertainty. Usage of Invar instead of RVS capillaries for the stylet tube and adhesives with a lower CTE or fusing the optical fibers into the ferrule could result in minor reductions of the cross-sensitivity of the FPI to temperature, as was observed with FE-modeling of the concept (although it will also make the needle MRI-unsafe, as Invar is ferromagnetic). Usage of filtering methods presented in the previous chapter or calibration of the sensor at 37°C will however likely already result in a sufficient reduction of measurement errors due to cross-sensitivity to temperature for most applications. Usage of a glue with less viscous behavior or preferably fusing the optical fiber into the ferrule, could result in a more useful improvement of the measurement uncertainty of the sensor, particularly with respect to the measurement of dynamic forces. The effect of using glue with 'good' properties, which was severely underestimated in the design phase, was clearly deduced from experiences with the performance of UV-curable glue with a relatively low viscosity in its cured state. The measurement error due to transverse forces on the needle tip, which can be quite significant according to FE-models and estimates based on calibration results, can only be reduced effectively by using a triaxial instead of uniaxial force sensor. A triaxial force sensor, with three FPIs to sense axial force on the needle tip and bending of the needle, will make the design more expensive and also mechanically weaker when the three FPIs are all located in the quartz ferrule. Placing a triaxial force sensor, with a possibly high cross-sensitivity to temperature for forces in axial direction, below the currently used uniaxial force sensor in the needle tip would result in a stronger but complex design. A small improvement for FPIs with a short cavity length in the order of 100µm (more appropriate when large forces have to be measured with homodyne interferometry and to prevent too much required protrusion of the ferrule from the capillary which makes the design fragile) is usage of a chromium instead of highly reflective gold coating as second FPI mirror, as was the intention in the concept phase.

The largest weakness of the unmachined-quartz-column concept is the fragility of the needle tip and in particular the quartz ferrule. The strength of the prototype has according to FE-modeling no safety margin at all, which is unacceptable if this were also the case in practice. Testing with a 'fake' needle tip showed that the quartz ferrule is capable to carry transverse

forces on the fake needle tip of more than 1 N, the maximum expected transverse force on the tip, without issues in combination with compressive axial force on the needle tip. No ferrule was fractured unintentionally during calibration of prototypes of the concept. Simple experiments, presented in section D.5 of the appendix, show that the ferrules should be capable to carry possibly even three times as much transverse force as expected due to the good surface quality of the quartz ferrules (without taking fatigue into account). It is however required to perform far more (reliable) tests of the strength of the design, with a real needle tip placed on the ferrule by means of a partial lock-in connection, to determine whether the design could be safe for usage. The needle should furthermore be tested with ex-vivo experiments to determine whether the assumed 1 N transverse force was a good estimate of the maximum transverse force on the needle tip of a 18 G, 20 cm long trocar needle.

Increasing the safety margin of the design as much as possible, even at the cost of a reduction in measurement uncertainty, remains however preferred, given the brittle behavior of quartz glass and the strong dependence of the strength of glass on its surface quality. Usage of a ferrule with a slightly larger diameter (0.8 mm or more) than the diameter of the ferrules used for prototypes (0.7 mm) is therefore strongly recommended. This could go at the cost of an increase in cross-sensitivity to temperature, as at least the sensitivity of the sensor to force will decrease. A still acceptable constant measurement error due to cross-sensitivity to temperature in the order of 150 mN due to a 24°C temperature disturbance should be achievable according to the used FE-model for an FPI with a cavity length of 100 μm , usage of an Invar stylet tube, a 0.8 mm diameter ferrule and EPO-TEK 353ND epoxy. The safety margin of the design will increase with approximately 30% (or more) due to the small increase in diameter of the ferrule. Containing the ferrule within the needle by moulding a compliant, tough plastic needle tip over the ferrule, such that glass particles are contained in the needle case the ferrule fractures, could also be an option to increase the safety of the design. This will unfortunately go at the cost of an extreme increase in cross-sensitivity of the design to temperature. The used FE-model of the unmachined-quartz-column concept, adapted such that a polyimide needle tip surrounds the ferrule protruding from an RVS stylet containing an FPI with a cavity length of 100 μm , shows that the constant measurement error due to cross-sensitivity to temperature increases to about 3.5 N due to a change in temperature of 24°C. It can thus be concluded that the quartz-column-concept is only suited for needles with a gauge of 18 or smaller (thus larger in diameter). Moreover, the concept becomes better suited for larger diameter needles, as the maximum stress inside the quartz ferrule scales with the inverse cube of the diameter of the ferrule, while the cross-sensitivity to transverse forces scales with the inverse square of the diameter. The decrease in sensitivity to axial forces should be no issue, as the axial forces on the needle tip seem to scale with more than the square of the needle diameter (table 2.1).

5 Stylet tube concept

5.1 Design and manufacturing of the prototype

5.1.1 Manufacturing method

A proposal for the design and manufacturing method of a prototype of the stylet-tube concept were briefly described in chapter 2.2. A large scale prototype of the stylet-tube concept, with a slightly different design and manufacturing method, was however made first to determine whether a needle tip could be polished sufficiently (with grit size P-2000) to act as FPI mirror [165]. The large scale prototype was furthermore used to investigate whether a screw connection of the needle tip to the stylet tube could be used instead of a press fit connection to enable adjustment of the FPI cavity length during manufacturing (figure D.17). The design of the large scale prototype was partially inspired by the machined-quartz-column concept to ensure a compliant long column as force sensitive element while the FPI cavity remains short. The FPI cavity length could be adjusted relatively easily, such that a short cavity length of 40 μm could be achieved. Testing of the large scale prototype showed however that slip of the screw joint results in large measurement errors during fast changing forces on the needle tip. The slip could not completely be prevented by locking the screw joint with superglue. Attaching the needle tip with a screw joint was therefore discarded. Some calibration results of the large scale prototype can be found in section D.7 of the appendix.

The first real prototype of the stylet-tube concept was manufactured to have dimensions as shown in figure 5.1 (the assembled prototype is shown in figure 5.2). The Invar capillary of the stylet tube was machined with EDM from Invar plate material. An optical fiber was glued into the borehole of a quartz ferrule using UV-curable adhesive (Norland adhesive 68) before the ferrule was placed into the Invar capillary. The ferrule, positioned in the capillary with a custom made positioning tool shown in figure 5.3, was glued into the Invar capillary with UHU PLUS sofortfest epoxy such that the FPI cavity length should become approximately 100 μm . Aiming at a much shorter cavity length was regarded to be unrecommended due to limited manufacturing precision of the positioning tool and needle tip. The needle tip with polished mirror was initially attached to the stylet tube by means of a press fit (insertion depth of 1 mm), though this connection also slipped when fast changing or large forces were exerted on the needle tip. It was therefore decided to also glue the needle tip into the Invar stylet tube with epoxy. The back side of the Invar needle tip, polished with grit size P-2500 to create the second FPI mirror, did seem slightly less reflecting than the polished RVS mirrors of the large scale

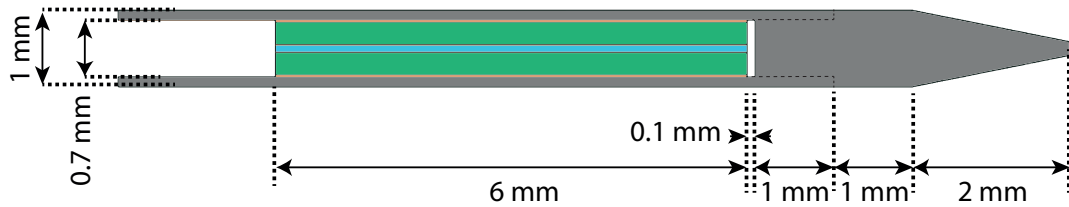


Figure 5.1: Geometry and dimensions of the used FE-model of the stylet-tube concept, showing Invar parts in grey, a fused quartz ferrule in green, an optical fiber in blue and glue layers in orange. The press-fit connection between the needle tip and the stylet tube is shown as a dashed line. The geometry is identical to the geometry of prototypes of the concept, except that the needle tip was glued with a bond length of 1 mm into the capillary instead of a press fit after the first prototype. The goal of the FPI-cavity length was 100 μm .



Figure 5.2: Assembled prototype of the stylet-tube concept.



Figure 5.3: Tool used to position the quartz ferrule in the Invar stylet tube and determine the FPI cavity length.

prototype (although a finer grit size was used). Reflectivity of the Invar mirrors was however sufficient to achieve a fringe pattern of the FPI that nearly spanned the entire dynamic range of the photodetector of the OP1550 when the power of the source was set to the maximum for a cavity length of approximately 160 μm .

5.1.2 Sensitivity of the FPI to force and temperature and other causes of measurement errors

The elastic modulus of epoxies can vary from less than 1 GPa to more than 6 GPa while the Poisson's ratio is in general about 0.3 [153, 160, 166]. Investigation of the sensitivity of the force sensing FPI to force on the needle tip and temperature of the needle tip as function of the modulus of the epoxy used to bond the ferrule in the capillary, the CTE of the epoxy, the thickness of the epoxy layer, the CTE of the Invar capillary and the type of adhesive used to bond the optical fiber into the ferrule, by means of a FE-model, indicated that the cross-sensitivity to temperature is nearly impossible to control as the exact mismatch of the CTE of the ferrule and the Invar stylet tube is unknown and the glue layer thickness between the ferrule and the stylet tube badly controllable (table D.8 of the appendix). Usage of a stiff epoxy with a medium CTE or a compliant epoxy with a high CTE (of the investigated values of the stiffness and CTE) seemed to result in the highest chance of achieving the lowest possible cross-sensitivity to temperature for the investigated bond line thicknesses, although the average advantage is not very significant (averaged over the uncontrollable parameters). It will be pure chance that the force sensing FPI can achieve the requirements on the measurement uncertainty with varying temperatures of the environment on itself, even with the most optimal chosen glue properties, without resorting to compensation methods for cross-sensitivity to temperature like filtering of measurements with a time dependent model. A little bit extra cross-sensitivity to temperature of the force sensing FPI due to non-optimal glue will not resort in issues when these methods or an additional temperature sensitive FPI are used to diminish the measurement error due to cross-sensitivity of the force sensing FPI in the needle tip to temperature. UHU-plus sofortfest epoxy was therefore chosen to glue the ferrule into the Invar capillary for its availability, curing time and viscosity in its uncured state. This proved later to be an unwise decision, as the epoxy's mechanical and thermal properties were not specified by the manufacturer. The type of adhesive used to bond the optical fiber into the borehole of the ferrule seems to have marginal effect on the sensitivity of the sensor to either force or temperature. A change in FPI cavity length due to a 10 N force on the needle tip in the order of 200-300 nm and a constant measurement error up to 1.5 N due to temperature change of 24°C were expected based on the FE-analysis. The change in cavity length and cross-sensitivity to temperature could however be significantly larger when the ferrule is not glued or positioned perfectly into the capillary. Furthermore, the FE-model did not account for the glue used to attach the needle tip to the Invar stylet, but assumed a rigid press fit connection. This omission can result in a significant underestimation of the sensitivity of the FPI to force on the needle tip, as the epoxy used to bond the ferrule to the capillary determines

a large part of the sensitivity of the FPI to forces on the needle tip according to the FE-model. The cavity length would change with only approximately 140 nm due to a 10 N force on the needle tip assuming that the ferrule is connected rigidly to the Invar capillary without usage of any epoxy.

Sources of measurement errors for the stylet-tube concept are expected to be the same as error sources identified for the unmachined-quartz-column concept, shown in table D.7. The cross-sensitivity to temperature (already shown by means simple models and a FE-analysis) and the cross-sensitivity to transverse forces on the needle tip are however expected to be higher. The force sensitive element is furthermore expected to behave more viscous compared to the force sensitive element of the unmachined-quartz-column concept. The cross-sensitivity to transverse forces is expected to be higher, despite the larger second moment of area of the cross-section of the needle at the location of the FPI compared to the unmachined-quartz-column concept. The eccentricity of the FPI cavity in a needle manufactured according to the stylet-tube concept will be worse compared to the eccentricity of the FPI cavity of a needle manufactured according to the unmachined-quartz-column concept. This is caused by the quite large tolerance on the outer diameter of the ferrule and inner diameter of the Invar capillary and thus on the eccentricity with which the ferrule will be positioned in the capillary. Furthermore, transverse forces might more easily cause a significant wedge angle of the FPI mirrors, because the needle tip, of which the polished back side acts as second FPI mirror, will be able to tilt a little bit inside the capillary due to transverse forces on the tip. The force sensitive element is expected to behave more viscous compared to the unmachined-quartz-column concept because the glue layers contributing to the force sensitive element, showing viscoelastic instead of elastic behavior, are far thicker in the stylet-tube concept.

5.2 Calibration method

Calibration of prototypes of the stylet-tube concept was performed as described in section 4.3. Dynamic calibration was however only performed at room temperature, while cross-sensitivity to temperature was tested in water baths with an unloaded sensor.

5.3 Calibration results

The prototype of the stylet-tube concept of which calibration results will be presented had an FPI cavity length of approximately 160 μm (estimate based on a scan of the fringe pattern as function of wavelength). The change in FPI cavity length due to a force of 10 N on the needle tip is approximately 700 nm, which is significantly larger than anticipated based on FE-models. The prototype was therefore not very suited to be interrogated with homodyne interferometry. Only calibration results obtained with interrogation by means of 'low coherence interferometry' will therefore be presented.

Results of static calibration of the prototype are presented in figure 5.4 and 5.6. Five instead of three calibration cycles were performed as the sensor seemed to suffer from significant drift, possibly due viscoelastic creep of the force sensitive element. The maximum observed measurement error was 445 mN. The drift does however not occur in the most logical direction to be explained by viscoelastic creep. The deflection of the spring of the force sensitive element becomes for a given calibration load gradually smaller instead of larger during the calibration procedure. Correcting for the variation in the resultant transverse force on the needle tip by incorporating the resultant transverse force according to the reference sensor as additional explanatory variable in the interpolation function for the axial calibration force shows that the apparent drift could also be caused by a slight change in the magnitude of the resultant transverse force on the needle tip during the calibration procedure. The measurement error of the axial

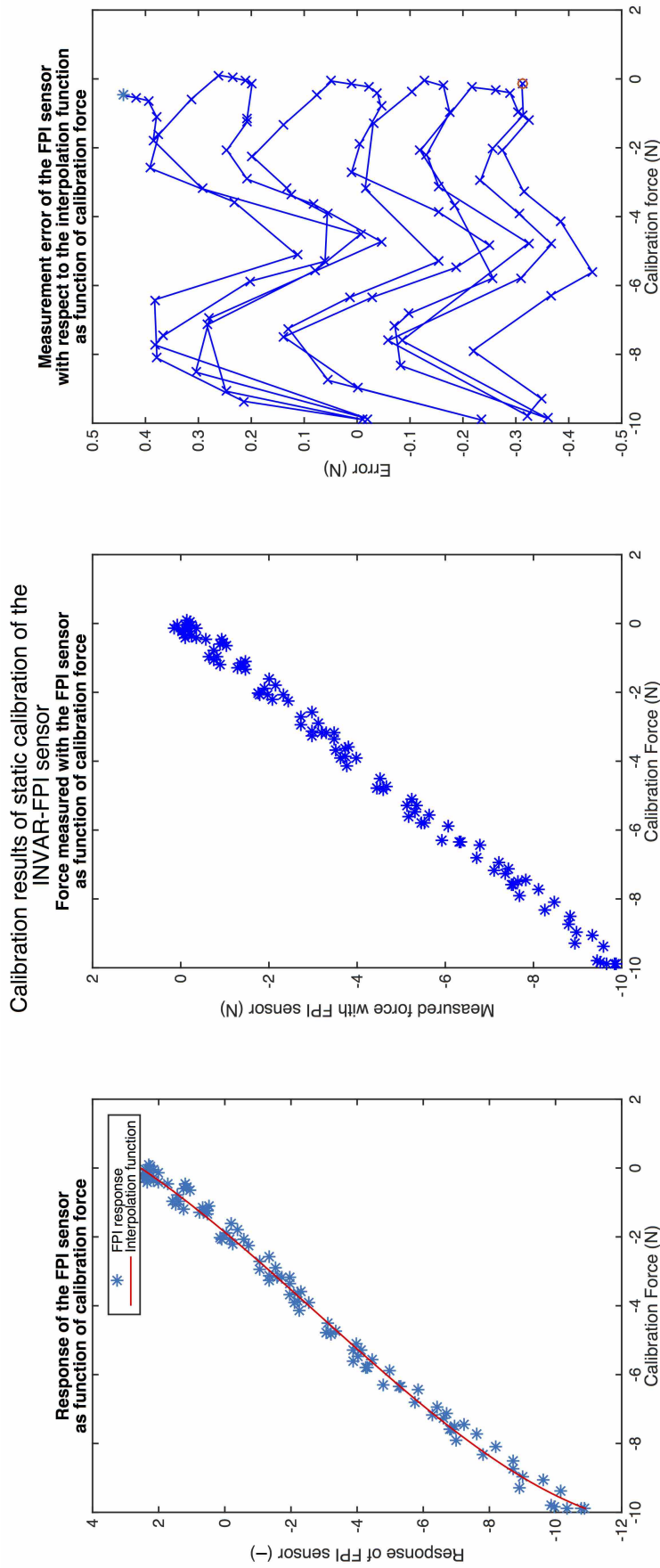


Figure 5.4: Results of static calibration of a prototype of the stylet-tube concept, not accounting for transverse force on the needle tip, interrogated using low coherence interferometry. The response of the FPI as function of the calibration force, together with a fitted 3rd order polynomial interpolation function is shown on the left. The graph in the center shows the force measured with the FPI, calculated using the interpolation function, as function of the calibration force. The measurement error of the FPI-based sensor as function of the calibration force is shown on the right. The blue star and the red circle indicate respectively the first and last reading obtained during static calibration.

force, after 'correction' for variation of the transverse force is shown in figure 5.5. Equation 4.2 was used as interpolation function with a polynomial of the third order, to still be able to describe some nonlinearity of the response of the FPI interrogated with 'low coherence interferometry'. The figure also shows the measurement error when the same interpolation function would be used, but either the measured response of the FPI or the resultant transverse force, both used as explanatory variable, is assumed to be zero to illustrate the influence of each explanatory variable on the calculated axial force on the needle tip. The maximum observed error of the FPI for the measurement of axial forces, after correction for variation in the resultant transverse force, is about 350 mN. A small hysteresis loop seems still present. The response of the FPI measured with low coherence interferometry, using the method described in the appendix (section D.6), contains a nonlinearity with a periodicity that correlates with the period of the fringe pattern as function of calibration force.

The noise of the measurements performed with the prototype is not very Gaussian. The resolution of the force sensor of the prototype, estimated as three times the standard deviation of the noise, is a sinusoidal function of the calibration force. The periodicity of the resolution correlates with the periodicity of the fringe pattern of the FPI as function of calibration force. Both the resolution of the prototype and the reference sensor deteriorate slightly with increasing calibration force. This could be caused by a reduction of the resonance frequency of the calibration setup due to the added calibration masses, allowing vibrations to be coupled more easily into the system and thereby preventing accurate estimation of the resolution. The resolution of the prototype is estimated to be in the worst case, disregarding outliers, about 8 mN, which is about 2.5 times worse than the resolution of the ATI Nano 17 sensor (estimate based on the resolution for a calibration force of about -2 N). The resolution of the prototype is in the best case about equal to the resolution of the reference sensor.

Results of dynamic calibration of the prototype of the stylet-tube concept at constant temperature are shown in figure 5.7 and 5.8. The maximum observed measurement error during dynamic calibration using a 3rd order polynomial interpolation function is about 800 mN. Histograms of the distribution of measurement errors observed during static and dynamic calibration are shown in figure 5.9. Results of dynamic calibration of the prototype show a hysteresis loop. A correlation between sudden large changes of the calibration force and sudden changes in measurement error can be observed in the calibration results shown in figure 5.8. The correlation becomes more distinctive in the last two 15 second segments of the dataset obtained during dynamic calibration, where changes in axial calibration force occur more abruptly. This is can be an indication of quite viscoelastic instead of elastic behavior of the force sensitive element of the force sensor. A simple phase delay between the measurements performed with the prototype and the reference sensor did not seem to be the cause of the sudden changes in measurement error correlating with sudden changes in calibration force.

A significant sensitivity of the FPI-based force sensor to transverse force could be observed during the calibration procedure. Exerting transverse forces correlating with axial forces on the weight platform of the calibration setup resulted in a reduction of the fringe visibility of the FPI, likely due to an increasing wedge angle of the FPI mirrors. The reduction of the fringe visibility could be deduced from the spiraling trajectory described by the vector of the the average light intensity and the amplitude of the intensity oscillation at the photodetector as function of the calibration force (as described in section D.6 of the appendix). A reduction of the fringe visibility due to transverse forces on the needle tip does on itself only result in measurement errors when homodyne is performed and not when 'low coherence interferometry' is performed (as long as the FPI cavity length does not change). Multiple linear regression using the parts of the two orthogonal components of the transverse force uncorrelated with the axial calibration force as explanatory variables for the measurement error did indicate a correlation between the transverse

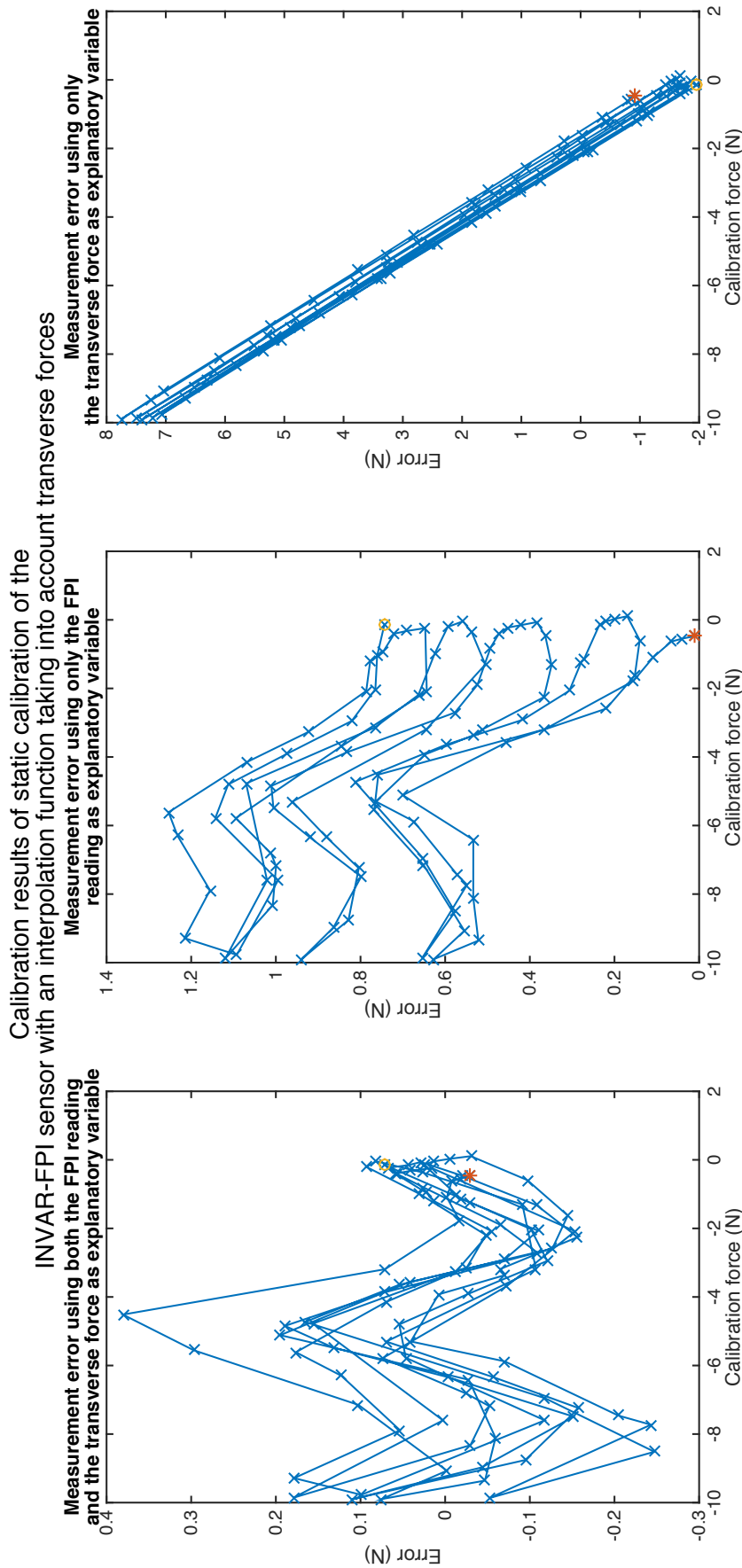


Figure 5.5: Results of static calibration of a prototype of the stylet-tube concept, interrogated using low coherence interferometry, after correction for variation of transverse force on the needle tip. Equation 4.2 was used as interpolation function to calculate the measured force based on the reading of the FPI and the resultant transverse force on the needle tip according to the reference sensor. The star indicates the first measurement of the calibration series, while the dot indicates the last measurement. The graph on the left shows the measurement error when both explanatory variables are measured and used with the determined interpolation function, while for the graph in the middle and on the right the same interpolation function is used but respectively the measured response of the FPI or the measurement of the resultant transverse force is assumed to be zero.

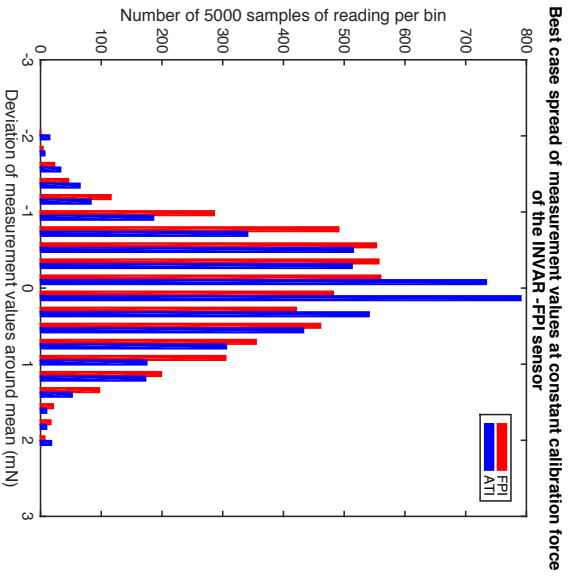
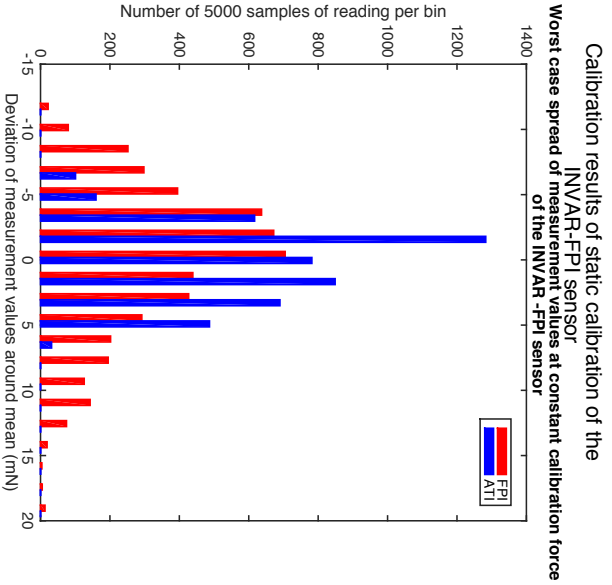
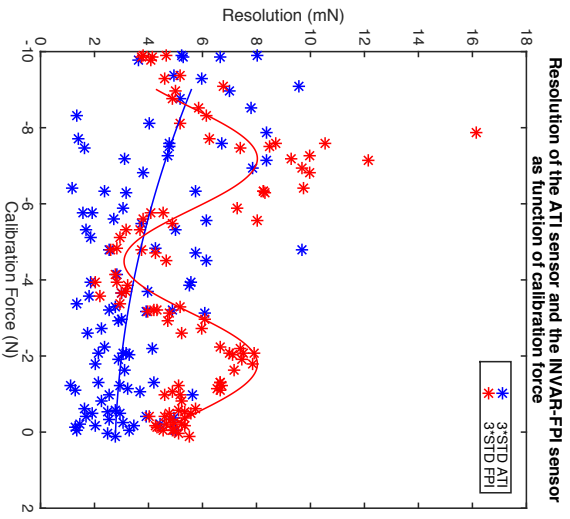


Figure 5.6: Analysis of the resolution of the styler-tube concept. The resolution of the FPI-based sensor of the prototype and the ATI Nano 17 sensor, used as reference sensor, are shown as function of calibration force on the left, together with a second order polynomial and a sinusoidal fit to the data to illustrate the relation between the resolution and the calibration force. The histograms show the largest and smallest observed spread of measurement values around the mean of 1 second long readings (sampled at 5 KHz) of the force sensor of the prototype obtained during static calibration and the corresponding spread of measurement values of the reference sensor.

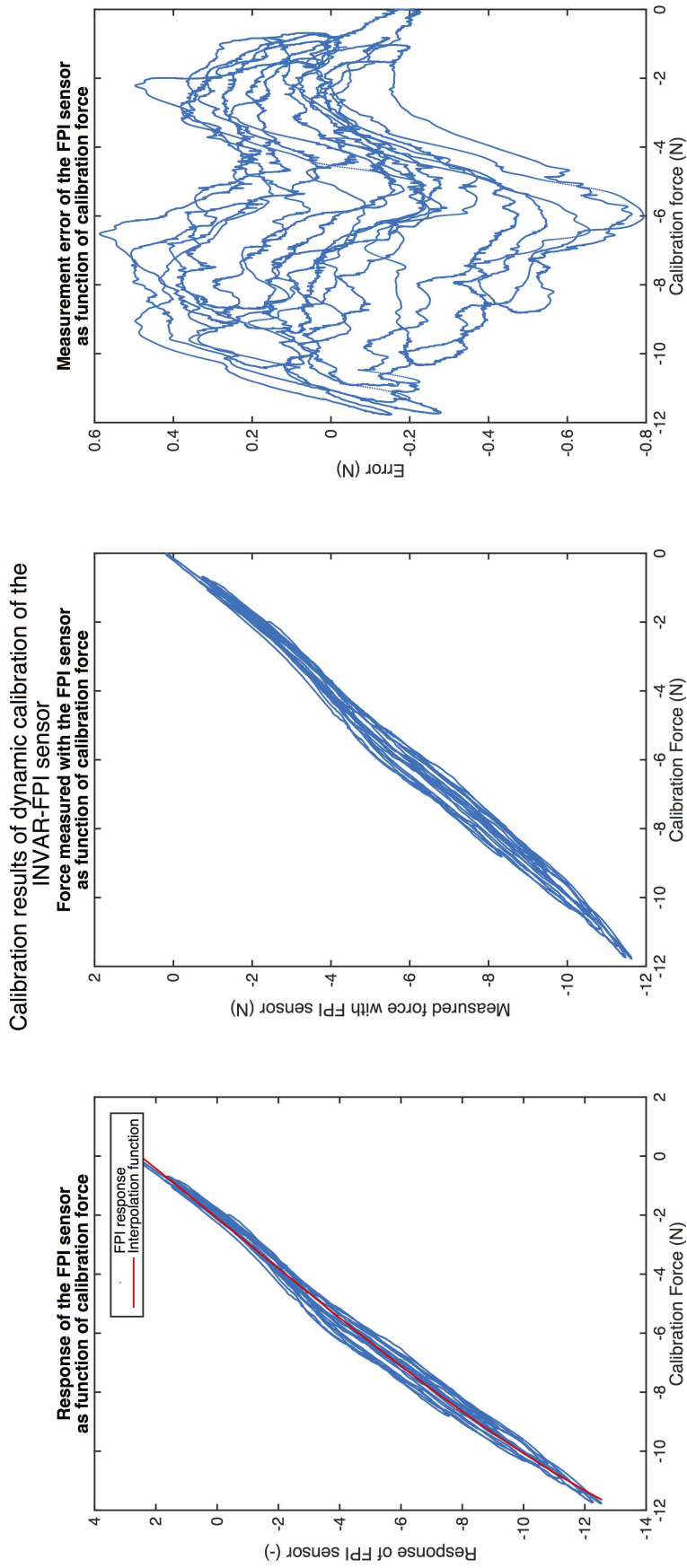


Figure 5.7: Results of dynamic calibration of a prototype of the stylet-tube concept interrogated with low coherence interferometry. The response of the FPI as function of the calibration force, together with a fitted third order polynomial interpolation function, is shown on the left. The graph in the center shows the force measured with the FPI-based sensor; calculated using the interpolation function, as function of the calibration force. The measurement error of the FPI-based sensor as function of the calibration force is shown on the right.

Force measured with the INVAR-FPI sensor
 subjected to dynamic calibration forces as function of time

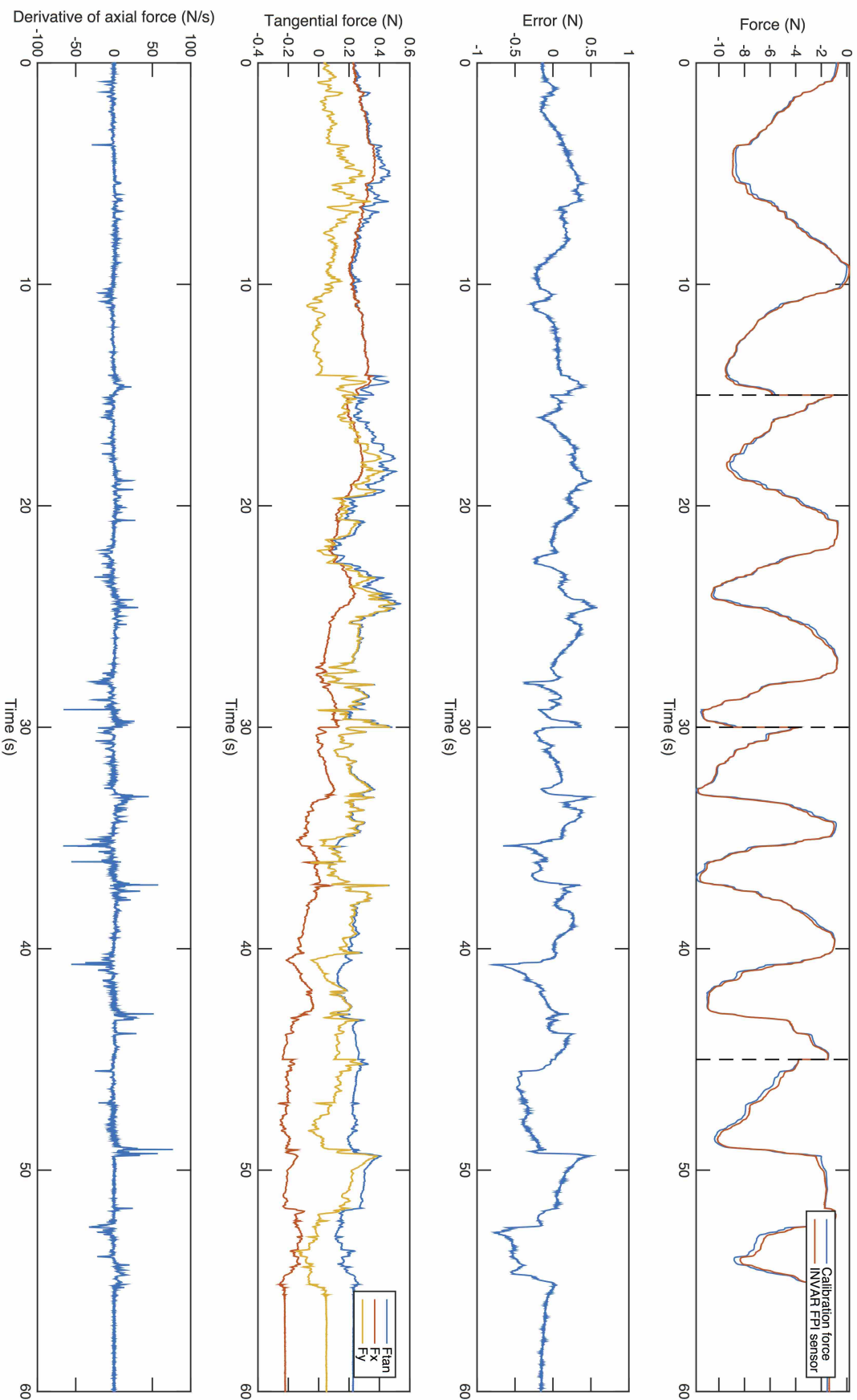


Figure 5.8: Results of dynamic calibration of a prototype of the stylet-tube concept at room temperature, interrogated with low coherence interferometry, shown as function of time. The graphs show, from top to bottom: (1) the calibration force and the force measured with the prototype, calculated using the interpolation function shown in figure 5.7, (2) the measurement error of the prototype, (3) the transverse force on the needle tip, shown as the resultant transverse force 'Ftan' and its two orthogonal components 'Fx' and 'Fy', and (4) the derivative of the calibration force to time. The dotted lines in the top graph (1) indicate the 15 second long fragments of which the dataset obtained during dynamic calibration is composed.

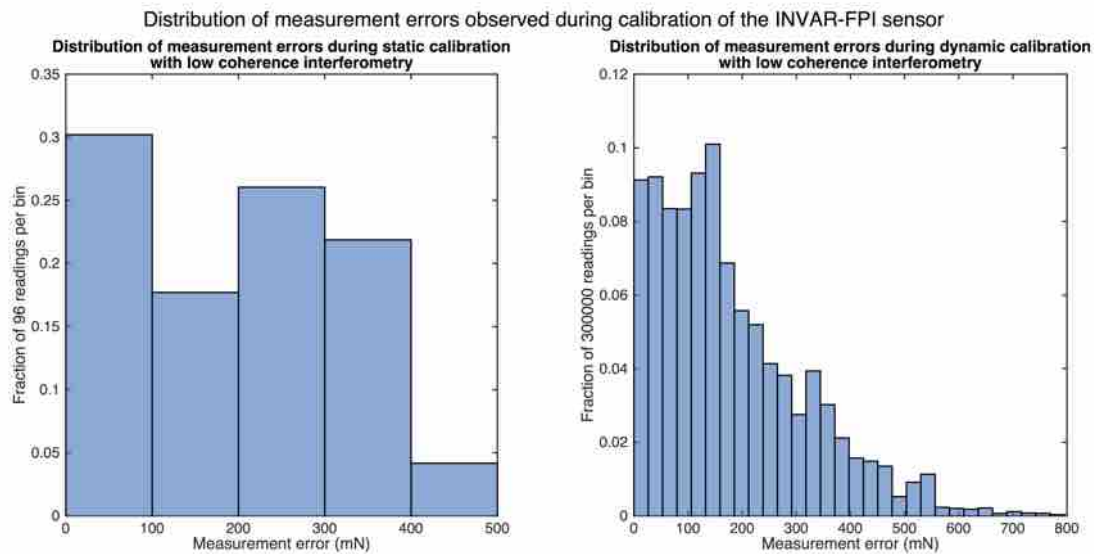


Figure 5.9: Histograms of the distribution of measurement errors observed during static and dynamic calibration of a prototype of the stylet tube concept at room temperature, based on data shown in respectively figure 5.4 and 5.7.

force and the measurement error (the fitted model is shown in figure D.21 of the appendix, the model was based on data shown in figure D.22 of the appendix). However, the two orthogonal components of the transverse force uncorrelated with the axial calibration force do explain only a fraction of the variation of the measurement error ($R^2 = 0.44$). The cross-sensitivity of the FPI to transverse forces was estimated to be about 0.3 to 1.7 N/N based on the regression model. Not much value is given to these estimates, as they varied reasonably for different selections of the data acquired during dynamic calibration.

The prototype showed a peculiar response to changes in temperature. Results of a test of the response of the prototype to changes in temperature, performed by submerging the prototype in water baths at room temperature and a very feverish body temperature (respectively 19°C and 42°C), are shown in figure 5.10 (a magnification of a part of the data is shown in figure D.23 of the appendix). A linear interpolation function, based on data obtained during dynamic calibration of the force sensor at room temperature, was used to describe the response of the FPI. A linear instead of a 3rd order interpolation function was used, as the response of the FPI to changes in temperature exceeded the response of the FPI observed during dynamic calibration. The sensor was first loaded a few times in air at room temperature with a significant force to initialize interrogation of the FPI with low coherence interferometry, after which no more force was exerted onto the sensor during the test. A drift of the measurement error of about 120 mN occurs during the first few minutes after submerging the prototype in a water bath at room temperature. The direction of the drift corresponds to an increase in temperature, while the water temperature was more likely a bit below than above the air temperature. A viscous response of the sensor after unloading could however result in a gradually increasing FPI cavity length, which is a change in FPI cavity length that corresponds to increasing temperature. Submerging the sensor in hot water results in a relatively quick rise of the measurement error with about 900 mN in about 4 seconds. The measurement error drifts afterwards for approximately a minute far more slowly, seemingly due to a process with a different time constant than the initial response to the change in temperature. The drift of the measurement error seems to stabilize thereafter for approximately 2 minutes. A sudden kink in the development of the measurement error as function of time

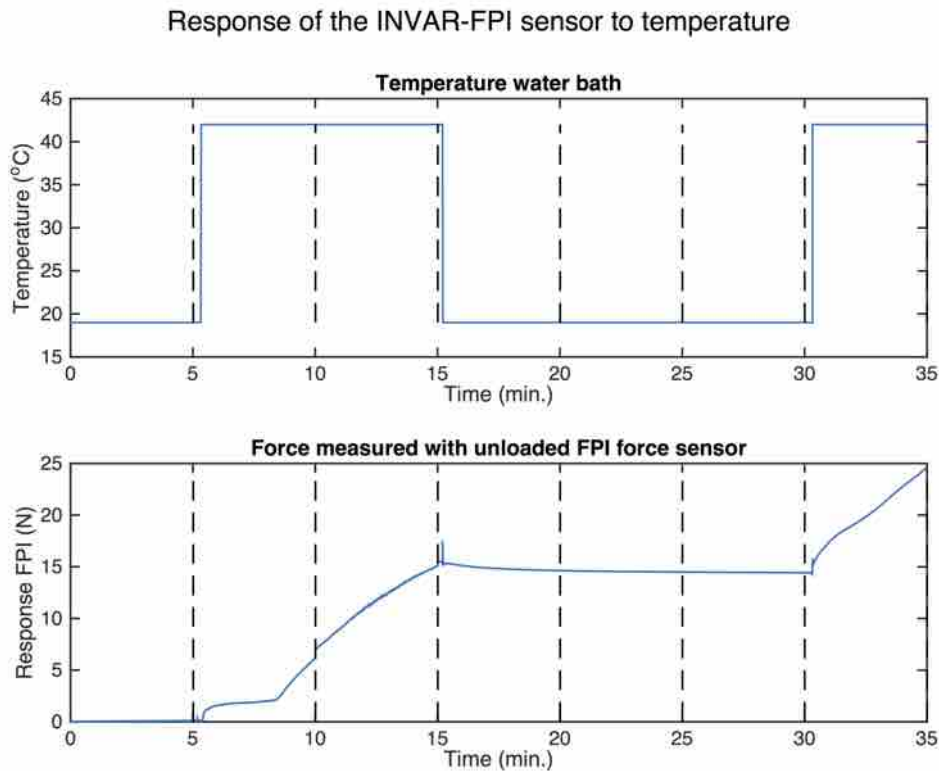


Figure 5.10: Test of the response of a prototype of the stylet-tube concept to changes in temperature. The temperature of the water baths in which the prototype is submerged is shown in the top graph, while the peculiar response of the prototype is shown in the bottom graph expressed as measurement error in Newtons. The dotted black vertical lines indicate short interruptions of the data acquisition for a few seconds.

occurs thereafter, when the speed of the drift of the measurement error drastically increases. The speed of the drift of the measurement error declines only very slowly in the subsequent 7 minutes. The measurement error increases in the 7 minutes with about 12.5 N. Submerging the sensor back in water at room temperature does not result in a quick return of the state of the sensor to its state at room temperature at the start of the experiment. The measurement error decreases very slowly with about 1 N in 15 minutes and seems to stabilize at a total measurement error of roughly 14 N. Submerging the prototype back into hot water results again in a very quick drift of the measurement error, which is this time not preceded by an initial phase of slower drift as was observed during the first time the prototype was submerged in hot water.

5.4 Discussion

Calibration results show that the prototype of the stylet-tube concept struggles to achieve the requirements on the measurement uncertainty. This is even the case when the sensor is subjected to semi-static axial calibration forces with as less disturbances as possible while some corrections for accidental variations in the resultant transverse force on the needle tip are performed. The largest part of the measurement error of static forces without presence of disturbances seems caused by the way low-coherence interferometry was implemented, which causes a periodic nonlinearity in the response of the FPI as function of the calibration force. The used interpolation function cannot sufficiently describe the nonlinearity. The measurement error therefore still

contains an apparent, quite large, systematic error. The nonlinearity should however be easily removable by introducing a lowpass filter between the photodetector of the OP1550 and the digital lock-in amplifier (as concluded in section D.6 of the appendix).

Correction for accidental variations in transverse force during static calibration, investigation of the sensitivity to transverse forces during dynamic calibration and the observed reductions in fringe visibility during dynamic calibration showed that the FPI in the needle tip is very sensitive to transverse forces. Correction for variations in transverse force on the needle tip during static calibration was based on the resultant transverse force instead of its two orthogonal components (as the components were not separately measured during static calibration). This hampers complete and correct compensation for variations in the transversal force on the needle tip. The estimate of the measurement uncertainty of the prototype for pure uniaxial static forces, without presence of disturbances, could therefore be an overestimation. Usage of measurements performed with the 'accurate' reference sensor for the correction for varying transverse forces could have caused an underestimation of the achievable measurement error of the FPI without variation of transverse forces on the needle tip. This effect should however have been marginal, given the small influence of the resultant transverse force as explanatory variable in the interpolation function for the measured axial force. A better calibration setup or method to compensate for variation in transverse forces on the needle tip would nonetheless have been useful to be able to assess the performance of the FPI for the measurement of purely axial forces better.

The sensitivity of the force sensitive element of the prototype is far larger than expected based on FE-modeling. This can be caused by numerous reasons, like a thinner Invar capillary or longer FPI cavity than modeled, incorporation of the sensitivity to transverse forces in the estimate of the sensitivity to axial forces, but also by a thicker glue layer than expected, the presence of a glue layer bonding the needle tip to the capillary (which was not modeled) or a bad glue layer bonding only a part of the surface of the ferrule to the the capillary. The viscoelastic properties of the glue could therefore have had an even larger impact than expected on the compliance and thus the observed behavior of the force sensitive element of the force sensor. The drift of the measurement error observed during the static calibration procedure could potentially be the result of (extreme) viscoelastic behavior of the used epoxy instead of changes of the resultant transverse force on the needle tip. The viscous response could be caused by preloading the prototype for three minutes with the maximum calibration load before the static calibration procedure commenced. The force sensitive element will slowly restore itself during the calibration procedure. This could cause the observed drift of the measurement error in the data obtained during static calibration of the prototype. This explanation is corroborated by the long slow drift of the unloaded sensor in the first phase of the test of the response of the FPI to temperature. The prototype was for this test preloaded with a very large force for a short while before this test commenced to initialize low coherence interferometry. The drift of the measurement error during static calibration would according to this explanation correlate by chance with the general change in resultant transverse force on the needle tip. A measurement of the step response of the sensor would have given more insight in the presence of extreme viscoelastic creep of the force sensitive element, or confirmed that the observed drift of the measurement error during static calibration is entirely caused by varying transverse forces on the needle tip. Extreme viscous behavior would however not be surprising given the results of the test of the response of the sensor to changing temperatures. This test indicates that the epoxy used to bond the ferrule and needle tip to the capillary is used around or near its glass transition temperature. This would cause the epoxy to behave rubbery instead of glassy.

Viscoelastic instead of elastic behavior of the force sensitive element seems to result in significant measurement errors during dynamic calibration when suddenly changing forces have

to be measured. The presence of these errors could indicate an apparent 'mechanical bandwidth' of the force sensor significantly lower than 100 Hz (the cutoff frequency of the lowpass filter used for measurements performed with the reference as well as the FPI-based sensor). The viscous behavior of the adhesive increases the sensitivity of the force sensor to slowly varying forces, as stress creep/stress relaxation of the epoxy can occur. It should however not prevent measurement of forces with a high frequency, although the sensor does have a slightly lower sensitivity to those forces as no stress relaxation of the glue can take place. This should be tested by performing a measurement of the frequency response of the sensor. A filter, based on the inverse of the measured frequency response of the sensor, could in theory be used to obtain a 'flat' frequency response of the sensor within the required bandwidth, as long as the response of the sensor is linear and time invariant. Temperature dependence of the viscoelastic behavior of the adhesive might however make such compensation quite difficult.

The peculiar response of the FPI to a change in temperature cannot be explained with certainty. The quick initial change in measurement error with about 900 mN, due to a change of the temperature of the needle tip from room temperature to body temperature, could be due to the expansion of the different materials used in the needle tip. The change in measurement error has an order of magnitude that was expected based on FE-models. The quick small change in measurement error followed by a far slower increase of the measurement error caused by a sudden increase in temperature of the needle tip was also observed in experiments where the prototype was alternately submerged for a few seconds in cold and hot water baths. The effect becomes even more clearly visible when the prototype has been submerged for a while in a hot water bath before the prototype is alternately submerged in water baths with different temperatures (of which an example is shown in figure D.24 of the appendix). The slow increase of the measurement error, that occurs after submerging the prototype in the hot water bath for the first time, is expected to be due to viscous behavior of the force sensitive element caused by the presence of the epoxy used to glue the ferrule into the Invar capillary (although this cannot be proved, as no prototypes with different glue or without glue were made). The ferrule is initially forced to strain due to the larger expansion of the Invar capillary compared to the expansion of the ferrule caused by the change in temperature. A slow creep of the epoxy will occur due to the stress in the epoxy caused by the difference in expansion coefficients. This will allow the forced strain of the ferrule to reduce slowly. The top surface of the ferrule will thereby move away of the second FPI mirror, increasing the FPI cavity length and thereby the measurement error further. The rather sudden increase in the speed of the creep, occurring after a few minutes in the hot water bath, is likely the result of the transition of the epoxy to a more rubbery state because the epoxy is used near or above its glass transition temperature. This cannot be verified, as thermal properties of the glue were not specified by the manufacturer. A glass transition temperature of about 50°C is however presented as a typical average glass transition temperature for epoxies by an epoxy manufacturer (note that the glass transition occurs over a temperature range around the glass transition temperature) [153]. Stresses in the epoxy due to the difference in CTE of the quartz ferrule and the Invar capillary disappear when the temperature of the needle tip returns back to room temperature. The cavity length reduces subsequently very slowly but does not return back to its original length at room temperature. This behavior can be explained when the epoxy behaves like a Maxwell or Burger's solid (the latter is proposed by a supplier of epoxies [153]). It takes some time for an epoxy to transform to its rubbery state when the temperature of the epoxy suddenly changes to a temperature near the glass transition temperature. This explains why the fast drift of the measurement error only starts after a few minutes when the needle is submerged for the first time in the hot water bath [153]. It is however a bit peculiar that it seems to take a much longer time for the epoxy to transform back to its normal glassy state. Increasing the temperature of the needle back to body temperature, after the needle has cooled down for

a fifteen minutes in the cold water bath, immediately results in quick drift of the measurement error corresponding to the rubbery state of the epoxy. The difference in the development of the change in measurement error after alternately submerging the prototype shortly in a cold water bath and then in a warm water bath, before which the prototype was acclimatized for an extremely long time at respectively room temperature or body temperature, could be replicated in other experiments performed with the prototype (not shown in this report). The drift of the measurement error is likely not caused by the humid environment that influences the properties of, for example, the epoxy, as no extreme drift occurs when the sensor is submerged for a very long time in cold water. The large observed measurement errors in the response of the prototype to a change in temperature seem to be caused almost entirely by the result of viscous behavior of the used adhesives. The results of the tests therefore indicate that it should be possible to obtain a relatively low constant error due to cross-sensitivity to temperature with a needle designed according to the stylet-tube concept, given usage of a far less viscous adhesive to bond the ferrule into the stylet tube.

The stylet-tube concept has some distinct advantages, like a good strength, that make the concept attractive despite the quite poor performance of the prototype. Assembly of the prototype of the stylet-tube concept was for example also (unexpectedly) quite straightforward, certainly compared to assembly of the prototypes of the unmachined-quartz-column concept. The epoxy used to bond the ferrule and needle tip to the capillary did, due to its high viscosity, not cause feared issues with contamination of the mirrors of the FPI during assembly. Some improvements to the design are however required to be able to benefit from these advantages.

It is in the first place recommended to adapt the design to a 'triaxial' force sensor, by incorporating three FPIs in the needle tip in a triangle configuration around the neutral axis, to compensate for bending of the needle (figure 5.11). The ability to correct for bending of the needle will significantly improve the accuracy with which axial forces on the needle tip can be measured under practical conditions where transverse forces will be present. Reducing the sensitivity to transverse forces of an uniaxial force sensor, designed according to the stylet-tube concept, is difficult due to the limitations of the manufacturing precision. The apparent large change in wedge angle of the FPI mirrors due to transverse forces could however probably be reduced by inserting the needle tip more than 1 mm into the Invar capillary before fixation. A simple uniaxial force sensor could still be attractive for haptic feedback purposes where the occurrence of 'events' is only of interest, despite cross-sensitivity to transverse forces on the needle tip. Accurate sensing of tissue stiffness by means of haptic feedback during needle insertion will however likely be hampered by the rather large cross-sensitivity of an uniaxial design to transverse forces.

The largest improvements have to be made with respect to the cross-sensitivity/response of the design to temperature. The response of the prototype to an increase in temperature seems to be terrible due to viscoelastic behavior of the used epoxy. Incorporation of a temperature sensing FPI, as was the intention, would not be sufficient to reduce the measurement error caused by the highly nonlinear and time dependent response of the force sensing FPI to a change in temperature. Results of FE-analyses and tests of the prototype indicate that the design should be able to have a reasonably small constant error due to cross-sensitivity to temperature, given the CTEs of used materials and the thermo-optic coefficient of air, when the viscous behavior of the adhesive used to bond the ferrule into the Invar capillary can be reduced significantly. The reduction in viscous behavior would also increase the apparent 'mechanical bandwidth' of the sensor. An adhesive should therefore be searched, likely with a very high glass transition temperature, that behaves sufficiently elastic instead of viscoelastic. A first candidate could be EPOTEK 353ND epoxy, also used for the prototype of the unmachined-quartz-column concept. The curing behavior of this epoxy increases however the chance of contamination of FPI mirrors, as the epoxy becomes

liquid for a short duration during the curing process. Addition of a temperature sensitive FPI, initially proposed for the stylet-tube concept, might not be required for some applications, given that a reasonably low constant error due to cross-sensitivity to temperature in the order of 1 N due to a change of 24°C in temperature change should be achievable by using a good adhesive. This would correspond to a cross-sensitivity to temperature in the order of about 0.05 N/°C. This is still more than an order of magnitude lower than the cross-sensitivity to temperature of the FBG-based force sensor to measure forces on the tip of a needle shown in literature [2]. Such a cross-sensitivity to temperature is quite acceptable when a time dependent model or a sensor calibrated at body temperature is used to reduce measurement errors when the needle is inserted into the warm body of a patient. Modifying error due to cross-sensitivity to temperature might however still cause large measurement, depending on the properties of the used adhesive.

The usage of ferromagnetic Invar for the stylet tube and the needle tip, chosen for its particularly good dimensional stability, makes the needle likely unsuited to be used in combination with MRI for safety and imaging reasons. Non-ferromagnetic metals could be chosen to replace Invar to increase MRI-safety, but will in most cases result in a very significant cross-sensitivity to temperature due to the increase in CTE mismatch with the quartz ferrule/silica fiber. A temperature sensor to correct for the cross-sensitivity to temperature, as well as usage of 'low coherence interferometry' to achieve the required measurement range of the force sensing FPI will certainly be required in such a case. Furthermore, the properties of the used adhesives will in such a case become even more important to prevent drift of the measurement error due to a CTE mismatch and viscoelastic behavior of the adhesive, as was observed in the constructed prototype of the stylet-tube concept. Simulations with the FE-model of the stylet-tube concept show that replacing Invar with extremely compliant Nitinol will result in a constant error due to cross-sensitivity to temperature of approximately 1.6 N to 1.8 N caused by a temperature change of 24°C, taking into account the CTE of used materials and the thermo-optic coefficient of air (using Nitinol in its martensitic state). The properties of Nitinol are however highly temperature dependent, which might result in a cross-sensitivity to temperature in the form of large modifying errors [167]. Changes in FPI cavity length due to a load of 10 N on the tip will, with the used geometry, be larger than 700 nm when Invar is replaced with Nitinol. Interrogation of the force sensing FPI with 'low coherence interferometry' will in that case clearly be required. Decreasing the compliance of the force sensitive element is not recommendable, as it will increase the cross-sensitivity to temperature. Usage of a non-magnetic stainless steel alloy with a relatively low CTE (15 μ strain/K) will result in a constant measurement error in the order of 15 N to 20 N caused by a change in temperature of 24°C. The 'equivalent' change in FPI cavity length due to the change in temperature will be in the order of 200 nm to 400 nm. A needle according to the stylet-tube concept with a stainless steel (or similar metal) capillary will therefore require a very good temperature sensor and model of the behavior of the force sensing FPI to be able to sufficiently correct for the error. Usage of stiff materials with a 'normal' CTE is thus not recommended to make the stylet-tube concept MRI-safe. Moreover, perfect MRI compatibility will never be achieved due to usage of metals for the strong stylet tube, as those will always cause some imaging artifacts. Nitinol is for example used for 'MRI compatible' needles, but noted to result in quite large imaging artifacts [117].

The slightly lacking resolution of the prototype interrogated with 'low coherence interferometry' could be improved quite easily. The resolution achievable with homodyne interferometry is much better, but the extreme sensitivity of the prototype makes usage of homodyne interferometry for the required measurement range impossible. The factor that causes the 'worst' resolution within the measurement range is, for the prototype, the resolution with which the lock-in amplifier can measure the sensitivity of the FPI to a change in wavelength of the source. This is mostly caused by suboptimal settings of the lock-in amplifier and wavelength modulation

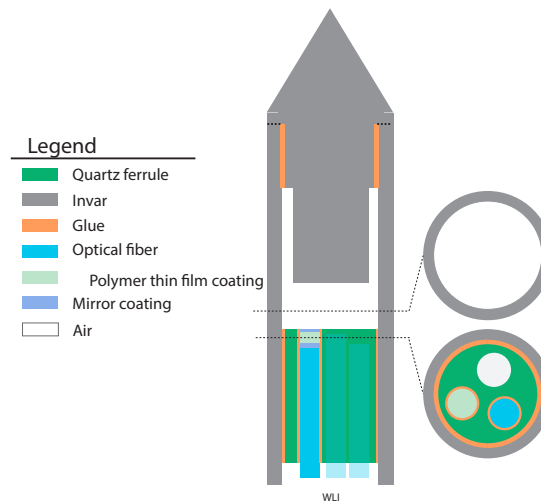


Figure 5.11: Conceptual design of an improved version of the stylet-tube concept. The needle tip contains three force sensing FPIs (a triaxial force sensor), each with a different cavity length, an extra long Invar 'column' to increase the sensitivity to force while a short FPI cavity remains possible. An optional temperature/force sensing FPI according to the thin-film concept is fabricated on top of one of the fibers (with a very thin second FPI mirror, such that a temperature/force and a force sensing FPI form in series). It could be easier to produce such a force/temperature sensing FPI on all three optical fibers. The four/six FPIs are interrogated with low coherence interferometry.

of the optical source. These 'suboptimal' settings for the resolution were chosen to prevent too large nonlinearities in the response of the FPI to calibration forces, caused by the absence of a lowpass filter between the photodetector and the lock-in amplifier (as explained in the appendix D.6). Addition of a lowpass filter, which removes the nonlinearities, and optimization of settings of the lock-in amplifier will therefore likely result in a significant improvement of the resolution. Investigation of prototypes (of other concepts) with a very long FPI cavity (500 μm) shows furthermore that the resolution with which the lock-in amplifier can measure the sensitivity of the FPI to a change in wavelength improves with increasing FPI cavity length. This is expected, as the same oscillation of the wavelength of the source will scan over a relatively larger part of the fringe pattern, therefore cause a larger amplitude of the oscillation of the light intensity at the photodetector and thus a better signal to noise ratio in the signal supplied to the lock-in amplifier. Increasing the FPI cavity length is however not recommended because the reflectivity of the polished Invar FPI mirror is not very high. This could be improved by coating the mirror, for example, with gold. An alternative option to increase the resolution, is increasing the length of the 'column' of the force sensitive element and thus the sensitivity of the sensor to force. An attractive method to increase the length of the column without increasing the cavity length is using the machined-quartz-column concept as inspiration, modifying the concept as shown in figure 5.11). Increasing the length of the Invar column will furthermore ensure that the (visco)elastic behavior of the force sensitive element of the force sensor is dominated more by the (supposedly) elastic behavior of Invar instead of the viscoelastic behavior of the used adhesives. The sensor does however become susceptible to 'large' transient errors during changes of temperature of the needle.

6 Thin film concept

6.1 Design and manufacturing of a proof-of-concept

A proof-of-concept of the (parallel/series) thin-film concept was made with some modifications to the design proposed in chapter 2.2. The intention was to make the force sensing FPI for the needle tip force sensor by means of deposition of a titanium dioxide, polymer and chromium layer on a ferruled optical fiber. Deposition of titanium dioxide was unfortunately not possible due to equipment failure. Silicon nitride and silicon carbide, both materials with a high refractive index but a low coefficient of extinction, could have been used as replacements for a titanium dioxide FPI reference mirror with a good reflectivity and very small absorbance losses. It was however chosen to use a very thin chromium film as replacement instead, to limit the usage of different deposition equipment. Experiments with a 'large scale' prototype using two gold films, of which the thickness could not be controlled very well, with an UV-curable glue layer sandwiched in between as FPI cavity medium, resulted in a FPI with a far too high finesse that caused issues with the measurement range. The chromium film acting as reference mirror was therefore chosen to have a 2 nm thickness (estimate based on data presented in literature [168]), which is on the thin side, to ensure a very low finesse FPI and prevent issues with absorbance of light. Furthermore, it was already shown for prototypes of the unmachined-quartz-column concept that glueing a needle tip on top of a force sensing FPI does not result in a design sufficiently strong to survive calibration of the sensor. It was therefore chosen to make a proof-of-concept without needle tip, due to limitations in available time, but with a glue layer to protect the force sensing FPI during calibration (figure 6.1).

A cleaved standard single mode optical fiber was glued into a 0.7 mm diameter quartz ferrule with Norland Optical Adhesive 68, an UV-curing adhesive. The cleaved end face of the fiber was chosen to reside slightly into the ferrule to prevent damage to the fiber-top during transport between fabrication steps of the proof-of-concept. A slight protrusion of the fiber out of the ferrule might however improve the sensitivity of the FPI to force. A 2 nm thick chromium layer was deposited on top of the ferrule and optical fiber with electron beam physical vapour deposition (using a Baltzers evaporator at a pressure of 10^{-7} Torr), while the ferrule was mounted on a custom made support as shown in figure D.29 of the appendix). The chromium layer was subsequently coated with an adhesion promotor (VM-652 from HD Microsystems [169], with the ferrule mounted with a custom made support on a spin coater, spinning 10 seconds at 500 rpm and 45 seconds at 3500 rpm) to improve adhesion of the subsequent polymer layer to the

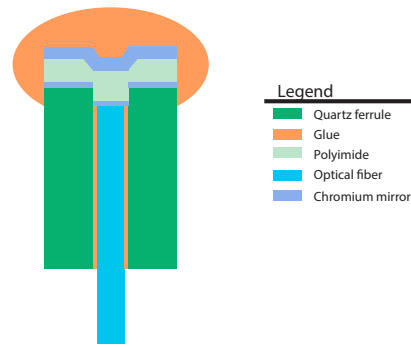


Figure 6.1: Sketch of the proof-of-concept of the thin-film concept.

chromium layer. Polyamic acid (Durimide 115A from Fujifilm [156]) was afterwards deposited by means of a spin coating (15 seconds at 350 rpm, 45 seconds at 1000 rpm and 2 seconds at 3500 rpm). Curing of the polyamic acid, which forms a polyimide coating, was performed in a furnace in a nitrogen atmosphere at 200 mbar. The curing was not performed according to the standard protocol recommended by the supplier at 400°C for half an hour, as the acrylate buffer coating of the used optical fiber will degrade very quickly at this temperature [170]. Curing was therefore performed at 225°C for 2 hours (this temperature should be more than sufficient to start the imidization reaction [156]), including warm-up of the Heraeus VT5042EKP furnace, after which the furnace was allowed to cool down slowly. The spin speed of the polyamic acid coating was such that a polyimide coating of 10 μm thick should form after curing according to the recipe supplied by the manufacturer. The thickness, after curing at a lower than recommended temperature, was estimated to be in the order of 10 μm, based on the part of the fringe pattern that could be observed with the OP1550 used to interrogate the FPI (estimated using a refractive index of polyimide of 1.8, as stated by the supplier [156]). The polyimide was found to adhere well to the aluminum of the custom made support and was therefore expected to be sufficiently cured for its usage as FPI cavity medium. A 100 nm thick chromium film was deposited on top of the polyimide coating by means of electron beam PVD to serve as second FPI mirror and double cavity preventing element. A droplet of superglue was used as protective coating for the chromium layer. The droplet also ensures that forces are transmitted to the polyimide layer directly above the optical fiber, which slightly resides inside the ferrule.

Degradation of the buffer coating of the optical fiber during fabrication of the FPI due to high temperatures would not have been an issue when a parylene instead of polyimide coating was used as FPI cavity medium. This was the intention at first, but was not possible due to limited equipment availability. The higher glass transition temperature of polyimide compared to the glass transition temperature of parylene (371°C versus approximately 50°C) might however be advantageous to reduce the (visco)elastic behavior of the force sensitive element. Degradation of the buffer coating of the optical fiber can for further research be prevented easily by using polyimide buffer coated fibers or using the fibers without buffer coating, which makes the fibers quite a bit more fragile.

The constant measurement error due cross-sensitivity of the FPI to temperature was initially expected to be quite low based on back-of-the-envelope calculations. The thermo-optic coefficient of polymers can be estimated with following equation, that uses the volumetric thermal expansion coefficient of the polymer to predict its thermo-optic coefficient (using values for the parameters presented in the reference) [136]:

$$\frac{dn}{dT} = -\left(\rho \frac{dn}{d\rho}\right)_T \cdot CTE_{VOL} - \left(\frac{dn}{dT}\right)_\rho \quad (6.1)$$

The change in OPD of the FPI as function of force applied on the needle tip was estimated with the equation 6.2, which is only valid for a thin film when the substrate of the thin film has

identical mechanical properties as the polymer of the thin film itself and the stress distribution in the thin film due to the applied force is uniform, and disregards any elasto-optic effects, which are estimated to reduce the sensitivity of the OPD to a change in force with 10 to 20% (see chapter 2.2).

$$\Delta OPD(\Delta F) = \frac{2 \cdot n_{polyimide} \cdot L_{cavity}}{E_{polyimide} \cdot A_{ferrule}} \cdot \Delta F \quad (6.2)$$

The change in OPD due to a change in temperature was estimated with equation 6.3, which is only valid when the thin film is deposited on a substrate with the same thermal and mechanical properties.

$$\Delta OPD(\Delta T) = 2 \cdot \left(\frac{dn}{dT}_{polyimide} + n_{polyimide} \cdot CTE_{polyimide} \right) \cdot L_{cavity} \cdot \Delta T \quad (6.3)$$

The constant measurement error due to a change of temperature of 24°C for a FPI made on a 0.7 mm diameter ferrule with a polyimide layer with a stiffness of 3.3 GPa, CTE of 32 μ strain/K and a layer thickness of 10 μ m is estimated using these equations to be a mere 8 mN (expected to be marginally worse when the elasto-optic effect would have been taken into account). The low cross-sensitivity to temperature of the thin-film concept, predicted using back-of-the-envelope calculations, is the result of the influence of the CTE and the thermo-optic coefficient of polyimide on the change in OPD of the FPI due to a change in temperature that cancel each other nearly out. This is however not the case when the polyimide film is deposited on a substrate with different mechanical and thermal properties than the polymer film.

Modeling the proof-of-concept with a FE-model in COMSOL Multiphysics shows a severe impact of the quartz glass substrate, with a high stiffness and a low CTE, on the cross-sensitivity of the proof-of-concept to temperature. The polyimide film was modeled to be deposited on a quartz ferrule in which an optical fiber is glued with NOA68 adhesive (the fiber was not modeled to reside slightly in the borehole of the ferrule). The change in geometrical FPI cavity length was defined as the change in thickness of the polyimide film along the axis of symmetry of the model. The elasto-optic effect was not taken into account. The change in OPD of the FPI due to a change in temperature was calculated based on the thermal expansion of the thin film along the axis of symmetry of the model and the change in refractive index of the polymer film using equation 6.1, calculated using the average volumetric coefficient of thermal expansion of the thin film along the symmetry axis of the model. The 'force on the needle tip' was modeled as a distributed load over the entire polymer film. The change in FPI cavity length due to a 10 N load is expected to be approximately 52 nm based on the FE-model (about equivalent to a change in length of 100 nm of an air-filled FPI cavity, due to the difference in refractive index). A change in FPI cavity length due to a 10 N force in the order of 79 nm would be anticipated had the thin polymer layer been deposited on a polyimide ferrule with identical mechanical properties as the polyimide film. The apparent stiffness of the FPI cavity medium increases thus significantly due to the stiff glass substrate. The constant measurement error due to a 24°C temperature change is expected to be approximately 2 N based on the FE-model. The 'large' sensitivity to temperature is, according to the FE-model, due to the low expansion coefficient of the quartz/silica substrate that prevents the polyimide layer from expanding in lateral direction. The polyimide expands more in axial direction instead, which is not compensated by extra change in refractive index of the polyimide, as the volumetric expansion of the polyimide layer and therefore the thermo-optic coefficient does not suddenly become larger. The presence of the adhesive used to bond the fiber in the ferrule does barely effect the sensitivity of the FPI to either temperature or force according to the FE-model (for a perfectly glued fiber and a ferrule that does contain no taper where glue accumulates). Furthermore, literature indicates, despite a high glass transition temperature, quite some dependence of the Young's modulus of polyimides on temperature (about 5% change in

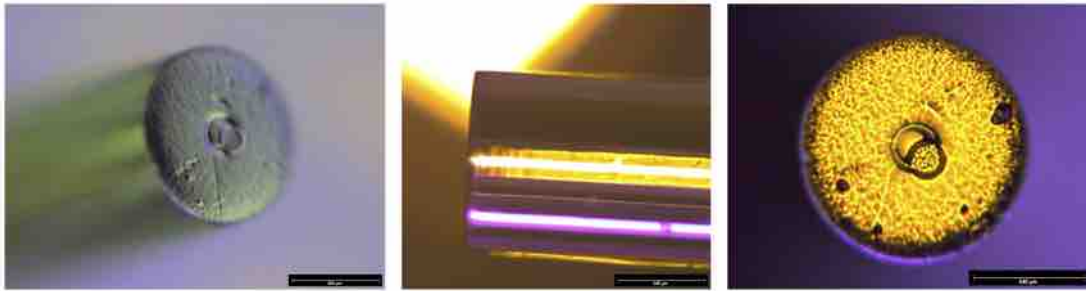


Figure 6.2: Close up images of the proof-of-concept of the thin-film concept, after deposition of the last 100 nm thick chromium layer. A small particle seems to be partially covering the optical fiber located in the center of the ferrule.

modulus for a temperature change from 20°C to 40°C, corresponding to a modifying error due to cross-sensitivity to temperature of about 0.5 N for a force of 10 N on the needle tip) [171].

6.2 Calibration method

The proof-of-concept of the thin-film concept was tested with the method described in section 4.3 and solely interrogated with homodyne interferometry.

6.3 Calibration results

The FPI cavity length of the proof-of-concept was estimated to be slightly less than 10 μm (in the order of 8.5 μm to 9.5 μm). This could not be validated with certainty as (seemingly) slightly less than half a fringe could be observed by tracing the fringe pattern as function of wavelength of the optical source. The reflection of the FPI was less than expected. This could be due to bad transmittance of the polyimide, as no special fluorinated polyimide was used with an especially high optical transparency [172]. 'Normal' polyimide should however be only weakly absorbing in the used wavelength range [173]. The bad transmittance is therefore more likely caused by a dirt particle on the fiber-top, which was observed under a microscope (figure 6.2). The sensitivity of the FPI to force was estimated to be approximately 20% to 40% of the sensitivity predicted based on the FE-model, based on the measured change in light intensity at the photodetector as function of the applied force.

Results of static calibration of the proof-of-concept, using a 3rd order polynomial interpolation function instead of a sinusoidal interpolation function normally used in combination with homodyne interferometry, are shown in figure 6.3 and 6.4. The maximum observed measurement error within the measurement range is about 800 mN. The resolution of the proof-of-concept is quite poor, on average in the order of 40 mN. This is significantly worse than the resolution of the reference sensor used during the calibration procedure. However, the resolution of the reference sensor seems to be slightly worse compared to the resolution of the same sensor during calibration of for example prototypes of the unmachined-quartz-column concept. Hence, there could have been some issues with interference between electronics in the lab. Furthermore, the resolution of the proof-of-concept deteriorates strongly after the first 30 measurements of the static calibration procedure, before which the resolution was at worst approximately 25 mN. The deterioration of the resolution seems to be caused mainly by (increased) drift of the response of the proof-of-concept during the 1 second long measurements of the response of the proof-of-concept to calibration forces. The reason for the increase in drift remains unclear.

Results of dynamic calibration at constant temperature of the proof-of-concept, using a 3rd order polynomial interpolation function, are shown in figure 6.5 and 6.6. The maximum

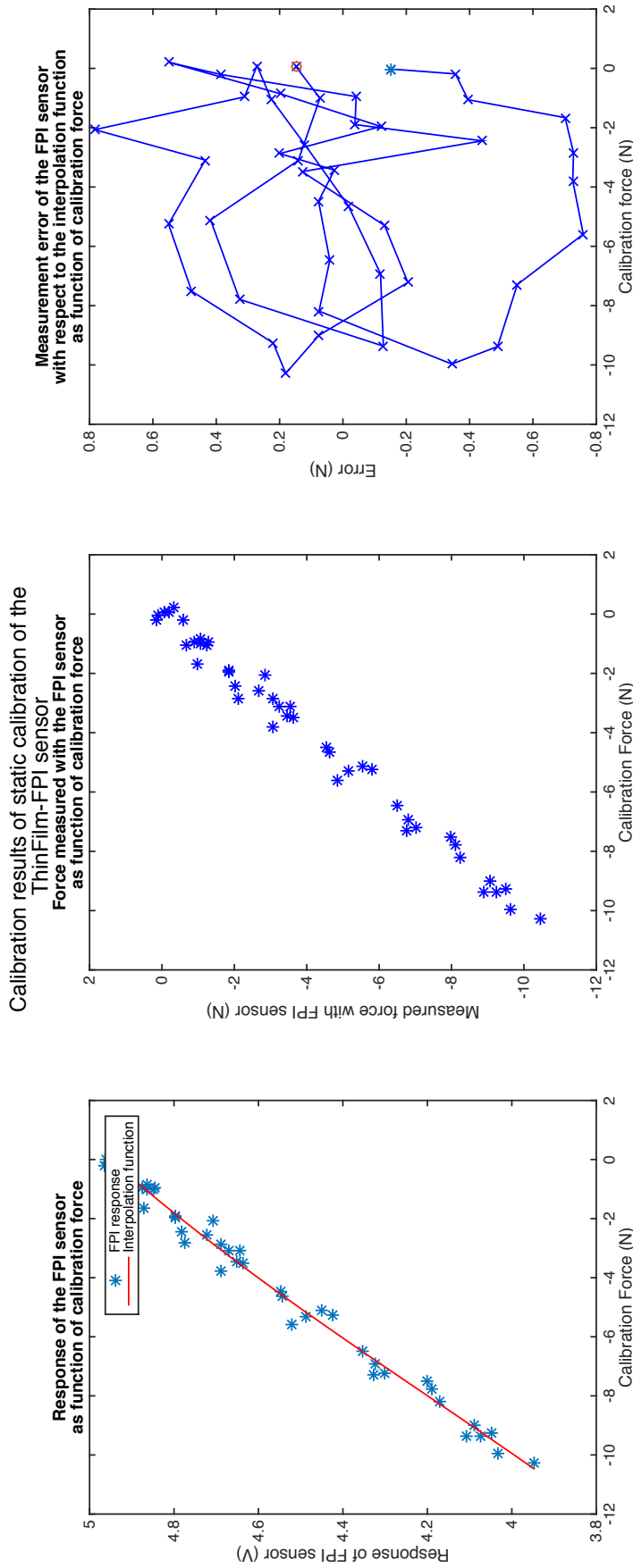


Figure 6.3: Results of static calibration of a proof-of-concept of the thin-film concept interrogated using homodyne interferometry. The response of the FPI as function of the calibration force, together with a fitted 3rd order polynomial interpolation function is shown on the left. The center figure shows the force measured with the FPI, calculated using the interpolation function, as function of the calibration force. The measurement error of the FPI sensor as function of the calibration force is shown on the right. The blue star and the red circle indicate respectively the first and last reading obtained during static calibration.

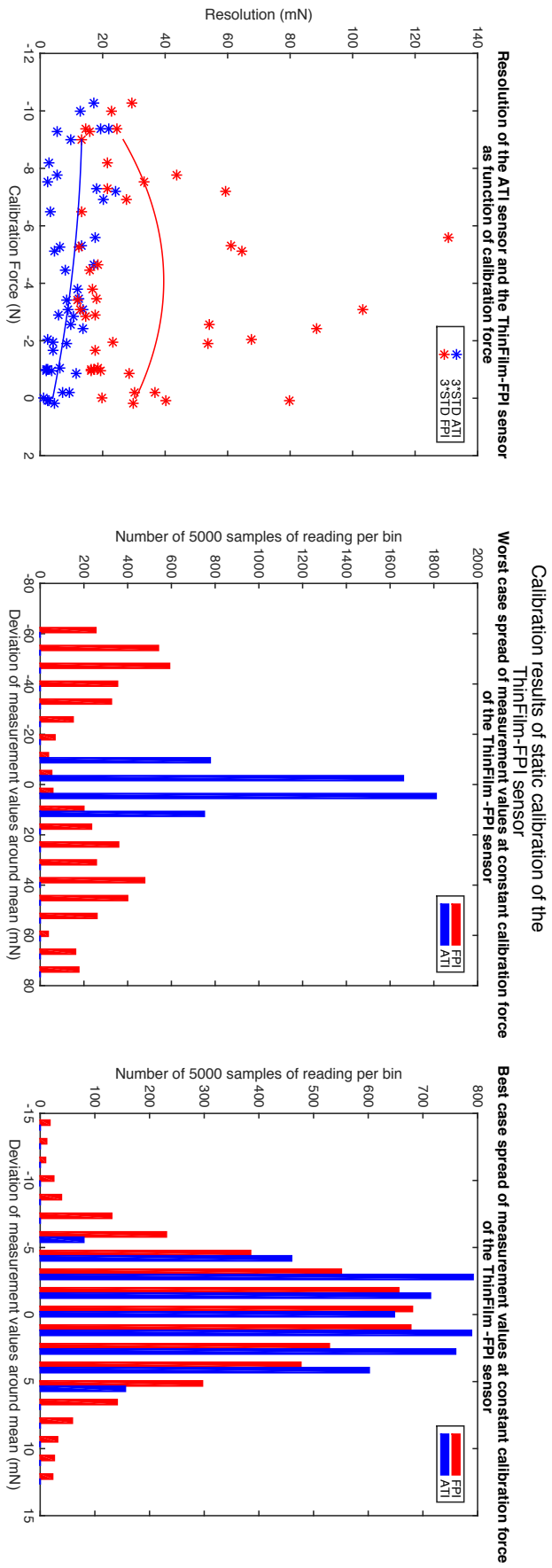


Figure 6.4: Analysis of the resolution of a proof-of-concept of the thin-film concept. The resolution of the FPI-based sensor and the ATI Nano 17 sensor, used as reference sensor, are shown as function of calibration force on the left, together with a second order polynomial fit to the data to illustrate the relation between the resolution and calibration force. The histograms show the largest and smallest observed spread of measurement values around the mean of 1 second long readings (sampled at 5 KHz) of the proof-of-concept obtained during static calibration and the corresponding spread of measurement values of the reference sensor.

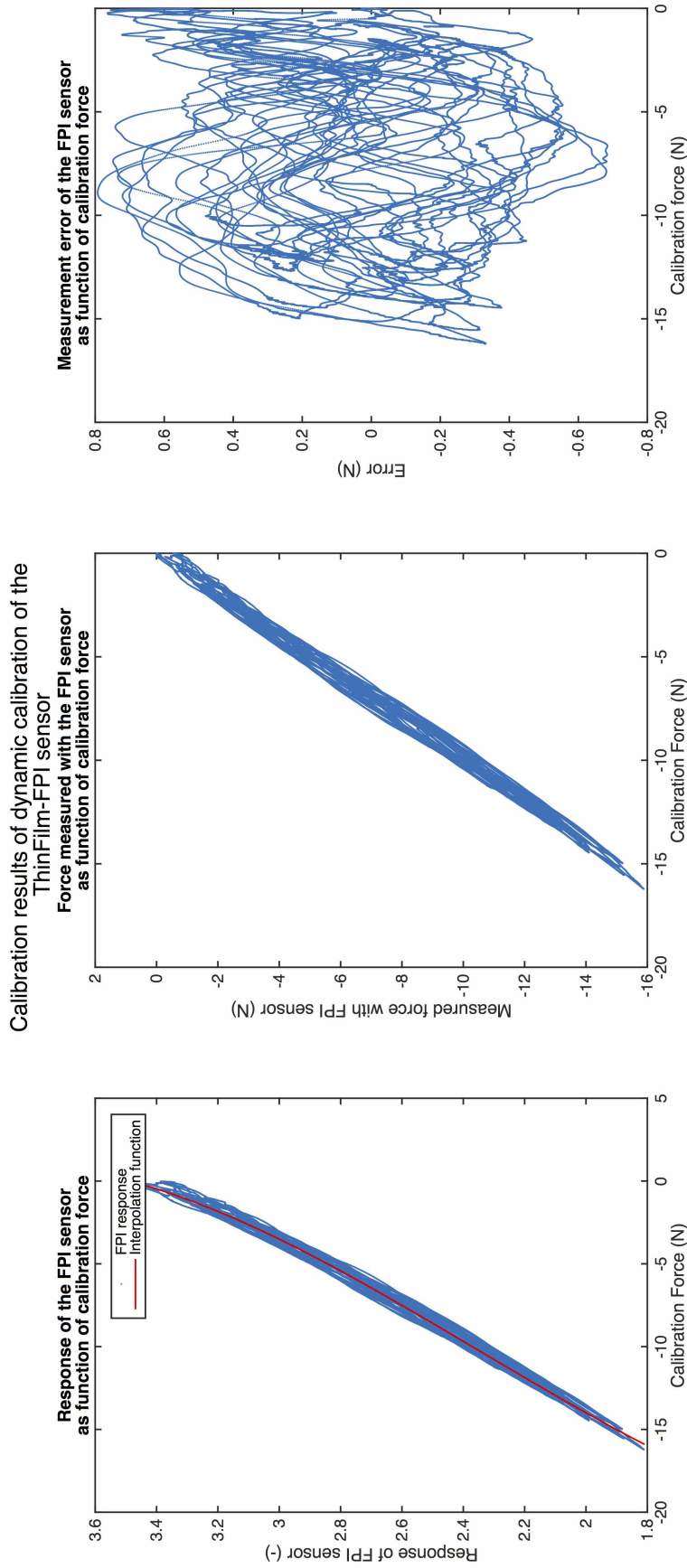


Figure 6.5: Results of dynamic calibration of a proof-of-concept of the thin-film concept at room temperature, interrogated with homodyne interferometry. The response of the FPI as function of the calibration force, together with third order polynomial interpolation function, fitted to the data, is shown in the figure on the left. The figure in the middle shows the force measured with the proof-of-concept, calculated using the interpolation function, as function of the calibration force. The measurement error of the proof-of-concept as function of the calibration force is shown on the right.

Force measured with the ThinFilm-FPI sensor
subjected to dynamic calibration forces as function of time

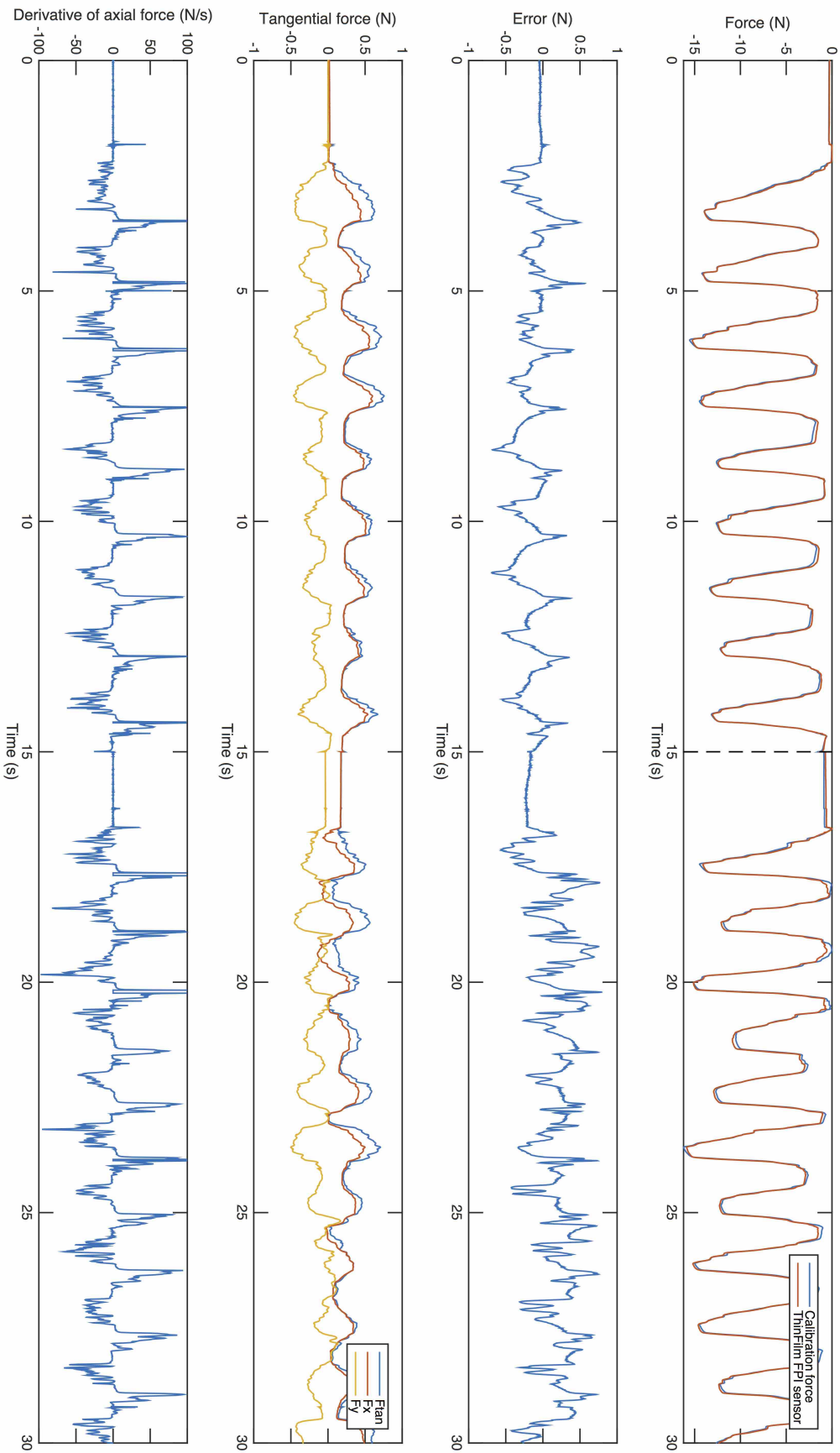


Figure 6.6: Calibration results of dynamic calibration of a proof-of-concept of the thin-film concept at room temperature, interrogated with homodyne interferometry, shown as function of time. The graphs show, from top to bottom: (1) the calibration force and the force measured with the proof-of-concept, calculated using the interpolation function shown in figure 6.5, (2) the measurement error of the proof-of-concept, (3) the transverse force on the needle tip, shown as the resultant transversal force 'Ftan' and its two orthogonal components 'Fx' and 'Fy', and (4) the derivative of the calibration force to time. The dotted lines in the top graph (1) indicate the 15 second long fragments of which the dataset obtained during dynamic calibration is composed.

observed measurement error within the shown dataset, consisting out of two separate 15 second long measurements, is about 800 mN. The maximum observed error varies however quite significantly between different datasets (with maximum observed measurement errors as low as 500 mN to more than 1.4 N). There is a visible correlation between fast changing calibration forces and the quick changes in measurement error. The effective maximum observed error can be reduced slightly by introducing a phase shift between the readings of the proof-of-concept and the reference force sensor, though a quick change in measurement error correlating with a quick change in calibration force remains. This indicates that the peaks in the measurement error are more likely the result of limitations of the mechanical bandwidth of the sensor than phase delays within the used electronics.

Results of the analysis of the cross-sensitivity of the proof-of-concept to temperature, using linear interpolation functions, is shown in figure 6.7 and figure D.25 of the appendix. The measurement error due to cross-sensitivity to temperature cannot be separated precisely in a constant error and a modifying error, as the sensor was preloaded with the weight of the calibration setup for a calibration force of zero Newtons. Moreover, the sinusoidal response of the sensor, due to usage of homodyne interferometry, prevents simple and accurate estimation of the constant and modifying error due to cross-sensitivity to temperature. The measurement error due to cross-sensitivity to temperature is for a temperature change from about 23°C to 39°C estimated to be on average about 3.5 N when linear interpolation functions are used to describe the response of the FPI. The measurement error seems to vary throughout the measurement range with about 1 N, possibly due to a modifying error but certainly also partially due to the sinusoidal response of the FPI. The change in stiffness of the force sensitive element of the FPI due to a change in temperature, causing the modifying error, could not be estimated with certainty by comparing the periods of fitted sinusoidal interpolation functions for the response of the FPI as function of the calibration force. The 'intensity offset' of the fringe pattern differed significantly between the two interpolation functions for the response of the FPI at room and body temperature, which is highly improbable. This indicates that the difference in period of the interpolation functions can neither be estimated accurately.

6.4 Discussion

The low reflectance of the FPI in combination with the quite low sensitivity of the FPI to force and temperature results in a quite poor resolution of the proof-of-concept. There was unfortunately no time to fabricate more than one proof-of-concept, to determine whether the bad reflectance is caused by dirt on optical fibers before thin film deposition was performed. It seems however recommended that a polymer FPI cavity medium with a confirmed very good transmittance for near infrared is used, for example by using fluorinated polyimide instead of 'normal' polyimide [172]. It is furthermore recommended to increase the thickness of the polymer layer to increase the sensitivity of the FPI to force (and temperature). The thickness of the polymer layer seems to be close to the expected thickness of the polyimide layer based on documentation of the manufacturer and the used spin speed, despite the fact that curing was not performed according to the 'normal' recipe [156]. Some research will however be required, in case the same polymer is used for further prototypes, to determine the required spin speed and curing process parameters to achieve a controlled thicker polyimide layer. Using an 'uncontrolled' very thick layer remains an option when 'low coherence interferometry' is used to interrogate the FPI.

The maximum observed measurement error during static and dynamic calibration is quite large. This is not unexpected, as no needle tip was used. Exertion of a certain calibration force on the proof-of-concept is therefore not expected to result in an approximately uniform and repeatable strain of the polyimide film. The strain in the polyimide film will depend strongly on the way the proof-of-concept touches the surface of the water bath of the calibration device and

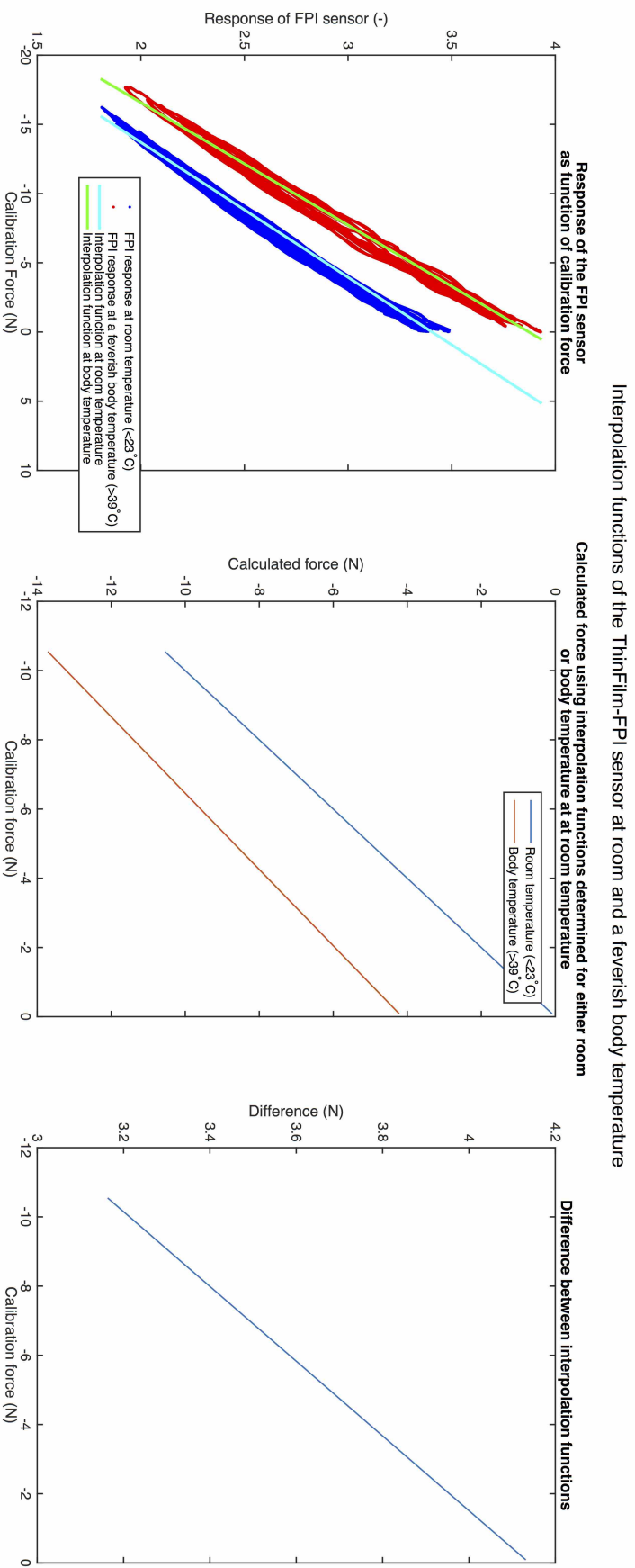


Figure 6.7: Analysis of the cross-sensitivity to temperature of the proof-of-concept of the thin-film concept interrogated with homodyne interferometry, based on results of dynamic calibration at room temperature (23°C) and a feverish body temperature (39°C) using linear interpolation functions to describe the response of the proof-of-concept as function of the calibration force. The graph on the right shows the response of the proof-of-concept as function of calibration force at room temperature and at body temperature and the corresponding interpolation functions fitted to the data. The graph in the middle shows the force that would be 'measured' at room temperature based on the response of the FPI, calculated using either the interpolation function for the response of the FPI at room temperature or the interpolation function for the response based at body temperature, shown as function of the calibration force. The calibration force is equal to the force that would be measured using the interpolation function for the response of the FPI at room temperature, assuming the interpolation function perfectly describes the response of the FPI. The graph on the right shows the difference between the 'measured' force calculated using the interpolation for the response of the FPI at room temperature and response of the FPI at body temperature, as function of the calibration force. The difference is equal to the measurement error due to cross-sensitivity to temperature.

the plastic deformation of the glue droplet used as protection for the chromium coating (which was found to deform significantly during the calibration procedures). These effects are likely the cause of large repeatability errors of the proof-of-concept. It is expected that most of these measurement errors can be reduced by integrating the thin film based FPI in a needle with a needle tip, such that compression of the polymer thin film as function of calibration forces on the needle tip becomes repeatable. The sensor is expected to be rather insensitive to transverse force in its current form, as it should only result in shear of the polymer layer. Integration of the FPI into a needle will however introduce cross-sensitivity to transverse forces, hence a triaxial configuration of the concept might be preferred to correct for cross-sensitivity to transverse forces on the needle tip.

The constant error due to cross-sensitivity to temperature of the prototype is, based on the average observed error in the measurement range due to a 16°C temperature change, estimated to be about a factor 2.5 higher than expected based on the FE-model. The 'cross-sensitivity' to temperature is approximately 0.22 N/°C. The higher constant error due to cross-sensitivity to temperature can partially be explained by the incorporation of the modifying error in the estimate, as the prototype was preloaded with the weight of the calibration setup for a calibration force of zero Newtons. Another, likely more important factor, is that the sensitivity of the FPI to force is significantly lower than expected, which results in a higher cross-sensitivity to temperature when the sensitivity of the FPI to temperature remains the same. The lower sensitivity to force than predicted with the FE-model could be caused partially by the fact that the optical fiber and the polyimide film on top of the fiber are retracted slightly into the borehole of the ferrule, which was not modeled in the FE-model. Compression of the polymer film above the optical fiber could therefore be slightly less in practice, due to the stiffness of the quartz glass surrounding the polymer film. A more important factor affecting the sensitivity of the FPI to force, according to FE-simulations, is the protective droplet of glue covering the proof-of-concept (figure 6.1). The droplet increases the cross-sectional area at the location of the FPI and transfers part of the forces on the droplet directly to the quartz ferrule instead of the polymer film. Both effects reduce the sensitivity of the FPI to force, while the sensitivity to temperature likely remains approximately the same. It can in every case be concluded that a FPI made out of a polymer thin film, deposited on a silica fiber, works also well as temperature sensor besides that it can be used as force sensor with a reasonably high cross-sensitivity to temperature. An FPI made with a thin polymer film could thus serve as temperature sensing FPI in other proposed concepts, to correct for cross-sensitivity to temperature. The presence of a modifying error due to cross-sensitivity to temperature cannot be confirmed with high certainty based on the fitted interpolation functions to the response of the FPI at room and body temperature. The presence of a modifying error seems however likely, given the reports of the significant dependence of the Young's modulus of polyimide on temperature [171].

Calculations show that a large constant error due to cross-sensitivity to temperature could be avoided by depositing the thin slightly film of the FPI cavity medium on a substrate with identical thermal and mechanical properties. This might be interesting for further research to minimize the constant error due to cross-sensitivity to temperature of the force sensing FPI in the needle. This is possible by depositing the film on a polymer optical fiber instead of a silica optical fiber/quartz ferrule. Plastic optical fibers can be made of PMMA (although higher performance fibers are nowadays made out of other types of polymers), while PMMA is also frequently used as photoresist in lithography processes and can be deposited as thin film [174, 175]. Manufacturing an entire stylet with a cross-section of 1 mm out of PMMA, including the polymer FPI cavity medium, (assumed modulus of 3 GPa and a CTE of 75 $\mu\text{strain/K}$ [176]), would in theory result in a constant measurement error of about 210 mN due to a 24°C temperature change (taking into account the elasto-optic effect as shown in section 3.2.8). This would be lower than the constant

error due to cross-sensitivity to temperature of the prototype of the unmachined-quartz-column concept using highly dimensionally stable quartz glass as force sensitive element for the force sensor. A polymer based force sensitive element is however more prone to have a dependence of the compliance on temperature, compared to a force sensitive element made out of quartz glass, which might introduce modifying errors due to changes in temperature. Incorporation of an additional temperature sensing FPI inside the needle tip might therefore still be required when no appropriate polymer for the thin film can be found with a reasonably constant elastic modulus within the range of temperatures that the sensor will be used (see also section 3.2.6).

The polyimide layer, used as force sensitive element, could be causing some viscoelastic behavior of the force sensitive element given the correlation between peaks in the measurement error and the sudden large changes of calibration forces during dynamic calibration. This could indicate that polymers, despite having a high glass transition temperature, are not particularly suited for a force sensitive element of a force sensor with an intrinsic large apparent 'mechanical bandwidth'. The viscoelastic behavior could however also be caused by incomplete curing of the polyimide, which was performed at a much lower temperature than recommended and not compensated by extremely long curing. Usage of polymers with a high glass transition temperature remains therefore recommended to construct a FPI cavity medium with as less as possible viscous behavior. Another explanation of the viscous behavior of the force sensitive element, is viscoelastic behavior of the protective glue layer covering the FPI. Viscoelastic behavior of the protective glue layer can affect the deformation of the thin polymer film used as FPI cavity medium and force sensitive element, while it does not affect transmittance of forces to the reference sensor. Correction for the non-flat frequency response of the sensor due to viscoelastic behavior of the polyimide film could in theory be performed by using a filter based on the inverse of a measured frequency response of the sensor, as long as the response of the sensor is linear and time invariant. This could however be rather complex, as the viscoelastic behavior of polyimide will depend likely on the temperature.

Recommendations for improvements of the thin-film concept are deposition of the thin film based FPIs on plastic optical fibers instead of silica optical fibers to minimize cross-sensitivity to temperature. Sufficiently thick polymer layers, with a good transparency for NIR, should be used to maximize the sensitivity of the FPI to force and thereby improve the resolution. Usage of a triaxial instead of uniaxial force sensor design, by incorporating two additional force sensing FPIs, is strongly recommended to achieve a good measurement accuracy in practical conditions, based on experience with prototypes of other concepts. An uniaxial design could be however be sufficient for some applications related to haptic feedback. Moulding a polymer needle tip on top of the stylet tube seems the most effective method to connect a needle tip to the needle, while ensuring a good sensitivity of the FPI to force. Usage of a sharp metal, wear resistant tip is only possible when the tip is connected to the needle shaft by a polymer connection that contains the force sensor to ensure sufficient sensitivity of the FPI to force on the needle tip. Moulding a ferrule inside an entirely polymer needle seems however not recommended, based on FE-simulations (not shown in this thesis). The polymer surrounding the ferrule will not sufficiently relieve the ferrule of bending stresses due to transverse forces on the tip. This will result of fracture of the ferrule and optical fiber inside the polymer needle. Hence, plastic optical fibers, or non-ferruled pristine silica fibers are recommended for construction of a flexible, entire plastic needle containing an FPI based on the thin film concept to sense forces on the tip of the needle.

7 Discussion

An exploratory study of different concepts for a small fiber-optic force sensor based on Fabry-Pérot interferometry to measure forces in axial direction on the tip of a needle was made during this thesis project. The goal was to design a sensor or measurement system with a low cross-sensitivity to temperature of the needle tip, as sensors currently presented for this application, based on FBGs, suffer from an extremely large cross-sensitivity to temperature (approx. $1 \text{ N}/^\circ\text{C}$) [1, 2]. The needle with sensor was furthermore preferred to be easily manufacturable, MRI compatible and contain a uniaxial force sensor (specifically for this project due to limitations in equipment). Three different concepts for a force sensor in the needle tip with distinctly different advantages were investigated in more detail. The first concept was for a sensor with an intrinsic low cross-sensitivity to temperature, a second concept focussed on a needle tip with a good mechanical strength and the third concept focussed on a force sensor that is simple to manufacture with high reproducibility. Simulations and experiments with prototypes gave some general insights in the difficulties of the design of such a sensor and the limitations of the available equipment.

7.1 General insights

FPIs with an air cavity are presented in literature to have a much lower cross-sensitivity to temperature compared to FBGs (for example [111, 112]). The stated lower cross-sensitivity to temperature is however solely based on comparing the FPI-based and FBG-based strain gages as strain gage themselves, without attachment of the strain gage to a mechanical structure of which strain should be measured, like a medical device. This makes FPIs appear to have a very low cross-sensitivity to temperature, but this can in practice only be harnessed when the structure to which the FPI-based strain gage is adhered is dimensionally stable, which is almost never the case.

The initial restriction that homodyne interferometry had to be used to interrogate the force sensing FPI in the needle tip, instead of low coherence interferometry or a variant that can measure changes in OPD over an extremely large range, severely complicated the design of a sensor with an intrinsic low cross-sensitivity to temperature. The sensitivity of the FPI to force has to be quite low to ensure that the required range of forces can be measured with homodyne interferometry. The sensitivity of the FPI to temperature should therefore be extremely low to ensure a sufficiently low cross-sensitivity to temperature. Extreme design and material choices

were therefore necessary for the design of an FPI force sensor with an intrinsic very low cross-sensitivity to temperature using silica optical fibers. 'Unattractive' construction materials, like fragile quartz glass, were found to be required to minimize the difference in CTE of materials in the needle tip and force sensor and thereby prevent a large cross-sensitivity to temperature. Usage of low coherence interferometry enables usage of less 'unattractive' construction materials. A higher sensitivity of the FPI to temperature can in such case be compensated with a very high sensitivity to force, such that the cross-sensitivity to temperature (in °C/N) remains acceptable (e.g. such that the suggested improvement of the stylet-tube concept shown in figure 5.11, inspired on the machined-quartz-column concept, becomes an option). Usage of homodyne interferometry is even problematic for designs that use a temperature sensing FPI to correct for cross-sensitivity to temperature of the force sensing FPI in the needle tip. The sensitivity of the force sensing FPI to temperature quickly results in changes in OPD due to temperature changes that exceed the measurable range or severely limit the range of the change in OPD of the FPI that can be used to measure force on the needle tip. Compensation for cross-sensitivity to temperature becomes furthermore somewhat complicated due to the sinusoidal response of the low-finesse FPIs interrogated with homodyne interferometry. Hence, usage of low coherence interferometry or a variant of interferometry capable to measure extremely large changes in OPD is for multiple reasons more convenient.

A weak link with respect to the measurement uncertainty is in most concepts the method to bond components of the force sensor in the needle tip together. Most components had to be bonded together with adhesives. This resulted in general in issues with viscoelastic instead of elastic behavior of the force sensitive element of the force sensor, due to viscoelastic behavior of the used adhesives, and dependence of behavior of the force sensitive element on temperature, due to dependence of properties of the used adhesives on temperature. The required usage of adhesives prevents construction of force sensitive elements entirely made out of a ceramic or metal. Issues with dependence of compliance on temperature and viscoelastic behavior of the force sensitive element was also found to be an issue for 'adhesive-less designs' when the force sensitive is made of a polymer material deposited on top of an optical fiber. Usage of a polymer FPI cavity medium as force sensitive element, with a polymer with a high glass transition temperature, could nonetheless still be possible to avoid usage of viscoelastic adhesives for a force sensitive element with a high 'mechanical bandwidth', as the viscous behavior of the proof-of-concept of the thin film concept could not be proven to be caused by the polyimide FPI cavity medium. Usage of a polymer force sensitive element instead of a ceramic or metal force sensitive element kept together with adhesives seems however a bit like fighting fire with fire. It was concluded that designs should be such that the sensitivity of the force sensor is affected as less as possible by the presence of glue or polymers to achieve as less as possible viscoelastic behavior and an as small modifying error due to changing temperatures. Compensation for viscoelastic behavior of the force sensitive element should however in theory be possible by using a filter based on the inverse of the measured frequency response of the force sensor, as long as the response of the force sensor is linear and time invariant.

Usage of an uniaxial force sensor in the needle severely limits the accuracy with which axial forces on the needle tip can be measured under practical circumstances where varying transverse forces on the needle tip occur. It is in all concepts practically impossible to achieve zero or extremely low cross-sensitivity to transverse force. The sensitivity to transverse force was reasonably low in the prototype of the unmachined-quartz-column concept, but measurement errors due to transverse forces are still expected to exceed requirements on measurement uncertainty under practical conditions. Some cross-sensitivity to transverse force can be acceptable when the force sensor is used for haptic feedback purposes, as transverse forces also indicate occurrence of interesting 'events' [29]. Usage of an uniaxial force sensor is in such a case cheaper, although

the increase in cost of a triaxial design will be minimal when low coherence interferometry is used in both cases to interrogate the FPI(s).

7.2 Achievements

Calibration of the force sensor of prototype of the unmachined-quartz-column concept, of which the part of the needle tip containing the force sensor is entirely manufactured out of quartz glass, showed significant improvement in measurement uncertainty of static axial forces, without presence of disturbances, compared to a prototype of an FBG-based needle designed earlier at the TU Delft [1]. The maximum observed measurement error in the measurement range is reduced with about an order of magnitude to approximately 65 mN, which more than meets the requirements on the measurement uncertainty. It even approaches the accuracy of the ATI Nano 17, the reference sensor used during calibration, of which the accuracy served as goal. Comparing the measurement accuracy of the prototype with another FBG-based needle tip force sensor, designed by Elayaperumal et al., is unfortunately not possible, as that design uses a triaxial force sensor of which the measurement accuracy is reported in a form that makes fair comparison difficult [2]. The resolution of the sensor, interrogated with the used equipment, was found to be approximately equal to the goal on the resolution, the resolution of the ATI Nano 17 sensor. The maximum observed measurement error of the prototype was under practical conditions however significantly worse, mainly due to sensitivity to transverse forces on the needle tip, supposed viscoelastic behavior of the used adhesives, for which no compensation was performed, and a small cross-sensitivity to temperature. The intrinsic low cross-sensitivity of the prototype to temperature was with about 12 mN/°C nearly two orders of magnitude better than FBG-based needle tip force sensors shown in literature [2]. The exceptional low cross-sensitivity of the prototype comes at the cost of a quite fragile needle tip. More reliable strength tests are required to determine the safety margin of the design. Ex-vivo needle insertion experiments will be required to determine whether the estimate on the maximum transverse force on the needle tip, used for the requirements on the design, were a reasonable. There is a slight chance, given good surface quality of the used quartz ferrules for the design, that the design could be sufficiently strong for 18 G needles. It seems however, based on calculations and tests, that the concept of the unmachined-quartz-column concept is better suited for (slightly) larger than 18 G diameter needles. The design seems furthermore best suited for haptic feedback purposes where a bit cross-sensitivity to transverse force is tolerated. Only small improvements of the design could be proposed to improve the measurement accuracy of the design, like the usage of better glue to bond optical fibers in the quartz ferrule or fusing the fibers into the ferrule and optionally usage of an Invar instead of RVS capillary as stylet tube. The concept is not particularly suited to be adapted to a triaxial instead of uniaxial force sensor. The adaptation to a triaxial design would furthermore require more complex interrogation equipment for the three FPIs in the needle tip (e.g. low coherence interferometry). This will make addition of a temperature sensing FPI to compensate for some cross-sensitivity to temperature only slightly more complicated. Usage of FPIs with an intrinsic very low cross-sensitivity to temperature, which requires usage of fragile quartz glass, would in such a case be unnecessary.

Finite element simulations and tests of prototypes of the stylet-tube concept, where the FPI-based force sensor is made from an Invar stylet and needle tip and a ferruled optical fiber, showed promising results although prototypes of the stylet-tube concept did not achieve a particularly low measurement uncertainty. The measurement accuracy is supposed to be not particularly good due to a poor choice of used adhesives and a very large cross-sensitivity to transverse forces on the needle tip, of which the latter is unavoidable with an uniaxial force sensor design. The maximum observed measurement error in the measurement range of the prototype for semi-static axial forces at constant temperature, after correction for varying transverse forces on the needle tip

during the calibration procedure, is about 350 mN. This maximum observed measurement error is in the same order of magnitude as the performance of the uniaxial FBG-based needle tip force sensor previously designed at the TU Delft [1]. The response of the prototype to temperature was however, likely due to the used adhesives, very time dependent and resulted in large measurement errors. Problems caused by viscoelastic and temperature dependent behavior of the epoxy used to bond components in the force sensor should be (at least partially) solvable by selecting an adhesive with better thermal and mechanical properties for bonding the various components of the design. Increasing the sensitivity of the sensor by increasing the length of the Invar 'column' of the force sensitive element with a method as shown in figure 5.1 should reduce the influence of the properties of the used adhesives on the measurement uncertainty. The cross-sensitivity of the prototype of the stylet tube concept to transverse forces was found to be such that altering the design to a triaxial force sensor, with three FPIs inside the needle tip, is strongly recommended to reduce measurement errors. FE-simulation results indicate that the concept can be suited to create a force sensor with a relatively low cross-sensitivity to temperature. A cross-sensitivity to temperature of approximately 50 mN/N should be achievable for a force sensor manufactured according to the stylet tube concept using an Invar stylet tube and appropriate adhesives, while maintaining the geometry of the prototype. This seemed to be corroborated by tests with the prototype, but could not be confirmed with certainty. This cross-sensitivity to temperature is quite acceptable, although its more than a factor four larger than the cross-sensitivity to temperature of the prototype of the unmachined-quartz-column concept. Measurement errors due to the large disturbance in temperature during penetration of the skin should be sufficiently reducible by using proposed filtering methods using a time-dependent model or using the sensor calibrated at body temperature and accepting a measurement error during puncture of the skin. A very low cross-sensitivity to temperature, required when the needle is used for research on needle insertion forces, can still be achieved by integrating an additional temperature sensing FPI based on the thin-film concept. This combination was not tested, but a separate proof-of-concept (the thin-film concept) was shown to work as temperature sensor. Manufacturing of a prototype of the concept proved, unexpectedly, that the design of the stylet tube concept is, besides strong, quite easily manufacturable. A disadvantage of the stylet-tube concept is the usage of ferromagnetic Invar, which is not beneficial for MRI-safety and MRI-compatibility. Invar could be replaced with a more MRI-safe metal for applications of the sensor during MRI-guided needle insertion. This will however almost certainly introduce a very large cross-sensitivity to temperature requiring compensation with an additional temperature sensitive FPI. Excellent MRI compatibility will however never be obtained with the stylet tube concept, as the usage of metal will always cause imaging artifacts.

Brief investigation of the thin-film concept, where the FPI of the force sensor is made by deposition of reflecting films with an elastic polymer film in between on an optical fiber, and testing of a proof-of-concept showed promising results. Fabrication of the FPI by means of thin film deposition proved to be quite convenient. The controllability of the sensitivity of the sensor during manufacturing makes the thin-film concept better suited for usage in combination with homodyne interferometry compared to the other two concepts and in particular the stylet-tube concept. Usage of low coherence interferometry remains nonetheless more convenient, particularly because a triaxial variant of the design or a temperature sensor can in such a case be interrogated with a single device. Moulding or glueing a polymer needle tip on the stylet tube, which were the only identified options to attach a needle tip to the force sensor without affecting the sensitivity of the sensor significantly, might however prove a bit more challenging and was not tested. Testing the proof-of-concept without a needle tip made assessment of the actual achievable measurement uncertainty difficult. Usage of a thin polyimide film as force sensitive element and FPI cavity medium did result in an anticipated significant cross-sensitivity

to temperature when the polymer is deposited on a glass substrate and seems also to result in a modifying error due to temperature and possibly some viscoelastic effects limiting the apparent 'bandwidth' of the sensor. Measurement errors due to first two issues can be reduced by integrating a temperature sensing FPI, based on the same thin-film fabrication principle, in the needle. Measurement errors due to the latter issue could possibly be solved by using a frequency based filter, based on the measured frequency response of the sensor, at the cost of a reduction in the signal-noise-ratio. Calculations showed furthermore that deposition of the FPI on plastic optical fibers and using a polymer FPI cavity medium with the same properties as the plastic fiber might result in a force sensor that suffers from very small constant errors due to cross-sensitivity to temperature, comparable or even smaller than constant errors due to cross-sensitivity to temperature of the unmachined-quartz-column concept. A (small) modifying error due to cross-sensitivity to temperature resulting from the dependency of the Young's modulus of the polymer on temperature will in most cases remain present though, depending on the used polymer. A sufficiently low cross-sensitivity to temperature, such that no compensation is required, could be achievable for needles containing a force sensor manufactured according to this variant of the thin-film concept, but will have to be verified with a prototype. A triaxial force sensor design is also strongly preferred for needles with a sensor according to the thin film concept. The thin-film concept is the only concept suited to create a completely polymer MRI-compatible needle (using silica but preferably plastic optical fibers), without usage of any metal components.

7.3 Conclusions

The exploratory study showed that there are opportunities to design a force sensor based on Fabry-Pérot interferometry for the measurement of forces on the tip of a needle with a relatively low cross-sensitivity to temperature. The reduction in costs and complexity of the design of the needle tip and force sensor by not requiring to include a temperature sensor to compensate for cross-sensitivity to temperature remains however debatable given the requirements on materials used for a sensor with an intrinsic very low cross-sensitivity to temperature. The unmachined-quartz-column concept seems, based on the observed measurement errors of the tested prototypes, the best concept for a needle tip force sensor. The design will suffer the least from presence of adhesives or polymers that introduce measurement errors in the form of additional temperature dependence by means of modifying errors or viscoelastic behavior. Placing measurement uncertainty over safety is however not tolerated for medical devices. The unavoidable cross-sensitivity to transverse forces, the expected difficulty to adapt the design to a triaxial force sensor, the difficulties with assembly and the fragility of the needle tip are therefore reasons to recommend the unmachined-quartz-column concept to be avoided, except for applications of haptic feedback using large diameter needles where a cheap homodyne interrogation method in combination with an uniaxial force sensor is preferred. A triaxial force sensor variant of the stylet tube concept, optionally including a temperature sensor, seems recommended for applications requiring no MRI-compatibility, as it will be by far the strongest and thus safest design. However, usage of an electronic force sensor instead of an optical force sensor could in such a case, although they have not been shown yet, prove an equally effective solution. The thin-film concept, using plastic optical fibers and a triaxial force sensor configuration, has however much potential as very small, completely MRI compatible sensor and is therefore regarded as the most interesting concept for further research. The possible low cross-sensitivity to temperature of the concept using plastic instead of silica optical fibers might be of interest for further research. Moreover, the force sensor might be interesting for various other types of medical minimal invasive devices, as the sensitivity of the force sensor can be quite easily adapted to a specific application by altering the thickness of the polymer film serving as FPI cavity medium and force

sensitive element while the sensitive part of the sensor remains exceptionally small and can be located on the tip of the instrument.

7.4 Recommendations for further research

The calibration setup used for this thesis project was sufficient to get an idea of the performance of prototypes. It is for further research however recommended to improve the calibration setup, such that controlled axial as well as transverse forces can be exerted on the needle tip and sensitivity to transverse forces can be better quantified. It would however also be possible to remove the frame of the calibration setup and test the sensitivity of the force sensor to axial as well as transversal forces by exerting forces under various angles on the needle tip, while the prototype is mounted on the ATI Nano 17 sensor used as reference sensor. The sensitivity and measurement error can then be determined by fitting a model to readings of the transversal and axial force according to the reference sensor and readings of the FPIs in the prototype of the needle. An additional calibration setup or method to test the frequency response of the sensors is required to be able to assess whether requirements on the bandwidth of the sensor can be met or to be able to compensate for a non flat frequency response of the sensor. Moreover, usage of a larger water bath in combination with a thermostat would be convenient to investigate the cross-sensitivity of sensors to temperature.

It is recommended to continue with either investigation of the stylet-tube concept or a thin-film concept, based on results of simulations and results of experiments. These concepts are regarded to (be far more likely to) result in a design that is sufficiently strong and therefore safe for real usage and should, with some modifications to details of the design, be able to achieve a sufficiently low measurement uncertainty and low cross-sensitivity to temperature. There could however be cases where the unmachined-quartz-column concept remains attractive. It is for these cases recommended to first investigate in more detail the maximum transverse forces that can occur on the tip of the used needles and thereafter extensively test the strength of the quartz ferrules used for the concept, before improving further on the design. One of the subsequent required steps is looking into methods to attach a short needle tip to the ferrule, likely by looking into methods to fabricate a sufficiently short needle tip with a borehole such that it can be placed as a cap over the quartz ferrule before it is attached with glue.

Adapting the uniaxial design of all proposed concepts to a triaxial design is strongly recommended, as already stated. It should however be researched, particularly for the stylet tube concept, whether integration of three FPIs that all use the same FPI cavity (as shown in figure 5.11) does cause interference of FPIs between each other. Occurring interference can be minimized by reducing the FPI cavity length, but this is only possible within margins.

Biocompatibility (and safety) was not of particular concern during the design of the first prototypes of the needle tip force sensors. In particular adhesives will have to be changed to biocompatible variants. This is nonetheless very important, even when the used adhesives are not expected to come into contact with patient tissue or detach from the needle (as demonstrated by recent news reports, stating that a large batch of vaccination needles has to be recalled due to issues with used adhesives [177]). Furthermore, it could not be confirmed whether Invar alloy is regarded as safe for invasive usage. Only vague mentions of usage of Invar or variants of Invar in medical devices or for medical applications could be found [178, 179]. It is therefore required to confirm first whether Invar is suited for invasive medical devices, before considering whether continuing with the stylet-tube concept is worthwhile. It could furthermore be worthwhile to investigate the MRI compatibility of an Invar needle, although it is unlikely that this will be the case, given that it is a ferromagnetic material.

Testing of adhesives by means of DMA (dynamic mechanical analysis) or TMA (thermo mechanical analysis) seems recommended to select a good adhesive for the stylet-tube concept.

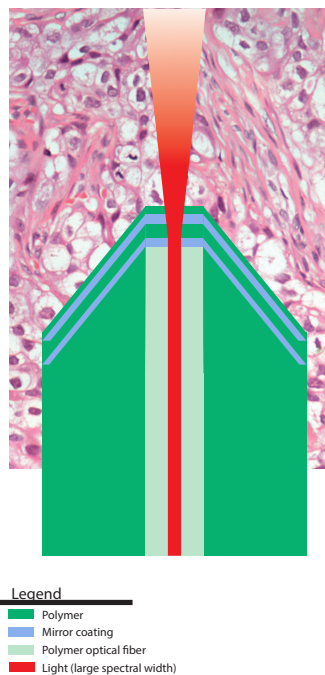


Figure 7.1: Proposal for a polymer needle, containing a polymer optical fiber with a force sensing FPI on top, made by deposition a thin reflective film, a polymer film, a second thin reflective film and a protective polymer film. The force sensing FPI can be used in combination with optical coherence elastography (as described in literature [180]) to measure tissue stiffness during needle insertion. Optical coherence elastography can be regarded as measuring the change in OPD of many FPIs in series, multiplexed on the same fiber, of which the FPI mirrors are made out of 'reflecting' membranes and tissue layers. The change in OPD of the FPIs due to a force applied with the needle tip indicates the stiffness of tissue between the 'FPI mirrors'.

Selection of an adhesive with an as high as possible elastic modulus, a moderate CTE, an as high as possible glass transition temperature and a high viscosity in its uncured state seems in every case recommended. EPOTEK 353ND was found to have sufficient good thermal and mechanical properties for the unmachined-quartz-column concept and is biocompatible. The curing process, during which the epoxy becomes very liquid, might however result in contamination issues during assembly of a sensor according to the stylet tube concept. The properties of the cured EPOTEK 353ND epoxy could however serve as a guideline for selecting an alternative adhesive.

The thin film concept seems an interesting concept to be combined with optical coherence elastography. Optical coherence elastography is a technique shown to be capable to 'measure' the stiffness of tissue a few millimeters in front of a needle tip and thereby detect diseased tissue during needle insertion [180]. Optical coherence elastography is used to quantify the difference in deformation of tissue between two 'images' of the tissue in between which the force causing deformation of the tissue changes (1D images are currently acquired when imaging is performed with a fiber optic system integrated in a needle). The deformation of specific parts of tissue gives information about the stiffness of the tissue (eg. stiff tissue deforms less than soft tissue). Only the stiffness of tissues within a single image can currently be compared with the technique relative to each other. An FPI-based force sensor, based on the thin-film concept, could in such a situation be used as a sensor to measure the force used to deform tissue (figure 7.1). The force measurement at the needle tip could be used to make an estimate of the stress distribution in the tissue that causes the deformation observed with optical coherence elastography, such that a quantitative estimate of the tissue stiffness could be made. Low coherence interferometry, performed with a single low coherent source, could be used to interrogate the force sensing FPI and perform the optical coherence elastography simultaneously.

Acknowledgements

First of all, I would like to thank my supervisor Dr. Dennis van Gerwen for his enthusiasm and advice during my graduation project. Moreover, I would like to thank especially Steven Beekmans for his guidance and support and the VU Amsterdam for allowing me to use their facilities. Thanks go also to Dr. John van den Dobbelsteen, Mario van der Wel from DEMO and the staff of the MISIT lab and DIMES for their help and advice. I am last but not least very grateful for the motivational support and sympathetic ear from family and friends who cheered me up during moments of frustration.

Appendices

A The Fabry-Pérot interferometer

A.1 Operating principle

A (fiber-optic) Fabry-Pérot interferometer (FPI) consists of two parallel partially reflective mirrors with some space in between [90, 181]. The space between both mirrors is called the Fabry-Pérot cavity or sometimes the 'etalon' [90, 110]. Light propagating through an optical fiber towards a Fabry-Pérot cavity will partially reflect on the first mirror of the FPI, while the remainder enters the cavity and will be reflected back-and-forth inside the Fabry-Pérot cavity. A small fraction of the light is transmitted through the mirrors of the Fabry-Pérot interferometer upon each reflection inside the cavity, directed either back towards the optical source or away from the optical source (figure A.1) [182]. The light waves propagating back towards the light source will interfere with each other, while the same occurs with the light waves transmitted out of the cavity in the direction away from the light source (figure A.1) [110, 108]. The light propagating back towards the optical source can be analyzed by directing it towards a detector with a fiber-optic circulator or a fiber-optic coupler.

The OPD between interfering light waves that have propagated 'x' and 'x+1' times through the FPI cavity can be calculated with equation A.1 for a Fabry-Pérot cavity with length L and a medium with refractive index n inside the cavity [90].

$$OPD = 2nL \quad (A.1)$$

This quantity is referred to as the OPD of the FPI in this thesis. The measurand which will be measured with an FPI-based sensor should modulate the OPD of the FPI. The phase difference between light waves that have propagated 'x' and 'x+1' times through the FPI cavity can be calculated with equation A.2 as function of the free-space wavelength λ or wavenumber $\tilde{\nu}$ [90].

$$\phi = \frac{2\pi OPD}{\lambda} = \frac{4\pi Ln}{\lambda} = 4\pi Ln\tilde{\nu} \quad (A.2)$$

The intensity of the light reflected by the FPI, propagating back in the direction of the optical source, depends on the reflectivity of both FPI mirrors ' R_1 ' and ' R_2 ', the intensity of incident light on the FPI ' I_i ' and is a periodic function of the phase difference ϕ that can be described with equation A.3, neglecting losses due to light scattering out of the sensor or attenuation inside the cavity and with a few assumptions about phase shifts occurring at the mirrors (figure A.2) [90].

$$I_r = I_i \frac{R_1 + R_2 + 2\sqrt{R_1 R_2} \cos \phi}{1 + R_1 R_2 + 2\sqrt{R_1 R_2} \cos \phi} \quad (A.3)$$

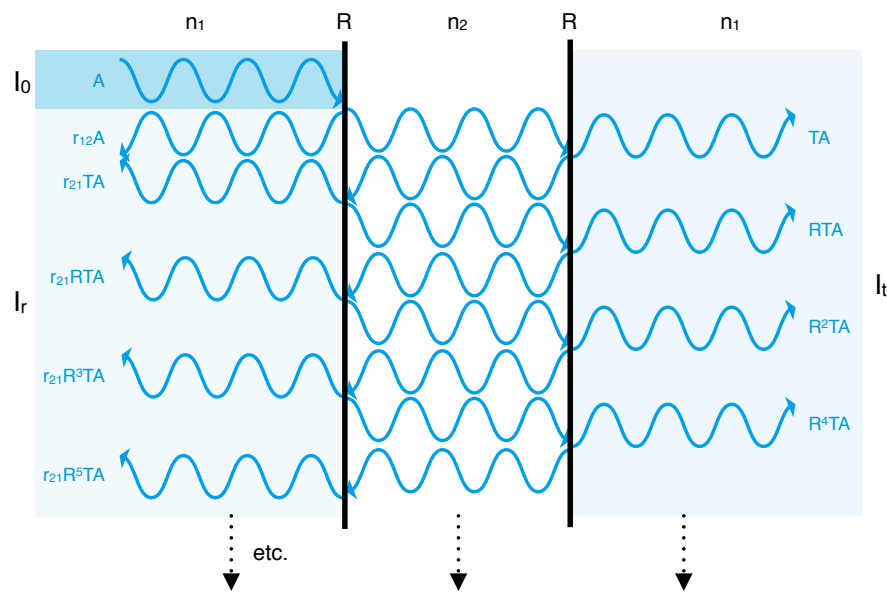


Figure A.1: Propagation of light 'beams' in a Fabry-Pérot interferometer with two mirrors with a reflectivity R , created by a difference in refractive index (n) between two media (the reflectance and reflection coefficients can be calculated with equation A.8 and A.9), assuming no losses. The figure shows an incident 'beam' with intensity I_0 and amplitude A that will partially reflect on the first mirror, while the transmitted part will start to resonate within the Fabry-Pérot cavity. The 'beam' returning from the cavity back to the source with intensity I_r is the sum of the light 'beam' reflected by the first mirror of the cavity when the beam entered the cavity and the multiple returning 'beams' that were transmitted out of the cavity in the direction of the light source. The 'beam' transmitted through the cavity with intensity I_t is the sum of multiple 'beams' transmitted out of the cavity in the direction away from the source. It can be observed that only the amplitude of the second returning and transmitted beam are not negligible with respect to their predecessor when $R \ll 1$. Hence, a Fabry-Pérot interferometer behaves like a two beam interferometer when $R \ll 1$.

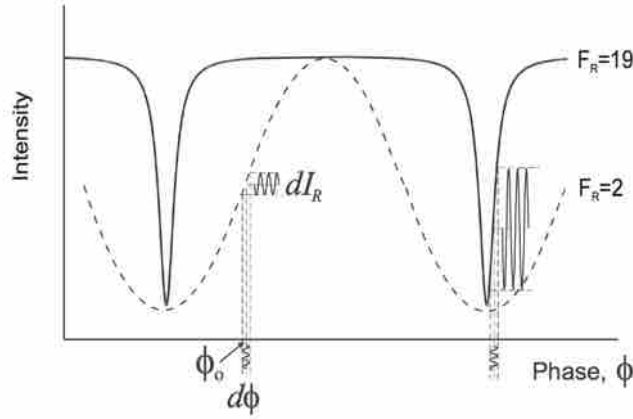


Figure A.2: The intensity of light reflected by a Fabry-Pérot interferometer as function of the phase difference between interfering light waves that have propagated 'x' and 'x+1' times through the FPI cavity for a FPI with a low and a high finesse [184].

The periodic dark and bright bands of the intensity as function of the phase difference are referred to as fringes [108].

The amount of 'resonance' of light in the Fabry-Pérot cavity is characterized by the finesse of the Fabry-Pérot interferometer [90]. The sensitivity of FPI-based sensors, interrogated with homodyne interferometry, to a change in OPD increases with increasing finesse, though the range of phase differences for which the sensor is sensitive to a change in phase difference decreases with increasing finesse (figure A.2) [90, 183, 184]. Resonance of light inside the cavity can be neglected for Fabry-Pérot interferometers with mirrors with a very low reflectivity (figure A.1). The Fabry-Pérot interferometer will then behave as a simple two beam interferometer [183]. Equation A.3 can in that case be further simplified to equation A.4 when $R_1 = R_2 \ll 1$ [90].

$$I_r \cong 2RI_i(1 + \cos \phi) = 2RI_i \left(1 + \cos \left(\frac{2\pi \cdot 2nL}{\lambda}\right)\right) = 2RI_i (1 + \cos (4\pi nL\tilde{\nu})) \quad (\text{A.4})$$

The fringe pattern as function of the phase difference of low finesse FPIs is often given in a generalized form as a function of the fringe visibility γ , a function of the maximum fringe intensity I_{max} , the minimum fringe intensity I_{min} and the average intensity of the fringe pattern I_0 , and the phase difference (equation A.6 and A.5) [114, 115, 116, 108].

$$\gamma = \frac{I_{max} - I_{min}}{I_{max} + I_{min}} \quad (\text{A.5})$$

$$I = I_0(1 + \gamma \cos \phi) = I_0 \left(1 + \gamma \cos \left(\frac{2\pi \cdot OPD}{\lambda}\right)\right) \quad (\text{A.6})$$

The fringe visibility determines largely the signal-to-noise ratio of an FPI-based sensor [116]. The fringe visibility depends strongly on the difference in reflectivity of both FPI mirrors. The fringe visibility depends furthermore strongly on the length of the Fabry-Pérot cavity in extrinsic FPI (EFPI) sensors, where the FPI cavity is not made of an optical fiber, as light diverges when it leaves the optical fiber and will therefore scatter out of the FPI cavity [116]. Cavity imperfections, in particular non-parallelism of the cavity mirrors, will also cause a significant reduction in fringe visibility [116]. The fringe visibility of EFPI sensors based on multimode fibers is in particular sensitive to the cavity length and non-parallelism of the mirrors [116]. For example, the fringe visibility of an EFPI with a 60 μm long air filled FPI cavity is 80% for an EFPI using single mode fibers and only 10% for an EFPI using multimode fibers. The fringe visibility of an EFPI

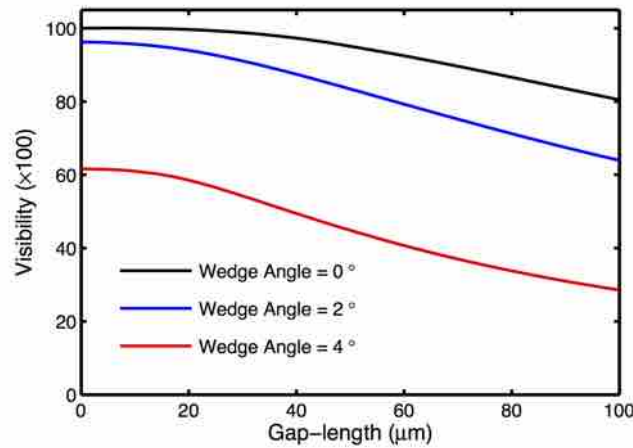


Figure A.3: The fringe visibility of EFPIs reduces for increasing cavity lengths as well and non-parallelism (increase in wedge angle) between the FPI mirrors (plot is for a sensor based on a single-mode fiber) [116]

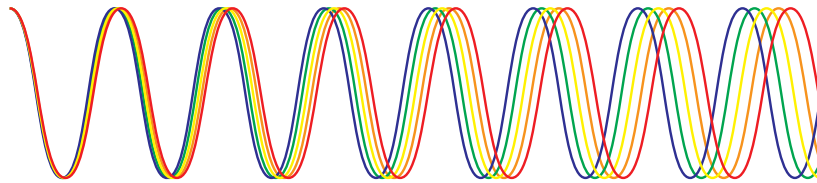


Figure A.4: A light bundle containing several wavelengths becomes incoherent after a certain length of its optical path

sensor with a 20 μm long air filled FPI cavity using multimode fibers with a core of 100 μm reduces from about 85% to 5% when the angle of the second mirror of the interferometer is tilted by only 0.55° with respect to the first mirror according to mathematical models [116].

Homodyne or low coherence interferometry are two types of interferometry that are frequently used to 'interrogate' FPI-based sensors to determine the change in OPD of an FPI [114, 185, 90, 116]. A source with a narrow spectral width (approximately monochromatic light) is used for homodyne interferometry, while a source with a large spectral width or a source with a narrow spectral width, capable of scanning its center wavelength very fast over a large range is required for performing low coherence interferometry [109, 90]. FPI-based sensors interrogated with homodyne interferometry show strong similarities with intensity modulating sensors (with similar disadvantages, but a better sensitivity), while FPI-based sensors interrogated with low coherence interferometry show many similarities with wavelength modulating sensors (including high costs). Light with an infinitely narrow spectral width is not achievable in practice, which effectively means that the OPD of an interferometric sensor, interrogated with homodyne interferometry, should be less than the coherence length of the source to ensure that the light will behave like it contains light of a single wavelength [89, 90]. The coherence length can be calculated with equation A.7 for a source with a Gaussian spectral distribution with a linewidth $\Delta\lambda$ and a central wavelength λ_0 (figure A.4) [186].

$$L_c = \frac{2 \ln 2}{\pi} \frac{\lambda_0^2}{\Delta\lambda} \quad (\text{A.7})$$

The change in phase between interfering waves is measured as a change in intensity of the light after interference when homodyne interferometry is performed (figure 1.6). This is very cheap and simple, as only a single photodiode and a relatively cheap laser source are required to perform the measurement [114, 97]. Measurement of the change in OPD of an FPI with a high resolution and a high bandwidth can generally be achieved better by using homodyne interferometry instead of low coherence interferometry [187, 90]. The sensitivity of FPI-based sensors, interrogated with homodyne interferometry, to strain of the FPI cavity increases with increasing length of the cavity. The range with which the change in OPD of an FPI can be measured is limited to changes in OPD corresponding to a difference in phase of maximal π radians with homodyne interferometry, due to the periodicity of the fringe pattern [90]. The direction of the change of the OPD cannot be determined (with certainty) after a minimum or maximum fringe intensity has been measured [90]. Low finesse FPI-based sensors, interrogated with homodyne interferometry, are only very sensitive and behave approximately linear to changes of the OPD around the quadrature point, the point where the phase difference is equal to $\pi/2 \pm k\pi$ (figure 1.6) [90, 97]. Operation of the FPI in the region around the quadrature point can be achieved by very precise manufacturing of the OPD of the interferometer, which is practically impossible according to some [188]. A definitely more convenient option is to use a light source with a tunable wavelength, such that a wavelength can be selected for which the interferometric sensor will operate around the quadrature point [188]. Power fluctuations of the light source can cause significant errors in interferometric sensors interrogated with homodyne interferometry, as power fluctuations mimic the change in intensity at the photodetector due to a change in OPD of the FPI [189]. Complex modulation algorithms have been proposed to reduce the effect of power fluctuations [138]. Using a fiber-optic coupled and an additional photodetector to assess the power output of the source seems however a far simpler option [83].

Low coherence interferometry is sometimes called 'white light' interferometry, although nearly always only infrared light is used [97, 185, 90]. Low coherence interferometry seems more popular than homodyne interferometry for interrogation of FPI-based sensors based on studies presented in literature. The OPD of the interferometer in the sensor should be larger than the coherence length of the used light source when low coherence interferometry is performed [97]. Low coherence interferometry makes use of the spectral content of the interfering light beams to observe a fringe pattern as function of wavelength and relate the observed fringe pattern to an OPD or the change in the fringe pattern to a change in OPD (see equation A.6) [90]. Low coherence interferometry can enable a significant reduction in noise level, insensitivity to optical power fluctuations, absolute measurement of the OPD and high resolution measurements compared to homodyne interferometry and can be used to interrogate multiple FPIs multiplexed on the same fiber [116]. Achieving absolute measurement in combination with high resolution measurement of the OPD is however challenging [116]. Equipment used to perform low coherence interferometry, containing an optical source and a detector, are more complex and quite more expensive compared to the simple photodiodes and laser sources required for homodyne interferometry [97]. Spectral low coherence interferometry is performed with a broadband source in combination with a sensor array with an optical spectrum analyzer to observe the fringe pattern as function of the wavelength of light [185, 116, 190]. An alternative is to use a wavelength scanning light source to trace the fringe pattern as function of the wavelength of the light source [190]. A scanning wavelength source can for example be made from a broadband source placed behind a scanning filter, made from a high finesse Fabry-Pérot interferometer. The fringe pattern can with this setup be measured with a single photodiode [190]. Scanning interferometers suffer however from hysteresis and therefore require some kind of calibration during operation [190]. Scanning low coherence interferometry systems are moreover quite slow [190, 187]. The absolute OPD can be calculated easily from the distance between two adjacent peaks in the

observed fringe pattern as function of the wavelength [90]. Other methods to derive the OPD of the FPI from the spectrum after interference include Fourier transforms of the spectrum (with the fringe pattern as function of wavenumber instead of wavelength) and curve fitting methods [116, 190]. Techniques using phase information of the Fourier transform of the fringe pattern as function of wavenumber can be used to track changes in OPD of (multiplexed) FPI-based sensors with very high resolution [191, 192, 186, 193, 194, 195, 120]. This technique is also used for optical coherence elastography (a method to measure tissue stiffness using optical coherence tomography, which is a form of low coherence interferometry) and is in such applications capable of resolving changes in OPD with a resolution of approximately 300 pm [193, 194, 195, 120].

A.2 Fabrication methods

A plethora of methods to fabricate Fabry-Pérot cavities is shown in literature. A brief overview will be presented in this section. The mirrors of a FPI are created by the interfaces of media with a different index of refraction (and extinction coefficient). The reflectivity of the transition between a silica fiber and air, which is frequently used in fiber-optic FPIs, is for example about 4% [89]. The fresnel reflection coefficient of a transition between two media for normal incident rays can be calculated with equation A.8 and the reflectance with equation A.9 for a beam propagating from medium 1 with refractive index n_1 and extinction coefficient k_1 into medium 2 with refractive index n_2 and extinction coefficient k_2 [196].

$$r_{12} = \frac{n_1 - n_2 + i \cdot (k_2 - k_1)}{n_1 + n_2 - i \cdot (k_2 + k_1)} \quad (\text{A.8})$$

$$R = \frac{(n_1 - n_2)^2 + (k_2 - k_1)^2}{(n_1 + n_2)^2 + (k_2 + k_1)^2} \quad (\text{A.9})$$

A.2.1 Air-filled cavities

FPIs constructed in a silica fiber using an air filled FPI cavity are very popular in literature. FPIs with FPI mirrors connected to each other a very low mechanical stiffness show a high sensitivity to force, as the change in OPD due to application of force will be large. Micro-machining of optical fibers with various techniques has been shown to fabricate FPIs in an optical fiber. Air-filled Fabry-Pérot cavities with a very low stiffness can be made on top of optical fibers by means of focussed ion-beam milling (FIB) [114]. The technique has been used to machine a fiber-optic atomic force microscope (AFM) out of the tip of an optical fiber (see figure A.5 for an example of an AFM on the top of a silica fiber) [114]. The air between the fiber-top and the cantilever of the AFM acts as a Fabry-Pérot cavity [197]. FIB milling is not particularly suited for series production and quite expensive [115]. An attempt was made to reduce fabrication costs of the fiber-top AFMs by using femtosecond laser irradiation of silica fibers in combination with etching of the irradiated areas to remove material [198]. The surface roughness of the etched surfaces is however much higher than the roughness of the surfaces created with FIB milling, which results in a significantly lower signal-to-noise ratio due to a larger amount of light diffusion at the surfaces (figure A.5) [198]. Some studies have shown femtosecond laser-machining to produce an approximately 30 to 75 μm long, simple notch in a single-mode fiber, which can serve as a Fabry-Pérot cavity (figure A.6) [199, 200]. The cavity suffers however from large losses due to light scattering at the rough ablated surfaces and the non-perpendicularity of the surfaces, which results in a reduced signal-to-noise ratio [199, 200]. The measured fringe visibility (14 dB) was nonetheless expected to be sufficient for most measurement purposes and could possibly be improved by slower and more precise manufacturing of the notch [199, 200]. A sensitivity of 6 pm/ μe and -2 pm/ $^\circ\text{C}$ was achieved with a 75 μm long notch [200]. Machining

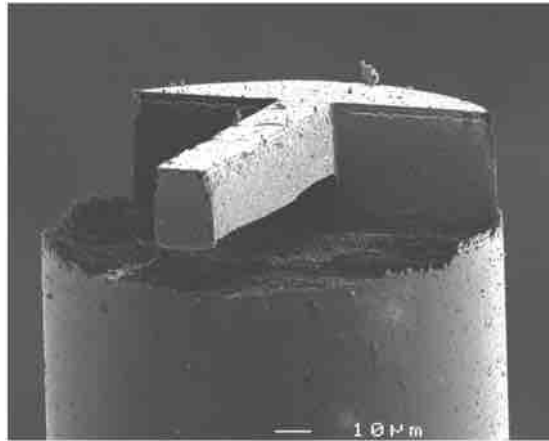


Figure A.5: Fiber-top AFM cantilever manufactured with femtosecond laser-irradiation and etching [198]

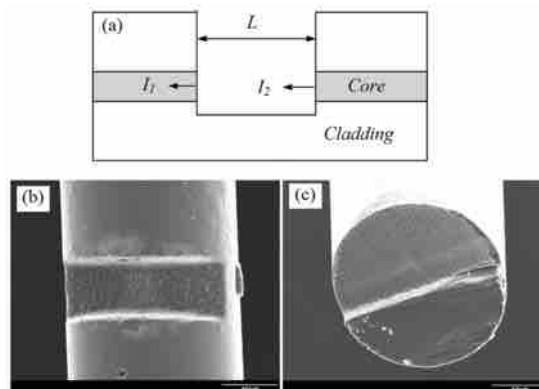


Figure A.6: Notch created in a single mode fiber with femtosecond laser ablation, serving as Fabry-Pérot cavity [199]

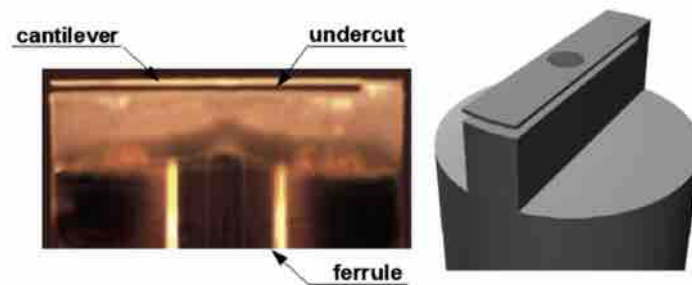


Figure A.7: Fiber-top Fabry-Pérot cavity made with a micro-machined cantilever on a ferruled single-mode fiber [201]

of a ferruled fiber, a standard single-mode fiber glued into a borosilicate glass cylinder (cylinders of 1.8 mm or larger in diameter were shown in literature), was presented as a technique to reduce manufacturing costs of FPIs on the end of a fiber by means of upscaling of dimensions. Upscaling of dimensions allows rougher machining methods like laser ablation and diamond coated wire cutting instead of FIB-milling to machine very sensitive FPIs that can be used for fiber-optic AFMs [143, 115].

Additive manufacturing techniques based on lithography were proposed as cheaper fabrication method, compared to subtractive manufacturing techniques like laser ablation and FIB, for the manufacturing of complex fiber-top FPI sensors with an air filled cavity. Additive manufacturing techniques can potentially be used to create cavities isolated from the environment surrounding the sensor [202, 203]. The align-and-shine technique uses a shadow mask on a multimode fiber, created with FIB milling [203]. The cleaved end of a single-mode fiber, on which the Fabry-Pérot cavity will be manufactured, is coated with photoresist, aligned with the multimode fiber in a fusion splicing machine and exposed to UV-light coupled into the multimode fiber with the shadow-mask [203]. The exposed resist is removed and the fiber-end can then be coated with a metal, after which also the unexposed photo-resist can be removed [202]. This technique was used to manufacture a fiber-top AFM with a metallic cantilever, though the technique is still regarded as being in its infancy. An alternative technique for fabrication of less complex shaped FPI sensors is presented for fabrication of FPIs on top of multimode fibers [204]. The exposing laser beam can be directed either via a small diameter fiber or by means of a magnification objective onto the end of a larger diameter multimode fiber coated with photoresist, hence no mask is required [204]. A cavity for a pressure sensor was made with this technique by etching a cavity on the fiber top of a borosilicate multimode fiber on top of which a silicon wafer was attached by means of anodic bonding to serve as a reflecting membrane [204].

An extremely sensitive FPI strain/force sensor near the end of a fiber can be made out of two normal single-mode fibers and a (self made) microfiber spliced to one end of each single-mode fiber, to keep two single-mode fibers together while acting as a spacer to create an FPI cavity [205]. The sensor with the shortest cavity length presented in the study ($21\ \mu\text{m}$) had a sensitivity of $200.9\ \text{pm}/\mu\epsilon$ and a slightly longer version a cross-sensitivity to temperature of $-2.48\ \text{pm}/^\circ\text{C}$ [205]. Maintaining reasonably parallel mirrors to ensure a good fringe visibility seems however difficult with this design and splicing the very small microfiber to the single mode fibers seems even harder.

The cavities of the FPIs made with the presented subtractive and additive manufacturing techniques are open to the environment in which the sensor is submerged, which can be a source of measurement noise due to changes in refractive index of the medium inside the cavity or increased attenuation due to contamination, for example by blood when the sensor is inserted into a patient [206, 207]. An open cavity design might therefore be not optimal for application

in a needle as contamination of the cavity might not be controlled very easily.

A closed air filled Fabry-Pérot cavity near the end of a fiber can be made by fusion splicing a hollow core photonic crystal fiber to a single-mode fiber [208]. The hollow core fiber is then cut at some distance from the first fusion splice with several arc discharges from the fusion splicer [208]. The hollow core fiber will partially collapse and form a proper Fabry-Pérot cavity when the length of the hollow core fiber is between 100 μm and 350 μm [208]. The cavity length is however not very easy to control [208]. Very small air filled cavities, up to the size that they act as a single mirror, can be created with a differential etching technique. The technique relies on the difference in etching rate of the cladding and the germanium doped core of a fiber in a buffered hydrofluoric acid or an erbium doped fiber in a hydrochloric and hydrofluoric acid to create a small pit in the end of the fiber [181, 209, 210, 211, 212]. The etched end of a fiber is then fusion spliced to an end of an un-etched fiber, which creates a small air gap in the core of the fiber at the location of the fusion splice [181]. Sensitivities of 3.15 $\text{pm}/\mu\epsilon$ and 0.65 $\text{pm}/^\circ\text{C}$ and 6.99 $\text{pm}/\mu\epsilon$ and 0.95 $\text{pm}/^\circ\text{C}$ were obtained with the technique [211, 212]. Somewhat larger micro-cavities can be made by fusion splicing two single mode fibers with both fiber ends 'coated' with a liquid film of 'refractive index matching liquid' [121]. The fiber ends are pressed together in the splicer and spliced together with an arch discharge during which the liquid coating turns into vapor and leaves a small micro-cavity in the fiber at the location of the splice (45-80 μm) depending on the specific fusion splicer settings [121]. A sensor made out of a standard single-mode fiber showed a sensitivity of 6 $\text{pm}/\mu\epsilon$ and 1.1 $\text{pm}/^\circ\text{C}$ [121]. A similar procedure, used to create micro air filled cavities by splicing fibers with hemispherical ends, resulted in sensors with sensitivities of 4 $\text{pm}/\mu\epsilon$ and 0.9 $\text{pm}/^\circ\text{C}$ [185]. Other groups constructed Fabry-Pérot cavities by splicing a (hollow-core) photonic crystal fiber between two pieces of single mode fiber [112, 213, 214, 215]. One group succeeded in constructing cavities with a particularly high fringe visibility of 38 dB due to the spherical shape of the cavity that minimizes diffraction of the beam inside the cavity [112]. A sensitivity of 10.3 $\text{pm}/\mu\epsilon$ and 0.95 $\text{pm}/^\circ\text{C}$ was achieved by optimizing the shape and size of the cavity. This corresponds to a cross-sensitivity to temperature a factor 90 lower than the cross-sensitivity to temperature of an FBG [112]. Photonic crystal fibers are noted to be quite expensive [185].

Quite a few FPI sensors based on two fibers inserted into a glass capillary have been presented in literature [216, 23, 217, 218, 219, 220, 221, 222]. The two fiber ends inside the capillary form the mirrors of the Fabry-Perot cavity. One of the ends of the fibers can be coated with a metallic layer to increase the reflectivity of one of the mirrors [222]. Some use commercially available glass capillary FPI sensors where the fibers are fusion welded into the capillary [216, 23]. Glueing the fibers inside the capillary with epoxy was noted as limiting in harsh environments due to limited thermal stability and mechanical strength [221]. Glue will furthermore affect the thermal cross-sensitivity of the sensor. Fusion welding of very thin capillaries should result in mechanically stronger sensors with a lower thermal cross-sensitivity [221]. A sort of variant on the glass-capillary FPI sensors is the sensor presented by Liu et al. where one fiber is inserted into a nitinol capillary (containing some flexures) and the second reflecting mirror is created with a polished metal surface, glued to the end of the nitinol capillary [81].

A.2.2 Non-air filled cavities

Usage of FPIs with non-air filled FPI cavities results (in most cases) in sensor with quite a large cross-sensitivity to temperature due to the large thermo-optic coefficients of the materials used as medium inside the cavity compared to the thermo-optic coefficient of air. Non-air-filled fiber-top Fabry-Pérot cavities on the tip of a fiber manufactured by using a polymer thin-film coating as Fabry-Pérot cavity sandwiched between a partially metallic films have been shown for fiber-optic ultrasound transducers [184, 223]. The technique is presented as a low cost manufacturing

technique suited for mass production with good repeatability and resulting in rugged sensors [184]. Very simple temperature sensors using a droplet of UV-curable glue as Fabry-Pérot cavity on the end of a fiber have also been shown [137]. The fringe visibility of the FPI manufactured with this method seems however somewhat questionable, because the difference in refractive index of the optical fiber-UV curable glue transition is rather small and no additional reflective coatings are used.

Partially reflective mirrors inside an optical fiber can be made by splicing two fibers together [90]. The cooling process after fusion splicing determines the refractive index of the fusion splice [224]. The process effectively forms a thin film between both fiber ends with a different refractive index than the unaffected core of the fibers and thus a partially reflective mirror [224]. The maximum achieved reflectivity in a study by Wu et al., based on the estimated refractive index of the thin film and the refractive index of the core is a mere 0.1% [224]. A quite powerful source is thus required to achieve a good signal-to-noise ratio. Fiber-ends are therefore often coated with a metallic or dielectric material before splicing, to enhance the reflectivity of mirrors made with fusion splicing and increase the finesse of the Fabry-Pérot cavity [90]. Particularly TiO_2 coatings, sputtered on a fiber end with a typical thickness of about 100 nm, are frequently used [90]. Aluminum and silver coatings are also used [181, 90]. The reflectivity generally decreases monotonically as function of the number of arc discharges used to splice the two fibers and allows the reflectivity to be tuned from 10% to much less than 1% [90]. A higher reflectivity, reflectivity's up to 86% are shown in literature, can be achieved by using multilayer coatings [90, 95]. FPI mirrors within a fiber can furthermore be made by fusion splicing two fibers with cores with a different refractive index and different diameter, which causes a interface with a relatively low reflectance [225]. Some groups have shown Fabry-Pérot cavities made of two fiber Bragg gratings with a little space in between serving as the cavity, to perform simultaneous temperature and strain measurements or perform absolute measurements of the OPD with very high resolution over a range of multiple interference fringes [226, 227, 187].

B Calibration of the ATI Nano 17

B.1 Objective of the calibration procedure

The ATI Nano 17 sensor is the most popular force sensor for the measurement of needle insertion forces for various purposes. Its performance can thus be used as a benchmark for other, new force sensors for similar applications. The manufacturer does however not specify the precise performance characteristics of the sensor and only states a resolution for the SI-12.0.12 model of approximately 3.1 mN for a measurement range of 17 N in axial direction of the sensor [64]. The objective of the performed calibration of the ATI Nano 17, of which the method and results are presented in this chapter, was quantification of the accuracy of the ATI Nano 17 for the measurement of static forces in axial direction throughout the relevant part of its measurement range (up to 10 N). Goals on the measurement uncertainty of a new fiber-optic sensor for the measurement of forces on the tip of a needle, of which the design is described in this thesis, could therefore be defined.

The accuracy of a measurement consists of two components according to ISO 5725, the trueness and the precision of the measurement [228]. The trueness refers to agreement between the mean of many measurements and the true or accepted value, while the precision refers to the agreement between separate measurements. The trueness of force measurement should ideally be based on calibration forces traceable to the (national) standard for force or weight. Assessment of the measurement trueness of the ATI Nano 17 based on the national standard is however unnecessary complex and expensive, as only performance characteristics like non-linearity, resolution, repeatability, reproducibility and hysteresis are of interest for characterization of the performance of a prototype of the ATI Nano 17. An assessment based on a set of calibration forces derived from a self defined standard for true force, each calibration force ideally with an identical bias with respect to the true force according to the national standard (such as shown in equation B.1), is thus sufficient to assess the performance of the force sensor.

$$F_{true-defined} = \alpha \cdot F_{true-national-standard} \quad (B.1)$$

The standard calibration procedure for force proving instruments, force sensors used for static verification of uniaxial testing machines, is described in ISO 376 [164]. The resolution, relative repeatability error, relative reproducibility error, relative zero error, relative reversibility error and the relative interpolation error should be assessed for force proving instruments used to measure increasing as well as decreasing loads according to ISO 376. Resolution is defined in

ISO 376 as either the last active number on the numerical indicator of the measurement system or half of the range of random fluctuations of obtained readings of the sensor, whichever is larger [164]. Repeatability errors refer to differences between measurements performed under identical conditions, while reproducibility errors relate to differences between measurements acquired under conditions that are allowed to vary (often up to some extent for calibration purposes) [164, 228]. The dynamic performance of the ATI sensor will not be assessed, as this requires a specialized device to apply oscillating calibrated loads up to high frequencies, which was not readily available.

B.2 Definition of the true value

The weight of a set of masses was used for calibration of the ATI sensor. The weight of each mass was determined with a very precise analytic balance that served as the defined true force standard. A balance displays weight as a mass, which was therefore converted back to a weight by multiplying with the standard gravity of 9.80665 m/s^2 , as defined by the Bureau International des Poids et Mesures [229]. Errors introduced by the variation of the density of air, (local) variations in the gravitational field and centrifugal forces due to rotation of the earth are ignored (as their influence on the accuracy of the calibration forces with respect to the defined true force is negligible compared to the expected accuracy of the ATI Nano 17). However, a balance cannot be used as a semi-perfect true force standard, as a balance itself shows non-linearity, reproducibility and repeatability errors and has a limited resolution. Calibration forces derived from this defined standard will thus inherit those errors. This was partially circumvented by using 20 weights with an approximately identical mass of 50 g as calibration forces such that linearity errors of the balance should be negligible, although repeatability and reproducibility errors and errors due to a finite resolution will still limited the accuracy of the 20 calibration forces. Increasing calibration forces can be simply made by stacking the calibration weights on top of each other. Repeatability and reproducibility errors and limited resolution of the balance will introduce small non-linearity errors in calibration forces generated by stacking weights. Errors in the assessment of the nonlinearity/interpolation errors of the ATI Nano 17 using such a stack of weights should therefore be caused solely by (the extremely small) reproducibility and repeatability errors of the balance and handling of the weights. The influence of the limited accuracy of the calibration weights on the assessment of the repeatability and reproducibility errors of the ATI Nano 17 was minimized by always using the same sets of weights to generate a certain calibration force. Only handling of the weights should therefore introduce errors in the assessment of the repeatability and reproducibility errors of the ATI Nano 17.

The weights of the 20 calibration masses were measured with a Mettler PJ360 DeltaRange balance of which both the reproducibility and readability in the 'DeltaRange' (range up to 60 g) were estimated to be 1 mg (10 μN) based on the specifications mentioned in the manual of a newer device, the PE360 DeltaRange and the specifications of the PJ360 outside the DeltaRange [230, 231]. Fluctuations up to 20 μN were observed between separate reweighings of a particular calibration mass, which is somewhat larger than the reproducibility error. Each mass was therefore weighed 3 times and 'the mean weight' and the standard error of the mean, which is the uncertainty of the weight of a calibration mass, were calculated for each calibration mass. The uncertainty of the weight of each mass is only a very coarse estimate, as the sample size per mass was very small and the measurement error was assumed to be Gaussian, although this is not really the case. The uncertainty (SEM) of the weight of the calibration masses was on average 3.1 μN and at most 6.5 μN . The calibration masses were also weighed twice on a Scaltec SBC33 analytic balance with a reported reproducibility error of 0.1 mg (1 μN) and an identical readability. Fluctuations up to 0.2 mg were observed occasionally between re-weighings of an identical mass [232]. The difference between the measured 'mean weight' of each calibration

mass determined with the Mettler balance and the 'mean weight' of the same calibration mass determined with the Scaltec balance was $393 \pm 6 \mu\text{N}$. The weighings performed with each balance can thus be regarded as very precise, as the difference between mean of the measurements of the two balances is almost constant. The difference between the means determined with each balance does vary with less than twice the 'estimated' uncertainty of the weight of the calibration mass with the highest uncertainty of the weight ($6.5 \mu\text{N}$), based on weighing of the twenty masses with the Mettler balance. The uncertainty of the weight of the calibration mass with the highest uncertainty of the weight was therefore used as a 'safe' over-estimation of the uncertainty of the weight of each of the calibration masses. The uncertainty of the weight of a stack of calibration masses with respect to the self defined true force standard was therefore determined using the uncertainty of the weight of the mass with the highest uncertainty of the weight ($6.5 \mu\text{N}$), instead of the (somewhat dubiously estimated) uncertainty of the weight of each separate mass. The calculated uncertainty of the weight of a stack of calibration masses should therefore be an overestimation of the uncertainty. The uncertainty of the weight a stack of of N calibration masses was calculated with equation B.2 (based on the equation of the sum of independent tolerances [233]) and with $SEM_{max} = 6.5 \mu\text{N}$.

$$\sigma_{stack} = \sqrt{N \cdot SEM_{max}^2} \quad (\text{B.2})$$

The uncertainty of the weight a calibration force exerted with a stack containing a single calibration mass is thus in the worst case $6.5 \mu\text{N}$, which corresponds to 13 ppm of the total weight, while the uncertainty of weight of the entire stack of 20 calibration weights (9.84931 N) should be lower than $29 \mu\text{N}$, which is only 3 ppm of the total weight of the stack. The 'estimated' uncertainty of the calibration forces created with the stack of calibration weights is orders of magnitude lower than the uncertainty of the force measurements performed with the ATI Nano 17, as can be observed in the results of the calibration of the ATI Nano 17 presented in this chapter. The uncertainty of the calibration forces will therefore not significantly affect the assessment of the measurement uncertainty of the ATI Nano 17.

B.3 Experimental setup

Calibration of an ATI Nano 17 SI-12.0.12 (serial number FT06661) was executed by following ISO 376 as closely possible. The ATI Nano 17 sensor was attached to the needle insertion stage normally used at the TU Delft to perform needle insertions while measuring insertion forces with the ATI Nano 17 sensor (figure B.1). The disturbances acting on the sensor during calibration should therefore be similar to the disturbances acting onto the sensor during practical usage of the sensor (although it was noted that activation of the motorized stage, that was not active during calibration, would introduce significantly more noise). Elayaperumal et al. report for example a noise level equivalent to 160 mN of their setup used to measure needle insertion forces using an ATI Nano 17 for haptic feedback purposes, which is significantly worse than the resolution of the ATI Nano 17 reported by the manufacturer and thus likely caused by vibrations from the environment [29]. The measurement noise introduced by the disturbances experienced during calibration should thus be acceptable for the measurement of needle insertion forces. The resolution of the ATI Nano 17 sensor was only determined for an unloaded sensor, as the used calibration masses will lower the resonance frequency of the sensor and thus increase the sensitivity of the sensor to vibrations of the environment. The lowered resonance frequency due to the added mass of the calibration masses is however not representative for needle insertion experiments.

The sensor was fixated on its normal support in an inverted orientation, such that application of calibrated forces on the sensor, exerted by stacking weights on top of the sensor, would result



Figure B.1: Motorized stage used at the TU Delft to perform needle insertion experiments while insertion forces are measured with the ATI Nano 17.



Figure B.2: Stack of weights on the ATI sensor to generate a well defined calibration force.

in compressive loading of the sensor (figure B.2). A certain calibration force on the sensor was always exerted using the same combination of weights. The weights were placed onto a small tube normally used to connect needles to the force sensor (the offset introduced by the weight of the tube was removed during zeroing of the sensor). The sensor was powered with a custom 5 V DC source and connected to an ATI InterFace/PowerSupply box, which does not seem to contain a lowpass filter. Signals from the InterFace/PowerSupply box were sampled at 10 kHz with a National Instruments USB5210 D/A converter, without (additional) analog filtering (aliasing can occur, but will be minimal as static forces are measured).

The sensor was energized 30 minutes before the calibration procedure started. The calibration procedure commenced by loading the ATI sensor 3 times for 60 s with the maximum calibration force of 9.8493 N. The sensor was zeroed after all load was removed. The official calibration procedure according to ISO 376 consists of 6 calibration series, series X_1 to X_6 , consisting of application of gradually increasing or decreasing calibrated forces on the ATI sensor and obtaining a reading of the response of the force sensor to each applied calibration force. Additional 'verification' series were performed, in between the officially required series, to obtain more data, for example for validation purposes. A 3 minute pause was maintained before each series commenced. A reading of the response of the ATI sensor to a certain calibration force in a series was each time obtained at least 30 s after application of that calibration force on the sensor. A reading of the measured force was defined as the mean of 5 seconds of unfiltered measurement signal, converted with the calibration matrix supplied by the manufacturer of the sensor to force in axial direction on the sensor. A reading during practical usage of the sensor is of course not the mean of a 5 seconds long measurement signal. The resolution was therefore determined based on fluctuations observed in the 5 seconds of measured signal.

Calibration series X_1 and X_2 , mainly used to determine the repeatability uncertainty of the sensor, consisted of solely increasing calibration forces, increasing in 20 steps from a zero load reading to the maximum calibration force, and ended with a zero reading after all load was removed. Two identical calibration series were subsequently performed as additional verification measurements. All cables connecting the measurement equipment were disconnected afterwards and the sensor was rotated 120° on its support (the sensor is disconnected and reconnected and rotated to assess reproducibility of the ATI Nano 17). The sensor was again energized for 30 minutes before it was zeroed and calibration series X_3 and X_4 commenced. Series X_3 consisted of a zero reading followed by 20 increasing calibration loads up to the maximum calibration force. The maximum calibration force was not removed when the series ended, as it served as a starting point for series X_4 . Series X_4 consisted of a series of decreasing calibration forces, decreasing from the maximum calibration force to zero load. A verification series was then again performed, consisting out of increasing forces up to the maximum calibration force, followed by decreasing forces up to zero load. Finally, the sensor was turned by another 120° , after which calibration series X_5 and X_6 commenced, with a similar loading pattern as calibration series X_3 and X_4 respectively. The calibration procedure was concluded by yet another verification series of calibration forces increasing to the maximum force and decreasing back to zero load, such that calibration and verification series were available of the sensor in its original position on its support, its 120° rotated position and its 240° rotated position.

The components of the measurement uncertainty of the ATI Nano 17 sensor were then calculated according to ISO 376 based on calibration series X_1 to X_6 . The resolution was calculated as $6/2$ times the standard deviation of 5 seconds of measurement signal of the unloaded ATI Nano 17 (the range of 6 times the standard deviation should contain contain 99.7% of the measured values when the noise is Gaussian). Only series X_1 , X_3 and X_5 (series with only increasing calibration forces) were used to determine a linear interpolation function describing the reading of the ATI Nano 17 as function of the applied calibration force on the sensor. The

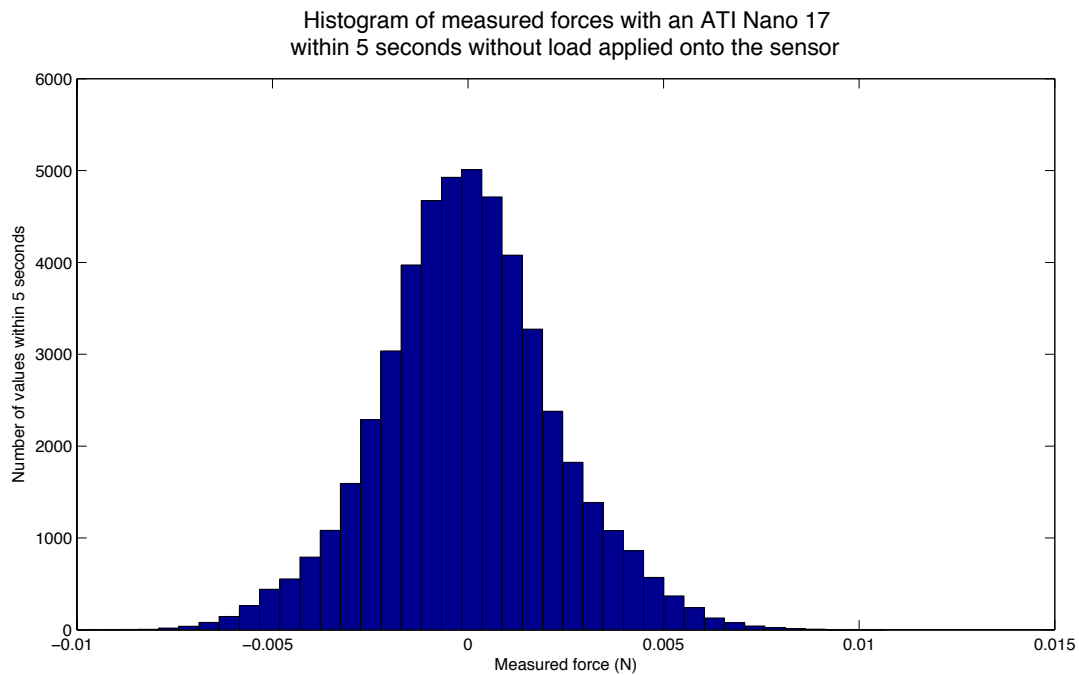


Figure B.3: Histogram of 5 seconds of measured force in axial direction of the ATI Nano 17 (sampled at 10 KHz), without any load applied onto the sensor, showing the measurement noise.

temperature uncertainty, as described in section C.1 of ISO 376, was not taken into account, only the calibration uncertainty, resolution and 'contribution due to reversibility' of section C.2 of ISO 376 were taken into account to calculate the uncertainty of measurements performed with the ATI Nano 17 during 'subsequent' use and the corresponding expanded uncertainty using a coverage factor of 3. The obtained data during calibration of the sensor, including verification series was also analyzed with an alternative method, which will be presented in the discussion.

B.4 Results

B.4.1 Noise and resolution

An analysis of the noise distribution of the unloaded ATI sensor was made to verify whether the standard deviation of 5 seconds of signal can be used to determine the resolution of the sensor. A histogram of 5 seconds of measurement noise of a force measurement in the axial direction of the ATI Nano 17 with no load exerted on the sensor and with the offset removed by subtracting the average of the measured force from the measurement is given in figure B.3. The noise seems reasonably Gaussian, although this is not the case according to the Kolmogorov-Smirnov test. The resolution of sensor, calculated from the observed standard deviation of the measurement shown in figure B.3, is 6.8 mN. The same noise is shown in figure B.4 as function of time, with red lines marking the range in between fluctuations should occur for a resolution of 6.8 mN. The range of fluctuations of the measured noise signal based on the observed minimum and maximum of the signal is 20.7 mN, which would correspond to a resolution of 10.3 mN. The average resolution of the ATI Nano 17 sensor without a calibration force applied onto the sensor, obtained from 16 measurements, is 7.1 mN (with a SEM of 0.1 mN).

A significant improvement of the resolution can be achieved by filtering the measurements performed with the ATI Nano 17. Figure B.5 shows the cumulative amplitude spectrum and the approximately achievable resolution of the ATI Nano 17 as function of the cutoff frequency

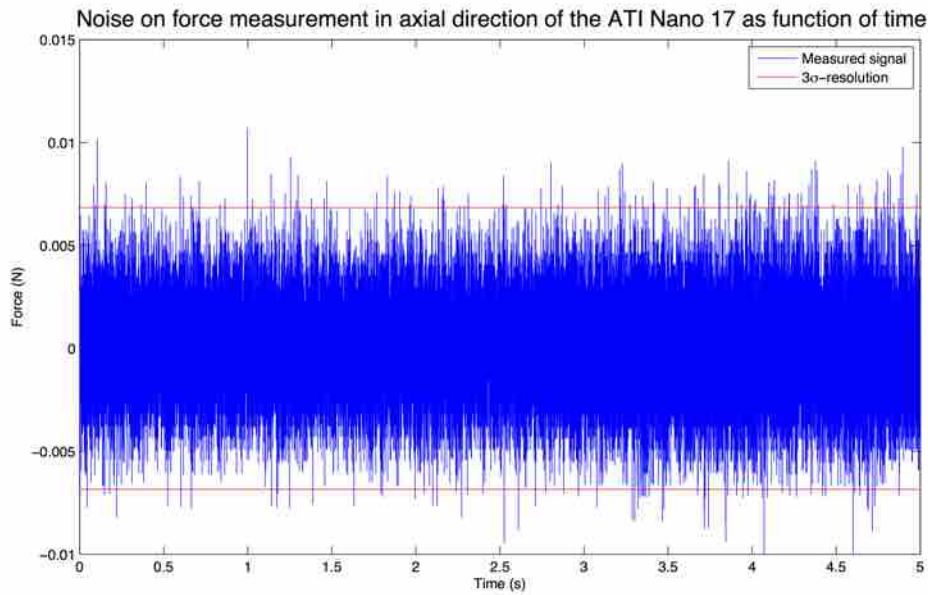


Figure B.4: Measured force in axial direction on the ATI Nano 17, without any load exerted onto the sensor, as function of time, showing the amount of noise on the force measurements performed with the ATI Nano 17. The red lines indicate the margin between which the signal should fluctuate when the resolution is determined as 3 times the standard deviation of the signal.

of the lowpass filter used to filter the measurements (based on the same noise measurement presented in figure B.3 and B.4). It can be observed that the resolution can be improved to approximately 2.3 mN by lowpass filtering measurements with a cutoff frequency at 500 Hz. The resolution would be 3.4 mN when the minimum and maximum of the observed fluctuations were used instead of the standard deviation to determine the resolution after lowpass filtering with a cutoff frequency of 500 Hz, which is approximately equal to the resolution of the ATI Nano 17 stated by the manufacturer.

B.4.2 Measurement uncertainty

The measurement uncertainty of the ATI Nano 17 and the components of which the measurement uncertainty is composed according to ISO 376, using the resolution of the unloaded ATI Nano 17 without lowpass filtering, calculated for each calibration force according to ISO 376, is shown in table B.1. The resolution uncertainty, calibration uncertainty, measurement uncertainty and the expanded measurement uncertainty (with a coverage factor of 3) using the resolution of the unloaded ATI Nano 17 with a digital lowpass filter with a cutoff frequency at 500 Hz is shown in table B.2. The linear interpolation function describing the force measured with the ATI Nano 17 as function of the calibration force is given in equation B.3.

$$F_{ATI} = 0.9682 \cdot F_{True} - 0.0016 \quad (B.3)$$

The 95% confidence interval for the slope is 0.9674 to 0.9691 and -0.0063 to 0.0031 for the intercept. The measurement error of all readings of the calibration and verification series with respect to the interpolation function (equation B.3) is shown in figure B.6, together with the expanded measurement uncertainty of the ATI Nano 17 in axial direction (as shown in table B.2).

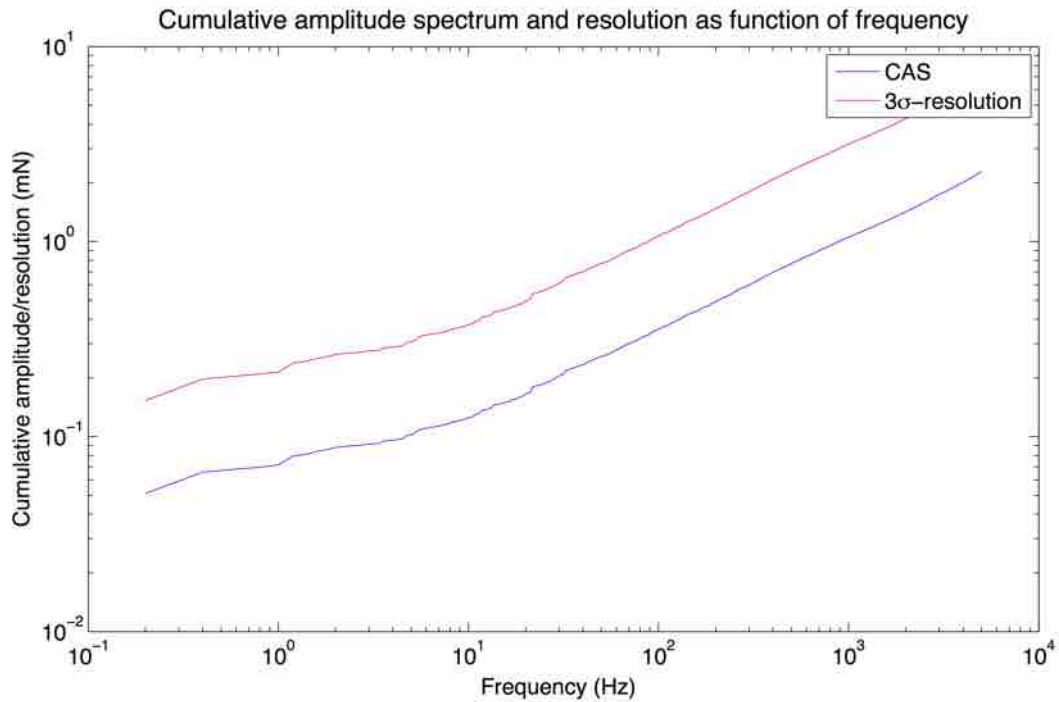


Figure B.5: Cumulative amplitude spectrum and the resolution of the ATI Nano 17 as function of the cutoff frequency of a digital lowpass filter, based on a 5 second noise measurement without load exerted on the ATI Nano 17.

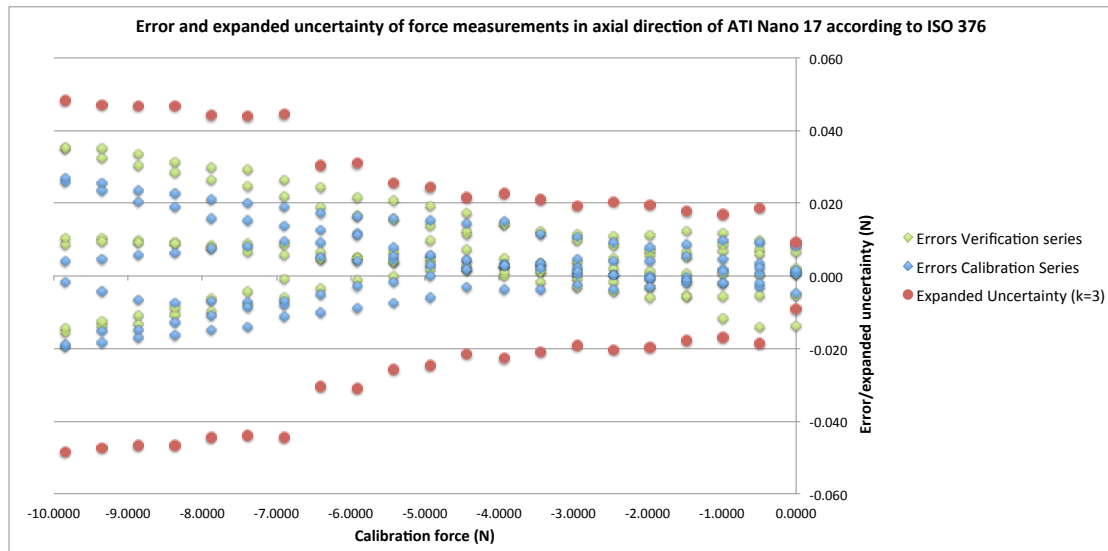


Figure B.6: Measurement error of all readings obtained during the calibration and verification series with respect to the interpolation function describing the (expected) reading of the ATI Nano 17 as function of the calibration force in respectively green and blue. The expanded measurement uncertainty of the ATI Nano 17, calculated according to ISO 376 using a coverage factor of 3 and the (approximate) resolution of the unloaded sensor after lowpass filtering with a 500 Hz cutoff frequency is shown in red.

Table B.1: The measurement uncertainty (last column) and all its components of force measurements performed with the ATI Nano 17 in axial direction of the sensor as function of calibration force. The resolution of an unloaded ATI Nano 17 without lowpass filtering was used.

Calibration force (N)	Uncertainty (mN)										Measurement
	Calibration force	Reproducibility	Repeatability	Resolution	Creep	Zero drift	Interpolation	Calibration	Reversibility	Measurement	
0.0000	0.00	0.20	0.00	2.89	0.00	0.00	0.00	2.89	0.00	0.00	4.09
-0.4928	0.01	1.57	-3.88	2.89	-1.07	-0.35	-0.81	5.27	-3.21	-3.21	6.81
-0.9856	0.01	1.20	-2.31	2.89	-1.23	-0.70	-0.36	4.15	-3.68	-3.68	6.26
-1.4771	0.01	0.49	-0.61	2.89	-1.51	-1.05	-1.19	3.71	-4.53	-4.53	6.53
-1.9693	0.01	0.97	-0.49	2.89	-1.70	-1.40	-1.18	3.97	-5.11	-5.11	7.09
-2.4615	0.01	1.33	-0.07	2.89	-1.75	-1.76	-1.06	4.17	-5.26	-5.26	7.31
-2.9531	0.02	1.17	-1.12	2.89	-1.58	-2.11	-0.40	4.25	-4.73	-4.73	6.98
-3.4445	0.02	2.22	-0.46	2.89	-1.66	-2.46	-0.64	4.76	-4.99	-4.99	7.48
-3.9381	0.02	2.32	0.00	2.89	-1.85	-2.81	-0.73	5.06	-5.54	-5.54	8.04
-4.4313	0.02	2.22	-1.41	2.89	-1.56	-3.16	-1.09	5.37	-4.67	-4.67	7.68
-4.9239	0.02	3.63	-1.56	2.89	-1.69	-3.51	-0.94	6.33	-5.07	-5.07	8.61
-5.4153	0.02	4.70	-0.69	2.89	-1.55	-3.86	-1.57	7.12	-4.64	-4.64	8.97
-5.9076	0.02	6.01	-4.59	2.89	-1.30	-4.21	-2.27	9.49	-3.89	-3.89	10.66
-6.3999	0.02	6.86	-2.50	2.89	-1.13	-4.56	-2.64	9.53	-3.38	-3.38	10.51
-6.8925	0.02	8.03	-10.37	2.89	-1.02	-4.91	-1.79	14.45	-3.07	-3.07	15.05
-7.3860	0.03	9.04	-8.92	2.89	-1.10	-5.27	-1.94	14.22	-3.30	-3.30	14.89
-7.8789	0.03	9.51	-8.52	2.89	-1.02	-5.62	-1.97	14.41	-3.05	-3.05	15.01
-8.3716	0.03	10.93	-8.19	2.89	-0.96	-5.97	-1.61	15.30	-2.87	-2.87	15.84
-8.8648	0.03	11.49	-7.41	2.89	-0.70	-6.32	-1.01	15.39	-2.11	-2.11	15.80
-9.3573	0.03	12.64	-5.43	2.89	-0.66	-6.67	-0.30	15.58	-1.99	-1.99	15.97
-9.8493	0.03	13.57	-3.48	2.89	-0.51	-7.02	-1.64	16.03	-1.53	-1.53	16.36

Table B.2: Resolution uncertainty, calibration uncertainty, measurement uncertainty and expanded measurement uncertainty (using a coverage factor of 3) of the ATI Nano 17, calibrated according to ISO 376, using a resolution determined as 3 times the standard deviation of the lowpass filtered noise of the unloaded sensor with a cutoff frequency of 500 Hz, as function of the calibration force.

Calibration force (N)	Resolution uncertainty (mN)	Calibration uncertainty (mN)	Measurement uncertainty (mN)	Expanded measurement uncertainty (mN)
0.0000	0.94	0.96	3.04	9.13
-0.4928	0.94	4.51	6.24	18.72
-0.9856	0.94	3.13	5.63	16.89
-1.4771	0.94	2.51	5.93	17.80
-1.9693	0.94	2.89	6.54	19.63
-2.4615	0.94	3.15	6.78	20.34
-2.9531	0.94	3.25	6.43	19.28
-3.4445	0.94	3.90	6.96	20.88
-3.9381	0.94	4.26	7.56	22.69
-4.4313	0.94	4.63	7.18	21.54
-4.9239	0.94	5.71	8.16	24.49
-5.4153	0.94	6.58	8.55	25.65
-5.9076	0.94	9.09	10.30	30.90
-6.3999	0.94	9.13	10.15	30.46
-6.8925	0.94	14.18	14.80	44.39
-7.3860	0.94	13.96	14.63	43.90
-7.8789	0.94	14.15	14.76	44.29
-8.3716	0.94	15.06	15.60	46.80
-8.8648	0.94	15.15	15.56	46.69
-9.3573	0.94	15.34	15.73	47.20
-9.8493	0.94	15.80	16.13	48.39

B.5 Discussion

ISO 376 defines the resolution of a force sensor as half the range of fluctuations of the obtained readings. It was however chosen to base the resolution on the standard deviation of readings, as using the maximum observed variation between readings is very sensitive to occasional outliers. Defining the resolution as 3 times the standard deviation, assuming that the noise is approximately Gaussian, seems adequate, as can be observed in figure B.4, despite the fact that the Kolmogorov-Smirnov test indicates that the noise distribution is not normal. One of the reasons that the noise distribution is not normal, could be the fact that force is measured as a discrete instead of continuous variable. Filtering of the measured signals of the ATI Nano 17 is furthermore strongly recommended, as a lot of high frequent noise is present in the measured signals. This will result in a significant gain in resolution, as can be observed in figure B.5. Using an appropriate analog lowpass filter besides a digital filter would be a preferable solution, as this will also prevent aliasing. The effect of aliasing should however be minimal when no forces, either forces that should be measured or disturbances, are being measured that have frequencies higher than the Nyquist frequency (in this case 5 kHz).

A large contributor to the expanded measurement uncertainty, calculated according to ISO 376, is the reproducibility uncertainty. This can also be observed in figure B.6, that shows that there appear to be three different responses of the sensor to the calibration forces. Each of the three responses consist of data from two calibration and verification series measured with the sensor in an identical orientation (the latter is not visible in the graph). The most 'probable' cause of this reproducibility error is that the sensor was not mounted perfectly level on the support after each rotation. The interval in which measurement forces are distributed for the maximum calibration load is roughly 60 mN. The error due not mounting the sensor identical

after each rotation, resulting a rotation of the axis along which forces are exerted on the sensor with angle ϕ , is equal to $(1 - \cos(\phi)) \cdot F_{calibration}$. The sensor should therefore be mounted with an approximately 6° deviation from one of the three positions regarded as 'perfectly' level. This would be quite non-level, while the sensor appeared to be mounted quite level according to a bubble level (and a 6° deviation from being mounted level on the support should be even visible by bare eye). The source of the reproducibility error is thus unclear. No corrections will therefore be made for accidental non-levelness of the ATI sensor during calibration for the determination of the requirements on the accuracy of a sensor that should have an equal accuracy as the ATI Nano 17.

The expanded measurement uncertainty is identified based on many components of the measurement uncertainty by ISO 376. The ISO norm does however not explain why components of the measurement uncertainty are calculated in a particular way. It is therefore for example difficult to explain why the expanded measurement uncertainty covers the errors of the readings in certain regions with a wide margin and in other regions with a very narrow margin. The errors of the readings are not spread in a symmetric way around the interpolation function, as shown in figure B.6. This is because the interpolation function is solely based on the response of the sensor to increasing calibration forces and not the response to decreasing calibration forces. This is reasonable when corrections are made for hysteresis of the sensor during actual usage of the sensor. This is however not the case during usage of the ATI Nano 17 (at the TU Delft). Furthermore, it should make more sense in the authors opinion to assess the performance of the sensor with compensation of hysteresis during the assessment, to determine how well can be compensated for hysteresis. Many of the calculated uncertainties are furthermore, according to the standard calibration protocol, based on a single measurement instead of the average of many measurements. 'Random errors' will therefore introduce sudden changes in the calculated measurement uncertainty of the sensor as function of the calibration force. This can for example be observed for the measurement uncertainty of the ATI sensor for a calibration load of 6.8925 N, where the uncertainty suddenly increases due to an increase in the repeatability uncertainty. The sudden increase in repeatability uncertainty could for example be caused by dropping a calibration weight with a bit more force than usual on the stack of calibration weights stacked on top of the force sensor or by adjusting the stack of weights slightly such that they are stacked more concentric with the z-axis of the ATI sensor. Such random effects will not occur, or at least to a less extend, during calibration procedures performed at a professional force sensor calibration facility where dead-weight machines can be used to exert forces on the sensor with a high repeatability in the way force is exerted. An alternative method, less sensitive to these 'random' disturbances, might therefore be appropriate to analyze the data acquired during calibration of the ATI Nano 17. ISO 376 specifies furthermore the lowest calibration force for which the calibration results are valid. This minimum calibration force depends on the resolution of the force sensor and the class of the force sensor. The worse the accuracy of a force sensor, the higher the class of the sensor and the lower the minimum calibration load for which the calibration results are regarded as valid. The ATI Nano 17 falls outside the accuracy classes specified in ISO 376, for example due to the large reproducibility error. 'Small' calibration loads should thus be allowed to calibrate the sensor, though it cannot be derived how small the calibration loads are allowed to be. Calibration results for zero calibration force should however in every case not be used according to ISO 376.

An alternative method, referred to as 'the alternative calibration method' in this thesis, was devised to analyze the performance of the ATI Nano 17 with less sensitivity to random disturbances during the calibration procedure. All readings obtained during the calibration of the ATI Nano 17, including verification series, were used to determine a linear interpolation function

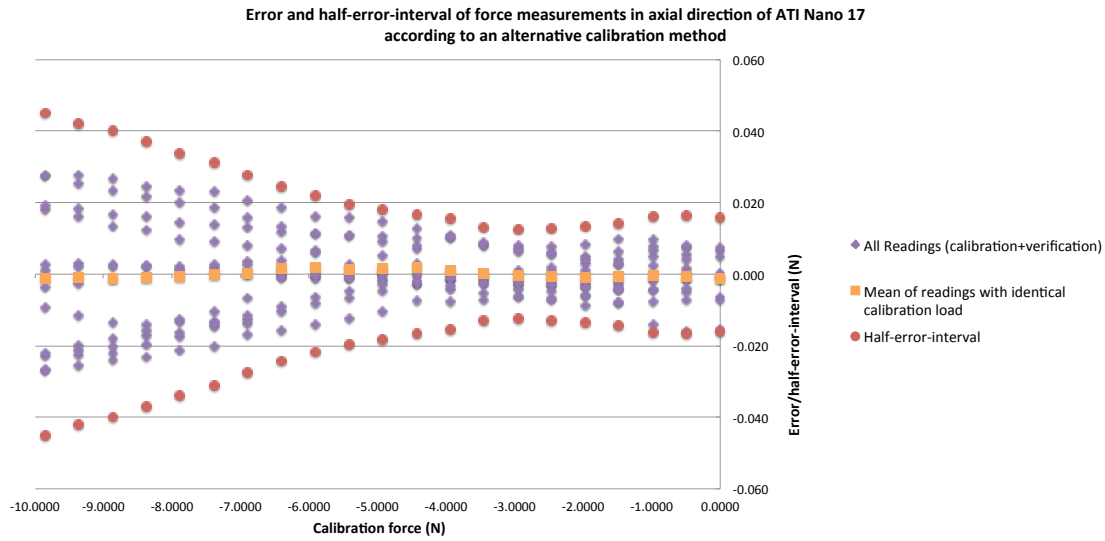


Figure B.7: In purple, the measurement error of all readings of the calibration and verification series with respect to the interpolation function describing the (expected) reading of the ATI Nano 17, determined using the alternative calibration method, as function of the calibration force. In orange, the mean of the error of readings of the calibration and verification series obtained with a certain calibration force with respect to the interpolation function. In red, plus and minus the estimated 'half-error-interval' of force measurements performed with the ATI Nano 17 sensor of forces in axial direction on the sensor.

describing the reading of the ATI Nano 17 as function of the calibration force (equation B.4).

$$F_{ATI} = 0.9676 \cdot F_{True} - 0.00003 \quad (B.4)$$

The 95% confidence interval for the slope is 0.9672 to 0.9681 and -0.0027 to 0.0027 for the intercept. The error of readings with respect to the interpolation function and the mean of the error of readings obtained with a certain calibration force with respect to the interpolation function are shown in figure B.7 as function of the calibration force.

The range in which measurement errors of the ATI Nano 17 occur, was not determined based on a firm statistical basis as an estimate of the interval in which measurement errors occur. The 'half-error-interval' is defined as the maximum observed/estimated difference in readings of the sensor and the true value. The error-interval is thus at most twice the half-error-interval, which is the case when errors are distributed symmetric round the true value. The 'half-error-interval' should be comparable in magnitude to the expanded measurement uncertainty. The standard deviation of the errors and the mean of the errors per calibration force were used to make an estimate of the interval in which measurement errors occur. The 'half-error-interval' of measurements performed with the ATI Nano 17 was estimated as the mean of the error of readings obtained with a certain calibration force plus two times the standard deviation of the error of readings obtained with a certain calibration load plus two times the resolution of an unloaded ATI Nano 17 using a lowpass filter with a cutoff frequency of 500 Hz. The coverage factor with which the standard deviation was multiplied was chosen as an integer number for which all observed errors fall within the error-interval. The estimated half-error-interval of the ATI Nano 17 is shown in figure B.7 as function of the calibration force and is compared table B.3 to the expanded measurement uncertainty according to ISO 376.

The estimated half-error-interval, determined with the 'alternative calibration method', is not based on any firm statistical basis. The half-error-interval does however seem to capture the range of measurement errors for very small calibration forces better than the expanded measurement uncertainty calculated according to ISO 376, that pretends to have statistical significance (but

Table B.3: *Estimated 'half-error-interval' of force measurements performed with the ATI Nano 17 in axial direction of the sensor according to the alternative calibration method and the expanded measurement uncertainty of force measurements performed with the ATI Nano 17 in axial direction of the sensor according to ISO 376 as function of the calibration force applied onto the sensor.*

Calibration force (N)	Half-error-interval (mN)	Expanded measurement uncertainty (mN)
0.0000	16.01	9.13
-0.4928	16.52	18.72
-0.9856	16.22	16.89
-1.4771	14.22	17.80
-1.9693	13.54	19.63
-2.4615	12.84	20.34
-2.9531	12.51	19.28
-3.4445	13.02	20.88
-3.9381	15.54	22.69
-4.4313	16.66	21.54
-4.9239	18.16	24.49
-5.4153	19.55	25.65
-5.9076	21.83	30.90
-6.3999	24.29	30.46
-6.8925	27.68	44.39
-7.3860	31.17	43.90
-7.8789	33.77	44.29
-8.3716	36.97	46.80
-8.8648	39.96	46.69
-9.3573	42.03	47.20
-9.8493	45.16	48.39

which for the way the ATI sensor was calibrated does not really seem to be the case). The errors of readings are furthermore distributed far more symmetrically around the interpolation function when the interpolation function is calculated using the alternative calibration method. This is the result of using all readings to determine the interpolation function, including readings obtained during unloading of the sensor. The half-error-interval is furthermore tighter around the errors of readings obtained with large calibration forces, while all errors still fall (even with quite a margin) within the half-error-interval. The half-error-interval calculated with the alternative calibration method seems therefore a more appropriate method to describe the accuracy of the ATI Nano 17 sensor for the measurement of forces in axial direction on the sensor.

C Requirements in detail

There are quite a few requirements which the final design of a force sensor for the measurement of axial forces on the tip of a needle should fulfill. Achieving all requirements and verifying whether all requirements are met, will be too time consuming for a thesis project. Requirements were therefore designated a certain priority. Requirements designated with a high priority should be validated and obviously preferably met during this thesis project. A distinction is made for most requirements between goals and what actually is required or seems reasonably achievable during this thesis project. Goals are the ultimate target, but might be extremely hard or even impossible to achieve. A (proposal for) a method to validate whether requirements are met, will be stated where it is appropriate.

C.1 Needle/stylet design

Needle gauge: Diameter of the needle in which the force sensor should fit.

Priority: High

Goal: Fits inside the stylet of a 18 G trocar needle ($\varnothing 1$ mm for the stylet of a Cook DTN-18-20.0-U trocar needle).

Required: Fits inside the stylet of a 14 G or smaller diameter needle.

Rationale: The range of 14 G to 18 G represents commonly used core needle biopsy needles. The effort to achieve the amount of miniaturization required to fit a force sensor inside a needle with these diameters is expected to be acceptable, as FBG-based force sensors were already integrated in needles with a similar diameter at the TU Delft and elsewhere [1, 2]. Integrating the sensor in a 18 G needle seems the most challenging and is therefore the best possible demonstration of the applicability of the sensor in real needles. Furthermore, the two other fiber-optic force sensors for the measurement of axial forces on a needle tip shown in literature were shown for 18 G needles, hence designing the sensor for a 18 G needle will make comparison with the performance of the sensors presented in literature possible [1, 2].

Needle length: Length of the needle for which the force sensor will be designed.

Priority: Low

Goal: About 200 mm.

Rationale: The 18 G trocar needles readily available at the university (Cook DTN-18-20.0-U) are 200 mm long and can be used to determine other requirements on the

design of a force sensor for such a needle.

Stylet tip shape: Shape of the tip that will be used for the stylet.

Priority: Medium, a good tip shape will minimize transverse force on the needle tip.

Goal: A reflectional symmetric stylet tip shape of a commercially available stylet of a trocar needle.

Required: A reflectional symmetric conventional needle tip shape.

Rationale: Conventional needle tips are accepted for clinical purposes. Reflectional symmetry of the tip (most standard needle tip shapes are reflectional symmetric) will ensure minimal transverse forces onto the needle tip that can be a cause of measurement errors and cause excessive loads on the force sensor.

Strength: Loads that the needle and sensor should be able to support without permanent damage (for a 200 mm long 18 G needle).

Priority: High

Goal: The needle should be able to support at least 2 times the maximum axial force at the needle hub reported in literature (table 2.1) in the axial direction towards the needle hub (compressive loading of the sensor) and 2 times the maximum estimated transverse load on the needle tip. The needle should furthermore be able to withstand the maximum reported load in axial direction at the needle hub towards the hub and the maximum estimated transverse load on the tip for a preferably infinite number of cycles or at least 10^4 loading-unloading cycles (respectively 9 N and 1 N for a 18 G needle).

Required: The needle should be able to support the maximum axial force at the needle hub reported in literature in axial direction towards the needle hub (compressive loading of the sensor) and the estimated maximum transverse force on the needle tip for a large number of cycles (100+) and should survive handling during calibration procedures.

Rationale: It is highly undesirable that the needle breaks down during needle insertion. Large pulling forces on the tip are not expected, hence only requirements with respect to axial forces towards the needle hub and transverse forces on the tip are defined. No (additional) safety margins are assumed for the requirements on the maximum forces that the needle should be able to support, as the used maxima are forces on the hub for the maximum axial load and a crude estimate for the maximum transverse load. The actual force on the force sensor and the needle tip (the focus of this thesis) will very likely be significantly less. Whether the needle shaft, far away from the sensor, has some safety margin to be capable to support the maximum loads is not of primary importance for this thesis (as it should be easily achievable). The goal is of course to have some additional safety margin after the prototype phase, because the chance that the needle breaks down should be absolutely minimal. The needle should furthermore preferably be capable of sustaining a large number of loading-unloading cycles and thus not fail due to fatigue. Assuming an infinite number of loading-unloading cycles will ensure a good safety margin. However, assuming a few thousand loading-and-unloading cycles should be sufficient, as the needle will be replaced quite frequently because the needle tip will become blunt during the insertions. The needle will not be exposed to a large number of loading-unloading cycles when it is used as a disposable instrument (not desirable as the needle with sensor will likely not be very cheap), hence the fatigue strength of the needle should not necessarily be taken into account. It seems unlikely that a disposable needle will be exposed more than a 100 times to the maximum load during single usage of the needle.

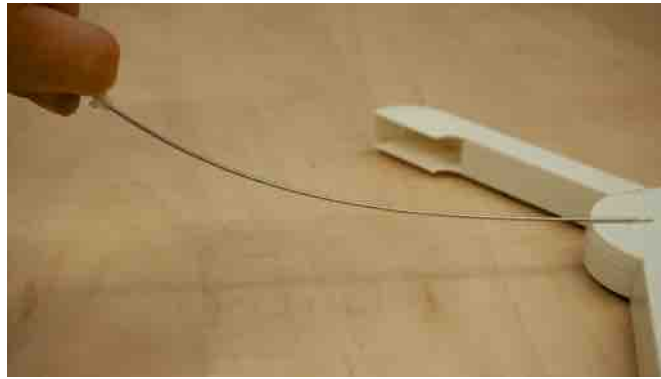


Figure C.1: Test to determine the maximum transverse load that can be exerted with reasonable effort onto the region of the needle tip of a 200 mm long 18 G needle, without inserting the needle into tissue, before bending of the needle becomes problematic.

Transverse forces on the needle tip are expected to be much lower than axial forces on the needle tip during normal usage of the needle. The magnitude of transverse forces on a needle tip is however not (well) quantified in literature, hence some estimates have to be used. Podder et al. found that the transverse force at the needle hub of a 18 G needle increases during robotic needle insertion from 0 N at the surface to a maximum transverse force of 0.2, 0.4 and 0.6 N with respectively a diamond, blunt and conical needle tip at an insertion depth of 12 cm (which was the maximum insertion depth) in 'stiff' phantom tissue (the maximum axial insertion force was respectively approximately 11, 9 and 19 N) [234]. The transverse force is in this experiment thus mainly the result of bending of the needle and transverse forces acting on the needle shaft and not specifically forces on the needle tip. Podder et al. experienced resultant transverse forces at the hub of a 18 G needle up to about 0.71 N during in vivo needle insertions into prostate tissue [67]. Misra et al. performed a study on transverse forces on beveled asymmetric needle tips by inserting scale models with a very large diameter (1.5 cm) into phantom tissue [235]. The transverse force was approximately zero for relatively blunt needle tips with a bevel of 45° or larger (although their model predicted transverse forces up to about 1 N for these bevel angles) [235]. It seems therefore reasonable that the transverse force on a smaller, symmetric needle tip should be significantly lower than 1 N in phantom tissue.

The 'maximum transverse tip force' to which a needle tip of a 200 mm long, 18 G trocar needle, consisting of a cannula and a stylet made of stainless steel, can be subjected without being inserted into tissue, was experimentally determined on a balance (figure C.1). The 'maximum' was defined as the moment that it becomes very difficult to exert more transverse force manually on the needle tip when the needle is held at the hub due to bending of the needle. It appeared to be difficult to exert more than 1.1 N (110 gr) onto the needle tip, where the needle tip in this case is considered as the actual tip and a part of the shaft in contact with the balance.

It seems appropriate to assume that transverse forces on a symmetric needle tip will remain below 1 N, based on some evidence found in literature and a simple experiment. It should however be noted that neither the experiment nor the presented literature is representative for in vivo needle insertion, as transverse forces measured at the needle hub are no actual measure for forces on the needle tip. Phantom tissue, and prostate tissue are furthermore not representative for the entire range of tissues

that a needle might experience. Moreover, tissue motion, like motion of muscles, might potentially induce very large transverse forces onto the needle tip that are difficult to simulate or estimate without inserting the needle into living tissue.

How to validate: The assembled needle should be subjected to the critical axial and transverse forces with a testing machine. The critical load should be applied with (at least) 100 loading-unloading cycles, after which the needle and in particular the sensor should be inspected for damage. This procedure should preferably be carried out for more than 1 prototype. The needle should then be subjected to increasing loads until the needle, in particular the sensor, visibly breaks down. A 18 G needle with sensor is hence required to be able to support at least a load of 9 N in the axial direction and 1 N in transverse direction on the needle tip for 100 loading cycles and survive handling in the lab. The strength of the design can then be tested with various insertions in, for example, cadavers, to verify that the assumed strength requirements are not exceeded in practice or whether certain critical load cases resulting in damage were not considered during the design of the sensor. It will have to be determined whether the estimated maximum transverse force on the needle tip is representative for in vivo needle insertion by means of a number of in vivo needle insertions in animal models or slightly moving phantom tissue samples and observing whether failure of the sensor in the needle tip occurs.

Material Materials used for the tubing of the stylet/needle and the needle tip.

Priority: Low, the prototype of the needle is not required to be biocompatible to assess the performance, while 'perfectly' MRI compatibility of the final needle is an advantage but not a requirement.

Goal: Biocompatible and MRI compatible materials.

Rationale: A hypodermic needle is a medical device for invasive usage. Biocompatibility of materials that will be in contact with patient tissue is thus required. Ensuring biocompatibility will require a lot of testing when 'strange' materials are used for which no reports of biocompatibility exist. ISO 10993 can be used as guideline to test whether the needle is biocompatible. MRI compatibility of used materials is an advantage as the main application of the needle with force sensor, enhancing haptic feedback during needle insertion, would be valuable during robotic insertion with MRI guidance. Stainless steels of the 300 and 400 series are commonly used for needles [14]. The majority of 'current' MRI compatible needles use materials like titanium, steel, cobalt-chromium alloys and nitinol for the mandrel and needle shaft, although it is noted that these needles introduce some small artifacts in the acquired MR images [117]. Usage of polymers or ceramics instead of metals for the needle and stylet shaft would be preferable to ensure 'perfect' MRI compatibility and MRI safety of the entire needle, not only the optical force sensor. Adaptability of a certain design to a MRI compatible design is regarded as an advantage but is not required, as pursuing 'perfect' MRI compatibility might be disadvantageous for applications that do not require MRI compatibility. Usage of a polymer needle might for example result in fast wearing needle tips or difficulties in designing a good force sensor that is also suited for research on needle-tissue interaction.

C.2 Measurement system/sensor design

Quantity to measure: Quantity that has to be measured with the sensor integrated in the tip of the needle.

Priority: High

Required: Force exerted axially on the tip of the needle.

Rationale: The quantity of interest for enhancing haptic feedback of a needle, research on needle insertion forces, measurement of tissue stiffness and prediction of buckling of the needle is the force in axial direction on the needle tip.

Range: Range of forces that the sensor should be able to measure with the required accuracy.

Priority: High

Goal: The force sensor should be able to measure forces (with the required accuracy) up to 110% of the in literature reported maximum axial load at the hub of needles with an identical gauge (table 2.1). The sensor for a 18 G needle is hence required to be able to measure forces up to approximately 10 N with the required accuracy.

Required: The sensor should be able to measure forces (with the required accuracy) up to the maximum axial force on the tip of needles with an identical gauge reported in literature (table 2.1) with a margin of 10%, as the reported maximum forces are generally average values. The maximum measurable force on the needle tip should therefore be about 6 N for a 18 G needle.

Rationale: Ideally the entire range of forces exerted on the needle tip should be measurable with the required accuracy during normal usage of the needle. Not much reliable data is available to make an estimate of the maximum force on a needle tip during normal usage of the needle, as needles equipped with adequate needle tip force sensors are scarce. Available data on axial forces measured at the needle hub and estimates of the tip force were therefore used. A study by Podder et al. shows that the maximum axial force occurs at a very low penetration depth [67]. The maximum force is therefore likely caused by forces due to cutting of skin-tissue, which consist mainly of forces acting on the needle tip instead of friction forces. The acquired data on axial forces on the needle from literature is not necessarily representative for all kinds of 'normal procedures', as the axial force depends strongly on the insertion location, tissue type, insertion depth, the insertion speed, axial rotation of the needle, lubrication, presence of a stylet and needle tip shape [13]. Increasing the safety margin on the measurement range of the sensor is however initially not preferable for the design of the prototype of the needle, as this will require an increase in dynamic range of the sensor to maintain identical resolution. It is furthermore expected that the peak insertion forces will generally be lower than the maximum insertion forces reported by Podder et al. as other studies (in which in some cases somewhat less representative experiments were performed) showed two to four times smaller maximum axial forces on the needle hub/needle tip compared to the maximum axial force reported by Podder et al. [67, 13, 28, 22]. Moreover, the blunt edge of the outer cannula surrounding the stylet tip is suspected to be a main contributor of axial force on a needle measured at the needle hub, though only force on the stylet tip will be measured. Assuming the maximum reported estimate of the tip force on a needle with some margin to determine the measurement range will therefore very likely be sufficient to measure all relevant needle insertion forces during most procedures. Needle insertion experiments with the prototype of the needle could give more information on the useful measurement range for a needle-tip force sensor, which can be used to modify the requirements for the next version of the design. Finally, depending on the measurement principle, forces outside the measurement range could still be measurable, although with less accuracy than the accuracy required within the measurement range. The exact magnitude of large forces is for the main application, haptic feedback, often not relevant. The presence of a force peak, irrespective of its exact magnitude, will indicate membrane punctures.

How to validate: The range of the sensor can be determined by calibrating the sensor

according to ISO 376 or an equivalent method and determining up to which calibration load readings of the sensor remain within the required accuracy. Usage of this definition of the measurement range will automatically ensure that the sensor meets requirements on the accuracy. An alternative definition of the measurement range, useful when the required accuracy cannot be met over a large range of loads, is the range for which monotonically increasing or decreasing loads on the needle tip result in monotonically increasing or decreasing readings of the sensor. The range according to this definition can be determined by plotting the output of the sensor versus the applied calibrated loads on the sensor and validating whether the response of the sensor keeps monotonically increasing or decreasing within the entire range of calibrated loads.

Measurement uncertainty/Accuracy: Dispersion of the obtained sensor readings around the true value of the measured quantity due to random and non-compensated systematic errors [109].

Priority: High

Goal: A 'half-error-interval' or measurement uncertainty equal to or lower than the measurement uncertainty of the ATI Nano 17, while the sensor is subjected to the entire range of disturbances that can reasonably be expected to act onto the sensor (as specified in definition C.2.1), in particular disturbances due to temperature variations of the environment between 17°C and 41°C. The goal is thus a maximum half-error-interval of ± 16 mN or smaller at zero load and a half-error-interval of ± 45 mN or smaller for a load of 10 N, as presented in appendix B, under disturbances induced by temperature fluctuations, transverse loads on the sensor, bending of optical cables, among others.

Required: A half-error-interval or measurement uncertainty of 500 mN or better throughout the entire measurement range under disturbances due to temperature variations of the environment between 17°C and 41°C, as specified in definition C.2.1.

Rationale: A low measurement uncertainty is particularly beneficial when the sensor is used for research on needle insertion forces or measurement of tissue stiffness. The ATI Nano 17 is at the moment regarded as sufficient for this application. Haptic feedback, the main application for which the sensor will be designed, is not expected to require a particularly low measurement uncertainty but requires a reasonable low cross-sensitivity to temperature as the application is (nearly) always in vivo. It might be (very) unrealistic to achieve a measurement uncertainty comparable to the measurement uncertainty of the ATI Nano 17 throughout the entire range and under all types of disturbances. The performance of the design of the fiber-optic needle tip force sensor that should be improved, the design by Gähler, is therefore used as minimum for the required performance [1]. Moreover, the measurement uncertainty is required to be improved such that the performance of the sensor by Gähler can be achieved throughout the entire range of expected temperature disturbances. The measurement uncertainty was not very clearly defined by Gähler, hence the 'half-error-interval' was based on the mean of the maximum measurement error observed in figure D.27 (0.75 N) and the maximum error reported in figure D.26 disregarding outliers (0.25 N).

How to validate: The 'half-error-interval' is defined as the maximum observed difference in readings of the force sensor and the true value. The error-interval is thus at most twice the half-error-interval, which is the case when errors are distributed symmetric round the true value. The 'half-error-interval' should be comparable in magnitude to the expanded measurement uncertainty. The sensor should be calibrated with an

accurate reference sensor according to ISO 376 or the 'alternative calibration method' presented in appendix B or a similar method to assess its measurement uncertainty, while the sensor is subjected in a controlled way to the expected disturbances to assess the influence of the disturbance on the measurement uncertainty. Whether the sensor meets the requirements can be validated (at least approximately) by comparing the sensor to the ATI Nano 17, while identical loads are applied onto both sensors by connecting them in series. Comparing whether the sensor meets the goal is more difficult and can be validated for the lower part of the range by testing the sensor on a precise analytic balance (without disturbances). A special calibration device with an extremely low measurement uncertainty will have to be used to verify whether the performance of the fiber-optic sensor approaches the performance of the ATI Nano 17 throughout its entire measurement range. Using very precise weights to calibrate the fiber-optic sensor, like the calibration of the ATI sensor was performed in appendix B to determine the goals on the accuracy, seems not feasible due to the small size of the sensor relative to the size of the weights used to exert 10 N.

Definition C.2.1 — Range of disturbances of the environment. Temperature, relative humidity and atmospheric pressure were determined to be potentially critical parameters of the environment of which disturbances could influence the measurement accuracy of a force sensor based on a fiber-optic Fabry-Pérot interferometer significantly. The temperature of the environment in which the force sensor is used, is expected to fluctuate between 17°C and 41°C during normal usage of the needle, respectively the temperature of a cold operation room (with some margin) and the temperature of a patient with very severe fever [236, 237, 238, 218]. A relative air humidity between 20% and 60% can be expected in an operating theatre according to the standards for ventilation of healthcare facilities, but the sensor can be exposed to wet environments when the needle is inserted into the body of a patient [239, 240]. Data of the KNMI, measured at De Bilt from september 2000 to september 2014 measured, show an average atmospheric pressure of 101.5 kPa, while the atmospheric pressure fluctuates daily on average with 0.6 kPa and fluctuated at most with 4.2 kPa on a single day (figure D.28) [241]. Transverse forces on the needle tip and handling and movement of the needle are other disturbances that could result in measurement errors. The maximum transverse force on the tip was assumed to be 1 N, as argued on page 168. Handling of the needle will mainly causes bending of cables connecting the needle with read-out equipment.

Bandwidth: Cut-off frequency (-3 dB) of the measurement system, which determines the frequency up to which the measurement system has a good sensitivity to the measured quantity.

Priority: Medium

Goal: 500 Hz or more.

Required: 100 Hz or more.

Rationale: Most interesting frequencies for needle insertion into soft tissue are in the tens of Hertz, although scraping over hard or textured surfaces might introduce frequencies over 100 Hz [2]. Frequencies up to 500 Hz are required for convincing kinesthetic feedback according to some [18]. A sample frequency of more than 1 kHz will be required to achieve this bandwidth to prevent aliasing effects. Reduction of the sampling frequency might however be required to satisfy the more important requirements on measurement accuracy and resolution.

Resolution: (Half the) range of fluctuations of acquired readings of the sensor under constant load after signal processing like lowpass filtering.

Priority: Medium

Goal: 3 mN or better.

Rationale: The performance of the ATI Nano 17 is used as a reference for the required resolution. It is expected that a good resolution is regarded as beneficial during haptic feedback to discern very small changes in force related to soft membranes. Whether the resolution of the ATI Nano 17 exceeds requirements on the resolution for applications like haptic feedback could not be determined. The goal for the resolution was therefore taken as the reported resolution of the ATI Nano 17 [31, 64]. The signal of the ATI Nano 17 is sometimes aggressively low-pass filtered to reduce the amount of noise for research on needle-tissue interaction performed at the TU Delft (for example to remove noise introduced by vibrations induced by the motors of the translational stage used to insert the needle into tissue). Hence, lowpass filtering below the required bandwidth is possible for some applications to achieve resolutions required for applications like research on needle interaction forces. No requirement was set on the resolution, as the resolution depends on the used bandwidth of the measurement system and largely on the optical source and photodetector supplied for the project. Optimizing the system to achieve a required resolution would therefore likely require changing the optical source and/or photodetector.

How to validate: The measurement signal of the unloaded needle tip force sensor should be recorded and appropriately filtered, after which the standard deviation of the fluctuations of the signal can be used to determine the resolution of the sensor, as was performed for the ATI Nano 17 in appendix B. It should be verified that the noise is approximately Gaussian, otherwise another measure, like the minimum and maximum of the fluctuations will have to be used to determine the resolution. The resolution of the loaded sensor should be quantified in case the sensitivity of the sensor is expected to depend significantly on force exerted on the sensor. Quantification of the resolution of the loaded sensor should be performed while the sensor is placed on a stabilized optical table. Stabilization is required to minimize the influence of the (change in) resonance frequency of the measurement setup used to apply forces on the needle on the assessment of the resolution of the sensor, as vibrations of the environment will couple into the system without stabilization.

Measurement principle: Principle of operation of the force sensor inside the needle tip.

Required: The sensor should make use of a fiber-optic Fabry-Pérot interferometer.

Rationale: Fiber-optic sensors were shown to be preferable over electronic sensors when the sensor is used in combination with MRI in chapter 1. Sensors based on Fabry-Pérot interferometry were shown to be suited for construction of very small, sensitive sensors with a relatively low cross-sensitivity to temperature.

Sensor location: Distance between beginning of the bevel of the needle tip and the sensitive part of the force sensor.

Priority: High

Goal: 5 mm or less.

Rationale: The sensor should be located as close as possible to the needle tip to reduce influence from friction between the stylet and tissue and friction between the outer cannula of the needle and the stylet on the measured force on the needle tip to a minimum.

Readout device: Device/equipment containing an optical source and photodetector to 'interrogate' the FPI in the needle tip.

Goal: The OP1550 of Optics11.

Rationale: The OP1550 is used (and designed) by the Vrije Universiteit Amsterdam as readout device for fiber-top sensors based on Fabry-Pérot interferometry using homodyne interferometry. This is ideal for the prototype phase of the fiber-optic needle-tip sensor, as an OP1550 is made available for this project and support for the device should be good. A change of readout device or modification of the interrogation principle can be made in later phases of the design process, as the primary focus of the current design process is on the design of the fiber-optic sensor located in the tip of the needle and not on the (expensive) electronics and optical components of the interrogation device.

Number of FPIs: Number of Fabry-Pérot interferometers used in the needle tip.

Goal: 1 FPI.

Rationale: The needle tip should preferably contain a uniaxial force sensor based on a single FPI, as it will be impossible or difficult to obtain interrogation equipment to interrogate more FPIs during this thesis project, for example for a triaxial force sensor. A design using a single FPI is furthermore cheaper to manufacture, which is an advantage. Work performed by Gähler suggests that an uniaxial force sensor should be sufficient to measure forces in axial direction on the needle tip without suffering from bending of the needle, as long as the force sensor is located on the neutral axis of the needle (this was found to be untrue in this thesis project) [1].

C.3 Guidelines FPI design

FPI cavity length Geometrical length of the cavity between the two mirrors of the FPI.

Goal: 10-100 μm (for an air filled cavity).

Rationale: The longer the cavity length, the worse the visibility of the fringe pattern becomes for extrinsic FPI sensors and hence the worse the signal to noise ratio of the sensor becomes. This becomes particularly apparent when the mirrors of the FPI sensor are not aligned perfectly parallel (figure A.3) [116]. Quantification of the maximum allowable cavity length is difficult, as it depends on many components of the measurement system, like the power of the light source, reflectivity of the mirrors of the FPI and the sensitivity of the optical detector. Yin et al. suggest that the practical maximum length of an EFPI cavity is a few hundred microns [90]. It seems advisable to keep the cavity length, if possible, shorter than 100 μm to ensure good visibility of the fringe, based on figures from literature (figure A.3). A physical limit on the minimum length of an FPI cavity does not seem to exist, as FPI sensors are shown in literature with cavity lengths shorter than the used wavelength [122, 242]. A very short cavity length can however become unpractical, as a source with a very large spectral width or ability to tune its wavelength over a very large range will be required to be able to select the optimal wavelength to ensure operation of the FPI around quadrature when homodyne interferometry is performed, or ensure the coherence length to be shorter than the cavity length when low coherence interferometry is performed. The optical source should be able to tune its wavelength such that a shift of at least $\Delta\phi = \pi/2$ radians in the fringe pattern can be achieved when homodyne interferometry is performed with a low finesse FPI, such that it is possible to tune from the worst case scenario, where the FPI is insensitive to a change in OPD, to quadrature, where the sensitivity of the FPI to a change in OPD is maximal. The minimum cavity length for which this is possible, can be calculated with the equation C.1 (derived from equation A.2) for a source that

can tune its wavelength between λ_1 and λ_2 .

$$\Delta\phi = 4 \cdot \pi \cdot L_{min} \cdot n \left(\frac{1}{\lambda_1} - \frac{1}{\lambda_2} \right) \quad (\text{C.1})$$

The minimum cavity length is about 8.5 μm when the OP1550 is used as optical source in combination with an FPI with an air filled cavity ($n=1$). Shorter cavity lengths are possible when quadrature can be ensured by design or a randomness in the sensitivity of the sensors can be accepted. The minimum safe cavity length of a (very) high finesse FPI sensor can be calculated with $\Delta\phi = 2\pi$. The minimum cavity length of a high finesse FPI is 34 μm when the OP1550 is used to interrogate the FPI with an air filled cavity ($n=1$).

Wedge angle mirrors Angle of deviation of parallelism of the mirrors of the FPI sensor.

Goal: A wedge angle below 2° .

Rationale: Non-parallelism of the mirrors should be minimized to ensure fringe visibility and a good signal to noise ratio [116]. Quantification of allowable non-parallelism is difficult, as is measurement of the non-parallelism of a manufactured FPI. It seems strongly advisable to keep the wedge angle below 2° based on literature (figure A.3).

C.4 Other guidelines

Manufacturability Ease of manufacturing parts of the system and assembling the system.

Priority: High

Goal: Designs using fewer and more simple manufacturing steps are preferred. Designs that are more robust to slight errors in manufacturing are also preferred. Designs that can be produced easily with high repeatability and controllability are strongly preferred.

The refractive index of air
 Material selection for the spring of a force sensitive element
 Determination of temperature and force by using two FPIs
 Selection of the optimal beam
 Strength of quartz glass
 'Low coherence interferometry' with the second generation OP1550
 Details calibration results
 Tables and graphs

D Details

D.1 The refractive index of air

The low cross-sensitivity to temperature of FPI-based strain gages using an air filled FPI cavity compared to the cross-sensitivity of FBG-based strain gages is mainly due to the relatively small dependency of the refractive index of air on the temperature (the thermo-optic coefficient) compared to dependency of the refractive index of silica glass ($\sim 1.2 \cdot 10^{-5}/C$) on the temperature, which is the material used for the 'cavities' of an FBG [95, 243]. The refractive index of air depends, besides on temperature, however also on the (relative) humidity (RH) and the atmospheric pressure [244].

The Fabry-Pérot cavity of the force sensor in the needle tip will in principle be sealed from the environment, hence the relative humidity and pressure inside the Fabry-Pérot cavity will not be equal to the relative humidity and pressure of the environment. The relative humidity will be a function of the temperature when the cavity is perfectly sealed and no absorption or emission of water vapor will take place by the materials surrounding the FPI cavity. This assumption is however far from certain, hence it was assumed, to acquire an estimate of the worst case scenario, that the relative humidity will vary between 0% and 100% in the FPI cavity and the changes in air pressure will correspond to changes in pressure of the environment on an average day. The refractive index of air for light with a wavelength of 1546 nm, the center wavelength of the band in which the OP1550 can tune its wavelength, as function of temperature, relative humidity and atmospheric pressure was calculated with the Ciddor equation [244].

The refractive index of air depends relatively strongly on temperature, modestly on the atmospheric pressure and is almost independent of the relative humidity in the range of normal environmental disturbances. The sensitivity of the refractive index to temperature (linearized between 17°C and 41°C) is $-9.1 \pm 0.4 \cdot 10^{-7}/^{\circ}C$ for relative humidities and atmospheric pressures in the defined range of environmental disturbances. The sensitivity of the refractive index of air to the relative humidity and atmospheric pressure, calculated in a similar way, is respectively $-1.7 \pm 1.0 \cdot 10^{-8}/\%$ RH and $2.6 \pm 0.1 \cdot 10^{-6}/kPa$. The change in refractive index can, within the defined range of fluctuations of the environment, be approximated with equation D.1, with the temperature T in degrees Celcius, the relative humidity RH in % and the pressure P in kilopascals.

$$dn = \frac{\partial n}{\partial T} dT + \frac{\partial n}{\partial RH} dRH + \frac{\partial n}{\partial P} dP = -9.1 \cdot 10^{-7} dT - 1.7 \cdot 10^{-8} dRH + 2.6 \cdot 10^{-6} dP \quad (D.1)$$

Fluctuation of the temperature, relative humidity and atmospheric pressure within the expected range of fluctuations of the air conditions can cause a change in refractive index of respectively $-2.2 \cdot 10^{-5}$, $-1.7 \cdot 10^{-6}$ and $1.3 \cdot 10^{-6}$ of the refractive index of air. The effect of fluctuations of temperature is more than one order of magnitude larger than the effect of changes in pressure and relative humidity. The refractive index was therefore assumed to be solely a function of temperature for this thesis, as the relative humidity and pressure are expected not to fluctuate as extremely as in this worst case scenario.

D.2 Material selection for the spring of a force sensitive element

A material selection procedure was performed to select the optimal material for the force sensitive element of a sensor designed according to the unmachined-quartz-column or the in-fiber-FPI concept. The force sensitive element in these concepts acts like a spring. The spring will be shaped like a tube and fabricated in a column with a circular cross-section protruding out of the stylet of the needle, as detailed on page 42 and shown in figure 3.6. The Fabry-Pérot cavity is located inside the tube and has a diameter equal to a single mode fiber. The column was assumed to be made of a single material, although it will in practice also contain an optical fiber attached to the column and the FPI mirrors.

D.2.1 Constraints

The part of the column protruding out of the stylet should be suited to withstand stresses due to transverse forces on the needle tip, which will be shear stresses and bending stress. The maximum expected transverse force on the needle tip of 1 N, experimentally determined for the requirements on the design, acted not on the very tip of the needle at all, but on the first few centimeters of the shaft of the needle near the needle tip (figure C.1). The part of the column protruding out of the stylet would in such a case be subjected barely to transverse forces. The point of application of transverse forces on the needle tip might however be more near the very tip of the needle when the sharp tip is inserted into tissue. The maximum moment arm of the transverse forces on the column is therefore assumed to be 1.5 mm (thus resulting in a maximum bending moment of $1.5 \cdot 10^{-3}$ Nm) (figure 3.6). Because of all assumptions already made about the magnitude of the transverse force on the needle tip, no additional safety factors were taken into account for the material selection.

The maximum shear stress will occur at the location where the cross-section of the column is the smallest, which is part of the column that contains the FPI cavity. The column will for the largest part be supported by the stylet tube. Only the part of the column protruding out of the stylet tube should be capable of carrying the moment resulting from the transverse force on the needle tip. The maximum bending moment will occur in the part of the column the furthest away from the needle tip, where the cross-section of the column contains the optical fiber. The combined effect of the the shear and bending stress will not be considered for sake of simplicity (though should be validated, for example with finite element simulations, for the final design).

The maximum shear stress in a thin-walled tube is two times the average shear stress (equation D.2) [245].

$$\tau_{\max} = 8 \frac{F_{\text{transverse}}}{\pi(d^2 - d_{\text{fiber}}^2)} \quad (\text{D.2})$$

This should be a conservative estimate for the maximum shear stress in the column, as the tube part of the column is very likely not thin walled, in which case the maximum shear stress will be significantly lower [245]. The shear stress can be converted to an equivalent tensile stress using the von Mises criterion with equation D.3, which is necessary to be able to determine whether

the column, made of a ductile material, will deform plastically based on the given yield stress of a certain material [245].

$$\sigma_{\max_1-MISES} = \sqrt{3}\tau_{\max} = \sqrt{3} \cdot 8 \frac{F_{\text{transverse}}}{\pi(d^2 - d_{\text{fiber}}^2)} \quad (\text{D.3})$$

The Tresca-criterion is more appropriate to calculate the equivalent tensile stress for brittle materials to determine whether the material will fail due to the shear stress [148]:

$$\sigma_{\max_1-TRESCA} = 2\tau_{\max} = 16 \frac{F_{\text{transverse}}}{\pi(d^2 - d_{\text{fiber}}^2)} \quad (\text{D.4})$$

The maximum tensile stress due to a bending moment for a column with a circular cross-section can be calculated with equation D.5. This equation neglects the stress concentration due to the step in diameter between the column and the supporting stylet tube. This assumption does likely result only in small errors, as the stress concentration can be reduced by the compliant glue layer connecting the stylet tube and the column of the elastic element (unless the column and stylet tube are one monolithic part, in which case the diameter step can be easily avoided or a diminished by a fillet).

$$\sigma_{\max_2} = \frac{Md}{2I} = \frac{Md}{2 \frac{\pi}{64} d^4} = \frac{32M}{\pi d^3} \quad (\text{D.5})$$

The selection of materials can thus be narrowed down based on the stress for which the material should not fail or deform plastically based on the occurring stresses for a given column diameter ($\sigma_{\max_1} \leq \sigma_{\text{yield}}$ and $\sigma_{\max_2} \leq \sigma_{\text{yield}}$). It is however not necessary to regard failure or plastic deformation due to shear at the location of the FPI cavity any further, as the equivalent stress due to shear will always be lower than the tensile stress due to the bending moment for columns with a diameter of 1 mm or smaller.

A minimum length of the Fabry-Pérot cavity 8.5 μm is preferable according to the requirements when the FPI will be interrogated with the OP1550 device and the FPI cavity is filled with air. The Young's modulus of the selected materials should thus be such that the FPI cavity has to be longer than 8.5 μm to achieve the desired change in cavity length due to application of the maximum axial force of 10 N on the needle tip. The desired change in FPI cavity length due to application of the maximum axial force on the sensor is about 100 nm, based on figure 3.9, which should result in a sensor with an approximately 10% difference in sensitivity within the measurement range when an air filled FPI cavity and FPI mirrors with a reflectivity of about 0.04 (glass-air transition) are used. The minimum Young's modulus of the material used for the column was estimated based on the cross-section of the column at the location of the FPI cavity and the minimum cavity length (equation D.6 and D.7).

$$8.5 \mu\text{m} \leq L_{\text{cavity}} = \frac{dl_{\text{cavity}} \cdot E \cdot A}{F_{\text{axialmax}}} = \frac{100 \cdot 10^{-9} \cdot E \cdot \pi(d^2 - d_{\text{fiber}}^2)}{40} \quad (\text{D.6})$$

$$E \geq \frac{40 \cdot 8.5 \cdot 10^{-6}}{\pi(d^2 - d_{\text{fiber}}^2) 100 \cdot 10^{-9}} = \frac{3.4 \cdot 10^3}{\pi(d^2 - d_{\text{fiber}}^2)} \quad (\text{D.7})$$

The effect of the glue connecting the optical fiber to the column was neglected for simplicity, although FE-simulations show that compliant glue can cause a significant (undesired) increase in sensitivity of the FPI to force applied on the needle tip.

D.2.2 Optimality criterion

The optimality criterion for the selection of materials for the column was based on equation 3.9. The compliance of the FPI should be written as function of the cross-section of the column, the

length of the FPI cavity and the Young's modulus of the material of which the column is made (equation D.8).

$$c = \frac{L_{cavity}}{EA} = \frac{4L}{\pi E (d^2 - d_{fiber}^2)} \quad (D.8)$$

Hence, the optimality criterion, to be minimized, was defined as:

$$C_{opt} = \left(\frac{(2L_{cavity} \frac{\partial n}{\partial T} + 2n \cdot CTE \cdot L_{cavity}) dT}{\left(2L_{cavity} \frac{\partial n}{\partial F} + 2n \frac{4L_{cavity}}{\pi E (d^2 - d_{fiber}^2)} \right) dF} \right) \quad (D.9)$$

The Fabry-Pérot cavity medium will be air, hence the refractive index ($n=1$), thermo-optic coefficient ($\frac{\partial n}{\partial T} = -9.1 \cdot 10^{-7}$ which was determined in appendix D.1) and the elasto-optic coefficient ($\frac{\partial n}{\partial F} = 0$) can be filled in, besides the diameter of the optical fiber (125 μm), the maximum change in temperature that will occur due to disturbances of the environment (24°C) and the range of axial forces that will be measured (10 N), while the length of the FPI cavity drops out of the equation because the compliance of the elastic element was assumed to be a function of the length of the FPI cavity for the investigated concepts. The criterion states the ratio of the change in OPD that occurs due to the maximum expected change in temperature and the change in OPD due to the maximum expected change in force on the sensor (that should be measurable). The criterion can be expressed as a maximum measurement error in Newtons due to a change in temperature of 24°C by multiplying the criterion with the maximum axial force that will be measured. The criterion, to be minimized, becomes then:

$$C_{opt} = 6 \cdot \pi \cdot (-9.1 \cdot 10^{-7} + CTE) \cdot E \cdot (d^2 - 1.56 \cdot 10^{-8}) \quad (D.10)$$

This criterion was used to determine the optimal material for the column with a given diameter that will result in the smallest possible measurement error due to disturbances of the temperature of the sensor, based on the CTE and the Young's modulus of the material of the column at constant temperature. Reduction of the column diameter results in a reduction of the cross-sensitivity of the sensor to temperature, as the sensitivity to force will increase. The minimal column diameter can be calculated as function of the yield strength of the material of the column, as the bending stress 'solely' constrains the column diameter for columns with a diameter smaller than 1 mm. The minimal column diameter is given by:

$$d = \sqrt[3]{\frac{32M}{\pi \sigma_{yield}}} \quad (D.11)$$

The optimization criterion for the ideal column with respect to geometry and material to be minimized becomes then:

$$C_{opt-criticaldiameter} = 6 \cdot \pi \cdot (-9.1 \cdot 10^{-7} + CTE) \cdot E \cdot \left(\sqrt[3]{\frac{0.048}{\pi \sigma_{yield}}}^2 - 1.56 \cdot 10^{-8} \right) \quad (D.12)$$

D.2.3 Results

Materials selection was performed using the materials database of the CES edupack software [131]. Only ceramics, glasses, metals and polymers were considered. Some manual filtering was performed to remove uninteresting variants of certain materials, very obscure or clearly unsuited materials and most of the fiber filled materials from the selection. The results of the material selection for columns with a diameter of 0.25 mm, 0.5 mm, 0.75 mm and 1 mm are presented in table D.1 to table D.4 and report the expected range of errors due to a change of temperature of the force sensor from 17°C to 41 °C, that should be occur according to this simple model for a

column made of a certain material and a given diameter. The results of a material selection for columns with the optimal diameter are presented in table D.5, which shows the lower and upper bound of the error induced by the cross-sensitivity to temperature of the force sensor and also displays the minimal diameter of the column, which should be feasible with the highest expected yield strength of the material, and the 'safe' diameter of the column, based on the lowest reported yield strength. The half-error-interval due to the considered effects is in practice only half of the error presented in the tables, as the sensor can be calibrated at the average temperature of the range of expected temperature disturbances.

Table D.1: Lower and upper bound of the estimate of the error induced by a change of temperature from 17°C to 41°C of a force sensor based on the unmachined-quartz-column concept or the in-fiber-FPI concept using a 1 mm diameter column as force sensitive element, as function of the material of which the column is made.

Diameter column: 1 mm		
Material	Min error (N)	Max error (N)
<i>Titanium silicate</i>	-1.1	-1.1
<i>Cold worked Invar</i>	-1.1	2.8
<i>Silica (quartz fused)</i>	-0.6	-0.5
<i>Silica (96%)</i>	-0.2	-0.2
<i>Glass ceramic -slipcast</i>	-0.2	-0.2
<i>Graphite</i>	-0.1	1.1
<i>Lithium aluminosilicate</i>	-0.1	0
<i>Glass ceramic - 0330</i>	0.1	0.1
<i>Carbon (industrial)</i>	0.1	0.7
<i>Polyester liquid crystal (30% carbon fiber)</i>	0.1	2.9
<i>Polyester liquid crystal (30% glass fiber)</i>	0.3	14.7
<i>Terracotta</i>	0.4	1.1
<i>TPU (40% bariumsulfate)</i>	0.7	1.4
<i>Invar (annealed)</i>	0.9	2.8
<i>Hard rubber (Ebonite)</i>	1	1.1
<i>Polypropylene (clarified/nucleated)</i>	1.1	1.2
<i>Polyamide (type 46)</i>	1.2	1.5
<i>Polyimide (thermoset)</i>	1.2	4.1

D.2.4 Discussion

It can be observed in table D.1 to table D.4 that, obviously given the optimality criterion, the error due to temperature disturbances reduces with a reduction of the diameter of the column. The amount with which the column diameter can be reduced is limited due to criterion on the yield strength of the materials. Usage of a glass as material for the column could result in particular in a low cross-sensitivity to temperature, mainly due to the low CTE of most glasses that nearly 'matches' the thermo-optic coefficient of air in some cases. The disadvantage of glasses is their brittleness, hence exceeding the maximum tensile stress due to bending will result in immediate failure of the column and thus loose parts of the needle inside a patient. Glass ceramic - 0330 appears to be the toughest well performing glass and only, together with nearly pure silica, 'suited' for columns with a diameter of 0.5 mm. The thermal expansion coefficient and Young's modulus of lithium aluminosilicate are however a fraction better than the CTE and Young's modulus of glass ceramic - 0330 when a somewhat larger column diameter is preferred.

Table D.2: Lower and upper bound of the estimate of the error induced by a change of temperature from 17°C to 41°C of a force sensor based on the unmachined-quartz-column concept or the in-fiber-FPI concept using a 0.75 mm diameter column as force sensitive element, as function of the material of which the column is made.

Diameter: 0.75 mm		
Material	Min error (N)	Max error (N)
<i>Zerodur</i>	-0.8	-0.8
<i>Cold worked Invar</i>	-0.6	1.6
<i>Silica (quartz fused)</i>	-0.3	-0.3
<i>Silica (96%)</i>	-0.1	-0.1
<i>Graphite</i>	-0.1	0.6
<i>Lithium aluminosilicate</i>	-0.04	0.01
<i>Glass ceramic - 0330</i>	0.03	0.05
<i>Polyester liquid crystal (30% glass fiber)</i>	0.1	1.62
<i>Polyester liquid crystal (30% glass fiber)</i>	0.2	8.2
<i>Invar (annealed)</i>	0.5	1.6
<i>Hard rubber</i>	0.6	1.4
<i>Polyimide</i>	0.7	2.3

The most interesting glass is fused quartz (silica), as it is available in ferrule form, which is a cylindrical element with a borehole for an optical fiber and thus perfectly suited to make the column of the force sensitive element. Ferrules are also available in various types of borosilicate glass (for example Duran glass, with a CTE of $3.3 \mu\text{strain/K}$, and used at the VU Amsterdam for ferrule-top AFM sensors). Borosilicates have however much worse properties compared to fused quartz glass for this particular application and were therefore not even worth mentioning in the material selection tables. Ferrules made of glass ceramic - 0330 or lithium aluminosilicate could not be found (references to glass ceramic - 0330 outside the CES software could not even be found at all). Making a precise borehole for an optical fiber in a glass column seems not possible with the facilities available at the TU Delft. Another advantage of a fused quartz column is that the elastic and thermal properties of the column will match the properties of fused silica optical fibers, which was found to be extremely important to achieve an intrinsic low cross-sensitivity to temperature and is elaborated on page 57. Constant measurement errors due cross-sensitivity to temperature of a sensor made with a fused quartz column will (according to this very simple model of an FPI based sensor) not exceed the required 'half-error-interval' of the force sensor, though result measurement errors larger than the half-error-interval of the ATI Nano 17, which was the goal for the accuracy of the sensor.

Plastics can only be used for relatively large diameter columns. They do not have a particularly good performance due to their quite large CTE although their Young's modulus is relatively low in general. Performance of plastics can be significantly worse than shown in the results, as their Young's modulus can depend significantly on temperature in some cases and thereby introduce a cross-sensitivity to temperature in the form of a modifying error, which was not considered in the criterion for the material selection. Usage of a plastic column seems therefore not recommended at all for a sensor with an intrinsic low cross-sensitivity to temperature and an air filled-FPI cavity. Plastics filled with either glass-fibers and carbon-fibers have in theory a better mechanical and thermal performance than unfilled plastics and would in theory be suited for very small diameter columns. The dimensions of the filling material will however be close to the actual dimensions of the column, which makes filled plastics not usable.

Metals are not preferable for applications of the sensor where MRI-compatibility and MRI-

Table D.3: Lower and upper bound of the estimate of the error induced by a change of temperature from 17°C to 41°C of a force sensor based on the unmachined-quartz-column concept or the in-fiber-FPI concept using a 0.5 mm diameter column as force sensitive element, as function of the material of which the column is made.

Diameter column: 0.5 mm		
Material	Min error (N)	Max error (N)
<i>Cold worked Invar</i>	-0.3	0.7
<i>Silica (96%)</i>	-0.1	0.0
<i>Glass ceramic - 0330</i>	0.01	0.02
<i>Polyester liquid crystal (30% carbon fiber)</i>	0.0	0.7
<i>Polyester liquid crystal (30% glass fiber)</i>	0.1	3.5
<i>Invar (annealed)</i>	0.2	0.7
<i>Nitinol (martensic)</i>	0.7	1
<i>Silicon</i>	0.7	1.6

Table D.4: Lower and upper bound of the estimate of the error induced by a change of temperature from 17°C to 41°C of a force sensor based on the unmachined-quartz-column concept or the in-fiber-FPI concept using a 0.25 mm diameter column as force sensitive element, as function of the material of which the column is made.

Diameter column: 0.25 mm		
Material	Min error (N)	Max error (N)
<i>Titanium beta alloy Ti-12Mo-6Zr-2Fe (single aged)</i>	0.4	0.6
<i>Metglas 2605SC (iron based)</i>	0.4	0.5
<i>Titanium alpha alloy Ti-6Al-2Sn-4Zr-2Mo (triplex annealed)</i>	0.7	0.8

safety is required. The requirement on MRI-compatibility has however a low priority, because the needle with force sensor can also be valuable for non-MRI related applications. Invar is the most interesting metal that can be used for the column, although it is in particular not very suited for a MRI-compatible sensor, as it is ferromagnetic. The advantage of a metal column will be the significantly decreased chance of complete fracture of the tip of the needle or the sensor, as (most) metals will first deform plastically before complete failure occurs due to unexpectedly large transverse forces on the needle tip. Errors due to cross-sensitivity of a sensor to temperature using a 0.5 mm diameter Invar column will be just within the required half-error-interval, according to the used (simple) model of an FPI. The thermal properties of Invar do however not match the properties of a fused silica fiber, which will result in additional cross-sensitivity to temperature, as will be shown on page 57 and in chapter 5. Very stiff and strong metals, like certain titanium alloys, become 'good' candidates when the column diameter becomes very small. It does however not make much sense to make the column diameter absurdly small, as in such a case even the yield strength of these materials will be approached when the needle is exposed to transverse forces due to the small column diameter. This can be observed when material selection is performed for a column with a 'critical' diameter, as shown in figure D.5.

Table D.5: Lower and upper bound of the measurement error induced by a change of temperature from 17°C to 41°C of a force sensor based on the unmachined-quartz-column concept or the in-fiber-FPI concept using a critical column diameter that should be just sufficient to withstand the bending moment due to the maximum expected transverse load on the needle tip without plastic deformation or fracture of the column.

Column with 'optimal' diameter				
Material	Min error (N)	Max error (N)	Min. \varnothing (mm)	'Safe' \varnothing (mm)
<i>Silica (quartz fused)</i>	-0.3	-0.2	0.7	0.7
<i>Graphite</i>	-0.2	1	0.5	1.2
<i>Cold worked Invar</i>	-0.1	0.2	0.3	0.3
<i>Silica (96%)</i>	-0.05	-0.04	0.5	0.5
<i>Lithium aluminosilicate</i>	-0.03	-0.01	0.7	0.7
<i>Glass ceramic - 0330</i>	0.01	0.02	0.4	0.5
<i>Polyester liquid crystal (30% carbon fiber)</i>	0.02	0.7	0.5	0.5
<i>Polyester liquid crystal (30% glass fiber)</i>	0.1	3.5	0.5	0.5
<i>Carbon (industrial)</i>	0.1	0.9	1	1.2
<i>Invar (annealed)</i>	0.1	0.4	0.4	0.4
<i>Metglas 2605SC</i>	0.3	0.5	0.2	0.2
<i>Polyimide (thermoset)</i>	0.3	1.1	0.5	0.6
<i>Terracotta</i>	0.4	1.0	0.9	1.0
<i>Hard rubber (Ebonite)</i>	0.4	0.9	0.6	0.6
<i>Titanium β alloy Ti-12Mo-6Zr-2Fe</i>	0.4	0.6	0.2	0.3

D.3 Determination of temperature and force by using two FPIs

The change in OPD of an FPI as function of a change in temperature or force exerted on the needle tip can be calculated approximated with equation 3.8 instead of 3.6 as long as the compliance of the 'spring' of the FPI is independent of temperature and the thermo-optic and elasto-optic coefficient of the FPI cavity medium and CTE of the FPI remain approximately constant for the range of forces that will be exerted on the needle tip and range of temperatures to which the sensor will be exposed. In other words, the sensitivity of the FPI to temperature and force should remain approximately constant. Equation 3.8 can be visually simplified by using the following quantities that should be determined by calibration of the FPI-based sensor:

$$A = 2L \frac{\partial n}{\partial T} + 2n \cdot CTE \cdot L \quad (D.13)$$

$$B = 2n \cdot c + 2L \frac{\partial n}{\partial F} \quad (D.14)$$

Hence, a change in OPD of an FPI can be described by the following equation:

$$\Delta OPD = A\Delta T + B\Delta F \quad (D.15)$$

The change in temperature of a needle tip and the change in force on the needle tip can thus be described by the change in OPD of two FPIs in the needle tip (1 & 2), both sensitive to force and temperature, with the following system of equations:

$$\begin{bmatrix} A_1 & B_1 \\ A_2 & B_2 \end{bmatrix}^{-1} \begin{bmatrix} \Delta OPD_1 \\ \Delta OPD_2 \end{bmatrix} = \begin{bmatrix} \Delta T \\ \Delta F \end{bmatrix} \quad (D.16)$$

It should be ensured that the ratio of the sensitivity to temperature and the sensitivity to force of each FPI is significantly different to calculate the change of both force on the needle tip and temperature of the needle tip accurately, because the inversion matrix will otherwise be conditioned poorly [100].

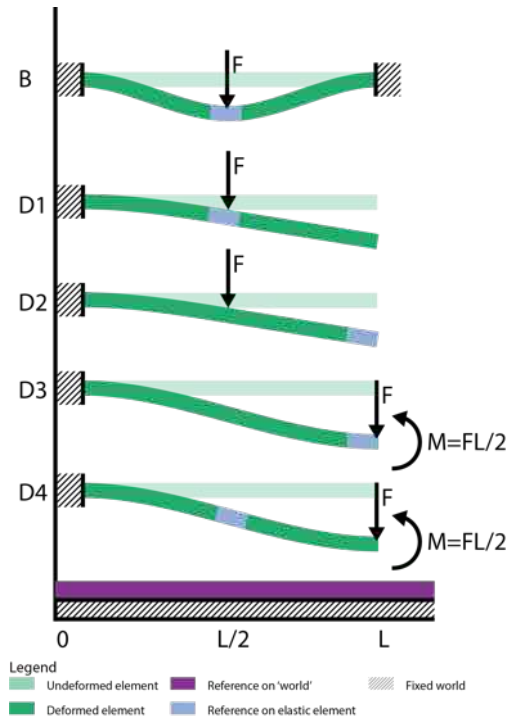


Figure D.1: Five variations on the fundamental elastic beam element with length L , fixated either at both or one side to the 'world'. Displacement of the elastic element can be measured either halfway the beam or at the free end of the beam. The load can be exerted on the middle of the beam by the needle tip, co-axial with the force exerted on the needle tip, or at the end of the beam for elastic elements with a free end. The latter will introduce an additional bending moment on the beam because the load exerted by the needle tip on the elastic element is not co-axial with an axial load on the needle tip

D.4 Selection of the optimal beam

The Euler-Bernoulli equations for beam deflection (all calculations were based on the standard equations from 'Het Polytechnische Zakboek' [245]) can be used to compare the performance of variations of elastic elements based on a beam for their usage as force sensitive element of the force sensor inside the needle tip (figure D.1). The beams can be fixated either at one side or fixated at two sides to the 'world'. The load exerted on the needle tip can be transferred either by the needle-tip-force sensor connection to the middle of the beam or onto the free-end of the beam (if present). The latter will introduce an additional bending moment on the beam, because the load exerted on the beam is not co-axial with the load exerted on the needle tip. The displacement of the reference on the beam with respect to the reference on the fixed world ' δ ', which will be measured with a Fabry-Pérot interferometer, can be measured halfway the beam or at the free end of the beam (figure D.1). Beams of equal length ' L ', width ' b ', (observed) compliance ' δ/F ' and made of a material with Young's modulus ' E ' will be compared. The width and length of beam elements will be limited by the cross-section of the needle. The longest and widest possible beams perform the best, as will be derived. The required compliance of the beams, as observed by the Fabry-Pérot interferometer, should be identical for all variations because a Fabry-Pérot interferometer using homodyne interferometry can only detect displacements of an elastic element up to a certain maximum displacement (roughly a quarter of the used wavelength when the FPI cavity is filled with air). The maximum measurable displacement should occur when the maximum load is exerted on the elastic element. The optimal material, allowing the highest amount of compliance without failure, will be the same for (at least the idealized) beam variations. The height ' h ' of the beam cross section is the free variable that can be tuned to achieve the desired compliance of the elastic beam element. The goal is to minimize the maximum stress occurring in a beam variation due to application of the maximum load on the needle tip, to minimize the chance of mechanical failure of the force sensor due to axial loads on the needle tip.

The cross-section of the beams will for simplicity be assumed as rectangular with height ' h ' and width ' b ' and constant in axial direction of the beam (which will not necessarily be the case

when the beam is manufactured out of a cylindrical element for a needle). The second moment of area of a rectangular beam is equal to:

$$I = \frac{bh^3}{12} \quad (\text{D.17})$$

The maximum bending stress inside a rectangular cross section due to bending moment M is equal to:

$$\sigma_{max} = \frac{Mh}{2I} \quad (\text{D.18})$$

The displacements of the reference on each beam variation (as shown in figure D.1) due to a force F can be calculated with equation D.19 to D.21 for small deflections.

$$\delta_B = \frac{FL^3}{192 \cdot EI} \quad (\text{D.19})$$

$$\delta_{D1} = \frac{FL^3}{24 \cdot EI} \quad (\text{D.20})$$

$$\delta_{D2} = \frac{FL^3}{24 \cdot EI} + \sin\left(\frac{FL^2}{8EI}\right) \frac{L}{2} \approx \frac{5FL^3}{48 \cdot EI} \quad (\text{D.21})$$

$$\delta_{D3} = \frac{FL^3}{12 \cdot EI} \quad (\text{D.22})$$

$$\delta_{D4} = \frac{FL^3}{24EI} \quad (\text{D.23})$$

The required beam height to achieve a certain given compliance δ/F can be calculated for each beam variation:

$$h_B = L\left(\frac{F}{8} \frac{1}{16Eb}\right)^{1/3} \quad (\text{D.24})$$

$$h_{D1} = L\left(\frac{1}{2Eb} \frac{F}{8}\right)^{1/3} \quad (\text{D.25})$$

$$h_{D2} = L\left(\frac{5}{4Eb} \frac{F}{8}\right)^{1/3} \quad (\text{D.26})$$

$$h_{D3} = L\left(\frac{1}{Eb} \frac{F}{8}\right)^{1/3} \quad (\text{D.27})$$

$$h_{D4} = L\left(\frac{1}{2Eb} \frac{F}{8}\right)^{1/3} \quad (\text{D.28})$$

The maximum bending moments occurring in the beam variations are:

$$M_B = \frac{FL}{8} \quad (\text{D.29})$$

$$M_{D1} = M_{D2} = M_{D3} = M_{D4} = \frac{FL}{2} \quad (\text{D.30})$$

The maximum bending moment, creating tensile and compressive stresses in the beam, reaches a maximum at the support(s) of each beam, for variation B also at the center of the beam and for variations D3 and D4 at the free end of the beam. The applied force furthermore results in a constant shear stress along the beam. The shear stress is neglected to simplify the analysis, as the contribution of the shear stress to failure of a long slender beam will be marginal compared to the contribution of the tensile stresses due to bending [246]. The maximum shear stress occurs furthermore at the neutral line of the beam, while the maximum tensile stress due to bending will occur at the surface of the beam [246].

The objective to be minimize the maximum stress in the beam per meter deflection of the reference on the beam with respect to the reference on the 'world':

$$\min\left(\frac{\sigma_{\max}}{\delta}\right) = \min\left(\frac{Mh}{2I\delta}\right) = \min\left(\frac{6M}{bh^2\delta}\right) \quad (\text{D.31})$$

This results for the beam variations in:

$$\min\left(\frac{\sigma_B}{\delta}\right) = \min\left(\frac{6}{\sqrt[3]{2}} \cdot \frac{E^{2/3}}{L \cdot b^{1/3}} \left(\frac{F}{\delta}\right)^{1/3}\right) \quad (\text{D.32})$$

$$\min\left(\frac{\sigma_{D1}}{\delta}\right) = \min\left(\frac{6}{\sqrt[3]{2}} \cdot \frac{E^{2/3}}{L \cdot b^{1/3}} \left(\frac{F}{\delta}\right)^{1/3}\right) \quad (\text{D.33})$$

$$\min\left(\frac{\sigma_{D2}}{\delta}\right) = \min\left(\frac{6\sqrt[3]{10}}{5} \cdot \frac{E^{2/3}}{L \cdot b^{1/3}} \left(\frac{F}{\delta}\right)^{1/3}\right) \quad (\text{D.34})$$

$$\min\left(\frac{\sigma_{D3}}{\delta}\right) = \min\left(3 \cdot \frac{E^{2/3}}{L \cdot b^{1/3}} \left(\frac{F}{\delta}\right)^{1/3}\right) \quad (\text{D.35})$$

$$\min\left(\frac{\sigma_{D4}}{\delta}\right) = \min\left(\frac{6}{\sqrt[3]{2}} \cdot \frac{E^{2/3}}{L \cdot b^{1/3}} \left(\frac{F}{\delta}\right)^{1/3}\right) \quad (\text{D.36})$$

It can be observed in equation D.33 to D.36 that the maximum occurring stress inside the beams for a certain deflection can be minimized by elongating the beam and by using wider beams. Beam length and width are unfortunately severely constrained by the cross-section of the needle, which was already anticipated in this analysis. The maximum occurring stress can furthermore be minimized by minimizing the Young's modulus of the material of the beam. A material with lower Young's modulus is however often also associated with a lower yield strength. Finally, it can be observed that the maximum occurring stress in the beams for a certain deflection can be minimized by maximizing the compliance (δ/F) of the beams. The required compliance depends on the required measurement range and the wavelength of the source when homodyne interferometry is performed and can therefore not be optimized. Beams with very limited lengths and widths are therefore in particularly suited for FPI-based force sensors for the measurement of very small forces, as the beams can then have a very high compliance, while the entire range of forces can still be measured with homodyne interferometry. This is demonstrated in fiber-optic atomic force microscopes based on Fabry-Pérot interferometers [143]. Mechanical failure of the beam used as elastic element is thus more likely to occur when very large forces have to be measured, despite the fact that the beam height can be increased. No parameter of

the beam design can be optimized to minimize the critical stress in the beam (at least for an ideal beam model) except the material of the beam and the choice for a specific variation of the beam element. Variations B, D1 and D4, all using a reference halfway the beam, perform equally well with respect to the chance of mechanical failure of the beam due to an axial force on the needle tip due to a certain displacement of the reference on the beam. The maximum tensile stress in beam variation D3 for a certain displacement of the reference on the beam is however 37% lower than the maximum stress in beam variations B, D1 and D4 for an identical deflection. The maximum tensile stress in beam variation D2 is 46% lower than the maximum tensile stress occurring in beams of variations B, D1 and D4 for a certain displacement of the reference on the beam.

In figure D.1 can be observed that the reference on some of the beams, the location to which the second mirror of the FPI will be attached, will tilt with respect to the reference mirror attached to the fixed world due to bending of the beam. This will result in a wedge angle between the two mirrors of the FPI and therefore in a reduction of the visibility of the fringe pattern. The 'best' variation of an elastic element based on a beam, variation D2, with a maximal compliance as function of the maximum occurring stress in the beam, is a concept where the mirrors will tilt with respect to each other due to bending of the beam. It is therefore interesting to calculate whether tilting of mirrors due to bending of the beams will have significant influence on the visibility of the fringe pattern. Displacement of the reference on the beam with respect to the reference on the 'world' should remain relatively small when homodyne interferometry is performed, certainly less than one fourth of the wavelength of the light used by the optical source. The displacement of the reference on the beam due to the maximum measurable force on the needle tip will therefore be around 400 nm in the worst case when a source with a 1550 nm wavelength is used. The stylet of an 18 G needle is about 1 mm in diameter. The beam of the force sensitive element of the force sensor inside the stylet will thus certainly not be longer than 1 mm and more likely be in the order of 0.6 mm, as some space will be required for the support of the beam. The tilt of the reference on the beam variations can be calculated for the worst case scenario (maximum deflection and a short beam of 0.6 mm) with the following equations:

$$\phi_{D1} = \phi_{D4} = \frac{FL^2}{8EI} = \frac{12FL^2}{8Ebh_{D1}^3} = \frac{3\delta}{L} = 0.11^\circ \quad (D.37)$$

$$\phi_{D2} = \frac{FL^2}{8EI} = \frac{12FL^2}{8Ebh_{D2}^3} = \frac{6\delta}{5L} = 0.05^\circ \quad (D.38)$$

The maximum tilt of the mirror connected to the beam with respect to the reference mirror will thus be far less than 1° according to these equations for ideal beams. This amount of tilting should not have significant consequences on the fringe visibility of the FPI sensor, based on graphs from literature (figure A.3). The response of the FPI interrogated with homodyne interferometry will not remain 'perfectly' sinusoidal due to the deflection, which should be no issue as it is a systematic error for which can be compensated.

D.5 Strength of quartz glass

Quartz glass is a brittle uneven material. Brittle uneven materials have a compressive strength far larger than their tensile strength (under practical conditions). The compressive strength of fused quartz glass is 1.05 to 1.16 GPa, while the tensile strength is in general reported to be between 45.7 and 50.4 MPa [131]. The tensile strength of quartz glass is in theory however far higher, but can only be achieved when the material, in particular the surface, is free of flaws [247, 248]. For example, flexure hinges fabricated out of fused quartz glass with femto-second laser ablation to have a very smooth surface were shown to be capable to support bending stresses up to 2.7 GPa

(which is close to the tensile strength of pristine silica fibers) [249]. Suppliers of quartz glass therefore sometimes note that the tensile strength of quartz glass can exceed 48 MPa when the material is without substantial surface flaws, but that a maximum tensile stress of only 6.8 MPa is often used for designs [161]. It is furthermore reported that moisture negatively affects the strength of quartz glass [248, 247]. The maximum tensile stress of quartz glass is an important parameter to determine whether a force sensor made of quartz glass will be capable of supporting transverse loads on the needle tip. Some verification is therefore preferred to validate whether usage of 50 MPa or 6.8 MPa as tensile strength of the quartz glass of ferrules used for this thesis is more appropriate. Experimentally determining the strength of the used quartz ferrules with a 'scientifically' appropriate method (a three point bend test) was not recommended by the materials engineering department of the university, due to the size of the specimen. The critical flaw size at the surface of the ferrules was therefore calculated and the surface of the ferrules was inspected under a microscope. Furthermore, a simple bend test was performed on the ferrules to obtain at least an estimate whether the used values for the tensile strength are appropriate.

Critical flaw size

The maximum allowed flaw size at the glass surface was calculated for the assumption of a maximum tensile strength of 50 MPa for quartz glass (fatigue was not taken into account). The maximum flaw size is a function of the critical stress intensity factor/fracture toughness (K_{Ic}) of quartz glass, which varies between 0.5 and $1 \sqrt{MPa \cdot m}$ [249, 131]. The stress intensity factor is a function of the stress intensity modification factor ' β ' (which depends on the geometry of the flaw and the specimen), the nominal tensile stress and the crack length ' a ' and is given by equation D.39 for a mode I fracture [250].

$$K_I = \beta \cdot \sigma \cdot \sqrt{\pi \cdot a} \quad (D.39)$$

The stress intensity modification factor suited for the most critical 'situations' is estimated to be about 1.1, based on data for a specimen in bending with a rectangular cross-section and a crack at the surface [250]. The maximum crack size (or rather crack depth) in the surface of the quartz glass varies therefore between 26 μm and about 105 μm , depending on the used critical stress intensity factor. Inspection of the quartz ferrules used for this thesis under a 'normal' binocular microscope did not show presence of any cracks at all. Cracks with the size of about 100 μm should be easily visible, though cracks in the order of ten microns could be overlooked easily. Hence, assuming a maximum tensile strength of 50 MPa for the used quartz glass seems reasonable based on visual inspection, but not with a high certainty. A bending test was therefore performed as additional confirmation.

Results of a simple bend test

A very simple and primitive experiment was conducted to estimate whether the order of magnitude of the assumed maximum tensile strength of the quartz glass of the used ferrules is appropriate. Two undamaged ferrules (that were only used to manufacture a prototype of a force sensor, but due to breakage of optical fibers during assembly of the prototype did not result in a working prototype) were tested. Both ends of each ferrule were glued in a metal capillary (see figure D.2). One capillary was clamped onto a force sensor (an ATI-Nano 17 sensor, capable of measuring force in three directions) while force was exerted on a marked position on the second capillary to bend the ferrule with a 'transverse' load. The force was exerted with the side of a thin rod, such that the moment arm of the force could be defined reasonably well. Axial forces on the ferrule were negligible according to measurements during bending of the ferrule. The test setup was modeled with a finite element model in COMSOL using the maximum measured transverse force before fracture, the measured dimensions of the metal capillaries and ferrules and some assumptions about the used to glue [129]. The model was used to determine the theoretical

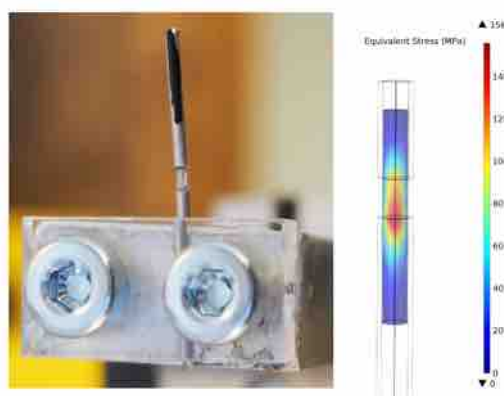


Figure D.2: On the left a quartz ferrule, glued into two metal capillaries, clamped onto a force sensor, used to test the tensile strength of the quartz glass of the ferrules. On the right an illustration of the equivalent stress inside the ferrule, according to the modified Mohr-Coulomb failure criterion, as calculated with a finite element analysis.

maximum equivalent stress in the ferrule at the moment of fracture. The modified Mohr-Coulomb criterion was used as failure criterion to calculate the equivalent stress in quartz glass [159]. The maximum tensile stress according to equation D.5 was also calculated (as verification). The ferrules fractured under an equivalent stress of approximately 156 and 198 MPa according to the FE model and a tensile stress of respectively 147 and 187 MPa according to the simple equation for stress in a beam due to a bending moment. The estimated stresses are shown with three digits to compare both models, but the precision with which the stress in the ferrule can be estimated is far lower due to inaccuracies of the experimental setup. The small difference between the FE-model and the equation is logical, as the finite element model takes stress concentrations, caused by the presence of the metal capillaries, into account.

Conclusion

Using 50 MPa as maximum tensile stress of the quartz used in the ferrules seems a reasonable assumption. The assumed maximum tensile stress might even imply a reasonable safety factor, as long as the ferrules are not scratched, because the ferrules fractured for a significantly higher than expected load in the simple bend test. Usage of a maximum tensile stress of 6.8 MPa will very likely result in an unnecessary large safety factor.

D.6 'Low coherence interferometry' with the second generation OP1550

The second generation of the OP1550 cannot perform real low coherence interferometry by quickly sweeping the wavelength of its source over a sufficiently large wavelength range or by having a source with a very broad spectral width to observe one or more entire fringes of the fringe pattern of one of the FPIs fabricated for this thesis project 'at once', such that the OPD of the FPI can be derived from the observed fringes (the OP1550 can only adjust its wavelength over a large range in slow discrete steps). The wavelength of the laser of the OP1550 can however be swept quickly over a very small wavelength range of 0.4 nm at most [163]. This is used to perform a variant of homodyne interferometry, showing some of the properties of low coherence interferometry, as oscillation of the wavelength of the source with a very high frequency allows the change in OPD of the FPI to be measured over a large range by means of an amplitude modulation technique. The method is not as effective as 'real' low coherence interferometry, because it is impossible to observe multiple fringes 'at once' by scanning the wavelength of the source. The method is therefore unsuited to be interrogate FPIs multiplexed

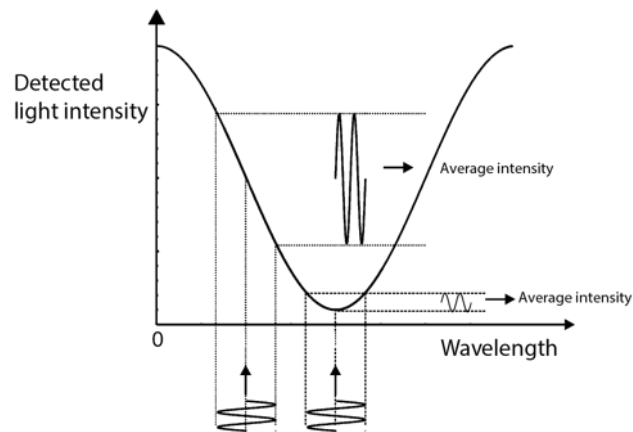


Figure D.3: Fringe pattern as function of wavelength. The distance between maxima and minima of the fringe pattern depends on the OPD of the FPI. The change in light intensity at the photodetector due to a change in wavelength of the source is minimal when the wavelength is such that the source scans over a maximum or minimum of the fringe pattern, while the change in intensity is maximal when the FPI is in quadrature for the used wavelength.

on a single optical fiber. The method also only works for low finesse FPIs of which the fringe pattern is approximately sinusoidal. The technique will however nonetheless be referred to as low coherence interferometry in this report, in lack of a better name.

The measured light intensity at the photodetector consist of two components due to 'oscillation' of the wavelength of the optical source. The first component, the average intensity at the detector, is the average intensity of light, with the range of wavelengths over which the optical source scans by oscillating its wavelength, after interference in the FPI (as in equation A.4). The average intensity of light at the photodetector is easily measured by passing the signals from the photodetector through a low pass filter with a cutoff frequency sufficiently below the frequency of the oscillations of the wavelength of the source. The second component of the measured light intensity is a high frequent oscillation of the intensity, with ideally only the frequency of the oscillation of the wavelength of the optical source. The amplitude of the oscillation depends on the sensitivity of the FPI to a change in wavelength (the derivative of equation A.4 to the wavelength), as the sensitivity of the FPI is literally probed with a small change in wavelength by oscillating the wavelength of the light source (figure D.3). A high frequent oscillation of the wavelength of the source, in case of the OP1550 with a sawtooth waveform, is thus used to generate a carrier signal such that the sensitivity of the FPI to a change in wavelength of the source behaves as the modulating signal. A (digital) lock-in amplifier, locked on the carrier frequency by means of a TTL synchronization between the OP1550 and the amplifier, is used to measure the amplitude of the oscillation of the light intensity at the photodetector at the carrier frequency.

The average intensity at the photodetector and the sensitivity of the FPI to a change in wavelength of the source are both a sinusoidal function of the OPD of the FPI, but shifted 90° with respect to each other. A unit circle is therefore described by the vector of the average intensity at the detector and the amplitude of the oscillation of the intensity, both appropriately scaled, as function of the change in OPD of the FPI (figure D.4). The change in OPD of the FPI is linearly proportional to the change in angle of the unit vector formed by the the scaled average detected light intensity and the amplitude of the oscillation of the light intensity. The angle of the vector is easily calculated by taking the arctangent of the orthogonal components of the vector. Rotation of the vector with more than 360° with respect to a reference position,

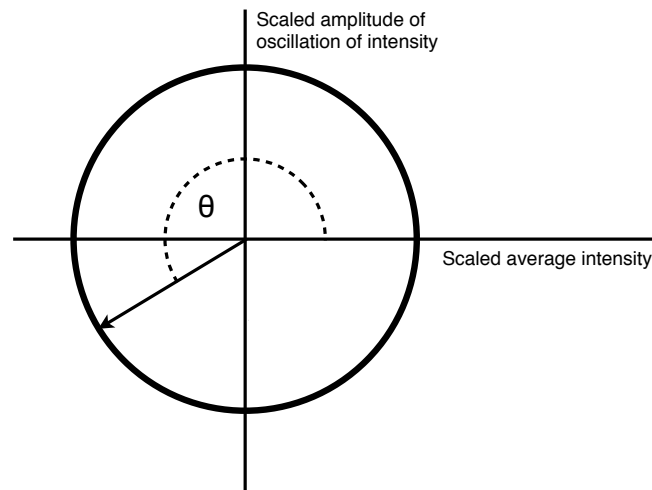


Figure D.4: A unit circle is described by the vector of the average intensity at the photodetector of the OP1550 and the amplitude of the oscillation of the light intensity at the photodetector caused by the oscillation of the wavelength of the source of the OP1550, both appropriately scaled, as function of the change in OPD of the FPI. The change in OPD of the FPI is linearly proportional to the change in angle of the unit vector.

due to large changes in OPD of the FPI, can be measured by means of phase unwrapping. Phase unwrapping is possible as long as the change in OPD does not occur too fast to 'observe' the direction of rotation of the vector between two subsequent 'samples'.

It was found out during calibration experiments that the vector formed by the scaled average detected light intensity and the scaled amplitude of the oscillation of the light intensity did in practice not describe a perfect circle but often a somewhat skewed ellipse or in a bad case a very skewed ellipse (which was noted to be common for the technique as performed at the VU Amsterdam). Several reasons could be identified for non-circular trajectories of the vector. Furthermore, some settings of the frequency modulation and lock-in amplifier were found to affect the described trajectory (an example of such elliptic trajectories and their variation, according to simulations, as function of the sample frequency of the lock-in amplifier is shown in figure D.5). The most important reason for deviations from a circular trajectory of the vector was however identified after performing all calibrations of prototypes. The change in angle of the vector formed by the the scaled average detected light intensity and the amplitude of the oscillation of the light intensity does not correspond linearly to the change in OPD of the FPI anymore, when the vector does not describe a circular trajectory. The relationship between the angle of the vector and the OPD of the FPI contains instead a periodical 'wobble', of which the period correlates with the period of the fringe pattern of the FPI as function of the OPD of the FPI. The angle of the vector does however still decreases/increases (within 360°) monotonic with the change in OPD of the FPI. Calibration results of prototypes of needle tip force sensors, obtained with 'low coherence interferometry', contain therefore a systematic error in the form of a wobble in the relationship between the measured response and the calibration force on the prototype. The periodical wobble is rather difficult to capture with a simple interpolation function and was therefore only marginally accounted for in most interpolation functions used to describe the response of the FPI-based force sensors.

A (potentially very) non-circular and non-elliptic trajectory of the vector can occur when the fringe pattern of the FPI is no perfect sinus, which becomes more and more the case when the finesse of the FPI increases. This effect was however not expected to occur very visibly with prototypes shown in this thesis project, as the finesse of FPIs of (nearly) all constructed

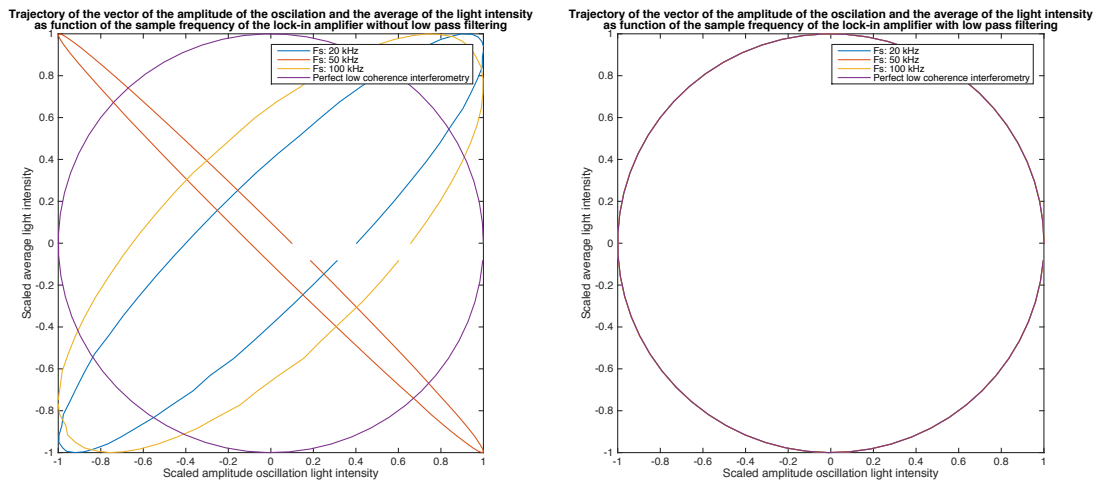


Figure D.5: Trajectories of the vector formed by the the scaled average detected light intensity and the scaled amplitude of the oscillation of the light intensity at the photodetector, according to a simplified Matlab model of the used principle to perform 'low coherence interferometry'. Elliptic trajectories shown on the left, as function of the sample frequency of the lock-in amplifier, will be described when the signal of the photodetector passed to the lock-in amplifier is not lowpass filtered. Circular trajectories, as shown in the graph on the right, will be described when lowpass filtering is performed, independent of the sample frequency of the lock-in amplifier (given that the sample frequency is sufficiently above the frequency of the oscillation of the wavelength of the source).

prototypes was very low. The trajectory becomes a spiral when the visibility of the fringe pattern changes due to a change in OPD, which can be the case when the wedge angle between the FPI mirrors changes due to a change in OPD (due to bending of the FPI for example). The skewed elliptic shape of the trajectory could however not be explained with these effects. Moreover, it was concluded that it is physically impossible that the sensitivity of an FPI to a change wavelength is not zero/at a minimum for a center wavelength where the fringe pattern of the FPI itself is at a maximum. An elliptic trajectory would indicate that the latter is possible. The reason for the observed elliptic trajectories was however discovered by means of simulations of the principle of the interrogation procedure in Matlab.

The amplitude modulation is not performed by literally multiplying the sensitivity of the FPI to a change in wavelength with the carrier wave. A 'sort-of-multiplication' is instead performed by letting light interfere in the FPI. The waveform of the oscillation of the wavelength, which can be a sawtooth or sinusoidal shaped waveform, used to 'probe' the sensitivity of the FPI to a change in wavelength, will therefore be measured in distorted form as oscillation of the light intensity, particularly when the center wavelength of the light source is around a maximum or minimum of a fringe of the FPI (see figure D.6 and D.7). This would not be the case when the sensitivity of the FPI to a change in wavelength could be multiplied literally with the carrier wave or when the amplitude of the wavelength oscillation could be infinitesimal (the latter makes detection of the amplitude of the oscillation of the intensity at the photodetector with the lock-in amplifier impossible). The distortion of the waveform of the carrier wave but in particularly a sawtooth shaped waveform of the oscillation of the wavelength introduce higher order harmonics of the carrier frequency in the measured oscillation of the light intensity at the photodetector. A lock-in amplifier measures the amplitude of a signal at the carrier frequency in a supplied signal, which is in this case the light intensity at the photodetector, by multiplying the supplied signal with (in general) a sine with the carrier frequency based on a supplied reference (the TTL synchronization), and lowpass filtering the outcome of the multiplication. A digital

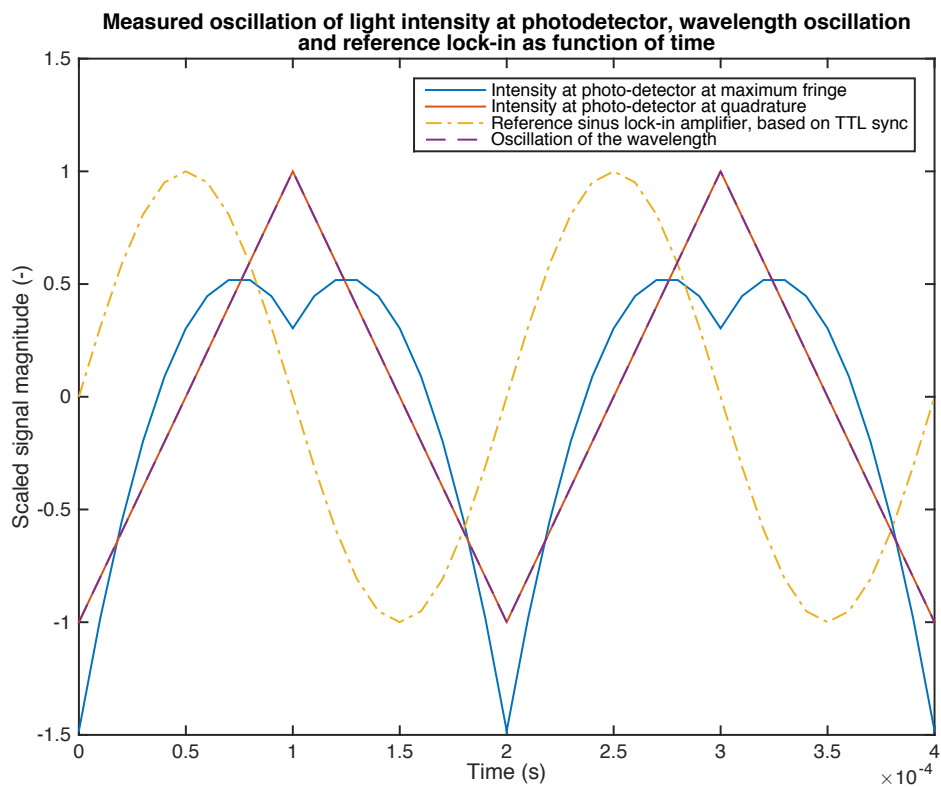


Figure D.6: Oscillation of the wavelength of the optical source with a saw-tooth waveform, the measured light intensity at the photodetector when the FPI is at the maximum of a fringe, the measured light intensity at the photodetector when the FPI is at quadrature and the sine generated by the lock-in amplifier at the carrier frequency based on the TTL-synchronization, as function of time.

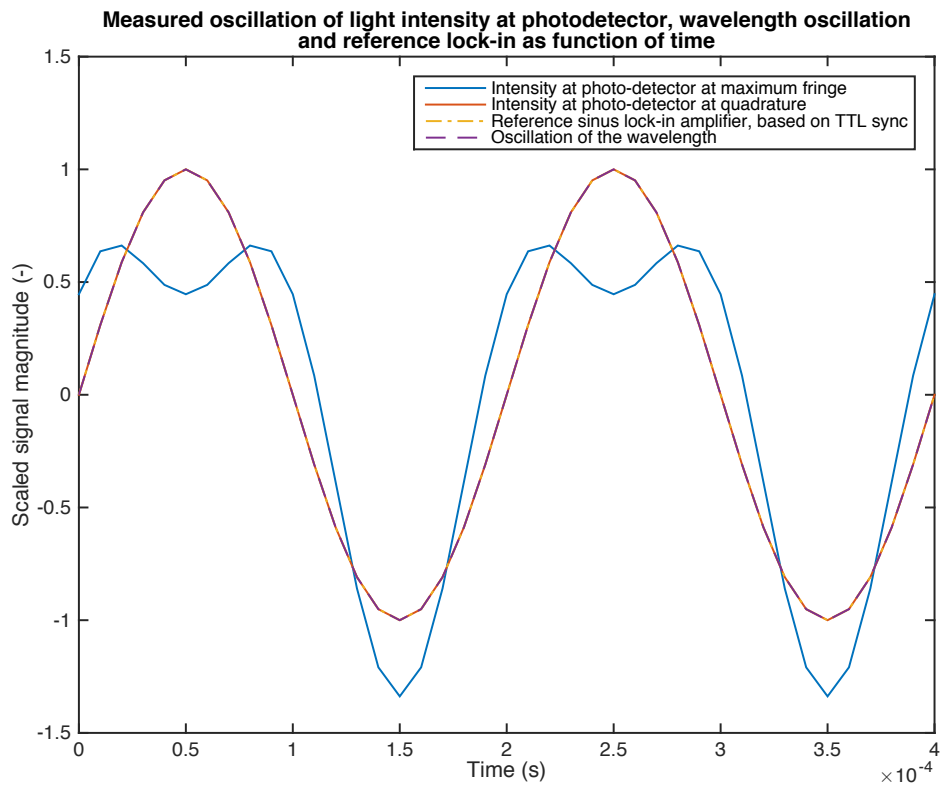


Figure D.7: Oscillation of the wavelength of the optical source with a sinusoidal waveform, the measured light intensity at the photodetector when the FPI is at the maximum of a fringe, the measured light intensity at the photodetector when the FPI is at quadrature and the sine generated by the lock-in amplifier at the carrier frequency based on the TTL-synchronization, as function of time.

lock-in amplifier measures the amplitude of the signal at the carrier frequency by calculating the dot product of (in general) a sine with the carrier frequency and the supplied signal over a short period. The combination of a finite bandwidth of the lock-in amplifier and the presence of higher order harmonics of the carrier frequency in the measured light intensity do however cause aliasing effects in a digital lock-in amplifier. Problems with correct measurement of the 'amplitude' of the (presumed sinusoidal) signal at the carrier frequency will occur due to aliasing effects, which was observed in the Matlab model of the interrogation principle. Aliasing issues can of course be solved easily by placing a lowpass filter between the photodetector and the lock-in amplifier with a cutoff frequency slightly above the carrier frequency and well below the sample frequency of the digital lock-in amplifier. Simulations performed with MATLAB to show that prevention of aliasing by means of lowpass filtering will solve the 'issues' with measurement of the amplitude of the oscillation of the light intensity at the carrier frequency that causes the trajectory of the 'vector' to be an ellipse instead of a circle.

D.7 Details calibration results

Dynamic calibration using homodyne interferometry of prototype of the unmachined-quartz-column concept manufactured with EPOTEK epoxy

Results of dynamic calibration at room temperature of a prototype of the unmachined-quartz-column concept constructed with EPOTEK epoxy, interrogated with homodyne interferometry, is shown in figure D.8 and D.9. The dataset used for analysis was slightly filtered during postprocessing to ensure that readings remained within an acceptable measurement range for homodyne interferometry. Transverse forces on the tip reached up to 950 mN during dynamic calibration. The maximum observed measurement error during dynamic calibration using homodyne interferometry is significantly larger than the maximum observed measurement error observed during static calibration, but remains within requirements on the measurement uncertainty. There seems to be a systematic error at the begin and end of the measurement range, which could be due to dynamic effects, sensitivity to transverse forces but also for a small part due to the disability of the sinusoidal interpolation function to describe the response of the FPI (which would be even more the case for a higher finesse FPI).

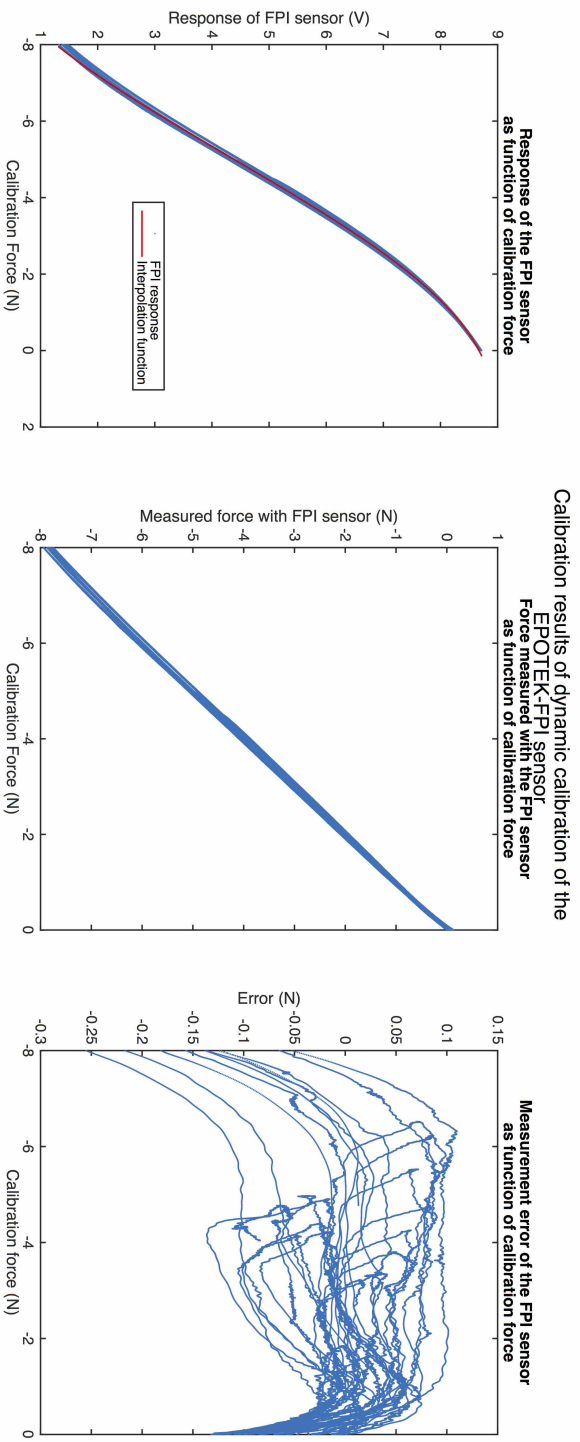


Figure D.8: Results of dynamic calibration at room temperature of a prototype of the unmachined-quartz-column concept manufactured using EPOTEK epoxy, interrogated with homodyne interferometry. The response of the FPI as function of the calibration force, together with a fitted sinusoidal interpolation function is shown on the left. The figure in the center shows the force measured with the FPI, calculated using the interpolation function, as function of the calibration force. The measurement error of the FPI-based sensor as function of the calibration force is shown on the right.

Force measured with the EPOTEK-FPI sensor
subjected to dynamic calibration forces as function of time

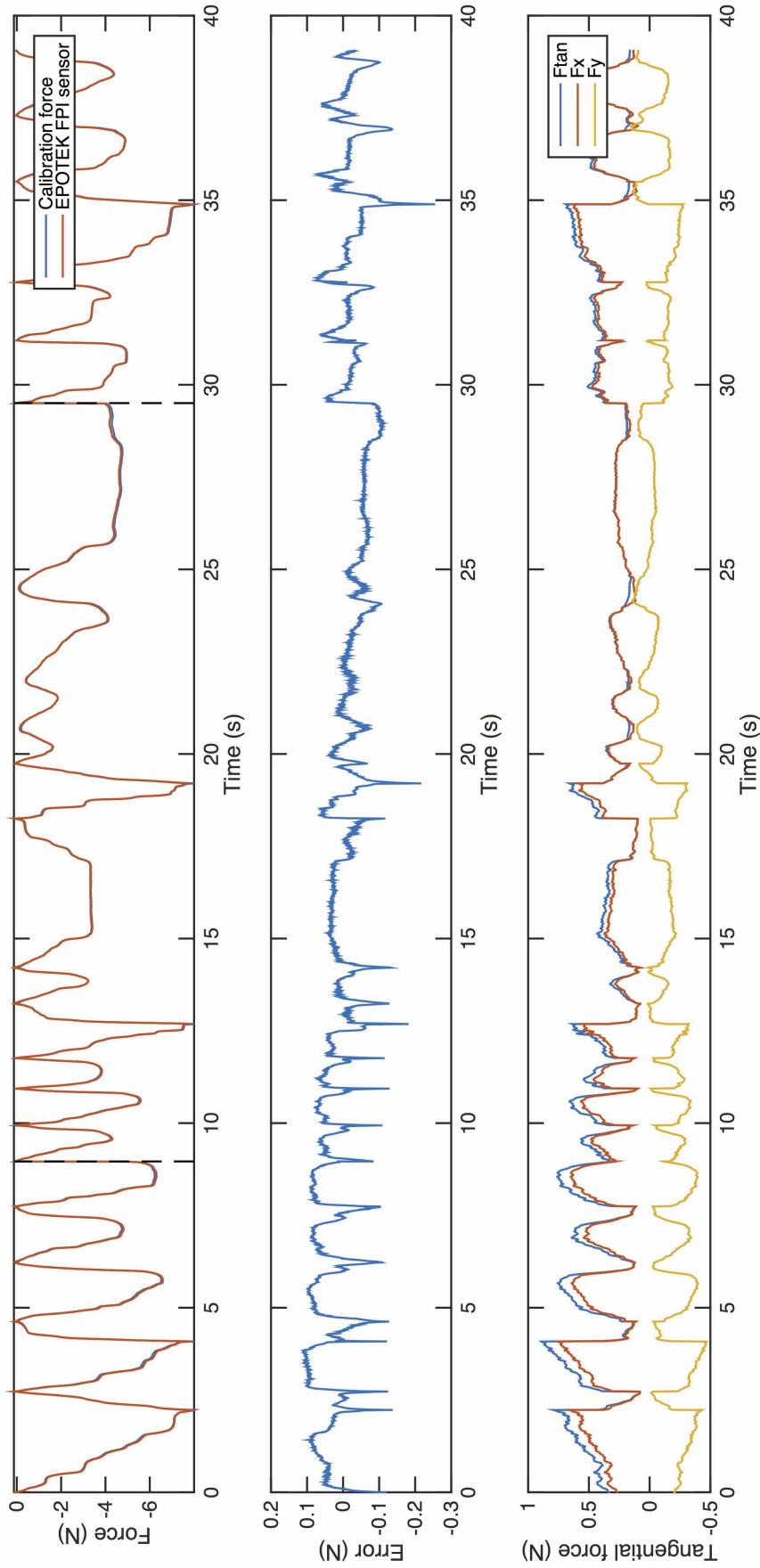


Figure D.9: Results of dynamic calibration at room temperature of a prototype of the unmachined-quartz-column concept manufactured with EPOTEK epoxy, interrogated using homodyne interferometry, shown as function of time and using the interpolation function shown in D.8. The graphs show, from top to bottom: (1) the calibration force and the force measured with the prototype using the interpolation function shown in figure D.8, (2) the measurement error of the prototype and (3) the transverse force on the needle tip, shown as the resultant transverse force 'Ftan' and its two orthogonal components 'Fx' and 'Fy'. The dotted lines in the top graph (1) indicate the fragments of which the dynamic calibration is composed.

Sensitivity of prototype of the unmachined-quartz-column concept to transverse forces

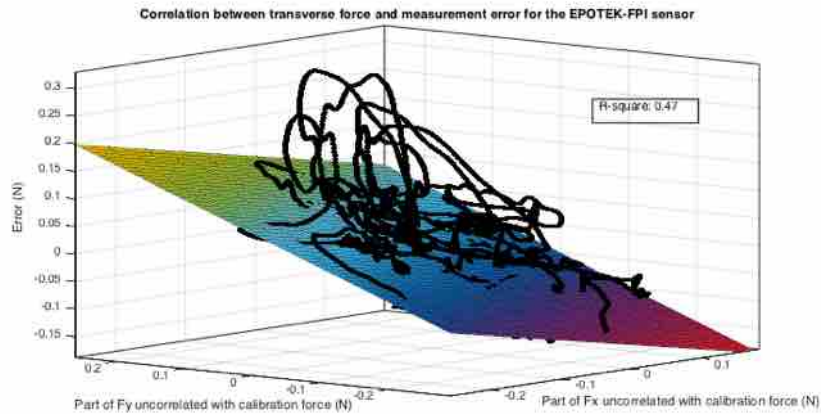


Figure D.10: Fit of a model explaining the measurement error of the axial calibration force using the part of the transverse forces (F_x and F_y) on the needle tip uncorrelated with the axial calibration force, for a prototype of the unmachined-quartz-column concept fabricated with EPOTEK epoxy, fitted to data shown in figure D.11. The model shown in equation 4.4 was fitted to the data in a least-squares sense. The measurement error as function of the transverse force on the needle tip according to the fitted model is shown as the colored plane, while the actual measurement error as function of the transverse forces uncorrelated with the axial calibration force are shown as a black line. The coefficient of determination of the fit is 0.47, indicating that the transverse forces on the needle tip do not explain the total variation in measurement error very well. The 95% confidence intervals of the sensitivity of the FPI to the orthogonal components of the transverse force on the needle tip (F_x and F_y) are according to the model respectively -0.278 N/N to -0.268 N/N and 0.489 N/N to 0.496 N/N .

Force measured with the EPOTEK-FPI sensor
subjected to dynamic calibration forces as function of time

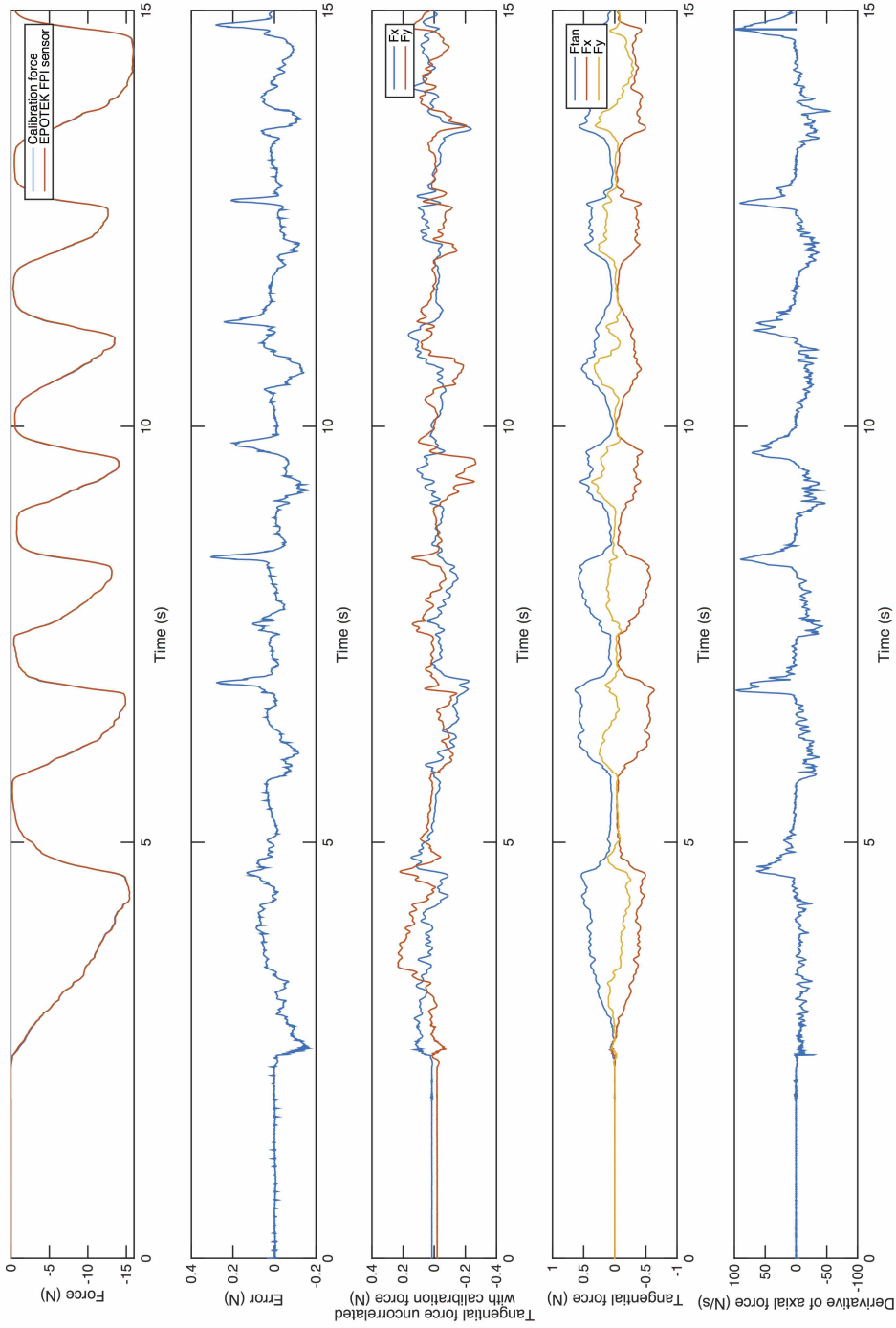


Figure D.11: Selection of results of dynamic calibration of a prototype of the unmachined-quartz-column concept manufactured with EPOTEK epoxy and interrogated with low coherence interferometry at constant temperature. The graphs show, from top to bottom: (1) the force measured with the prototype using a 3rd order polynomial interpolation function and the calibration force, (2) the measurement error of the prototype, (3) the parts of the transverse force on the needle tip during calibration uncorrelated with the axial calibration force, (4) the transverse force on the needle tip, shown as the resultant transverse force 'Ftan' and its two orthogonal components 'Fx' and 'Fy', and (5) the derivative of the calibration force to time. A strong correlation between peaks in the measurement error and peaks in the derivative of the calibration force to time can be observed.

Detail of the response of prototype of the unmachined-quartz-column concept to temperature

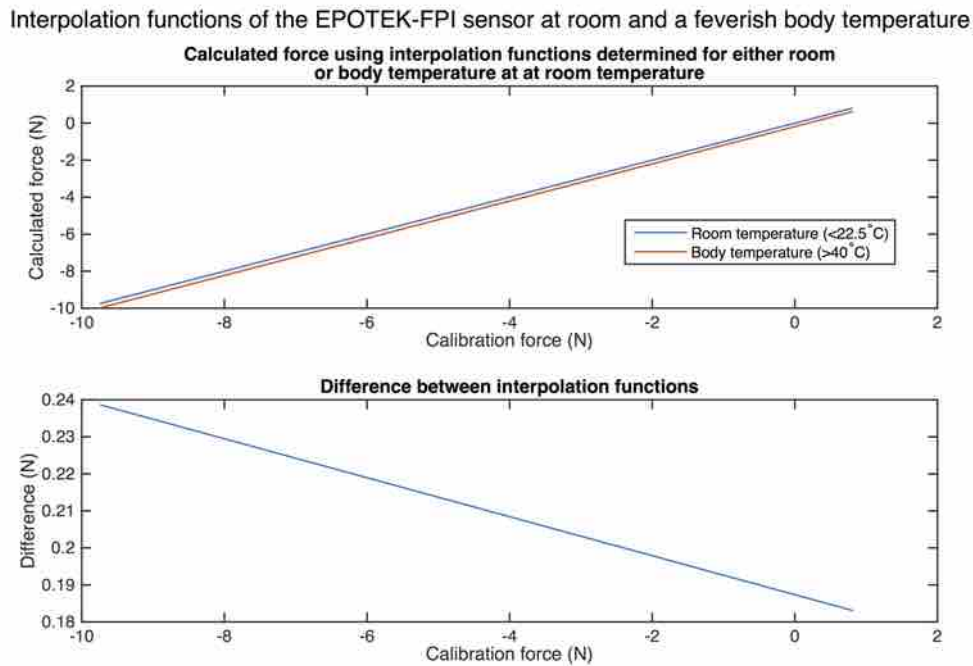


Figure D.12: Analysis of the cross-sensitivity to temperature of a prototype of the unmachined-quartz-column concept, manufactured with EPOTEK 353ND epoxy, interrogated with low coherence interferometry, based on results of dynamic calibration at room temperature (22.5°C) and a feverish body temperature (40°C). Two linear interpolation functions were fitted to the data to describe the response of the proof-of-concept as function of the calibration force at room and body temperature. The top graph shows the force that would be 'measured' at room temperature based on the response of the FPI. The measured force is calculated using either the interpolation function for the response at room temperature or the interpolation function for the response of the FPI at body temperature and shown as function of the calibration force. The calibration force is equal to the force that would be measured using the interpolation function for the response of the FPI at room temperature, assuming the interpolation function perfectly describes the response of the FPI. The bottom graph shows the difference in the 'measured' force calculated using the two interpolation functions, as function of the calibration force. The difference is equal to the measurement error due to cross-sensitivity to temperature.

Calibration results of a prototype of the unmachined-quartz-column concept manufactured with UV-curable glue

Calibration results of a prototype of the unmachined-quartz-column concept manufactured with Norland optical adhesive 81, an UV-curable adhesive, illustrate the typical performance of prototypes constructed with all tested UV-curable adhesives, although prototypes constructed with NOA68 and Loctite 350 UV curable adhesive did seem to perform slightly better. The prototype had a 'fake' needle tip, meaning that the quartz ferrule containing the FPI protruded about 1.5 mm instead of 0.5 mm out of the stylet tube, while no real needle tip was glued on top of the ferrule. The FPI cavity length of the prototype was about 110 μm , determined from a scan of the fringe pattern as function of wavelength. Results of static calibration of the prototype interrogated with low coherence interferometry, without taking into account transverse forces on the needle tip, are shown in figure D.13. It can be observed that the force sensor seems to suffer from an apparent the drift of the measurement error during the calibration procedure, possibly

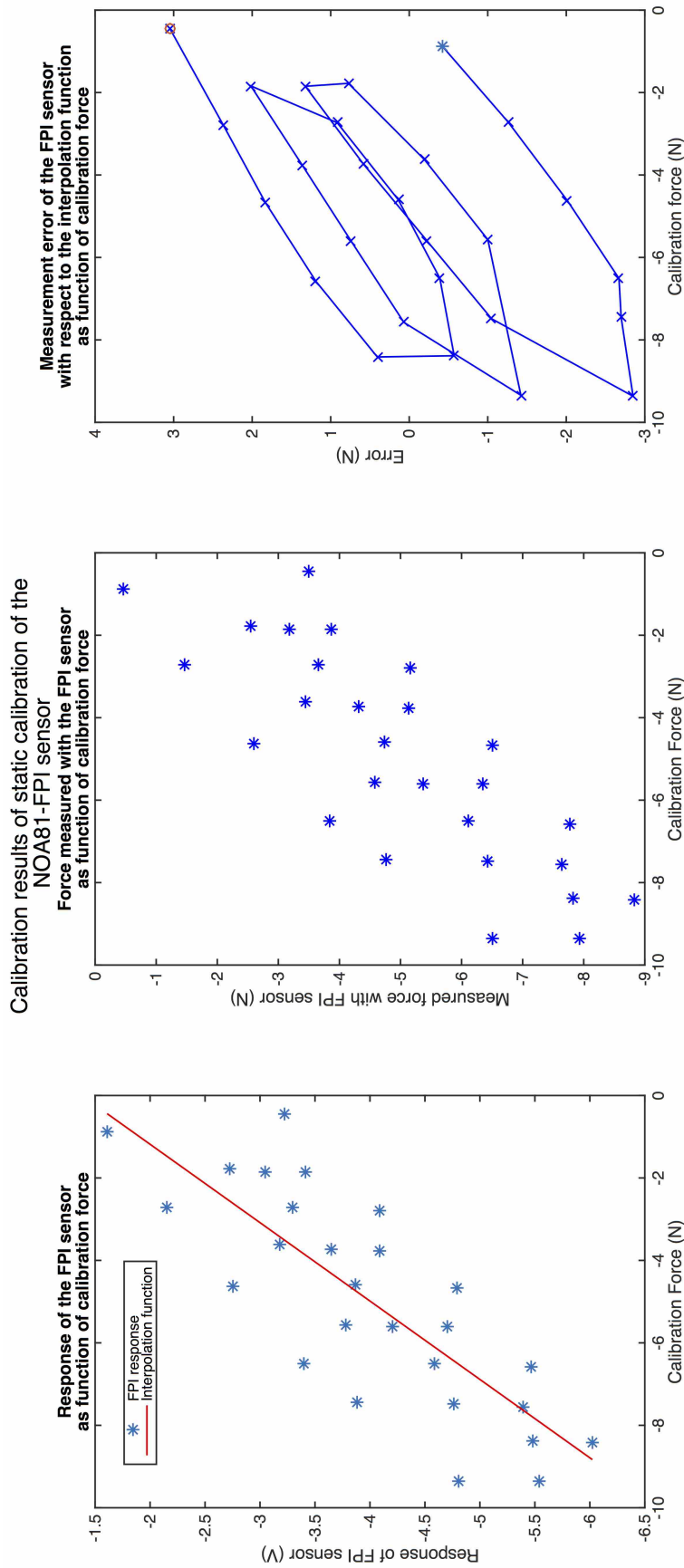
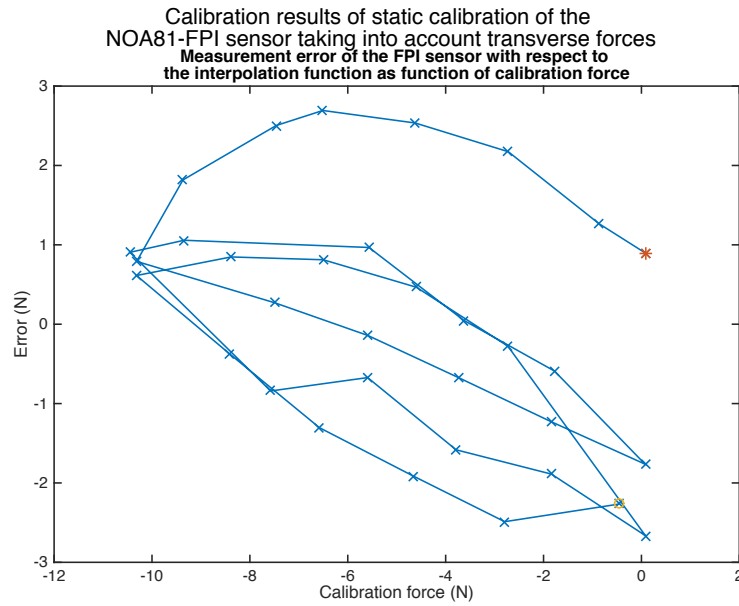


Figure D.13: Results of static calibration of a prototype of the unmachined-quartz-column concept manufactured using Norland optical adhesive 81 and interrogated with low coherence interferometry. The response of the FPI as function of the calibration force, together with a fitted linear interpolation function to the response of the FPI is shown on the left. The figure in the middle shows the force measured with the FPI (using the fitted interpolation function) as function of the calibration force. The measurement error of the FPI-based sensor is shown on the right. The blue star and the red circle indicate respectively the first and last reading obtained during the calibration procedure.



ferrule to the viscoelastic behavior of the entire force sensitive element. Testing of a prototype constructed with Norland Optical Adhesive 68 and a FPI with a 500 μm cavity length showed that merely increasing the FPI cavity length is not sufficient to reduce the measurement error due to viscous behavior of the used UV-curing adhesives to acceptable levels.

The viscous behavior of the force sensitive element of the prototype constructed with NOA81 UV-curable adhesive is prominently present in data acquired during dynamic calibration of the prototype using low coherence interferometry and temperatures varying between 22°C and 37°C (figure D.15 and D.16). The lagging response of the FPI-based force sensor with respect to the reference sensor is very visible in data acquired at 'body temperature'. It can be observed that sensitivity of the FPI-based force sensor increases strongly when temperature increases. Modifying errors introduced by this form of cross-sensitivity to temperature cause measurement errors that exceed 20 N. The increase in sensitivity is likely the result of both an increase in compliance and a decrease in viscosity of the adhesive used to bond the optical fibers in the ferrule. The viscous and elastic behavior of the force sensitive element of the prototype can however not be separated without a proper dynamic analysis assessing the frequency response of the sensor. It is nonetheless clear that the properties of the UV-curing adhesive depend significantly on temperature in the temperature range between room temperature and body temperature, as prototypes of the concept constructed with heat curing EPOTEK 353ND epoxy did not suffer from similar issues (or at least not to such an extent). Based on the strong dependence of the behavior of the adhesive on temperature can be concluded that the UV-curing adhesive is likely used around or above its glass transition temperature at room and body temperature.

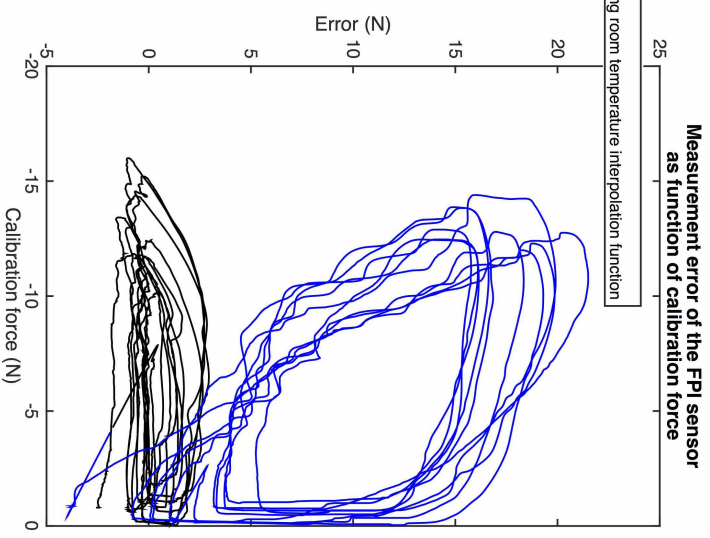
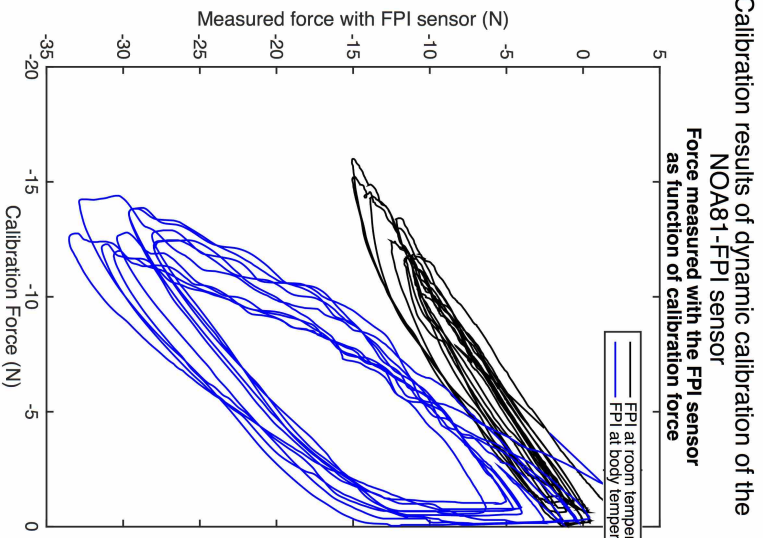
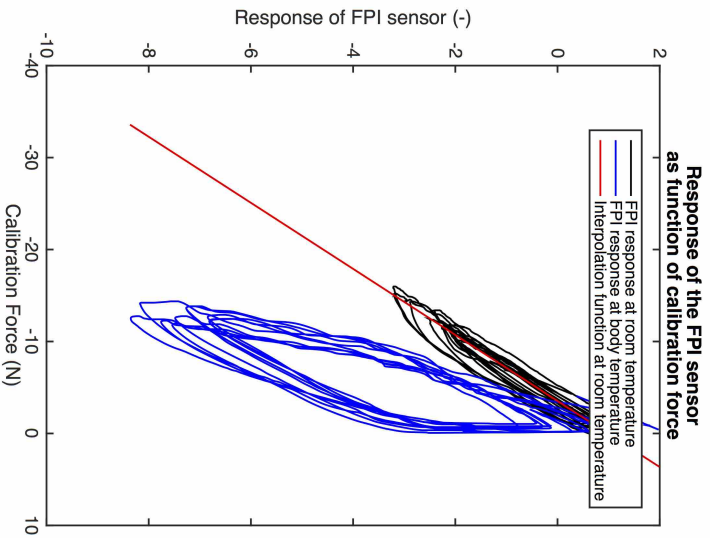


Figure D.15: Results of dynamic calibration of a prototype of the unmachined-quartz-column concept, manufactured using NOA81 adhesive and interrogated with low coherence interferometry, with temperatures varying between 22 °C and 37°C. The response of the FPI as function of the calibration force, together with a linear interpolation function fitted to data acquired at room temperature, is shown in the graph on the left. The figure in the center shows the force measured with the FPI, using the interpolation function determined for the response of the FPI-based sensor at room temperature, as function of the calibration force. The measurement error of the FPI-based force sensor using the interpolation function determined for the response of the sensor at room temperature is shown in the figure on the right as function of the calibration force.

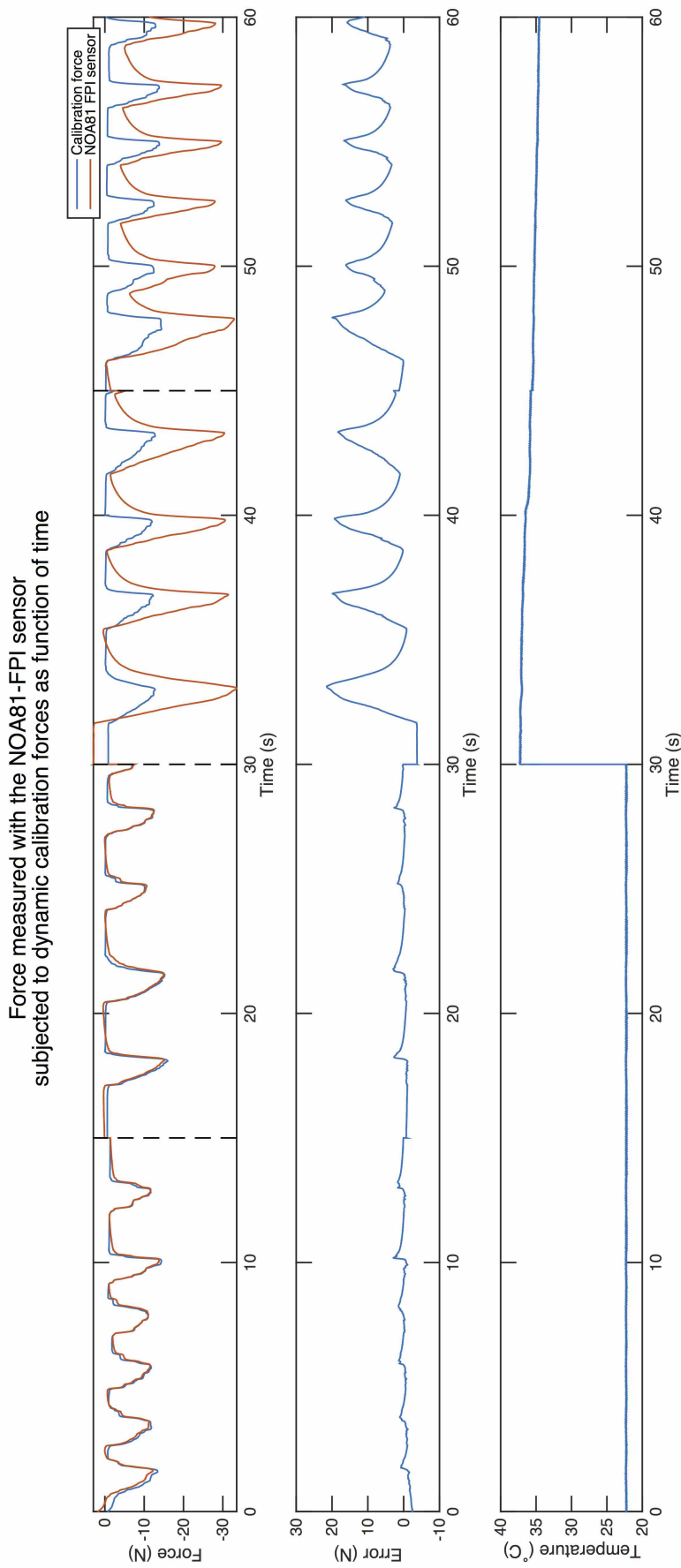


Figure D.16: Results of dynamic calibration of a prototype of the unmachined-quartz-column concept with temperatures varying between 22 °C and 37 °C, manufactured with NOA81 adhesive and interrogated with low coherence interferometry, shown as function of time. The graphs show, from top to bottom: (1) the calibration force and the force measured with the prototype, using the linear interpolation function determined for the response of the FPI-based sensor at room temperature shown in figure D.15, (2) the measurement error of the prototype and (3) the temperature of the water bath in which the prototype was submerged during the calibration procedure. The dashed lines in the upper graph (1), indicate the 15 second long fragments of which the dataset acquired during dynamic calibration is composed.

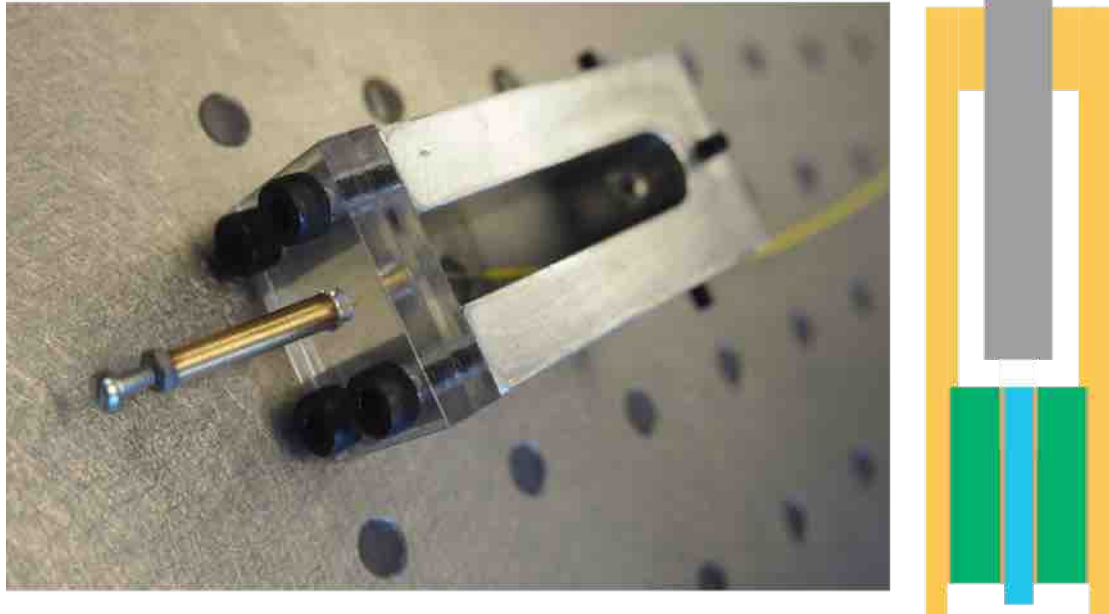
Calibration results of a large scale prototype of the stylet tube concept

Figure D.17: Photograph of the large scale prototype of the stylet tube concept, mounted on a support, on the left and drawing of a cross-section of the prototype on the right. The sensor was fabricated from a brass capillary in which a ferrule with optical fiber was glued on one side. An RVS bolt with a highly polished side acting as second FPI mirror was screwed in the other side of the capillary, such that an FPI cavity exist between the optical fiber top and the polished surface of the bolt. A nut and some superglue were used to fixate the bolt.

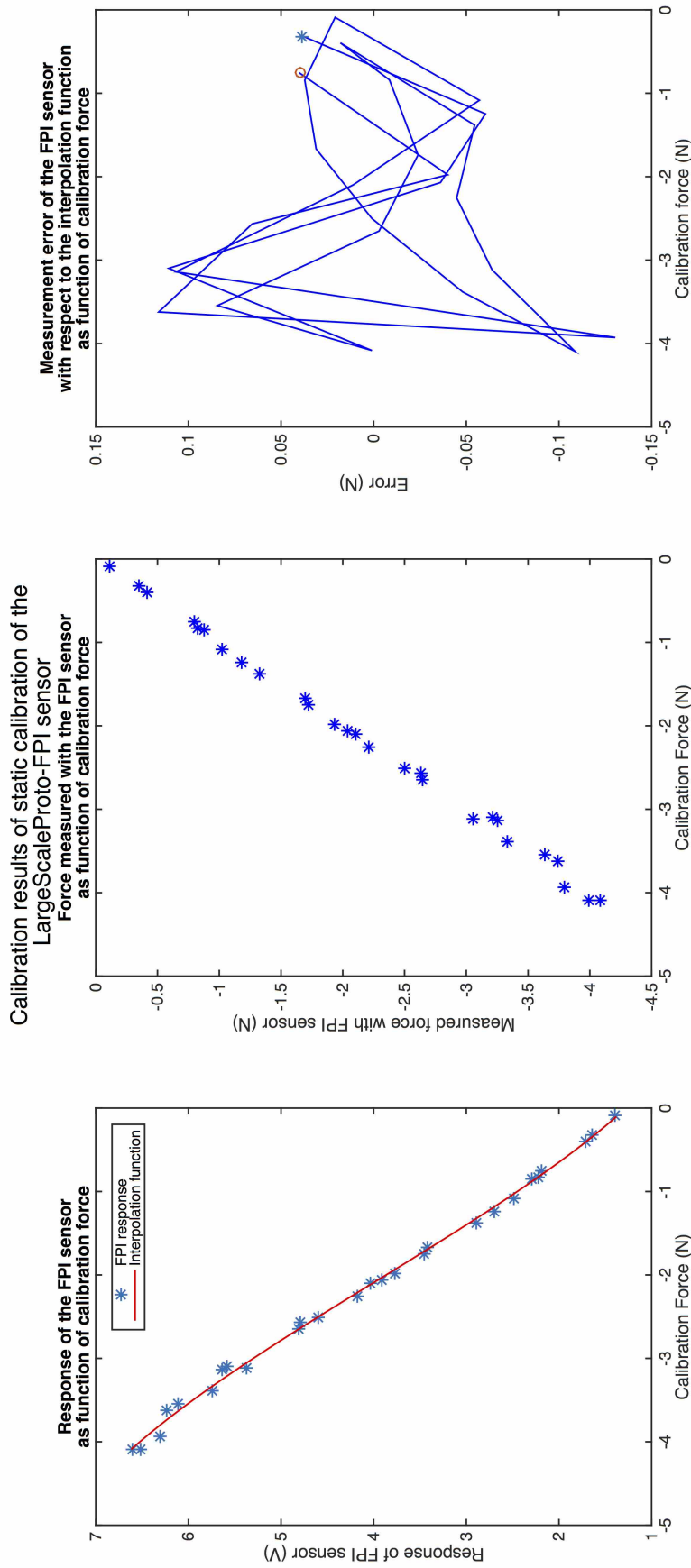


Figure D.18: Results of static calibration using homodyne interferometry of a large scale prototype of the stylet-tube concept shown in figure D.17. The response of the FPI as function of the calibration force, together with a fitted sinusoidal interpolation function is shown on the left. The center figure shows the force measured with the FPI, calculated using the interpolation function, as function of the calibration force. The measurement error of the FPI sensor as function of the calibration force is shown on the right. The blue star and the red circle indicate respectively the first and last reading obtained during static calibration.

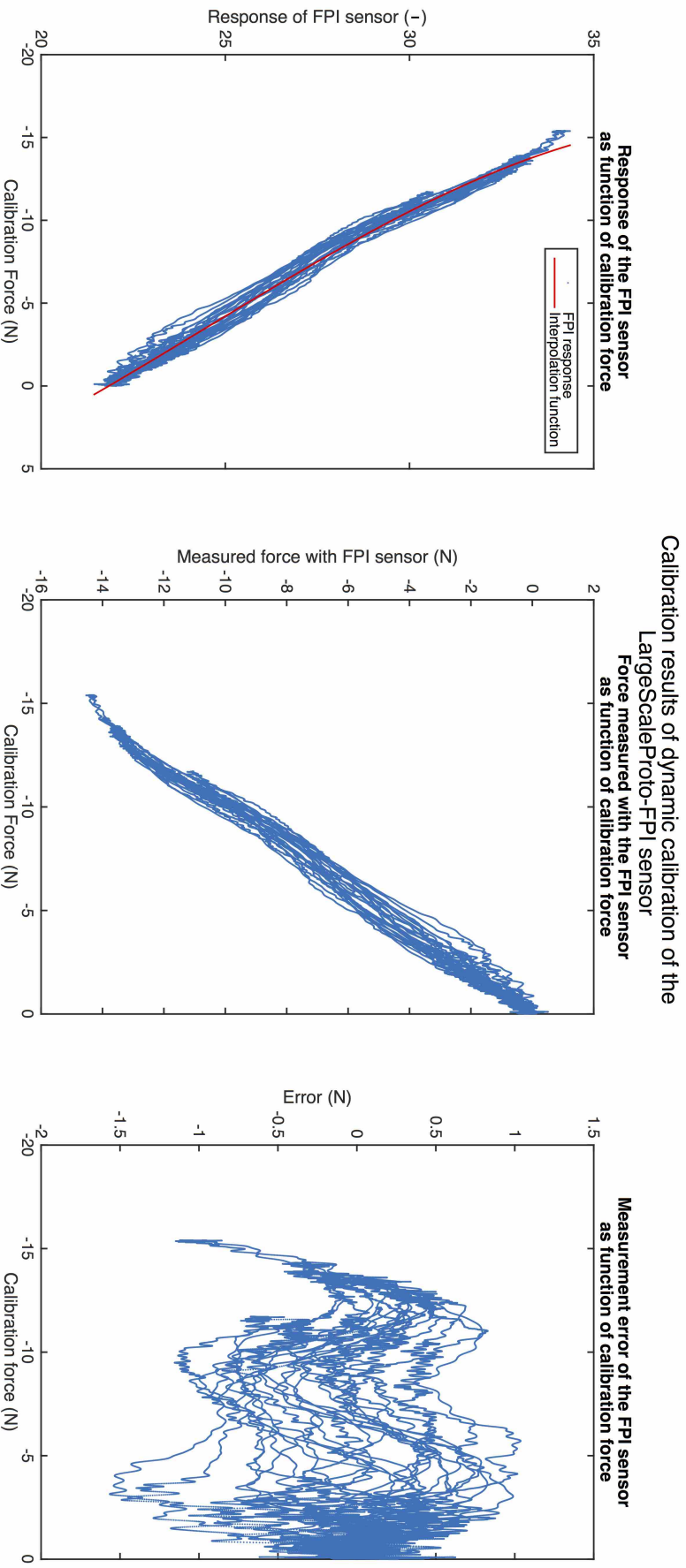


Figure D.19: Results of dynamic calibration at room temperature of a large scale prototype of the stylet tube concept and interrogated with low coherence interferometry. The response of the FPI as function of the calibration force, together with a fitted third order polynomial interpolation function is shown on the left. The figure in the center shows the force measured with the FPI, calculated using the interpolation function, as function of the calibration force. The measurement error of the FPI-based sensor as function of the calibration force is shown on the right.

Force measured with the LargeScaleProto-FPI sensor subjected to dynamic calibration forces as function of time

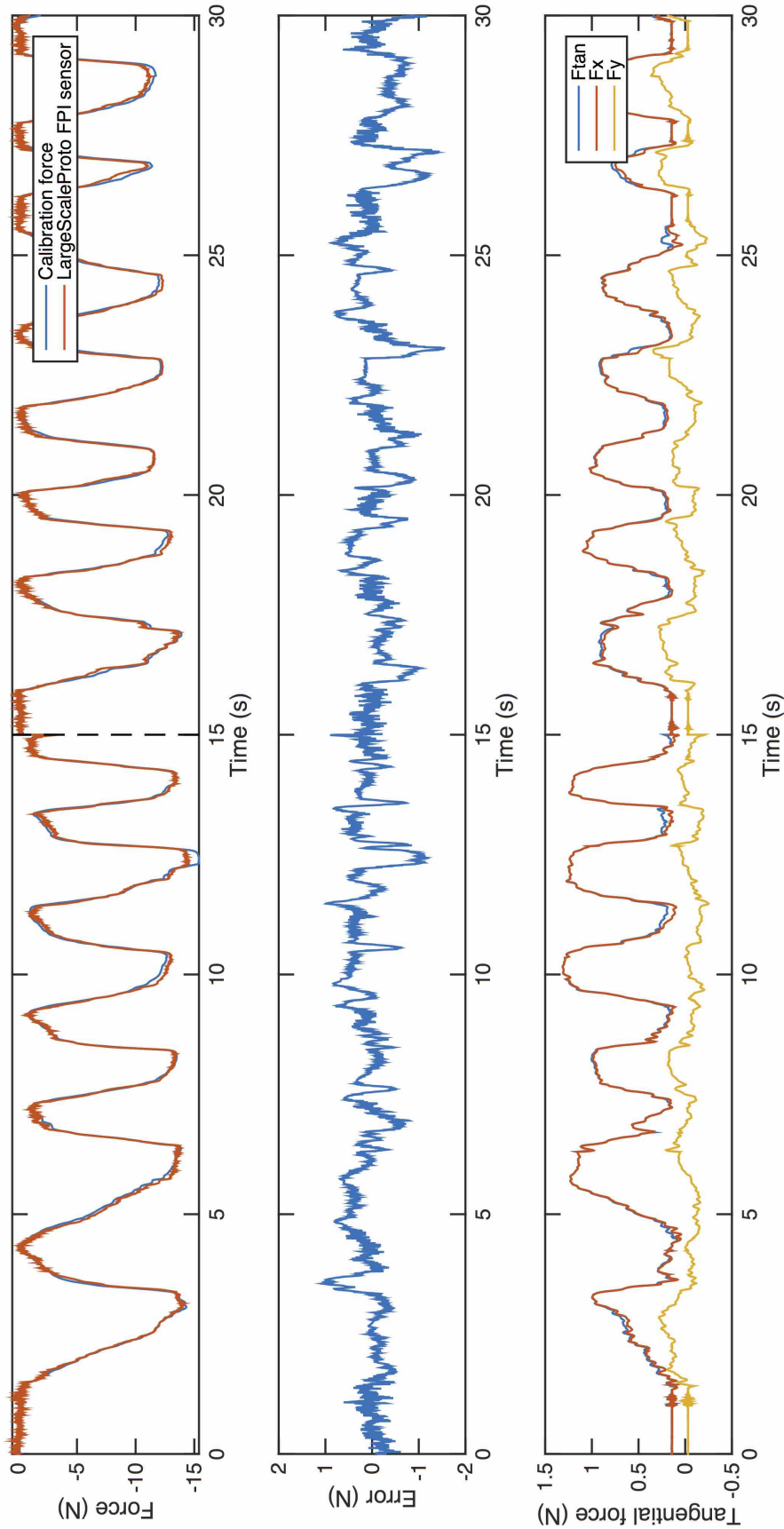


Figure D.20: Results of dynamic calibration at room temperature of a large scale prototype of the stylet tube concept interrogated with low coherence interferometry, shown as function of time. The graphs show, from top to bottom: (1) the calibration force and the force measured with the prototype, calculated using the interpolation function shown in figure D.19, (2) the measurement error of the prototype, (3) the transverse force on the needle tip, shown as the resultant transverse force 'Ftan' and its two orthogonal components 'Fx' and 'Fy'.

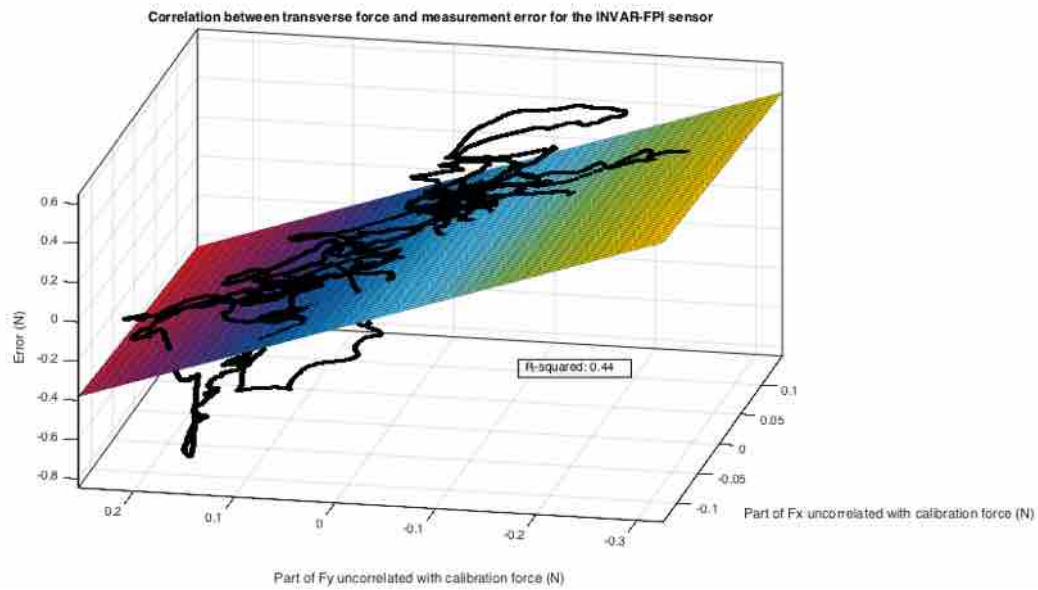


Figure D.21: Fit of a model explaining the measurement error of the axial calibration force using the part of the transverse forces (F_x and F_y) on the needle tip uncorrelated with the axial calibration force for a prototype of the stylet tube concept, fitted to data shown in figure D.22. The model shown in equation 4.4 was fitted to the data in a least-squares sense. The measurement error as function of the transverse force on the needle tip according to the fitted model is shown as the colored plane, while the actual measurement error as function of the transverse forces uncorrelated with the axial calibration force are shown as a black line. The coefficient of determination of the fit is 0.44, indicating that the transverse forces on the needle tip do not explain the total variation in measurement error very well. The 95% confidence intervals of the sensitivity of the FPI to the orthogonal components of the transverse force (F_x and F_y) are according to the model respectively -0.31 N/N to -0.26 N/N and -1.66 N/N to -1.63 N/N.

Sensitivity of a prototype of the stylet-tube concept to transverse force

Force measured with the INVAR-FPI sensor
subjected to dynamic calibration forces as function of time

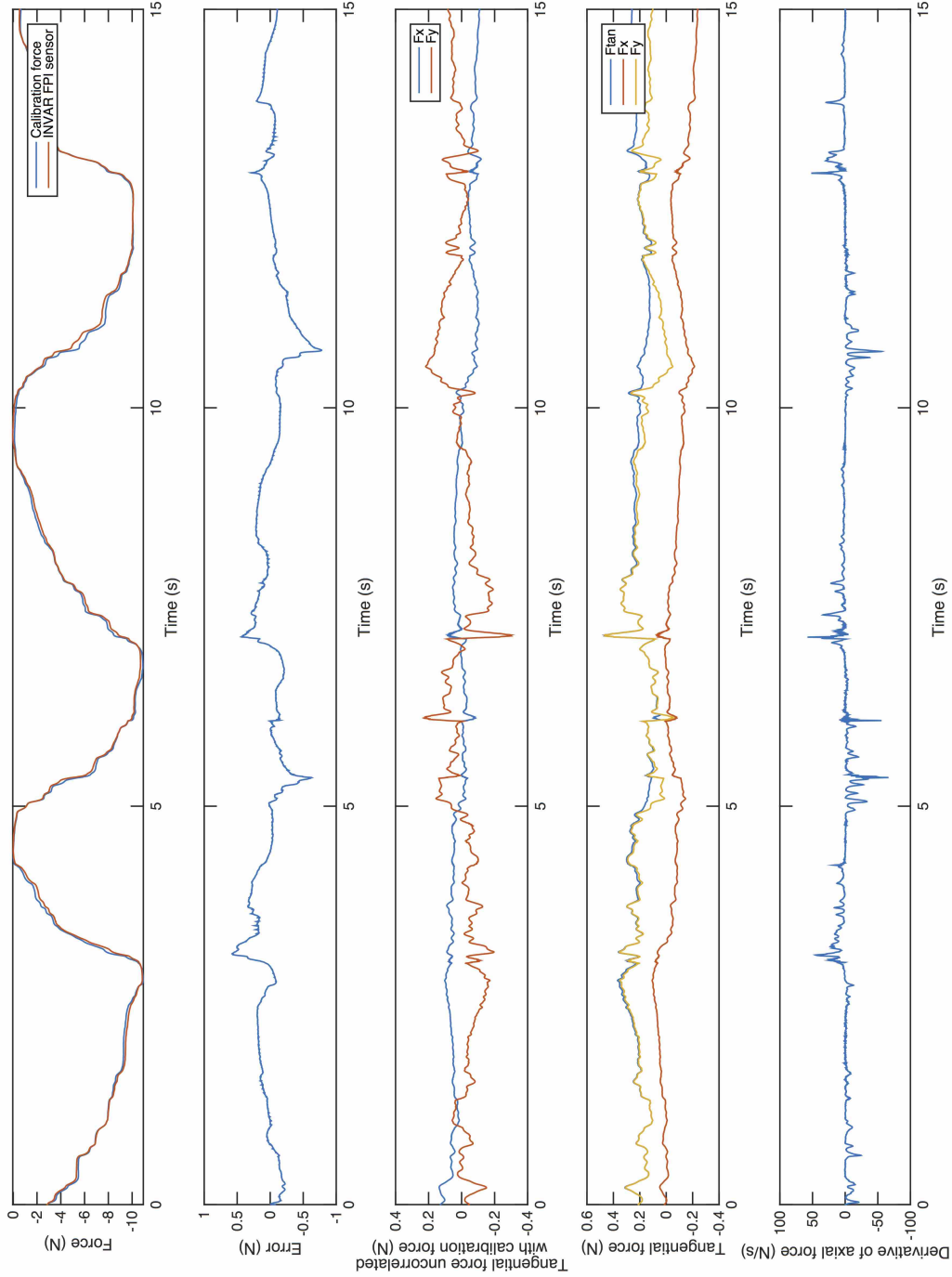


Figure D.22: Selection of results of dynamic calibration at room temperature of a prototype of the stylet tube concept interrogated with low coherence interferometry. The graphs show, from top to bottom: (1) the calibration force and the force measured with the prototype, calculated using a 3rd order polynomial interpolation function, (2) the measurement error of the prototype, (3) the parts of the transverse force on the needle tip uncorrelated with the axial calibration force, (4) the transverse force on the needle tip, shown as the resultant transverse force 'Ftan' and its two orthogonal components 'Fx' and 'Fy', and (5) the derivative of the calibration force to time.

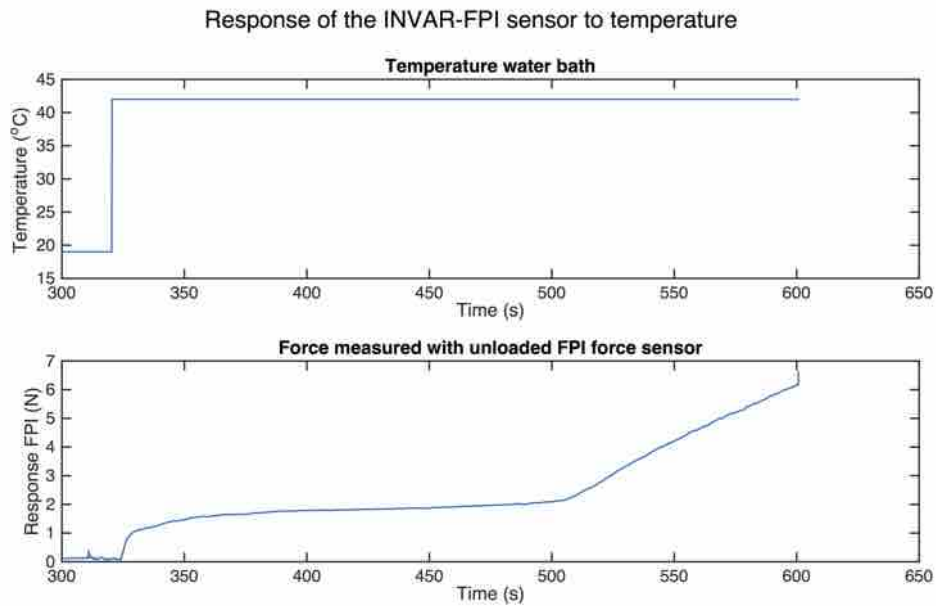
Response of a prototype of the stylet-tube concept to changes in temperature

Figure D.23: Detail of a test of the response of the stylet tube concept to a change in temperature. Three regimes can be observed in the response of the sensor to a change in temperature. The temperature of the water baths in which the prototype is submerged is shown in the top graph, while the peculiar response of the prototype is shown in the bottom graph expressed as measurement error in Newtons. A very fast and short response, resulting in an error of about 900 mN occurs first, after which a slow drift of the measurement error occurs that suddenly increases after a few minutes to a very fast drift.

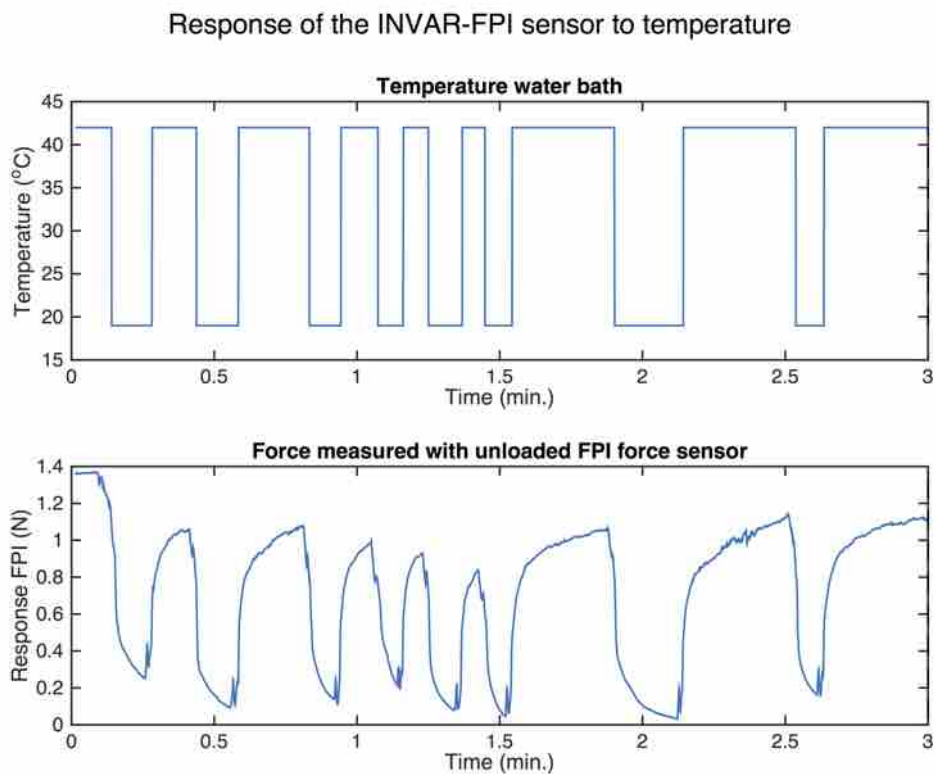


Figure D.24: Response of a prototype of the stylet tube concept to quick changes in temperature, after a long acclimatization in a hot water bath. The top graph shows the temperature of the water baths in which the prototype is submerged. The bottom graph shows the response of the FPI of the prototype in the form of a measurement error in Newtons.

Dynamic calibration of the thin film concept with varying temperatures

Force measured with the ThinFilm-FPI sensor
subjected to dynamic calibration forces as function of time

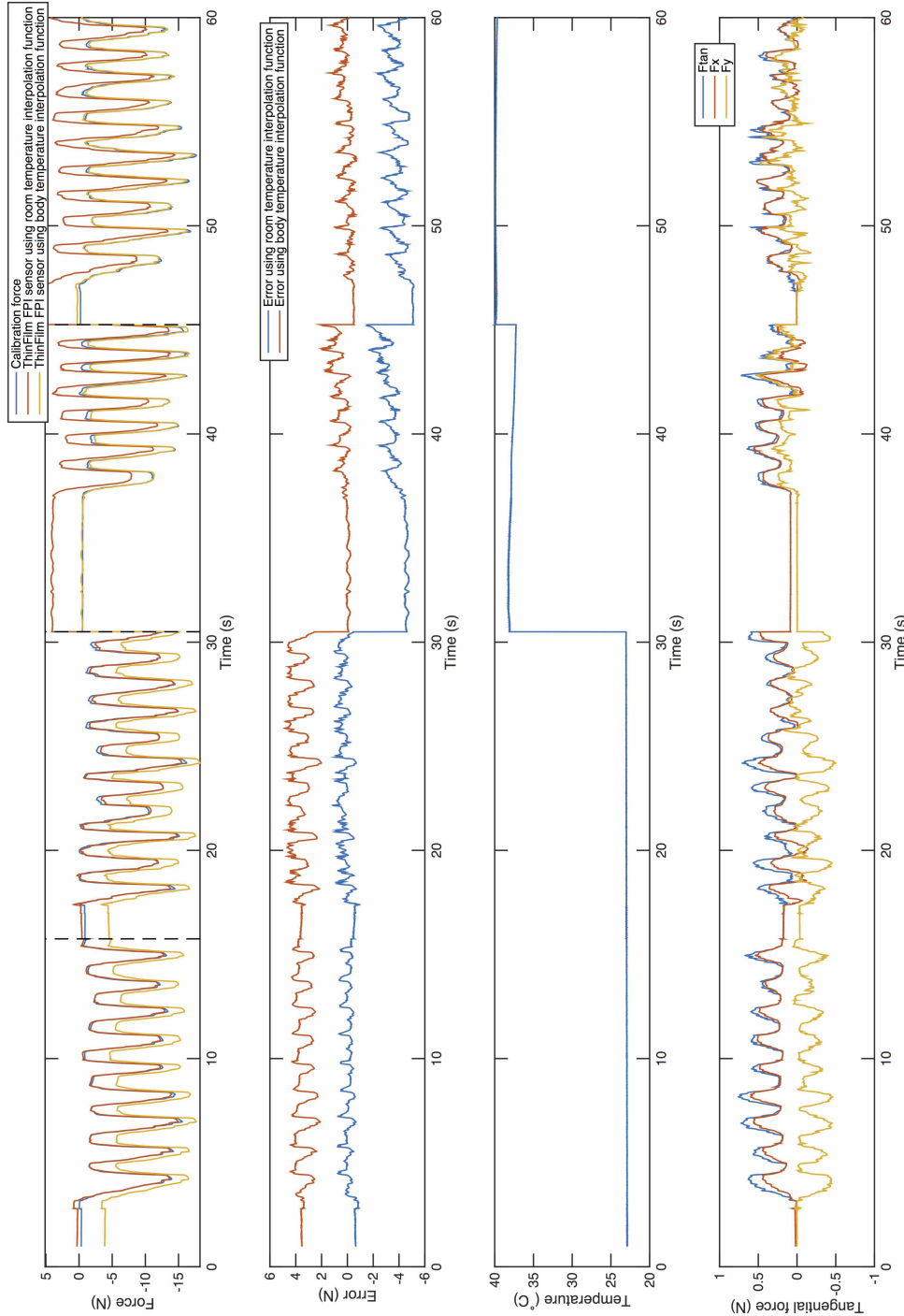


Figure D.25: Results of dynamic calibration of a proof-of-concept of the thin film concept with temperature varying between room temperature (approx. 23°C) and a feverish body temperature (approx. 39°C), interrogated with homodyne interferometry, shown as function of time. The graphs show, from top to bottom: (1) the calibration force and the force measured with the prototype, calculated using either the interpolation function for the response of the FPI at room temperature or the interpolation function for the response of the FPI at body temperature shown in figure 6.7, (2) the measurement error of the prototype, (3) the temperature of the water bath in which the prototype is submerged (4) the transverse force on the needle tip, shown as the resultant transverse force 'Fian' and its two orthogonal components 'Fx' and 'Fy'. The dashed lines in the top graph (1) indicate the 15 second long fragments of which the dataset obtained during dynamic calibration is composed.

D.8 Tables and graphs

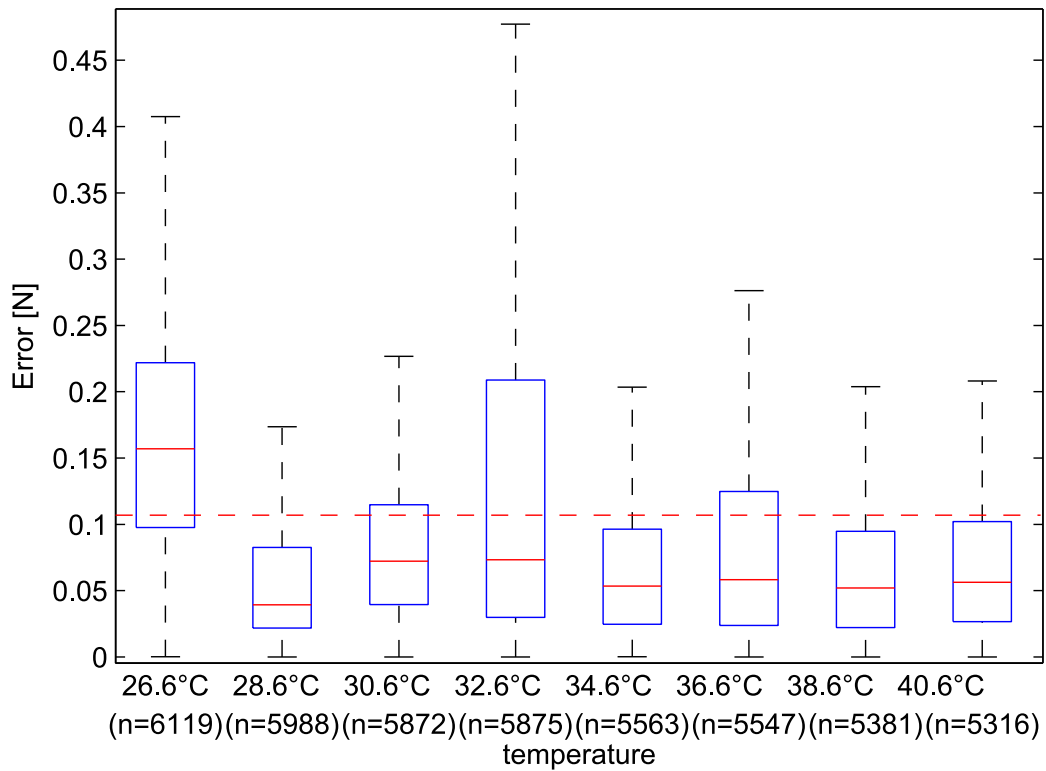


Figure D.26: Reported interpolation errors of an FBG-based needle tip force sensor designed by Gähler [1]. The sensor was calibrated at 8 different temperatures and the reported interpolation errors are the errors of measurements obtained during a calibration series at a certain temperature, consisting of 5 loading and unloading cycles, using the 'optimal' interpolation function determined for that specific temperature (it is therefore not possible to derive the magnitude of measurement errors due to cross-sensitivity of the sensor to temperature). The figure shows box plots of the (absolute value of) observed measurement errors.

Table D.6: Properties of adhesives used to bond optical fibers in ferrules according to specifications of manufacturers and suppliers. The CTE of Norland adhesives quoted by the supplier (Thorlabs), might be the CTE of the manufacturer specified for Norland Adhesive 61 (NOA 61 was not used for this project). The glass transition temperature of the used Norland adhesives was therefore also estimated using properties of NOA61 [251].

Type adhesive	General properties	Elastic modulus (GPa)	CTE ($\mu\text{strain/K}$)	Glass transition temperature	Cure	Sources
Norland optical adhesive 68	'Flexible adhesive'.	0.14 GPa	220	Below room temperature?	UV	[150, 252]
Norland optical adhesive 81	Fast curing adhesive producing a 'hard, resilient bond'. Can be polished after curing. Rapidly curing adhesive, forming 'tough, flexible' bonds that retain strength when exposed to water.	1.4 GPa	220	Below room temperature?	UV	[150, 252]
Loctite 350	High temperature epoxy for fiber optic and medical applications	?	100	50°C?	UV	[253, 254]
EPO-TEK 353ND		3.6 GPa	54	90°C	Heat curing	[255]

Table D.7: List of expected sources of measurement errors for prototypes of the unmachined-quartz-column concept. Expected impact of the error sources on the measurement accuracy was rated for interrogation of the FPI using either homodyne or low coherence interferometry (WLI). '0' indicates no impact at all on the measurement uncertainty using the interrogation method, '-' indicates likely unobservable contribution to measurement uncertainty compared to other contributions of other error sources, '+' indicates a significant contribution to the measurement uncertainty and '++' indicates a dominant contribution to the measurement uncertainty.

Element	Source measurement errors	Homodyne	WLI	Result
<i>FPI interrogation equipment</i>	Fluctuation wavelength optical source	-	-	Noise and/or drift
	Power disturbances source	-	0	Noise and/or drift
	Noise photodetector	+	+	Noise
	Noise other electronics (amplifiers etc.)	+	+	Noise
	Discretization A/D converter	-	-	Constant error
<i>Optical fiber</i>	Nonlinearity response FPI	+	+	Constant measurement error as function of force on tip/temperature of tip
	Attenuation due to bending	++	0	Constant error and modifying error varying with amount of bending
	Attenuation due to humidity	-	0	Constant error varying with humidity
	Attenuation due to temperature	-	0	Constant error varying with temperature
	Attenuation due to wavelength fluctuations light	-	0	Constant error varying with change in wavelength
<i>FPI mirrors</i>	Dependence reflectivity on temperature	+	0	Constant error varying with temperature
	Dependence of refractive index of air on temperature	+	+	Constant error varying with temperature
<i>FPI cavity medium</i>	Dependence of refractive index of air on humidity	-	-	Constant error varying with humidity
	Dependence of refractive index of air on air pressure	-	-	Constant error varying with humidity
<i>Force sensitive element</i>	Thermal expansion quartz glass	+	+	Constant error varying with temperature
	Thermal expansion glue in borehole	++	++	Constant error varying with temperature
	Thermal expansion stylet tube	+	+	Constant error varying with temperature
	Expansion of glue in borehole due to humidity	-	-	Constant error varying with humidity
	Dependence compliance quartz on temperature	-	-	Modifying error varying with temperature
	Dependence compliance glue in borehole on temperature	+	+	Modifying error varying with temperature
	Viscous behavior quartz	-	-	Limitation of (apparent) bandwidth
	Viscous behavior glue	+	+	Limitation of (apparent) bandwidth
	Creep quartz	+	-	Drift
	Creep glue	-	+	Drift
	Hysteresis quartz	-	-	Reversibility error
	Hysteresis glue	+	+	Reversibility error
	Hysteresis due to friction of unglued fiber in borehole	+	+	Reversibility error
	Transverse force	++	++	Constant error varying with transverse force

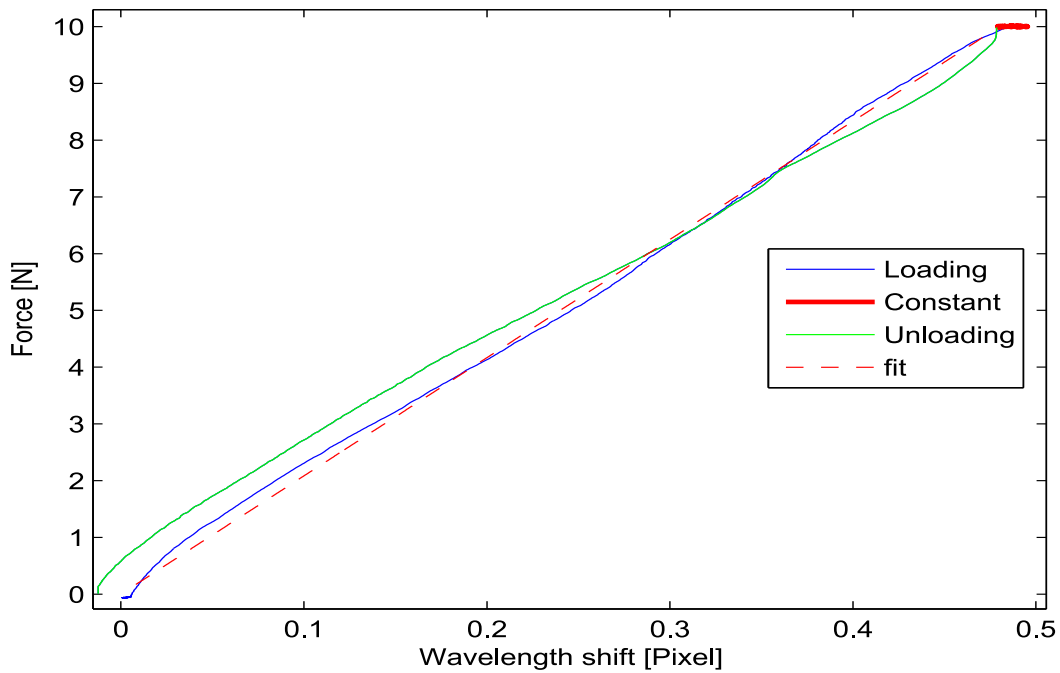
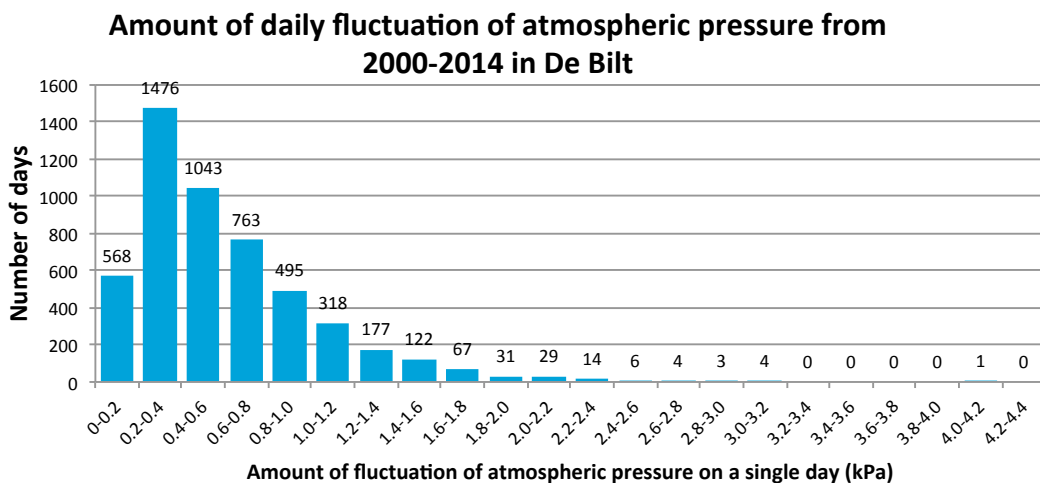


Figure D.27: Calibration results of an FBG-based needle tip force sensor designed by Gähler [1]. The response of the sensor for increasing loads is shown in blue, the response of the sensor to unloading in green, the drift due to a constant 10 N force in red and the interpolation function as a dashed red line. It can be observed that measurement errors up to about 0.75 N occur during unloading of the sensor when the shown interpolation function is used.



±

Figure D.28: Histogram showing the distribution of the difference between the maximum and minimum air pressure on a single day in kPa, measured in De Bilt from september 2000 to september 2014 (based on data from the KNMI [241])

Table D.8: Results of FE-analysis of the stylet tube concept, investigating the sensitivity of the force sensing FPI in the needle tip to force and temperature, as function of the CTE of Invar (for the range of CTEs of Invar presented in the CES edupack material database [131]), the thickness of the epoxy layer between the ferrule and Invar stylet tube, the modulus of elasticity of the epoxy, the CTE of the epoxy and the type of glue used to bond the optical fiber into the ferrule. The needle tip was assumed to be attached rigidly, without a glue layer, to the stylet tube. The FE-model accounts for the elastic modulus and CTE of used materials and the thermo-optic coefficient of air. The sensitivity to force is shown as the change in geometrical cavity length due to an applied force of 10 N on the needle tip. The sensitivity to temperature is shown as the equivalent change in FPI cavity length that results in an identical change in OPD of the FPI as the change in OPD due to a temperature change of 24°C. The constant measurement error after a temperature change of 24°C, due to cross-sensitivity to temperature, is shown in the last three columns.

Configuration: CTE _{INVAR} ($\mu\text{strain/K}$), modulus glue (GPa), glue borehole	Glue layer thickness (μm)	Change geometrical cavity length due to 10 N (nm)	Equivalent change geometrical cavity length due to temperature change of 24°C (nm)			Error due to temperature change of 24°C (N)		
			CTE _{epoxy} : 100 $\mu\text{strain/K}$	CTE _{epoxy} : 50 $\mu\text{strain/K}$	CTE _{epoxy} : 10 $\mu\text{strain/K}$	CTE _{epoxy} : 100 $\mu\text{strain/K}$	CTE _{epoxy} : 50 $\mu\text{strain/K}$	CTE _{epoxy} : 10 $\mu\text{strain/K}$
1.25, 0.5, NOA68	25	-297	-2.3	8.3	16.7	0.08	0.28	0.56
	50	-433	-12.9	5.5	20.1	0.30	0.13	0.46
2, 0.5, NOA68	25	-297	20.3	30.8	39.2	0.68	1.04	1.32
	50	-433	14.9	33.3	48.0	0.34	0.77	1.11
1.25, 0.5, EPOTEK	25	-293	-3.2	8.0	17.0	0.11	0.27	0.58
	50	-430	-14.1	5.1	20.5	0.33	0.12	0.48
2, 0.5, EPOTEK	25	-293	19.2	30.4	39.3	0.66	1.04	1.34
	50	-430	13.6	32.8	48.1	0.32	0.76	1.12
1.25, 3.5, NOA68	25	-185	-10.5	-0.3	7.8	0.57	0.02	0.42
	50	-246	-29.9	-9	7.7	1.22	0.37	0.31
2, 3.5, NOA68	25	-185	2.5	12.7	20.9	0.14	0.69	1.13
	50	-246	14.9	6	22.7	0.61	0.24	0.92
1.25, 3.5, EPOTEK	25	-178	-13.3	-1.5	7.9	0.75	0.08	0.44
	50	-239	-34.3	-10	7.6	1.44	0.42	0.32
2, 3.5, EPOTEK	25	-178	-0.6	11.2	20.6	0.03	0.63	1.16
	50	-239	19.6	3.8	22.4	0.82	0.16	0.94

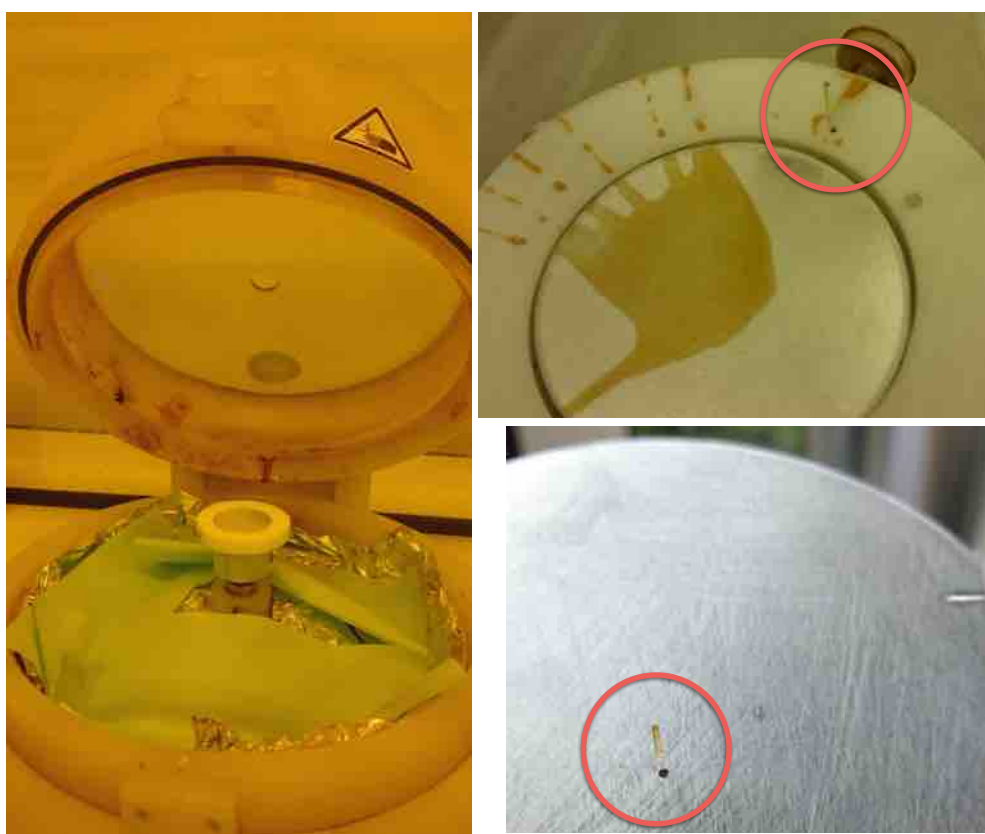


Figure D.29: On the left, a support made for applying spin coatings on top a ferrule, mounted on spin coater. Top right, detail of the same support. The ferrule was clamped with a PEEK bolt in a borehole in Teflon to prevent scratching of the quartz glass. Bottom right, the ferrule and optical fiber did hang through the borehole of an aluminum disk, fixated on the back side with a Teflon clamp, in the PECVD deposition device for the deposition of chromium coatings.

Bibliography

- [1] M. Gähler, “Forces in needle interventions,” Master’s thesis, 2012.
- [2] S. Elayaperumal, J. Bae, D. Christensen, M. Cutkosky, B. Daniel, R. Black, J. Costa, F. Faridian, and B. Moslehi, “MR-compatible biopsy needle with enhanced tip force sensing,” in *World Haptics Conference (WHC), 2013*, April 2013, pp. 109–114.
- [3] *Indian Journal of Physiology and Pharmacology*, “Evolution of medical application of syringe,” vol. 50, no. 3, pp. 199–204, 2006.
- [4] P. Sette, R. M. Dorizzi, and A. M. Azzini, “Vascular access: an historical perspective from Sir William Harvey to the 1956 Nobel prize to Andre F. Cournand, Werner Forssmann, and Dickinson W. Richards,” vol. 13, no. 2, 2012.
- [5] R. E. Kravetz, “Hypodermic syringe,” vol. 100, pp. 2614–2615, 2005.
- [6] A. Rivera, K. Strauss, A. van Zundert, and E. Mortier, “The history of peripheral intravenous catheters How little plastic tubes revolutionized medicine,” vol. 56, pp. 271–282, 2005.
- [7] O. Schwidetzky and N. J. Rutherford, “History of needles and syringes,” vol. 23, pp. 34–38, 1944.
- [8] Wikipedia. (2014, 1) Neuralgia. [Online]. Available: <http://en.wikipedia.org/wiki/Neuralgia> [Accessed: 30/1/2014]
- [9] R. D. Miller, L. I. Eriksson, L. A. Fleisher, J. P. Wiener-Kronish, and W. L. Young, *Miller’s Anesthesia*, 7th ed., R. D. Miller, Ed. Elsevier, 2009.
- [10] G. Lawrence, “The hypodermic syringe,” vol. 359, no. 9311, 2002.
- [11] N. Calthorpe, “The history of spinal needles: getting to the point,” vol. 59, pp. 1231–1241, 2004.
- [12] Getty Images. (1845) Rynd’s needle. [Online]. Available: <http://www.gettyimages.nl/detail/nieuwsfoto's/>

- the-first-hypodermic-needle-and-syringe-invented-by-irish-nieuwsfotos/81889937
[Accessed: 30/1/2014]
- [13] D. J. van Gerwen, “Needle-tissue interaction by experiment,” Ph.D. dissertation, 2013.
- [14] T. R. Kucklick, *The Medical Device R&D Handbook*. Taylor & Francis Group, 2006.
- [15] L. Barbé, B. Bayle, M. De Mathelin, and A. Gangi, “Online robust model estimation and haptic clues detection during in vivo needle insertions,” in *Biomedical Robotics and Biomechatronics, 2006. BioRob 2006. The First IEEE/RAS-EMBS International Conference on*, Feb 2006, pp. 341–346.
- [16] S. DiMaio and S. Salcudean, “Needle steering and motion planning in soft tissues,” *Biomedical Engineering, IEEE Transactions on*, vol. 52, no. 6, pp. 965–974, June 2005.
- [17] N. Abolhassani, R. Patel, and M. Moallem, “Needle insertion into soft tissue: A survey,” *Medical Engineering & Physics*, vol. 29, no. 4, pp. 413 – 431, 2007.
- [18] S. DiMaio and S. Salcudean, “Interactive simulation of needle insertion models,” *Biomedical Engineering, IEEE Transactions on*, vol. 52, no. 7, pp. 1167–1179, July 2005.
- [19] K. Cleary and T. M. Peters, “Image-guided interventions: technology review and clinical applications,” *Annual Review of Biomedical Engineering*, vol. 12, no. 1, pp. 119–142, 2010, pMID: 20415592.
- [20] A. Okamura, C. Simone, and M. O’Leary, “Force modeling for needle insertion into soft tissue,” *Biomedical Engineering, IEEE Transactions on*, vol. 51, no. 10, pp. 1707–1716, Oct 2004.
- [21] P. Brett, A. Harrison, and T. Thomas, “Schemes for the identification of tissue types and boundaries at the tool point for surgical needles,” *Information Technology in Biomedicine, IEEE Transactions on*, vol. 4, no. 1, pp. 30–36, March 2000.
- [22] B. Maurin, L. Barbe, B. Bayle, P. Zanne, J. Gangloff, M. De Mathelin, and A. Gangi, “In vivo study of forces during needle insertions,” in *Perspective in Image-guided Surgery Proceedings of the Scientific Workshop on Medical Robotics, Navigation, and Visualization (MRNV’04)*, 2004, pp. 415–422.
- [23] H. Su, M. Zervas, G. Cole, C. Furlong, and G. Fischer, “Real-time MRI-guided needle placement robot with integrated fiber optic force sensing,” in *Robotics and Automation (ICRA), 2011 IEEE International Conference on*, May 2011, pp. 1583–1588.
- [24] K. Henken, “Smart needles for percutaneous interventions,” PhD Thesis, 2014.
- [25] T. Lembrechts, “Tissue identification with fiber optic needle-tip sensors,” 2014, literature Report.
- [26] S. Misra, K. Reed, A. Douglas, K. T. Ramesh, and A. Okamura, “Needle-tissue interaction forces for bevel-tip steerable needles,” in *Biomedical Robotics and Biomechatronics, 2008. BioRob 2008. 2nd IEEE RAS EMBS International Conference on*, Oct 2008, pp. 224–231.
- [27] K. Salisbury, F. Conti, and F. Barbagli, “Haptic rendering: introductory concepts,” *Computer Graphics and Applications, IEEE*, vol. 24, no. 2, pp. 24–32, March 2004.

- [28] H. Kataoka, T. Washio, K. Chinzei, K. Mizuhara, C. Simone, and A. Okamura, "Measurement of the tip and friction force acting on a needle during penetration," in *Medical Image Computing and Computer-Assisted Intervention — MICCAI 2002*, ser. Lecture Notes in Computer Science, T. Dohi and R. Kikinis, Eds. Springer Berlin Heidelberg, 2002, vol. 2488, pp. 216–223.
- [29] S. Elayaperumal, J. H. Bae, B. L. Daniel, and M. R. Cutkosky, "Detection of membrane puncture with haptic feedback using a tip-force sensing needle," in *IROS 2014*, 2014.
- [30] C. Simone and A. Okamura, "Modeling of needle insertion forces for robot-assisted percutaneous therapy," in *Robotics and Automation, 2002. Proceedings. ICRA '02. IEEE International Conference on*, vol. 2, 2002, pp. 2085–2091 vol.2.
- [31] D. De Lorenzo, Y. Koseki, E. De Momi, K. Chinzei, and A. Okamura, "Experimental evaluation of a coaxial needle insertion assistant with enhanced force feedback," in *Engineering in Medicine and Biology Society, EMBC, 2011 Annual International Conference of the IEEE*, Aug 2011, pp. 3447–3450.
- [32] D. Abbink, "The human controller, class 2, perception," in *Course at Delft University of Technology*, 2014.
- [33] J. Peirs, J. Clijnen, D. Reynaerts, H. V. Brussel, P. Herijgers, B. Corteville, and S. Boone, "A micro optical force sensor for force feedback during minimally invasive robotic surgery," *Sensors and Actuators A: Physical*, vol. 115, no. 2–3, pp. 447 – 455, 2004, the 17th European Conference on Solid-State Transducers.
- [34] J. Hogervorst, "Percutaneous measurement of tissue compliance," Master's thesis, 2013.
- [35] J. F. Greenleaf, M. Fatemi, and M. Insana, "Selected methods for imaging elastic properties of biological tissues," *Annual Review of Biomedical Engineering*, vol. 5, no. 1, pp. 57–78, 2003.
- [36] I. Kang, D. Panneerselvam, V. P. Panoskaltsis, S. J. Eppell, R. E. Marchant, and C. M. Doerschuk, "Changes in the hyperelastic properties of endothelial cells induced by tumor necrosis factor-alpha," vol. 94, pp. 3273–3285, 2008.
- [37] M. C. Murphy, J. Huston, C. R. Jack, K. J. Glaser, A. Manduca, J. P. Felmlee, and R. L. Ehman, "Decreased brain stiffness in Alzheimer's disease determined by magnetic resonance elastography," *Journal of Magnetic Resonance Imaging*, vol. 34, no. 3, pp. 494–498, 2011.
- [38] J. Guo, S. Hirsch, A. Fehlner, S. Papazoglou, M. Scheel, J. Braun, and I. Sack, "Towards an elastographic atlas of brain anatomy," vol. 8, no. 8, 2003.
- [39] Y. K. Mariappan, K. J. Glaser, and R. L. Ehman, "Magnetic resonance elastography: A review," *Clinical Anatomy*, vol. 23, no. 5, pp. 497–511, 2010.
- [40] L. Sandrin, B. Fourquet, J.-M. Hasquenoph, S. Yon, C. Fournier, F. Mal, C. Christidis, M. Ziol, B. Poulet, F. Kazemi, M. Beaugrand, and R. Palau, "Transient elastography: a new noninvasive method for assessment of hepatic fibrosis," *Ultrasound in Medicine and Biology*, vol. 29, no. 12, pp. 1705 – 1713, 2003.
- [41] S. Hall and R. Buchbinder, "Do imaging methods that guide needle placement improve outcome?" *Annals of the Rheumatic Diseases*, vol. 63, no. 9, pp. 1007–1008, 2004.

- [42] J. A. Eustace, D. P. Brophy, R. P. Gibney, B. Bresnihan, and O. FitzGerald, "Comparison of the accuracy of steroid placement with clinical outcome in patients with shoulder symptoms," *Annals of the Rheumatic Diseases*, vol. 56, no. 1, pp. 59–63, 1997.
- [43] K. Raza, C. Y. Lee, D. Pilling, S. Heaton, R. D. Situnayake, D. M. Carruthers, C. D. Buckley, C. Gordon, and M. Salmon, "Ultrasound guidance allows accurate needle placement and aspiration from small joints in patients with early inflammatory arthritis," *Rheumatology*, vol. 42, no. 8, pp. 976–979, 2003.
- [44] G. Gherardi, *Fine-Needle Biopsy of Superficial and Deep Masses*. Springer, 2009.
- [45] M. R. Alison, Ed., *The Cancer Handbook*. Nature Publishing Group, 2001.
- [46] S. Gupta and D. C. Madoff, "Image-guided percutaneous needle biopsy in cancer diagnosis and staging," vol. 10, pp. 88–101, 2007.
- [47] J. L. Prince and J. M. Links, *Medical Imaging*. Pearson Prentice Hall, 2005.
- [48] P. Butler, A. W. M. Mitchell, and H. Ellis, *Applied Radiological Anatomy for Medical Students*, 3rd ed. Cambridge University Press, 2011.
- [49] J. S. Lewin, S. G. Nour, and J. L. Duerk, "Magnetic resonance image-guided biopsy and aspiration," vol. 11, pp. 173–183, 2000.
- [50] E. Morris and L. Liberman, *Breast MRI*. Springer Science+Business Media, Inc, 2005.
- [51] R. Kokes, K. Lister, R. Gullapalli, B. Zhang, A. MacMillan, H. Richard, and J. P. Desai, "Towards a teleoperated needle driver robot with haptic feedback for RFA of breast tumors under continuous MRI," *Medical Image Analysis*, vol. 13, no. 3, pp. 445 – 455, 2009. [Online]. Available: <http://www.sciencedirect.com/science/article/pii/S1361841509000061>
- [52] B. Maurin, O. Piccin, B. Bayle, J. Gangloff, M. de Mathelin, L. Soler, and A. Gangi, "A new robotic system for ct-guided percutaneous procedures with haptic feedback," *International Congress Series*, vol. 1268, no. 0, pp. 515 – 520, 2004, {CARS} 2004 - Computer Assisted Radiology and Surgery. Proceedings of the 18th International Congress and Exhibition. [Online]. Available: <http://www.sciencedirect.com/science/article/pii/S0531513104007599>
- [53] H. Su, W. Shang, G. Cole, K. Harrington, and G. Fischer, "Haptic system design for MRI-guided needle based prostate brachytherapy," in *Haptics Symposium, 2010 IEEE*, March 2010, pp. 483–488.
- [54] R. Monfaredi, R. Seifabadi, G. Fichtinger, and I. Iordachita, "Design of a decoupled mri-compatible force sensor using fiber bragg grating sensors for robot-assisted prostate interventions," pp. 867 118–867 118–9, 2013. [Online]. Available: <http://dx.doi.org/10.1117/12.2008160>
- [55] O. Gerovich, P. Marayong, and A. Okamura, "The effect of visual and haptic feedback on computer-assisted needle insertion," in *Medical Image Computing and Computer-Assisted Intervention — MICCAI 2002*, 2002, pp. 147–154.
- [56] W. Zarrad, P. Poignet, R. Cortesao, and O. Company, "Towards teleoperated needle insertion with haptic feedback controller," in *Intelligent Robots and Systems, 2007. IROS 2007. IEEE/RSJ International Conference on*, Oct 2007, pp. 1254–1259.

- [57] O. Piccin, L. Barbé, B. Bayle, M. de Mathelin, and A. Gangi, “A force feedback teleoperated needle insertion device for percutaneous procedures,” *The International Journal of Robotics Research*, 2009. [Online]. Available: <http://ijr.sagepub.com/content/early/2009/05/19/0278364909101408.abstract>
- [58] I. Brouwer, J. Ustin, L. Bentley, A. Sherman, N. Dhruv, and F. Tendick, “Measuring in vivo animal soft tissue properties for haptic modeling in surgical simulation,” in *Studies Health Technology and Informics*. IOS Press, 2001, pp. 69–74.
- [59] E. Dehghan, X. Wen, R. Zahiri-Azar, M. Marchal, and S. Salcudean, “Parameter identification for a needle-tissue interaction model,” in *Engineering in Medicine and Biology Society, 2007. EMBS 2007. 29th Annual International Conference of the IEEE*, Aug 2007, pp. 190–193.
- [60] D. J. van Gerwen, J. Dankelman, and J. J. van den Dobbelsteen, “Needle–tissue interaction forces – a survey of experimental data,” *Medical Engineering & Physics*, vol. 34, no. 6, pp. 665 – 680, 2012.
- [61] J. T. Hing, A. D. Brooks, and J. P. Desai, “A biplanar fluoroscopic approach for the measurement, modeling, and simulation of needle and soft-tissue interaction,” *Medical Image Analysis*, vol. 11, no. 1, pp. 62 – 78, 2007. [Online]. Available: <http://www.sciencedirect.com/science/article/pii/S1361841506000776>
- [62] K. Naemura, “Comparative phantom study on epidural anesthesia needle,” in *Engineering in Medicine and Biology Society, 2006. EMBS '06. 28th Annual International Conference of the IEEE*, Aug 2006, pp. 4995–4998.
- [63] N. Abolhassani, R. Patel, and M. Moallem, “Experimental study of robotic needle insertion in soft tissue,” *International Congress Series*, vol. 1268, no. 0, pp. 797 – 802, 2004, {CARS} 2004 - Computer Assisted Radiology and Surgery. Proceedings of the 18th International Congress and Exhibition. [Online]. Available: <http://www.sciencedirect.com/science/article/pii/S0531513104005394>
- [64] ATI Industrial Automation. Ati force / torque sensor. [Online]. Available: http://www.ati-ia.com/products/ft/ft_models.aspx?id=Nano17 [Accessed: 10/11/2014]
- [65] C. Schneider, “Systems for robotic needle insertion and tool-tissue interaction modeling,” Master’s thesis, 2004.
- [66] A. Asadian, “Robotics-assisted needle steering for percutaneous interventions: modeling and experiments,” Ph.D. dissertation, 2013.
- [67] T. Podder, D. Clark, J. Sherman, D. Fuller, E. Messing, D. Rubens, J. Strang, R. Brasacchio, L. Liao, W.-S. Ng, and Y. Yu, “In vivo motion and force measurement of surgical needle intervention during prostate brachytherapy,” vol. 33, no. 8, pp. 2915–2922, 2006.
- [68] J. Crouch, C. Schneider, J. Wainer, and A. Okamura, *A Velocity-Dependent Model for Needle Insertion in Soft Tissue*, 2005.
- [69] O. Bebek, M. J. Hwang, B. Fei, and M. Cavusoglu, “Design of a small animal biopsy robot,” in *Engineering in Medicine and Biology Society, 2008. EMBS 2008. 30th Annual International Conference of the IEEE*, Aug 2008, pp. 5601–5604.

- [70] K. Reed, A. Okamura, and N. Cowan, "Controlling a robotically steered needle in the presence of torsional friction," in *Robotics and Automation, 2009. ICRA '09. IEEE International Conference on*, May 2009, pp. 3476–3481.
- [71] N. Nillahoot and J. Suthakorn, "Development of veress needle insertion robotic system and its experimental study for force acquisition in soft tissue," in *Robotics and Biomimetics (ROBIO), 2013 IEEE International Conference on*, Dec 2013, pp. 645–650.
- [72] T. Wedlick and A. Okamura, "Characterization of robotic needle insertion and rotation in artificial and ex vivo tissues," in *Biomedical Robotics and Biomechatronics (BioRob), 2012 4th IEEE RAS EMBS International Conference on*, June 2012, pp. 62–68.
- [73] Roth Monzon, Emilio Loren, Chellali, Amine, Dumas, Cedric, and Cao, Caroline G.L., "Haptic sensitivity in needle insertion: the effects of training and visual aid," *BIO Web of Conferences*, vol. 1, p. 00065, 2011. [Online]. Available: <http://dx.doi.org/10.1051/bioconf/20110100065>
- [74] Z. Neubach and M. Shoham, "Ultrasound-guided robot for flexible needle steering," *Biomedical Engineering, IEEE Transactions on*, vol. 57, no. 4, pp. 799–805, April 2010.
- [75] D. Glozman and M. Shoham, "Flexible needle steering and optimal trajectory planning for percutaneous therapies," in *Medical Image Computing and Computer-Assisted Intervention–MICCAI 2004*. Springer, 2004, pp. 137–144.
- [76] E. Samur, M. Sedef, C. Basdogan, L. Avtan, and O. Duzgun, "A robotic indenter for minimally invasive characterization of soft tissues," *International Congress Series*, vol. 1281, no. 0, pp. 713 – 718, 2005, {CARS} 2005: Computer Assisted Radiology and Surgery Proceedings of the 19th International Congress and Exhibition. [Online]. Available: <http://www.sciencedirect.com/science/article/pii/S0531513105003420>
- [77] B. Tay, J. Kim, and M. Srinivasan, "In vivo mechanical behavior of intra-abdominal organs," *Biomedical Engineering, IEEE Transactions on*, vol. 53, no. 11, pp. 2129–2138, Nov 2006.
- [78] T. Hu, "Reality-based soft tissue probing: experiments and computational model for application to minimally invasive surgery," Ph.D. dissertation, 2006.
- [79] P. Polygerinos, A. Ataollahi, T. Schaeffter, R. Razavi, L. Seneviratne, and K. Althoefer, "Mri-compatible intensity-modulated force sensor for cardiac catheterization procedures," *Biomedical Engineering, IEEE Transactions on*, vol. 58, no. 3, pp. 721–726, March 2011.
- [80] I. Iordachita, Z. Sun, M. Balicki, J. U. Kang, S. J. Phee, J. Handa, P. Gehlbach, and R. Taylor, "A sub-millimetric, 0.25 mm resolution fully integrated fiber-optic force-sensing tool for retinal microsurgery," vol. 4, pp. 383–390, 2009.
- [81] X. Liu, I. I. Iordachita, X. He, R. H. Taylor, and J. U. Kang, "Miniature fiber-optic force sensor for vitreoretinal microsurgery based on low-coherence Fabry-Pérot interferometry," vol. 8218, 2012, pp. 82 1800–82 1800–6.
- [82] D. Stefanescu, *Handbook of Force Transducers*. Springer-Verlag, 2011.
- [83] E. Udd and W. B. Spillman, Eds., *Fiber Optic Sensors*, 2nd ed. Jonh Wiley & Sons, 2011.

- [84] F. L. Hammond, M. J. Smith, and R. J. Wood, "Estimating surgical needle deflection with printed strain gauges," in *Engineering in Medicine and Biology Society (EMBC), 2014 36th Annual International Conference of the IEEE*, Aug 2014, pp. 6931–6936.
- [85] J. Heijmans, L. Cheng, and F. Wieringa, "Optical fiber sensors for medical applications — practical engineering considerations," in *4th European Conference of the International Federation for Medical and Biological Engineering*, ser. IFMBE Proceedings, J. Sloten, P. Verdonck, M. Nyssen, and J. Haueisen, Eds. Springer Berlin Heidelberg, 2009, vol. 22, pp. 2330–2334.
- [86] A. Yamamoto, M. Rajendra, Y. Hirano, H. Kataoka, H. Yokota, R. Himeno, and T. Higuchi, "Motion generation in mri using an electrostatic linear motor for visualizing internal deformation of soft objects by tagged cine-mri," in *Industrial Electronics, 2007. ISIE 2007. IEEE International Symposium on*, June 2007, pp. 2741–2746.
- [87] R. Gassert, D. Chapuis, H. Bleuler, and E. Burdet, "Sensors for applications in magnetic resonance environments," *Mechatronics, IEEE/ASME Transactions on*, vol. 13, no. 3, pp. 335–344, June 2008.
- [88] Y. Koseki, T. Tanikawa, and K. Chinzei, "Mri-compatible micromanipulator; design and implementation and mri-compatibility tests," in *Engineering in Medicine and Biology Society, 2007. EMBS 2007. 29th Annual International Conference of the IEEE*, Aug 2007, pp. 465–468.
- [89] J. M. López-Higuera, Ed., *Handbook of Optical Fibre Sensing Technology*. John Wiley & Sons, Ltd, 2002.
- [90] S. Yin, P. B. Ruffin, and F. T. S. Yu, *Fiber Optic Sensors*. CRC Press, 2008.
- [91] B. Lee, "Review of the present status of optical fiber sensors," *Optical Fiber Technology*, vol. 9, no. 2, pp. 57 – 79, 2003.
- [92] H. Su and G. Fischer, "A 3-axis optical force/torque sensor for prostate needle placement in magnetic resonance imaging environments," in *Technologies for Practical Robot Applications, 2009. TePRA 2009. IEEE International Conference on*, Nov 2009, pp. 5–9.
- [93] P. Polygerinos, L. Seneviratne, R. Razavi, T. Schaeffter, and K. Althoefer, "Triaxial catheter-tip force sensor for mri-guided cardiac procedures," *Mechatronics, IEEE/ASME Transactions on*, vol. 18, no. 1, pp. 386–396, Feb 2013.
- [94] Y. Rao, "In-fibre bragg grating sensors," *Measurement Science and Technology*, vol. 8, no. 4, p. 355, 1997.
- [95] A. D. Kersey, "A review of recent developments in fiber optic sensor technology," *Optical Fiber Technology*, vol. 2, no. 3, pp. 291 – 317, 1996.
- [96] T. K. Gangopadhyay, "Prospects for fibre bragg gratings and Fabry-Perot interferometers in fibre-optic vibration sensing," *Sensors and Actuators A: Physical*, vol. 113, no. 1, pp. 20 – 38, 2004.
- [97] M. Connelly, *DETECTION — Fiber Sensors*. Oxford: Elsevier, 2005, pp. 191 – 200.
- [98] L. K. Cheng, R. Koops, A. Wielders, and W. Ubachs, "Development of a fringe sensor based on 3x3 fiber optic coupler for space interferometry," vol. 5855, 2005, pp. 1004–1007.

- [99] P. Harmsma, J. Staats, D. Lo Cascio, and L. Cheng, "Three-port interferometer in silicon-on-insulator for wavelength monitoring and displacement measurement," in *Lasers and Electro-Optics Europe (CLEO EUROPE/EQEC), 2011 Conference on and 12th European Quantum Electronics Conference*, May 2011, pp. 1–1.
- [100] E. Udd, "Review of multi-parameter fiber grating sensors," in *Optics East 2007*. International Society for Optics and Photonics, 2007, pp. 677 002–677 002.
- [101] Y.-L. Park, S. Elayaperumal, B. Daniel, S. C. Ryu, M. Shin, J. Savall, R. Black, B. Moslehi, and M. Cutkosky, "Real-time estimation of 3-d needle shape and deflection for mri-guided interventions," *Mechatronics, IEEE/ASME Transactions on*, vol. 15, no. 6, pp. 906–915, Dec 2010.
- [102] A. D. Kersey, M. Davis, H. Patrick, M. Leblanc, K. Koo, C. Askins, M. Putnam, and E. Friebele, "Fiber grating sensors," *Lightwave Technology, Journal of*, vol. 15, no. 8, pp. 1442–1463, Aug 1997.
- [103] M. Xu, J.-L. Archambault, L. Reekie, and J. Dakin, "Discrimination between strain and temperature effects using dual-wavelength fibre grating sensors," *Electronics Letters*, vol. 30, no. 13, pp. 1085–1087, Jun 1994.
- [104] O. Frazao, L. A. Ferreira, F. M. Araujo, and J. L. Santos, "Applications of fiber optic grating technology to multi-parameter measurement," vol. 24, no. 3-4, pp. 227–244, 2005. [Online]. Available: <http://dx.doi.org/10.1080/01468030590922966>
- [105] L. Li, X. Tong, C. Zhou, H. Wen, D. Lv, K. Ling, and C. Wen, "Integration of miniature fabry-perot fiber optic sensor with {FBG} for the measurement of temperature and strain," *Optics Communications*, vol. 284, no. 6, pp. 1612 – 1615, 2011. [Online]. Available: <http://www.sciencedirect.com/science/article/pii/S003040181001223X>
- [106] B. Gupta, *Fiber Optic Sensors: Principles and Applications*. New India Publishing Agency, 2006.
- [107] C. on new sensor technologies: materials and applications, *Expanding the Vision of Sensor Materials*, N. Eror, Ed. National academy press, 1995.
- [108] M. Bass, Ed., *Handbook of Optics*, 3rd ed. Mc Graw Hill, 2010, vol. 1.
- [109] R. Schmidt, G. Schitter, and J. van Eijk, *The Design of High Performance Mechatronics*. IOS Press, 2011.
- [110] B. H. Lee, Y. H. Kim, K. S. Park, J. B. Eom, M. J. Kim, B. S. Rho, and H. Y. Choi, "Interferometric fiber optic sensors," *Sensors*, vol. 12, no. 3, pp. 2467–2486, 2012.
- [111] D. Callaghan, M. McGrath, G. Rajan, Y. Semenova, G. Farrell, and E. Coyle, "Comparing FBG and PCF force sensors in a laparoscopic smart surgical scissor instrument," in *Proceedings of the Joint Workshop on New Technologies for Computer/Robot Assisted Surgery*, G. A. Holzapfel, J. V. Sloten, M. M. Sette, D. Pierce, and D. Stoyanov, Eds., 2011.
- [112] F. C. Favero, L. Araujo, G. Bouwmans, V. Finazzi, J. Villatoro, and V. Pruneri, "Spheroidal Fabry-Perot microcavities in optical fibers for high-sensitivity sensing," *Optics Express*, vol. 20, no. 7, pp. 7112–7118, Mar 2012.

- [113] É. Pinet, “Fabry-Pérot fiber-optic sensors for physical parameters measurement in challenging conditions,” vol. 2009, 2009.
- [114] D. Iannuzzi, S. Deladi, V. J. Gadgil, R. G. P. Sanders, H. Schreuders, and M. C. Elwenspoek, “Monolithic fiber-top sensor for critical environments and standard applications,” *Applied Physics Letters*, vol. 88, no. 5, p. 053501, 2006.
- [115] D. Chavan, G. Gruca, S. de Man, M. Slaman, J. H. Rector, K. Heeck, and D. Iannuzzi, “Ferrule-top atomic force microscope,” *Review of Scientific Instruments*, vol. 81, no. 12, pp. –, 2010.
- [116] M. Han, “Theoretical and experimental study of low-finesse extrinsic Fabry-Perot interferometric fiber optic sensors,” Ph.D. dissertation, 2006.
- [117] T. Penzkofer, N. Peykan, K. Schmidt, G. Krombach, and C. K. Kuhl, “How MRI Compatible is ”MRI Compatible”? A Systematic Comparison of Artifacts Caused by Biopsy Needles at 3.0 and 1.5 T,” vol. 36, pp. 1646–1657, 2013.
- [118] M. Bass, Ed., *Handbook of Optics*, 3rd ed. Mc Graw Hill, 2010, vol. 5.
- [119] X. Wu and O. Solgaard, “Short-cavity multimode fiber-tip Fabry-Pérot sensors,” *Opt. Express*, vol. 21, no. 12, pp. 14 487–14 499, Jun 2013.
- [120] K. M. Kennedy, B. F. Kennedy, R. A. McLaughlin, and D. D. Sampson, “Needle optical coherence elastography for tissue boundary detection,” *Optics Letters*, vol. 37, no. 12, pp. 2310–2312, Jun 2012.
- [121] S. Liu, Y. Wang, C. Liao, G. Wang, Z. Li, Q. Wang, J. Zhou, K. Yang, X. Zhong, J. Zhao, and J. Tang, “High-sensitivity strain sensor based on in-fiber improved Fabry-Perot interferometer,” Accepted 2014.
- [122] A. Micco, G. Quero, A. Crescitelli, A. Ricciardi, and A. Cusano, “Ultracompact optical fiber fabry-perot interferometer based on in-line integrated sub-micron silicon film,” pp. 87 940P–87 940P–4, 2013. [Online]. Available: <http://dx.doi.org/10.1117/12.2025866>
- [123] C. Yin, Z. Cao, Z. Zhang, T. Shui, R. Wang, J. Wang, L. Lu, S. Zhen, and B. Yu, “Temperature-independent ultrasensitive fabry-perot all-fiber strain sensor based on a bubble-expanded microcavity,” *Photonics Journal, IEEE*, vol. 6, no. 4, pp. 1–9, Aug 2014.
- [124] J. Davis, Ed., *Stainless steels*. ASM International, 1994.
- [125] S. Spinner, “Elastic moduli of glasses at elevated temperatures by a dynamic method,” *Journal of the American Ceramic Society*, vol. 39, no. 3, pp. 113–118, 1956. [Online]. Available: <http://dx.doi.org/10.1111/j.1151-2916.1956.tb15634.x>
- [126] T. Rouxel, “Elastic properties and short-to medium-range order in glasses,” *Journal of the American Ceramic Society*, vol. 90, no. 10, pp. 3019–3039, 2007. [Online]. Available: <http://dx.doi.org/10.1111/j.1551-2916.2007.01945.x>
- [127] L. Govaert, B. Brown, and P. Smith, “Temperature dependence of the young’s modulus of oriented polyethylene,” *Macromolecules*, vol. 25, no. 13, pp. 3480–3483, 1992. [Online]. Available: <http://dx.doi.org/10.1021/ma00039a027>
- [128] M. Kutz, Ed., *Applied Plastics Engineering Handbook*. William Andrew, 2011.

- [129] COMSOL inc. (2014) Comsol multiphysics. [Online]. Available: www.comsol.com
- [130] U. Tan, B. Yang, R. Gullapalli, and J. Desai, "Triaxial mri-compatible fiber-optic force sensor," *Robotics, IEEE Transactions on*, vol. 27, no. 1, pp. 65–74, Feb 2011.
- [131] Granta Design Limited. (2014) CES Edupack 2014.
- [132] R. Freitas. (2003) Thermography of the human body. [Online]. Available: <http://www.nanomedicine.com/NMI/8.4.1.1.htm> [Accessed: 7/1/2015]
- [133] M. N. Polyanskiy. (2014) Refractive index database. [Online]. Available: <http://refractiveindex.info>
- [134] M. Silva-López, A. Fender, W. N. MacPherson, J. S. Barton, J. D. C. Jones, D. Zhao, H. Dobb, D. J. Webb, L. Zhang, and I. Bennion, "Strain and temperature sensitivity of a single-mode polymer optical fiber," *Opt. Lett.*, vol. 30, no. 23, pp. 3129–3131, Dec 2005. [Online]. Available: <http://ol.osa.org/abstract.cfm?URI=ol-30-23-3129>
- [135] The Quartz Corp. Quartz glass properties. [Online]. Available: <http://www.thequartzcorp.com/en/applications/quartz-glass/quartz-glass-properties.html> [Accessed: 10/1/15]
- [136] Z. Zhang, P. Zhao, P. Lin, and F. Sun, "Thermo-optic coefficients of polymers for optical waveguide applications," *Polymer*, vol. 47, no. 14, pp. 4893 – 4896, 2006. [Online]. Available: <http://www.sciencedirect.com/science/article/pii/S0032386106006367>
- [137] X. Tan, Y. Geng, X. Li, Y. Deng, Z. Yin, and R. Gao, "Uv-curable polymer microhemisphere-based fiber-optic fabry-perot interferometer for simultaneous measurement of refractive index and temperature," *Photonics Journal, IEEE*, vol. 6, no. 4, pp. 1–8, Aug 2014.
- [138] D. Chavan, "Applications of fiber-top technology for material property characterization at nanoscale," Ph.D. dissertation, Vrije Universiteit Amsterdam, January 2014.
- [139] D. K. N. K. D. G. M. Ree, K.J. Chen, "Anisotropic properties of high-temperature polyimide thin films: dielectric and thermal-expansion behaviors," vol. 72, no. 5, 1992.
- [140] M. Ghorbanpour and C. Falamaki, "A novel method for the production of highly adherent au layers on glass substrates used in surface plasmon resonance analysis: substitution of cr or ti intermediate layers with ag layer followed by an optimal annealing treatment," vol. 3, no. 6, 2013.
- [141] Wikipedia. (2015, 1) Titanium. [Online]. Available: <http://en.wikipedia.org/wiki/Titanium> [Accessed: 10/1/2015]
- [142] ——. (2014, 12) Chromium. [Online]. Available: <http://en.wikipedia.org/wiki/Chromium> [Accessed: 10/1/15]
- [143] G. Gruca, S. de Man, M. Slaman, J. H. Rector, and D. Iannuzzi, "Ferrule-top micromachined devices: a new approach to fibre-top technology," vol. 7503, 2009, pp. 750 381–750 381–4.
- [144] ILSINTECH. Fiber cleaver products. [Online]. Available: <http://www.ilsintech.com/eng/sub/s2.asp?code=2>

- [145] J. Jackson. (2011) Mechanical splice with keyed angle cleave fibers. 3M. [Online]. Available: <http://multimedia.3m.com/mws/media/722424O/mechanical-splice-with-keyed-angle-cleave-fibers-white-paper.pdf> [Accessed: 10/1/2015]
- [146] J. Hanlon, *A User's Guide to Vacuum Technology*, 3rd ed. John Wiley & Sons, Ltd, 2003.
- [147] A. Roth, *Vacuum sealing techniques*. AIP Press, 1994.
- [148] A. van Beek, *Advanced engineering design*. Delft University of Technology, 2009.
- [149] MasterBond. Poisson's ratio and elongation. [Online]. Available: <http://www.masterbond.com/techtips/modulus-poisson\OT1\textquoterights-ratio-and-elongation> [Accessed: 7/1/15]
- [150] Norland Products. Norland adhesive selection guide. [Online]. Available: <https://www.norlandprod.com/adhchart.html> [Accessed: 7/1/2015]
- [151] P. R. Yoder, *Opto-Mechanical Systems Design*, 3rd ed. CRC Press, 2006.
- [152] E. A. Fisher. Adhesives for fiber optics assembly. Henkel Corp. [Online]. Available: <http://www.photonics.com/EDU/Handbook.aspx?AID=25147> [Accessed: 7/1/15]
- [153] Epoxy Technology. Epoxy adhesive application guide. [Online]. Available: http://www.epotek.com/site/files/brochures/pdfs/adhesive_application_guide.pdf [Accessed: 22/3/2015]
- [154] H. Kals, *Industriële productie*, 4th ed. Academic Service, 2007.
- [155] J. Lin, P. Deng, G. Lam, B. Lu, Y. K. Lee, and Y.-C. Tai, "Creep of parylene-c film," in *Solid-State Sensors, Actuators and Microsystems Conference (TRANSDUCERS), 2011 16th International*, June 2011, pp. 2698–2701.
- [156] Fujifilm. Polyamic acid. durimide 100. technical product information. [Online]. Available: http://www.fujifilm.ca/shared/bin/Durimide%20100_US12.pdf [Accessed: 12/3/2015]
- [157] VSI Parylene. Parylene specifications. [Online]. Available: <http://vsiparylene.com/pdf/ParyleneProperties2013.pdf> [Accessed: 8/1/2015]
- [158] M. Ashby, *Materials engineering, science, processing and design*, 2nd ed. Butterworth-Heinemann, 2010.
- [159] R. Norton, *Machine Design*, 3rd ed. Prentice Hall, 2006.
- [160] Epoxy Technology. Understanding mechanical properties of epoxies for modeling, finite element analysis (fea). [Online]. Available: <http://www.epotek.com/site/files/Techtips/pdfs/tip19.pdf> [Accessed: 22/3/2015]
- [161] Machined Glass Specialists, Inc. Fused quartz. [Online]. Available: <http://www.mgsfusedquartz.com/fusedquartz.html> [Accessed: 4/March/2015]
- [162] Corning. Corning SMF-28e+ Optical Fiber. [Online]. Available: <http://www.corning.com/WorkArea/showcontent.aspx?id=63939> [Accessed: 22/1/2015]

- [163] Optics11. Op1550. [Online]. Available: http://optics11.com/images/optics11-op1550_universal-tunable-wavelength-interferometer.pdf [Accessed: 12/9/2014]
- [164] ISO-376, "Metallic materials - calibration of force-proving instruments used for the verification of uniaxial testing machines," International Organization for Standardization, International Standard, 2011.
- [165] D. Zipperian. (2002) Silicon carbide abrasive grinding. /10/2014]
- [166] R. Driggers, Ed., *Encyclopedia of Optical Engineering*. Marcel Dekker, Inc., 2003, vol. 1.
- [167] D. Stöckel. Nitinol - material with unusual properties. /4/2015]
- [168] C. Bruce and W. Clothier, "Optical properties of thin chromium films," vol. 64, no. 6, 1974.
- [169] HD Microsystems. (2008) Vm-651 and vm-652 adhesion promoters. [Online]. Available: http://hdmicrosystems.com/HDMicroSystems/en_US/pdf/VM-651_VM-652_ProductBulletin.pdf
- [170] A. Mitra, I. Kouzmina, and M. Lopez. (2003) Thermal Stability of the CPC Fiber Coating System. [Online]. Available: <http://www.corning.com/WorkArea/downloadasset.aspx%3Fid%3D37455&prev=search>
- [171] C.-T. Kuo, M.-C. Yip, and K.-N. Chiang, "Time and temperature dependent mechanical characterization of polyimide materials in electronic packaging application," in *Electronics Packaging Technology Conference, 2002. 4th, Dec 2002*, pp. 413–421.
- [172] S. Ando, "Optical properties of fluorinated polyimides and their applications to optical components and waveguide circuits," vol. 17, no. 2, 2004.
- [173] Z. Zhang, G. Lefever-Button, and F. Powell, "Infrared refractive index and extinction coefficient of polyimide films," vol. 19, no. 3, 1998.
- [174] Wikipedia. (2015) Plastic optical fiber. [Online]. Available: http://en.wikipedia.org/wiki/Plastic_optical_fiber [Accessed: March/28/2015]
- [175] D. Bodas, R. Dabhade, S. Patil, and S. Gangal, "Comparative study of spin coated and sputtered pmma as an etch mask for silicon micromachining," in *Micromechatronics and Human Science, 2001. MHS 2001. Proceedings of 2001 International Symposium on, 2001*, pp. 51–56.
- [176] Wikipedia. (2015) Poly(methyl methacrylate). [Online]. Available: [http://en.wikipedia.org/wiki/Poly\(methyl_methacrylate\)](http://en.wikipedia.org/wiki/Poly(methyl_methacrylate)) [Accessed: 28/3/2015]
- [177] NOS. (2015) Veelgebruikte injectienaalden onveilig. [Online]. Available: <http://nos.nl/artikel/2026472-veelgebruikte-injectienaalden-onveilig.html>
- [178] Medical Metals, LLC. Materials. [Online]. Available: http://www.medicalmetals.com/?page_id=6 [Accessed: 30/3/2015]
- [179] Wikipedia. (2014) Nivarox. [Online]. Available: <http://en.wikipedia.org/wiki/Nivarox> [Accessed: 30/3/2015]

- [180] K. M. Kennedy, R. A. McLaughlin, B. F. Kennedy, A. Tien, B. Latham, C. M. Saunders, and D. D. Sampson, "Needle optical coherence elastography for the measurement of microscale mechanical contrast deep within human breast tissues," *Journal of Biomedical Optics*, vol. 18, no. 12, p. 121510, 2013.
- [181] X. Chen, F. Shen, Z. Wang, Z. Huang, and A. Wang, "Micro-air-gap based intrinsic Fabry-Perot interferometric fiber-optic sensor," *Applied Optics*, vol. 45, no. 30, pp. 7760–7766, Oct 2006.
- [182] M. Jiang and E. Gerhard, "A simple strain sensor using a thin film as a low-finesse fiber-optic Fabry-Perot interferometer," *Sensors and Actuators A: Physical*, vol. 88, no. 1, pp. 41 – 46, 2001.
- [183] J. Vaughan, *The Fabry-Perot Interferometer*. IOP Publishing Ltd, 1989.
- [184] B. T. Cox, E. Z. Zhang, J. G. Laufer, and P. C. Beard, "Fabry Perot polymer film fibre-optic hydrophones and arrays for ultrasound field characterisation," *Journal of Physics: Conference Series*, vol. 1, no. 1, p. 32, 2004.
- [185] D. Duan, Y. Rao, Y. Hou, and T. Zhu, "Microbubble based fiber-optic Fabry-Perot interferometer formed by fusion splicing single-mode fibers for strain measurement," *Applied Optics*, vol. 51, no. 8, pp. 1033–1036, Mar 2012.
- [186] W. Drexler and J. Fujimoto, *Optical Coherence Tomography*. Springer-Verlag, 2008.
- [187] Y. Rao, M. R. Cooper, D. Jackson, C. Pannell, and L. Reekie, "Absolute strain measurement using an in-fibre-bragg-grating-based Fabry-Perot sensor," *Electronics Letters*, vol. 36, no. 8, pp. 708–709, Apr 2000.
- [188] D. Chavan, T. C. van de Watering, G. Gruca, J. H. Rector, K. Heeck, M. Slaman, and D. Iannuzzi, "Ferrule-top nanoindenter: An optomechanical fiber sensor for nanoindentation," *Review of Scientific Instruments*, vol. 83, no. 11, pp. –, 2012.
- [189] D. Chavan, D. Andres, and D. Iannuzzi, "Note: Ferrule-top atomic force microscope. ii. imaging in tapping mode and at low temperature," *Review of Scientific Instruments*, vol. 82, no. 4, pp. –, 2011.
- [190] Y. Jiang and W. Ding, "Recent developments in fiber optic spectral white-light interferometry," vol. 1, no. 1, pp. 62–71, 2011.
- [191] Z. Yaqoob, J. Wu, and C. Yang, "Spectral domain optical coherence tomography: a better OCT imaging strategy," *Biotechniques*, vol. 39, 2005.
- [192] J. Izatt and M. Choma, *Theory of Optical Coherence Tomography*. Springer, 2008.
- [193] R. K. Wang, S. Kirkpatrick, and M. Hinds, "Phase-sensitive optical coherence elastography for mapping tissue microstrains in real time," *Applied Physics Letters*, vol. 90, no. 16, pp. 164 105–164 105–3, Apr 2007.
- [194] R. K. Wang, Z. Ma, and S. J. Kirkpatrick, "Tissue doppler optical coherence elastography for real time strain rate and strain mapping of soft tissue," *Applied Physics Letters*, vol. 89, no. 14, pp. –, 2006.
- [195] S. J. Kirkpatrick, R. K. Wang, and D. D. Duncan, "OCT-based elastography for large and small deformations," *Optics Express*, vol. 14, no. 24, pp. 11 585–11 597, Nov 2006.

- [196] O. Heavens, *Optical Properties of Thin Solid Films*. Dover Publications, 1995.
- [197] G. Gruca, D. Chavan, A. Cipullo, K. Babaei Gavan, F. De Filippis, A. Minardo, J. Rector, K. Heek, L. Zeni, and D. Iannuzzi, "Development of fiber optic ferrule-top cantilevers for sensing and beam-steering applications," vol. 8439, 2012, pp. 84 390E–84 390E–7.
- [198] A. A. Said, M. Dugan, S. de Man, and D. Iannuzzi, "Carving fiber-top cantilevers with femtosecond laser micromachining," *Journal of Micromechanics and Microengineering*, vol. 18, no. 3, p. 035005, 2008.
- [199] T. Wei, Y. Han, H.-L. Tsai, and H. Xiao, "Miniaturized fiber inline Fabry-Perot interferometer fabricated with a femtosecond laser," *Optics Letters*, vol. 33, no. 6, pp. 536–538, Mar 2008.
- [200] Y. Rao, M. Deng, D.-W. Duan, X.-C. Yang, T. Zhu, and G.-H. Cheng, "Micro Fabry-Perot interferometers in silica fibers machined by femtosecond laser," *Optics Express*, vol. 15, no. 21, pp. 14 123–14 128, Oct 2007.
- [201] G. Gruca, S. de Man, M. Slaman, J. H. Rector, and D. Iannuzzi, "Ferrule-top micromachined devices: design, fabrication, performance," *Measurement Science and Technology*, vol. 21, no. 9, p. 094033, 2010.
- [202] K. B. Gavan, J. H. Rector, K. Heeck, D. Chavan, G. Gruca, T. H. Oosterkamp, and D. Iannuzzi, "Top-down approach to fiber-top cantilevers," vol. 36, pp. 2898–2900, 2011.
- [203] A. Petrusis, J. H. Rector, K. Smith, S. de Man, and D. Iannuzzi, "The align-and-shine technique for series production of photolithography patterns on optical fibres," *Journal of Micromechanics and Microengineering*, vol. 19, no. 4, p. 047001, 2009.
- [204] D. Abeysinghe, S. Dasgupta, J. T. Boyd, and H. E. Jackson, "A novel mems pressure sensor fabricated on an optical fiber," *Photonics Technology Letters, IEEE*, vol. 13, no. 9, pp. 993–995, Sept 2001.
- [205] S. Gao, W. Zhang, Z. Bai, H. Zhang, W. Lin, L. Wang, and J. Li, "Microfiber-enabled in-line Fabry-Pérot interferometer for high-sensitive force and refractive index sensing," *Lightwave Technology, Journal of*, vol. PP, no. 99, pp. 1–1, 2014.
- [206] C. J. Alberts, S. de Man, J. W. Berenschot, V. J. Gadgil, M. C. Elwenspoek, and D. Iannuzzi, "Fiber-top refractometer," *Measurement Science and Technology*, vol. 20, no. 3, p. 034005, 2009.
- [207] D. Iannuzzi, S. de Man, C. J. Alberts, J. W. Berenschot, M. C. Elwenspoek, A. A. Said, and M. Dugan, "Fiber-top micromachined devices," vol. 7004, 2008, pp. 700 403–700 403–4.
- [208] D. Jáuregui-Vázquez, J. M. Estudillo-Ayala, R. Rojas-Laguna, E. Vargas-Rodríguez, J. M. Sierra-Hernández, J. C. Hernández-García, and R. I. Mata-Chávez, "An all fiber intrinsic Fabry-Perot interferometer based on an air-microcavity," *Sensors*, vol. 13, no. 5, pp. 6355–6364, 2013.
- [209] C. J. Tuck, R. Hague, and C. Doyle, "Low cost optical fibre based Fabry-Perot strain sensor production," *Measurement Science and Technology*, vol. 17, no. 8, p. 2206, 2006.
- [210] V. Machavaram, R. Badcock, and G. Fernando, "Fabrication of intrinsic fibre Fabry-Perot sensors in silica fibres using hydrofluoric acid etching," *Sensors and Actuators A: Physical*, vol. 138, no. 1, pp. 248 – 260, 2007.

- [211] Y. Gong, Y. Rao, Y. Guo, Z. Ran, and Y. Wu, "Temperature-insensitive micro Fabry Pérot strain sensor fabricated by chemically etching er-doped fiber," *Photonics Technology Letters, IEEE*, vol. 21, no. 22, pp. 1725–1727, Nov 2009.
- [212] P. Tafulo, P. Jorge, J. Santos, F. Araujo, and O. Frazao, "Intrinsic Fabry Pérot cavity sensor based on etched multimode graded index fiber for strain and temperature measurement," *Sensors Journal, IEEE*, vol. 12, no. 1, pp. 8–12, Jan 2012.
- [213] E. Li, G. Peng, and X. Ding, "High spatial resolution fiber-optic fizeau interferometric strain sensor based on an in-fiber spherical microcavity," *Applied Physics Letters*, vol. 92, no. 10, pp. –, 2008.
- [214] J. Villatoro, V. Finazzi, G. Coviello, and V. Pruneri, "Photonic-crystal-fiber-enabled micro-Fabry–Perot interferometer," *Optics Letters*, vol. 34, no. 16, pp. 2441–2443, Aug 2009.
- [215] M. S. Ferreira, J. Bierlich, J. Kobelke, K. Schuster, J. L. Santos, and O. Frazão, "Towards the control of highly sensitive Fabry-Pérot strain sensor based on hollow-core ring photonic crystal fiber," *Opt. Express*, vol. 20, no. 20, pp. 21 946–21 952, Sep 2012.
- [216] H. Su, M. Zervas, C. Furlong, and G. S. Fischer, "A miniature mri-compatible fiber-optic force sensor utilizing fabry-perot interferometer," in *MEMS and Nanotechnology, Volume 4*. Springer, 2011, pp. 131–136.
- [217] A. Wang, H. Xiao, R. G. May, J. Wang, W. Zhao, J. Deng, P. Zhang, and G. R. Pickrell, "Optical fiber sensors for harsh environments," in *International Conference on Sensors and Control Techniques (ICSC2000)*. International Society for Optics and Photonics, 2000, pp. 2–6.
- [218] J. Murphy, "Temperature & humidity control in surgery rooms," *ASHRAE Journal*, vol. 48, no. 6, 2006.
- [219] K. A. Murphy, M. F. Gunther, R. G. May, R. O. Claus, T. A. Tran, J. A. Greene, and P. G. Duncan, "Efpi sensor manufacturing and applications," pp. 476–482, 1996. [Online]. Available: <http://dx.doi.org/10.1117/12.239154>
- [220] A. Wang, "Optical fiber sensors for energy-production and energy-intensive industries," pp. 377–381, 2002. [Online]. Available: <http://dx.doi.org/10.1117/12.481999>
- [221] Q. Yu and X. Zhou, "Pressure sensor based on the fiber-optic extrinsic fabry-perot interferometer," *Photonic Sensors*, vol. 1, no. 1, pp. 72–83, 2011.
- [222] D.-H. Kim, J.-W. Park, H.-K. Kang, C.-S. Hong, and C.-G. Kim, "Measuring dynamic strain of structures using a gold-deposited extrinsic fabry–perot interferometer," *Smart materials and structures*, vol. 12, no. 1, p. 1, 2003.
- [223] P. Morris, A. Hurrell, A. Shaw, E. Zhang, and P. Beard, "A fabry–pérot fiber-optic ultrasonic hydrophone for the simultaneous measurement of temperature and acoustic pressure," *The Journal of the Acoustical Society of America*, vol. 125, no. 6, pp. 3611–3622, 2009.
- [224] D. Wu, T. Zhu, G. Wang, J. Fu, X. Lin, and G. Gou, "Intrinsic fiber-optic Fabry-Perot interferometer based on arc discharge and single-mode fiber," *Appl. Opt.*, vol. 52, no. 12, pp. 2670–2675, Apr 2013.

- [225] W. Tsai and C. Lin, "A novel structure for the intrinsic Fabry-Perot fiber-optic temperature sensor," *Lightwave Technology, Journal of*, vol. 19, no. 5, pp. 682–686, May 2001.
- [226] W. Du, X. Tao, and H. Tam, "Fiber bragg grating cavity sensor for simultaneous measurement of strain and temperature," *Photonics Technology Letters, IEEE*, vol. 11, no. 1, pp. 105–107, Jan 1999.
- [227] B. Guan, H. Tam, X. Tao, and X. Dong, "Simultaneous strain and temperature measurement using a superstructure fiber bragg grating," *Photonics Technology Letters, IEEE*, vol. 12, no. 6, pp. 675–677, June 2000.
- [228] ISO-5725-1, "Accuracy (trueness and precision) of measurement methods and results," International Organization for Standardization, International Standard, 1994.
- [229] "The international system of units (si)," Bureau International des Poids et Mesures, Tech. Rep., 2006. [Online]. Available: <http://www.bipm.org/en/publications/si-brochure/>
- [230] Mettler-Toledo. Mettler toledo balance types. [Online]. Available: http://www.mettler-toledo-support.com/fonte/pdf_downloader/download [Accessed: 2/12/2014]
- [231] ——. (2001) Operating instructions pe360 deltarange. [Online]. Available: https://www.labmakelaar.com/fjc_documents/5768_mettler-pe360-3600-manual.pdf [Accessed: 3/12/2014]
- [232] Scaltec. The professional line. [Online]. Available: <http://www.precisionbalance.co.uk/productattachments/index/download?id=179> [Accessed: 3/12/2014]
- [233] Mikrocentrum, *Werktuigbouw.nl Formuleboekje*, 2nd ed. Mikrocentrum.
- [234] T. Podder, D. Clark, J. Sherman, D. Fuller, E. Messing, D. Rubens, J. Strang, Y. Zhang, W. O'Dell, W. Ng *et al.*, "Effects of tip geometry of surgical needles: an assessment of force and deflection," in *IFMBE Proc*, vol. 11, no. 1, 2005, pp. 1727–1983.
- [235] S. Misra, K. Reed, B. Schafer, K. Ramesh, and A. Okamura, "Observations and models for needle-tissue interactions," in *Robotics and Automation, 2009. ICRA '09. IEEE International Conference on*, May 2009, pp. 2687–2692.
- [236] Wikipedia. (2014, 8) Human body temperature. [Online]. Available: http://en.wikipedia.org/wiki/Human_body_temperature [Accessed: 4/9/2013]
- [237] Veelgestelde vragen over de operatiekamer. [Online]. Available: <https://www.cwz.nl/patient/operatie-met-anesthesie/algehele-anesthesie/veelgestelde-vragen-operatiekamer.html>
- [238] F. Ellis, "The control of operating-suite temperatures," vol. 20, no. 4, pp. 284–287, 1963.
- [239] Association of periOperative Registered Nurses. (2013, 08) Environment of care. [Online]. Available: http://www.aorn.org/Clinical_Practice/Clinical_FAQs/Environment_of_Care.aspx#e [Accessed: 10/9/2014]
- [240] ANSI/ASHRAE/ASHE Standard 170-2008, "Ventilation of healthcare facilities," American Society of Heating, Refrigerating and Air-Conditioning Engineers, Standard, 2010.
- [241] Daily weather data for the netherlands. [Online]. Available: http://www.knmi.nl/climatology/daily_data/selection.cgi [Accessed: 8/9/2014]

- [242] J. J. Monzón, L. L. Sánchez-Soto, and E. Bernabeu, "Influence of coating thickness on the performance of a fabry–perot interferometer," *Appl. Opt.*, vol. 30, no. 28, pp. 4126–4132, Oct 1991. [Online]. Available: <http://ao.osa.org/abstract.cfm?URI=ao-30-28-4126>
- [243] J. J. Carr, S. L. Saikkonen, and D. H. Williams, "Refractive index measurements on single-mode fiber as functions of product parameters, tensile stress, and temperature," *Fiber and Integrated Optics*, vol. 9, no. 4, pp. 393–396, 1990.
- [244] J. A. Stone and J. H. Zimmerman. (2004, 11) Index of refraction of air. [Online]. Available: <http://emtoolbox.nist.gov/Wavelength/Ciddor.asp> [Accessed: 10/9/2014]
- [245] J. Fortuin, F. van Herwijnen, P. Leijendeckers, G. de Roeck, and G. Schwippert, *Polytechnisch Zakboek*, 51st ed. Reed business, 2006.
- [246] R. Hibbler, *Mechanics of Materials*, 7th ed. Pearson Prentice Hall, 2008.
- [247] R. Hummel, *Understanding Materials Science*, 2nd ed. Springer-Verlag, 2004.
- [248] Heraeus. (2014) Mechanical properties, strength and reliability. [Online]. Available: http://heraeus-quarzglas.com/en/quarzglas/mechanicalproperties/Mechanical_properties.aspx [Accessed: 4/3/2015]
- [249] Y. Bellouard, "On the bending strength of fused silica flexures fabricated by ultrafast lasers," vol. 1, no. 5, 2011.
- [250] K. N. R. Budynas, *Shingley's Mechanical Engineering Design*, 8th ed. McGraw Hill, 2006.
- [251] Norland Products. Norland optical adhesive 61. [Online]. Available: <https://www.norlandprod.com/adhesives/noa61pg2.html> [Accessed: 19/3/2015]
- [252] Thorlabs. Uv-curing optical adhesives. [Online]. Available: <https://www.norlandprod.com/adhchart.htmlhttps://www.norlandprod.com/adhchart.html> [Accessed: 16/3/2015]
- [253] Henkel. (2003) Loctite 350 technical datasheet. [Online]. Available: [https://tds.us.henkel.com/NA/UT/HNAUTTDS.nsf/web/5726B8F27E889FAC8525774500689015/\\$File/350-EN.pdf](https://tds.us.henkel.com/NA/UT/HNAUTTDS.nsf/web/5726B8F27E889FAC8525774500689015/$File/350-EN.pdf)
- [254] ——. (2003) Loctite 267423 loctite uv 350, 50ml. [Online]. Available: <http://nl.farnell.com/loctite/267423/loctite-uv-350-50ml/dp/1769536> [Accessed: 16/3/2015]
- [255] Epoxy Technology. (2014) Epo-tek 353nd technical data sheet. [Online]. Available: <http://oldwww.epotek.com/SSCDocs/datasheets/353ND.PDF>
- [256] W. Sandberg, R. Urman, and J. Ehrenfeld, *The MGH Textbook of Anesthetic Equipment*. Churchill Livingstone, 2010.
- [257] ISO-9626, "Stainless steel needle tubing for manufacture of medical devices," International Organization for Standardization, Technical Report ISO 9626:1991(E).
- [258] Becton, Dickinson and Company. (-) Needle/syringe facts. [Online]. Available: http://www.bd.com/hypodermic/pdf/needle_syringe_facts.pdf [Accessed: 2/2/2014]

Symbols and nomenclature

Symbols

Symbol	Name	Units
b	width	meter (m)
c	compliance	meter per Newton (m/N)
CTE	Coefficient of Thermal Expansion	microstrain per Kelvin ($\mu\text{strain}/K$)
d	diameter	meter (m)
E	Young's modulus	Pascal (Pa)
F	Force	Newton (N)
G	shear modulus	Pascal (Pa)
h	height	meter (m)
I	intensity (irradiance)	Watt per square meter (W/m^2)
K	stiffness	Newton per meter (N/m)
k	extinction coefficient	[-]
L	length	meter (m)
M	moment	Newtonmeter (Nm)
n	refractive index	[-]
R	reflectance	[-]
T	temperature	degrees Celcius or degrees Kelvin (°C or K)
$\tilde{\nu}$	wave number	per meter (m^{-1})
ϵ	strain	[-]
γ	fringe visibility	[-]
ϕ	phase	radians [-]
λ	freespace optical wavelength	meter (m)
ν	Poisson's ratio	[-]
σ	(tensile/compressive) stress	Pascal (Pa)
τ	shear stress	Pascal (Pa)

Nomenclature and abbreviations

Bevel: Ground surface of the cannula tip. A cannula with a 90° bevel is blunt.

Cannula: Hollow metal tube of a needle. Conventional cannula diameters range from 10 G (3.4 mm) to 30 G (0.31 mm) [13].

Extrinsic sensor: Optical sensor in which light leaves the optical fiber.

FBG: Fiber-Bragg Grating, a type of fiber-optic sensor using wavelength modulation.

FPI: Fabry-Pérot Interferometer, a type of fiber-optic sensor using phase modulation.

Gauge: The diameter of the 'cannula' of needles is measured using the Stubbs Iron Wire Gauge system [256, 14, 257]. The needle gauge, denoted by a capital 'G', increases with decreasing diameter of the cannula [256, 13].

Half-error-interval: The 'half-error-interval' is defined as the maximum observed difference in readings of the sensor and the true value. The error-interval is thus at most twice the half-error-interval, which is the case when errors are distributed symmetric round the true value. The 'half-error-interval' should be comparable in magnitude to the expanded measurement uncertainty.

Homodyne interferometry: Interferometry using monochromatic light [109].

Hub: Fitting attached to the proximal end of the cannula, used to connect the cannula to a syringe or other system and used by the surgeon to hold the needle. The hub is typically made of plastic and color coded to define the gauge of the cannula [258].

Intrinsic sensor: Optical sensor in which light remains within the fiber.

Low coherence interferometry: Interferometry performed with non-monochromatic light with a large spectral width, sometimes called white light interferometry. A variant of homodyne interferometry capable to measure the change in OPD of an FPI over a very large/infinite range (a property of low coherence interferometry) is referred to as low coherence interferometry in this report in lack of a better name.

Lumen: Open space inside the cannula.

Needle: Slender instrument, consisting of a cannula and a hub and optionally an obturator.

Needle tip: The distal part of a cannula, specifically the part containing the bevel. The tip may also include the beveled part of the stylet.

Obturator: A rod that can be inserted in the lumen to prevent tissue from entering the lumen.

Shaft: Part of the cannula that does not belong to the tip.

Stylet: A sharp obturator that can be inserted into the lumen of a cannula with a bevel ground to match the bevel of the cannula.